

## LA-UR-20-29881

Approved for public release; distribution is unlimited.

|               |   |
|---------------|---|
| Title:        | PAGOSA Theory Manual  |
| Author(s):    | Subramanian, Gopinath Santhana Ganapathy                          |
| Intended for: | Release of theory manual to collaborators and PAGOSA users<br>Web |
| Issued:       | 2020-12-03 (rev.1)  |

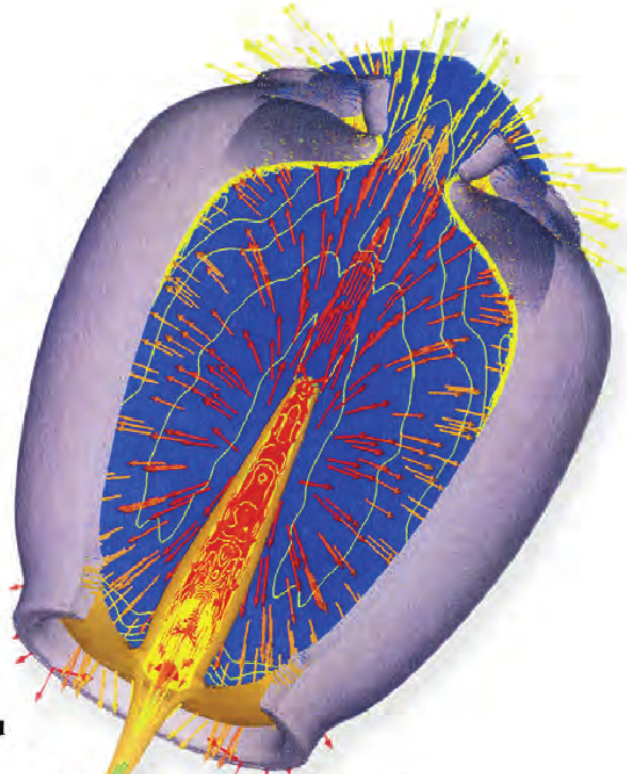
---

**Disclaimer:**

Los Alamos National Laboratory, an affirmative action/equal opportunity employer, is operated by Triad National Security, LLC for the National Nuclear Security Administration of U.S. Department of Energy under contract 89233218CNA000001. By approving this article, the publisher recognizes that the U.S. Government retains nonexclusive, royalty-free license to publish or reproduce the published form of this contribution, or to allow others to do so, for U.S. Government purposes. Los Alamos National Laboratory requests that the publisher identify this article as work performed under the auspices of the U.S. Department of Energy. Los Alamos National Laboratory strongly supports academic freedom and a researcher's right to publish; as an institution, however, the Laboratory does not endorse the viewpoint of a publication or guarantee its technical correctness.

# PAGOSA

## Theory Manual



$$\frac{\partial \rho}{\partial t} + U \frac{\partial \rho}{\partial x} + V \frac{\partial \rho}{\partial y} + W \frac{\partial \rho}{\partial z} = -\rho \nabla \cdot \mathbf{u}$$

$$\frac{\partial U}{\partial t} + U \frac{\partial U}{\partial x} + V \frac{\partial U}{\partial y} + W \frac{\partial U}{\partial z} = \frac{F_x}{\rho} - \frac{1}{\rho} \frac{\partial P}{\partial x} + \frac{1}{\rho} \left[ \frac{\partial S_{xx}}{\partial x} + \frac{\partial S_{xy}}{\partial y} + \frac{\partial S_{xz}}{\partial z} \right]$$

$$\frac{\partial V}{\partial t} + U \frac{\partial V}{\partial x} + V \frac{\partial V}{\partial y} + W \frac{\partial V}{\partial z} = \frac{F_y}{\rho} - \frac{1}{\rho} \frac{\partial P}{\partial y} + \frac{1}{\rho} \left[ \frac{\partial S_{yx}}{\partial x} + \frac{\partial S_{yy}}{\partial y} + \frac{\partial S_{yz}}{\partial z} \right]$$

$$\frac{\partial W}{\partial t} + U \frac{\partial W}{\partial x} + V \frac{\partial W}{\partial y} + W \frac{\partial W}{\partial z} = \frac{F_z}{\rho} - \frac{1}{\rho} \frac{\partial P}{\partial z} + \frac{1}{\rho} \left[ \frac{\partial S_{zx}}{\partial x} + \frac{\partial S_{zy}}{\partial y} + \frac{\partial S_{zz}}{\partial z} \right]$$

$$\frac{\partial E}{\partial t} + U \frac{\partial E}{\partial x} + V \frac{\partial E}{\partial y} + W \frac{\partial E}{\partial z} = -\frac{P}{\rho} \nabla \cdot \mathbf{u} + \frac{1}{\rho} \left[ S_{xx} \dot{e}_{xx} + S_{yy} \dot{e}_{yy} + S_{zz} \dot{e}_{zz} + 2(S_{xy} \dot{e}_{xy} + S_{xz} \dot{e}_{xz} + S_{yz} \dot{e}_{yz}) \right]$$

## Cover Art

The Eulerian three-dimensional compressible Navier Stokes equations are shown in their Cartesian component form under a PAGOSA simulation of a shaped charge at 27  $\mu\text{s}$  after detonation.

## Authorship

This manual was written by

Wayne N. Weseloh  
Sean P. Clancy  
James W. Painter

of Los Alamos National Laboratory

Los Alamos National Laboratory, an Affirmative Action/ Equal Opportunity Employer, is operated by Triad National Security, LLC, for the National Nuclear Security Administration of the U.S. Department of Energy under contract DE-AC52-06NA25396.



This report was prepared as an account of work sponsored by an agency of the U.S. Government. Neither Triad National Security, LLC, the U.S. Government nor any agency thereof, nor any of their employees make any warranty, express or implied, or assume any legal liability or responsibility for the accuracy, completeness, or usefulness of any information, apparatus, product, or process disclosed, or represent that its use would not infringe privately owned rights. Reference herein to any specific commercial product, process, or service by trade name, trademark, manufacturer, or otherwise does not necessarily constitute or imply its endorsement, recommendation, or favoring by Triad National Security, LLC, the U.S. Government, or any agency thereof. The views and opinions of authors expressed herein do not necessarily state or reflect those of Triad National Security, LLC, the U.S. Government, or any agency thereof. Los Alamos National Laboratory strongly supports academic freedom and a researcher's right to publish; as an institution, however, the Laboratory does not endorse the viewpoint of a publication or guarantee its technical correctness.

# Contents

|   |             |
|---|-------------|
| <b>Acknowledgements</b>                             | <b>xiii</b> |
| <b>Nomenclature</b>                                 | <b>xv</b>   |
| <b>1 Introduction</b>                               | <b>1</b>    |
| 1.1 Algorithm . . . . .                             | 2           |
| <b>2 Governing equations</b>                        | <b>9</b>    |
| <b>3 Eulerian grid</b>                              | <b>15</b>   |
| 3.1 Mixed cells . . . . .                           | 18          |
| 3.2 Finite differences . . . . .                    | 19          |
| 3.3 Momentum control volume . . . . .               | 19          |
| 3.4 Ghost cells . . . . .                           | 21          |
| 3.5 Grid decomposition . . . . .                    | 21          |
| <b>4 Strain rates</b>                               | <b>23</b>   |
| <b>5 Operator splitting</b>                         | <b>27</b>   |
| 5.1 Lagrangian phase . . . . .                      | 29          |
| 5.2 X-advective phase . . . . .                     | 29          |
| 5.3 Y-advective phase . . . . .                     | 30          |
| 5.4 Z-advective phase . . . . .                     | 30          |
| 5.5 Lagrangian phase . . . . .                      | 32          |
| 5.5.1 Lagrangian setup for advection . . . . .      | 34          |
| 5.6 Advection phases . . . . .                      | 35          |
| 5.6.1 Advection of momentum . . . . .               | 38          |
| 5.6.2 Energy advection . . . . .                    | 40          |
| <b>6 Integration of the hydrodynamics variables</b> | <b>41</b>   |
| 6.1 Predictor stage . . . . .                       | 43          |
| 6.2 Lagrangian velocity update . . . . .            | 45          |
| 6.3 Corrector stage . . . . .                       | 45          |
| <b>7 Equation of state</b>                          | <b>49</b>   |
| 7.1 Ideal gas EOS . . . . .                         | 50          |
| 7.2 Void EOS . . . . .                              | 50          |
| 7.3 Polynomial EOS . . . . .                        | 51          |

|           |  |           |
|-----------|--|-----------|
| 7.4       | Modified Osborne (or Quadratic) EOS . . . . .                    | 51        |
| 7.5       | Jones-Wilkins-Lee (or JWL) EOS . . . . .                         | 52        |
| 7.6       | Grüneisen (or $U_S - U_P$ ) EOS . . . . .                        | 53        |
| 7.7       | SESAME EOS . . . . .   | 54        |
| 7.7.1     | Ramp treatment . . . . .   | 55        |
| 7.7.2     | SESAME body internal energy iteration . . . . .                  | 57        |
| 7.8       | Exponential EOS . . . . .  | 58        |
| 7.9       | Davis EOS . . . . .  | 58        |
| 7.9.1     | Davis-Reactants . . . . .  | 58        |
| 7.9.2     | Products . . . . .   | 59        |
| 7.9.3     | Davis Mixing . . . . .   | 60        |
| 7.9.4     | AWSD Reactive Burn Model . . . . .                               | 60        |
| 7.10      | Becker-Kistiakowsky-Wilson High-Explosive (BKW-HE) EOS . . . . . | 62        |
| 7.10.1    | Solid components . . . . .                                       | 63        |
| 7.10.2    | Gaseous components . . . . .                                     | 63        |
| 7.10.3    | Mixed components . . . . .                                       | 64        |
| 7.11      | $P_{min}$ . . . . .  | 65        |
| <b>8</b>  | <b>Sound speed</b>   | <b>67</b> |
| 8.1       | Ideal gas EOS sound speed . . . . .                              | 69        |
| 8.2       | Void EOS sound speed . . . . .                                   | 69        |
| 8.3       | Polynomial EOS sound speed . . . . .                             | 69        |
| 8.4       | Modified Osborne (or quadratic) EOS sound speed . . . . .        | 70        |
| 8.5       | Jones-Wilkins-Lee (JWL) EOS sound speed . . . . .                | 71        |
| 8.6       | Grüneisen (or $U_S - U_P$ ) EOS sound speed . . . . .            | 71        |
| 8.7       | SESAME EOS sound speed . . . . .                                 | 72        |
| 8.8       | Exponential EOS sound speed . . . . .                            | 73        |
| 8.9       | PAGOSA sound speed . . . . .                                     | 73        |
| <b>9</b>  | <b>Artificial viscosity</b>                                      | <b>75</b> |
| <b>10</b> | <b>Computing a timestep</b>                                      | <b>79</b> |
| <b>11</b> | <b>Initial conditions</b>  | <b>83</b> |
| <b>12</b> | <b>Boundary conditions</b>                                       | <b>85</b> |
| 12.1      | Reflective boundary conditions . . . . .                         | 86        |
| 12.2      | Transmissive boundary conditions . . . . .                       | 87        |
| 12.3      | Other boundary conditions . . . . .                              | 89        |
| <b>13</b> | <b>Programmed burn</b>   | <b>91</b> |
| 13.1      | Simple point . . . . .   | 92        |
| 13.2      | Simple line . . . . .  | 93        |
| 13.3      | Simple plane . . . . .   | 93        |
| 13.4      | Simple cylinder . . . . .  | 93        |
| 13.5      | Simple sphere . . . . .  | 94        |
| 13.6      | Simple ring . . . . .  | 94        |
| 13.7      | Limitations of simple detonators . . . . .                       | 94        |
| 13.8      | Other detonation methods . . . . .                               | 96        |

|  |            |
|--|------------|
| <b>14 Divergence options</b>   | <b>97</b>  |
| 14.1 Uniform . . . . .   | 98         |
| 14.2 Void Closure . . . . .  | 98         |
| 14.3 Pressure relaxation . . . . .                                       | 100        |
| <b>15 Strength</b>   | <b>105</b> |
| 15.1 Cauchy stress tensor . . . . .                                      | 108        |
| 15.2 Strain rate splitting . . . . .                                     | 108        |
| 15.3 Yield criterion . . . . .   | 109        |
| 15.4 Flow stress models . . . . .  | 114        |
| 15.4.1 Elastic perfectly plastic . . . . .                               | 114        |
| 15.4.2 Modified Steinberg-Cochran-Guinan . . . . .                       | 114        |
| 15.4.3 Steinberg-Cochran-Guinan . . . . .                                | 115        |
| 15.4.4 Johnson-Cook (JC) . . . . .                                       | 116        |
| 15.4.5 Preston-Tonks-Wallace (PTW) . . . . .                             | 117        |
| 15.4.6 Mechanical threshold stress (MTS) . . . . .                       | 118        |
| 15.4.7 Kospall . . . . .   | 120        |
| 15.4.8 Thermal softening . . . . .                                       | 120        |
| 15.5 Work hardening . . . . .  | 121        |
| <b>16 MATCH</b>  | <b>123</b> |
| 16.1 MATCH and DEFLAGRATE Physics Description . . . . .                  | 124        |
| 16.2 MATCH-VPS . . . . .   | 124        |
| 16.3 MATCH-Hotspot . . . . .   | 124        |
| 16.4 DEFLAGRATE . . . . .  | 125        |
| 16.5 MATCH-BURN-DEFLAGRATE-SURF (future PAGOSA release) . . . . .        | 125        |
| <b>17 Fracture and damage</b>  | <b>127</b> |
| 17.1 Johnson spall . . . . .   | 128        |
| 17.2 Johnson-Cook damage . . . . .                                       | 129        |
| <b>18 Crush</b>  | <b>131</b> |
| <b>19 FLIP + MPM</b>   | <b>135</b> |
| 19.1 Overview . . . . .  | 136        |
| 19.2 Governing equations . . . . .                                       | 136        |
| 19.3 Algorithm for Mapping/Interpolation . . . . .                       | 137        |
| 19.4 FLIP+MPM Recipe . . . . .   | 138        |
| 19.4.1 Step I. Map Marker Quantities to Cells and Evaluate EOS . . . . . | 140        |
| 19.5 Use within PAGOSA . . . . .   | 140        |
| 19.6 Additional Features . . . . .                                       | 141        |
| <b>Appendices</b>  |            |
| <b>Appendix A Constitutive equations</b>                                 | <b>145</b> |
| <b>Appendix B Initial volume fraction calculation</b>                    | <b>147</b> |
| <b>Appendix C Youngs interface reconstruction</b>                        | <b>151</b> |

|   |  |            |
|---|--|------------|
| C.1   | Analytic geometry . . . . .                              | 151        |
| C.2   | Distance parameter $\rho$ . . . . .                      | 153        |
| C.3   | $\rho$ symmetry . . . . .                                | 154        |
| C.4   | Volume $v$ . . . . .                                     | 155        |
| C.5   | $v$ symmetry . . . . .                                   | 156        |
| <b>Appendix D Lagrangian phase equation</b>                             |  | <b>157</b> |
| <b>Appendix E First-, second-, and third-order advection</b>            |  | <b>159</b> |
| E.1   | First-order advection . . . . .                          | 160        |
| E.2   | Second-order advection . . . . .                         | 160        |
| E.2.1   | Third-Order Advection . . . . .                          | 161        |
| E.3   | Gradient limiters and monotonicity . . . . .             | 163        |
| E.4   | PAGOSA advection . . . . .                               | 165        |
| E.5   | Advection example: advection of a square pulse . . . . . | 167        |
| <b>Appendix F Initial timestep calculation</b>                          |  | <b>169</b> |
| <b>Appendix G Multi-material interface reconstruction for advection</b> |  | <b>171</b> |
| G.1   | Reconstruction . . . . .                                 | 171        |
| G.2   | Volume fraction identifier . . . . .                     | 172        |
| <b>Appendix H The Cauchy-Stokes decomposition theorem</b>               |  | <b>177</b> |
| H.1   | Translation . . . . .                                    | 178        |
| H.2   | Rotation . . . . .                                       | 178        |
| H.2.1   | Dilatation . . . . .                                     | 178        |
| H.2.2   | Shear Deformation . . . . .                              | 178        |
| <b>Appendix I Stress rotation</b>                                       |  | <b>181</b> |
| <b>Appendix J Diagnostics</b>   |  | <b>185</b> |
| J.1   | Volume . . . . .   | 185        |
| J.2   | Mass . . . . .   | 185        |
| J.3   | Internal Energy . . . . .                                | 185        |
| J.4   | Kinetic Energy . . . . .                                 | 186        |
| J.5   | Elastic Distortional Energy . . . . .                    | 186        |
| J.6   | Plastic Work . . . . .                                   | 186        |
| J.7   | Mass Melted . . . . .                                    | 186        |
| J.8   | Mass Burned . . . . .                                    | 187        |
| J.9   | Mixed-Cell Statistics . . . . .                          | 187        |
| J.10  | Minimum and Maximum Statistics . . . . .                 | 187        |
| <b>Appendix K Momentum advection</b>                                    |  | <b>189</b> |
| <b>Appendix L Pin package</b>   |  | <b>191</b> |
| L.1   | Four Points . . . . .                                    | 193        |
| L.2   | Three Points . . . . .                                   | 193        |
| L.3   | Two Points . . . . .                                     | 193        |
| L.4   | One Point . . . . .                                      | 193        |



|  |            |
|--|------------|
| L.5 Zero Points . . . . .                            | 194        |
| <b>Appendix M Tracers</b>                            | <b>195</b> |
| M.1 Interpolation . . . . .                          | 196        |
| M.2 Integration . . . . .                            | 196        |
| M.3 Comments . . . . .                               | 197        |
| <b>Appendix N Symmetry of the stress tensor</b>      | <b>199</b> |
| <b>Appendix O Operator splitting revisited</b>       | <b>201</b> |
| <b>Appendix P Direction cosines (Normal vectors)</b> | <b>205</b> |
| <b>References</b>                                    | <b>213</b> |



# List of Figures

|     |   |    |
|-----|---|----|
| 1.1 | Flowchart showing an overview of the PAGOSA algorithm. Chapters and sections containing the relevant physics are hyperlinked. . . . .   | 4  |
| 1.2 | Flowchart showing the Lagrangian phase of the PAGOSA algorithm. Chapters and sections containing the relevant physics are hyperlinked. . . . .  | 5  |
| 1.3 | Flowchart showing the advection phase of the PAGOSA algorithm. Chapters and sections containing the relevant physics are hyperlinked. . . . .   | 6  |
| 3.1 | A single Eulerian cell in the computational domain . . . . .  | 16 |
| 3.2 | A cross section of the momentum control volume. The two-dimensional cut of this control volume passes through the vertex $(i, j, k)$ . . . . .  | 20 |
| 3.3 | Domain decomposition of an Eulerian grid. The example shows the grid being decomposed onto eight processors. The size and shape of the decomposed grid are the same on each processor. . . . .  | 22 |
| 4.1 | The gradient finite difference computation . . . . .  | 25 |
| 5.1 | A typical sequence of Lagrangian and advection steps . . . . .  | 31 |
| 5.2 | A cross section of an Eulerian cell showing a material interface with a direction vector $\mu$ , a volume fraction to be advected $\varepsilon$ (relative to the full cell volume Vol), and the volume fraction of the advected portion of the material $V_p$ . . . . .   | 34 |
| 5.3 | An Eulerian cell containing four materials separated by three distinct interfaces (left) is simplified into a sequence of three separate two-material (one-interface) representations (right) by accumulating materials at each step in the sequence. The accumulation order depends on the specific material priorities [e.g., the priority 1 material is treated first (second left); the priority 2 material is accumulated next (third left), followed by the priority 3 material]. The numbers refer to the priority number. . . . . | 35 |
| 5.4 | The solution of the advection equation. . . . .   | 36 |
| 5.5 | Diagram of the advection cells involved in <a href="#">Equation 5.34</a> . For a positive velocity ( $U > 0$ ), the lower portion of the diagram defines the downwind, donor, and upwind cells. The negative velocity case is shown on top. The shaded area is the advection volume. . . . .  | 37 |
| 6.1 | The integration step begins with all the variables at a time $(n)$ . The velocities are shown as triangles and the state variables as circles. The velocities are spatially centered on vertices, whereas the other state variables are cell centered. . . . .  | 43 |

|      |  |     |
|------|--|-----|
| 6.2  | The predictor integration step advances the state variables to a time $(n + 1/2)$ . The velocities are advanced to a time $(n + 1)$ using the state variables, which are evaluated at a time $(n + 1/2)$ . . . . .   | 44  |
| 6.3  | The Lagrangian velocity update first integrates the velocities to the time $(n + 1)$ . It then averages the two velocities to create a temporally centered velocity $u^{n+1/2}$ . . . .  | 44  |
| 6.4  | The corrector integration step uses the time-centered velocity $u^{n+1/2}$ to update the state variables from time $(n)$ to time $(n + 1)$ . . . . .   | 46  |
| 7.1  | SESAME ramp treatment for foams and certain types of phase transitions . . . . .   | 56  |
| 7.2  | Example of the use of $P_{min}$ in an EOS with a van der Waals loop. . . . .   | 65  |
| 9.1  | A typical pressure and artificial viscosity in the region of a shock. . . . .  | 77  |
| 12.1 | The reflective (symmetry) boundary conditions . . . . .  | 86  |
| 12.2 | The transmissive boundary conditions . . . . .   | 88  |
| 13.1 | An explosive is to be detonated at the point shown. The lines $\alpha$ and $\gamma$ point to regions that are directly within the line of sight of the detonator. The lines $\beta$ and $\lambda$ point to the shadow regions. The distance calculation assumptions are violated because the line-of-sight path crosses another material. . . . .  | 95  |
| 13.2 | An explosive, shown in the previous figure, is to be detonated with four distinct detonation points. Region A is the line-of-sight region, which will be detonated with detonator 1 (the original detonator). Region B is a shadow region, detonated by detonator 2. Region C is the second shadow region, detonated by detonator 3. The remaining explosive material, D, will be detonated by detonator 4. The four regions A, B, C, and D have the same material properties. . . . .   | 95  |
| 14.1 | Schematic showing two different methods of contracting void in a mixed cell. At The beginning of the Lagrangian phase (a), the mixed cell contains solid material and void. If the contraction is apportioned between solid and void according to volume fractions, then the solid is preferentially compressed (b). If the void contracts before the solid is allowed to contract, then the result is (c). . . . .  | 99  |
| 15.1 | The elastic-plastic behavior of a typical ductile material (e.g., copper). Point <b>a</b> is the proportional limit, point <b>b</b> is the yield point, point <b>c</b> is a state in the plastic regime, point <b>d</b> is the ultimate tensile strength of the material, and point <b>e</b> is the fracture point. . . . .  | 106 |
| 15.2 | The elastic-plastic behavior of a PAGOSA material with strength. . . . .   | 107 |
| 15.3 | The two possible final states for a single timestep $\Delta t$ . In the case where the transition to a final state is elastic the strain rate deviator is all elastic. On the other hand, if the transition is to a final plastic state the strain rate deviator splits into two parts: elastic and plastic. The plastic contribution must lie on the yield surface. The elastic part cannot exceed the yield surface under these circumstances. The vector $\mathbf{S}^*$ is called the elastic predictor and has the value of the stress deviator if the total strain rate deviator was all elastic. The conditions do not uniquely determine $\mathbf{S}^1$ when the final state is plastic. The condition used in PAGOSA that provides a unique solution is given by the mathematical expression $\dot{\epsilon}_{ij}^p \Delta t = \lambda S_{ij}^1$ . . . . . | 112 |
| 15.4 | The vector components of an elastic-plastic state. . . . .   | 112 |
| 15.5 | An elastic-perfectly plastic material. . . . .   | 115 |

|      |  |     |
|------|--|-----|
| 15.6 | The thermal softening function $F_{melt}$ as a function of the specific internal energy. In the limit $\delta \rightarrow 0$ , the term becomes a step function. . . . .   | 121 |
| 19.1 | Schematic of a poor man's 2 <sup>nd</sup> order weighting of a <i>cell centered</i> particle that is scattered to the surrounding cells. While the particle is not shown, it is at the center of the middle cell. The yellow dashed lines refer to the "footprint" discussed in the text. . . . .  | 139 |
| B.1  | Volume fractions of a mixed cell containing three materials (four interfaces). . . . .   | 147 |
| B.2  | A pathological case where some materials can go missing from a cell. . . . .   | 148 |
| B.3  | Exact volume fractions and ideal interfaces. The ideal values for the volume fractions are 0.0%, $\frac{1}{12}\pi$ , $\frac{\sqrt{3}}{4} + \frac{1}{4} \approx 31.51467\%$ , $\frac{1}{3}\pi + \frac{\sqrt{3}}{2} - 1 \approx 91.322295\%$ , and 100%. . . . .   | 149 |
| B.4  | Reconstructed interfaces and volume fractions based on the PAGOSA initial volume fraction algorithm with a small sampling density. . . . .   | 150 |
| C.1  | Tetrahedron bounded by the $(\mu, \rho)$ plane . . . . .   | 152 |
| D.1  | Lagrangian expansion of a fluid . . . . .  | 158 |
| E.1  | Cell advection diagram . . . . .   | 159 |
| E.2  | Upwind, downwind, and third-order gradients . . . . .  | 164 |
| E.3  | The Youngs/van Leer gradient limiter. When (a), the gradients are monotonic, or when (b), the gradients indicate that the density has reached a local maximum (minimum). . . . .   | 165 |
| E.4  | Advection of a square pulse . . . . .  | 168 |
| G.1  | The advection volume (shown in yellow) contains three materials to be advected. The flux direction in this case is negative. . . . .   | 172 |
| G.2  | A cross section of an Eulerian cell showing a material interface with a direction vector $\mu$ , a volume fraction to be advected $\varepsilon$ (relative to the full cell volume $Vol$ ), and the volume fraction of the advected portion of the material $V_p$ . . . . .   | 173 |
| G.3  | The case of positive flux is simply the complement of the previous case shown in <b>Figure G.2</b> . . . . .   | 174 |
| G.4  | If we are given the volume behind the plane ( $v$ ) and the unit normal $\vec{\mu}$ , the algorithm will find the distance parameter $d$ . . . . .   | 174 |
| G.5  | The advection volume in the new coordinate system stretched to a unit cube. . . . .  | 176 |
| H.1  | The types of motion that, when superimposed, completely describes the kinematics of a small elemental mass. The cubical shape is arbitrary. . . . .  | 179 |
| L.1  | The material surface, shown as a yellow triangle, is represented as a plane possessing a unique direction vector $(\mu_1, \mu_2, \mu_3)$ that points to the pin location (shown as a blue dot). If the point $\mathbf{x}$ lies in front of the plane, the distances are positive. If the point $\mathbf{x}$ lies behind the plane, the distances are negative. . . . . | 192 |
| L.2  | A typical pin distance vs simulation time plot that points to the pin location (shown as a blue dot). If the point $\mathbf{x}$ lies in front of the plane, the distances are positive. If the point $\mathbf{x}$ lies behind the plane, the distances are negative. . . . .   | 192 |
| M.1  | A tracer particle at $(x, y, z)$ in an Eulerian cell. . . . .  | 195 |



# Acknowledgements

The authors wish to thank the many individuals who developed, documented, and commented on the original algorithms in PAGOSA. In particular, Rick Smith, Doug Kothe, Chuck Zemach, Ian Gray, Kathy Holian, Tom Bennion, Martin Torrey, and Tom Adams provided personal communications, notes, comments, and insights into the algorithmic construction of PAGOSA. The reviewers of this physics manual helped immeasurably in the quality and accuracy of the material presented. In many ways, this physics manual is the result of an archeological process. Many of the original algorithm authors have left Los Alamos National Laboratory or are now retired or deceased. Uncovering and deciphering the remaining artifacts from the original code development has been a painstaking endeavor filled with surprising moments. We thank Bob Webster, Bill Archer, and Ed Dendy for their help in the review process. Brendan Kullback and Mark Carrara assisted in verifying many of the equations and derivations presented. Thanks to the technical editor, Lisa Rothrock, for her valuable suggestions, comments, and contributions in making this document be good English.

The authors would like to additionally acknowledge the efforts and contributions of John Hopson, Burl Hall, Brad Holian, Ed Kober, Peggy Hubbard, Mike Hall, John Baumgardner, Bob Shea, John Cerutti, Phil Church, Richard Krajcik, Dave Ponton, Jay Mosso, Gary Dilts, and Jean Marshall.

## NOTICE

This version of the manual is built from two documents: (i) LA14425-M (including addenda and corrigenda): a PDF file that was originally generated using Microsoft Word, and (ii) A L<sup>A</sup>T<sub>E</sub>X format manual that was based on a translation of an older 17.3 manual generate this document.





# Nomenclature

| Term                       | Meaning   |
|----------------------------|---|
| $a$                        | characteristic speed (section 5.6)  |
| $a$                        | bulk material sound speed (subsection 7.7.1)  |
| $a_n$                      | EOS constants (section 7.3)   |
| $A$                        | JWL EOS constant (section 7.5)  |
| $A_{ijkln}$                | fourth-order tensor (Appendix A)  |
| $Area_i$                   | face areas of an Eulerian cell (Chapter 3)  |
| $b$                        | EOS constants (section 7.3)   |
| $B$                        | JWL EOS constant (section 7.5)  |
| $B_f$                      | burn fraction (section 7.5, Chapter 13)   |
| $B_t$                      | burn time (Chapter 13)  |
| $c$                        | isentropic sound speed (Chapter 8)  |
| $c_0$                      | Grüneisen EOS constant (section 7.6)  |
| $\tilde{c}$                | cell average sound speed (Chapter 9)  |
| $\mathbf{c}$               | constant vector (Chapter 4)   |
| $D$                        | discrete linear operator (Chapter 5)  |
| $D$                        | detonation velocity (Chapter 13)  |
| $D_i$                      | density gradient (section 5.6, subsection E.2.1, section E.3)   |
| $e_{ij}$                   | strain tensor (Chapter 2)   |
| $\dot{e}_{ij}$             | strain rate tensor for small strains, $\dot{e}_{ik} \equiv \partial e_{ik} / \partial t$ (Chapter 2, Chapter 4) |
| $e_{ij}^e$                 | elastic portion of the strain tensor (section 15.2)   |
| $e_{ij}^p$                 | plastic portion of the strain tensor (section 15.2)   |
| $\dot{\epsilon}_{ij}$      | deviatoric strain rate tensor (section 15.2)  |
| $E$                        | specific internal energy (per unit mass) (Chapter 2, section E.4)   |
| $E_H$                      | Hugoniot internal energy (section 7.6)  |
| $E_T$                      | tabular internal energy (SESAME) (section 7.7)  |
| $E_S$                      | energy shift (section 7.7)  |
| $E^*$                      | user-selected internal energy (subsection 7.7.2)  |
| $F$                        | function (Chapter 3, Chapter 4)   |
| $F_i$                      | body force vector, $\mathbf{F} \equiv (F_x, F_y, F_z)$ (Chapter 2)  |
| $F_{melt}$                 | flow-stress melt factor (subsection 15.4.2, subsection 15.4.3, subsection 15.4.7, subsection 15.4.8)            |
| $G$                        | shear modulus (Chapter 2, section 8.9, section 15.4)  |
| $G_0$                      | elastic-perfectly plastic shear modulus (subsection 15.4.1)   |
| $G_{max}$                  | maximum shear (section 15.4)  |
| CONTINUED ON THE NEXT PAGE |   |

| Term                       | Meaning  |
|----------------------------|--|
| $H_{melt}$                 | flow-stress melt factor (subsection 15.4.7)  |
| $i$                        | indices, $x$ , (Chapter 3)   |
| $I$                        | identity matrix/operator   |
| $j$                        | indices, $y$ , (Chapter 3)   |
| $J_n$                      | invariants of the deviatoric stress tensor ( $J_1, J_2, J_3$ ) (Chapter 2, section 15.3) |
| $k$                        | indices, $z$ , (Chapter 3)   |
| $L$                        | continuous linear operator (Chapter 5)   |
| $L$                        | length scale (Chapter 9)   |
| $m$                        | mass of an Eulerian cell (Chapter 3)   |
| Mass                       | mass on a momentum control volume (vertex mass) (Chapter 3)                              |
| $\hat{n}$                  | unit normal (C, D)   |
| $P$                        | pressure (Chapter 2, Chapter 7)  |
| $P_H$                      | Hugoniot pressure (section 7.6)  |
| $\tilde{P}$                | average cell pressure (section 6.2, Chapter 7, K)  |
| $Q$                        | artificial viscosity (Chapter 9)   |
| $Q_1$                      | linear artificial viscosity (Chapter 9)  |
| $Q_2$                      | quadratic (von Neumann) artificial viscosity (Chapter 9)                                 |
| $Q_{ik}$                   | orthogonal rotation tensor (section H.2)   |
| $R$                        | line-of-sight distance (Chapter 13)  |
| $R_1$                      | JWL EOS constant (section 7.5)   |
| $R_2$                      | JWL EOS constant (section 7.5)   |
| $R_{ij}$                   | stress rotation tensor (section H.2)   |
| $s$                        | Grüneisen EOS constant (section 7.6)   |
| $S$                        | entropy (Chapter 9)  |
| $S$                        | Youngs/van Leer advection gradient limiter (Appendix E)                                  |
| $\mathbf{S}$               | deviatoric stress tensor (Chapter 2, section 15.3, Appendix A)                           |
| $S_{ij}$                   | deviatoric stress tensor (component form) (Chapter 2, Appendix A)                        |
| $S_R$                      | scaling ratio (section 7.7)  |
| $t$                        | time (Chapter 2, Chapter 5, Chapter 6, Chapter 10, Chapter 11)                           |
| $t^n$                      | discrete time at interval (n) (2.2)  |
| $T$                        | temperature (6.9, 7.0, Chapter 9)  |
| $T$                        | solution time interval (2.2)   |
| $T_0$                      | tetrahedron volume (Appendix A)  |
| $T^*$                      | homologous temperature (subsection 15.4.4)   |
| $\mathbf{u}$               | velocity vector $\mathbf{u} \equiv (U, V, W)$ (Chapter 2, Chapter 14, section 5.1)       |
| $U$                        | x velocity component (Chapter 2)   |
| $\bar{U}$                  | face-averaged x velocity component (Chapter 4)   |
| $U_s$                      | shock velocity (section 7.6)   |
| $U_p$                      | particle velocity (section 7.6)  |
| $v$                        | truncation volume (Appendix A)   |
| $V$                        | y velocity component (Chapter 2)   |
| $\bar{V}$                  | face-averaged y velocity component (Chapter 4)   |
| $Vol$                      | cell volume (Chapter 3)  |
| $W$                        | z velocity component (Chapter 2)   |
| CONTINUED ON THE NEXT PAGE |  |

| Term                       | Meaning  |
|----------------------------|--|
| $W^e$                      | elastic distortional energy ( <a href="#">Appendix J</a> )   |
| $W^p$                      | plastic work ( <a href="#">Appendix J</a> )  |
| $\bar{W}$                  | face-averaged z velocity component ( <a href="#">Chapter 4</a> )   |
| $W_{ik}$                   | spin tensor ( <a href="#">section H.2</a> )  |
| $x$                        | Cartesian coordinate x ( <a href="#">Chapter 2</a> )   |
| $x_{min}$                  | minimum extent of the Eulerian mesh ( <a href="#">Chapter 3</a> )  |
| $x_{max}$                  | maximum extent of the Eulerian mesh ( <a href="#">Chapter 3</a> )  |
| $y$                        | Cartesian coordinate y ( <a href="#">Chapter 2</a> )   |
| $y_{min}$                  | minimum extent of the Eulerian mesh ( <a href="#">Chapter 3</a> )  |
| $y_{max}$                  | maximum extent of the Eulerian mesh ( <a href="#">Chapter 3</a> )  |
| $Y$                        | yield modulus ( <a href="#">section 15.4</a> )   |
| $Y_0$                      | elastic-perfectly-plastic yield modulus ( <a href="#">subsection 15.4.1</a> )  |
| $Y_{max}$                  | maximum yield ( <a href="#">section 15.4</a> )   |
| $z$                        | Cartesian coordinate z ( <a href="#">Chapter 2</a> )   |
| $z_{min}$                  | minimum extent of the Eulerian mesh ( <a href="#">Chapter 3</a> )  |
| $z_{max}$                  | maximum extent of the Eulerian mesh ( <a href="#">Chapter 3</a> )  |
| $\alpha$                   | exponential EOS constant ( <a href="#">section 7.8</a> )   |
| $\beta$                    | EOS constants ( <a href="#">section 7.10</a> )   |
| $\gamma$                   | EOS constants ( <a href="#">section 7.1</a> )  |
| $\gamma$                   | flow-stress constants ( <a href="#">subsection 15.4.3</a> )  |
| $\gamma'$                  | flow-stress constants ( <a href="#">subsection 15.4.3</a> )  |
| $\delta_{nk}$              | Kronecker delta ( <a href="#">Appendix A</a> , <a href="#">Appendix H</a> , <a href="#">section H.2</a> )  |
| $\varepsilon$              | internal energy per original volume ( <a href="#">Chapter 7</a> )  |
| $\varepsilon_l$            | advection coefficients ( <a href="#">section E.4</a> )   |
| $\eta$                     | Courant number ( <a href="#">section 5.6</a> ,E)   |
| $\theta$                   | angle ( <a href="#">Appendix A</a> )   |
| $\theta$                   | material temperature ( <a href="#">subsection 15.4.7</a> )   |
| $\kappa$                   | bulk modulus ( <a href="#">section 7.3</a> )   |
| $\lambda$                  | proportionality function ( <a href="#">section 15.2</a> )  |
| $\mu$                      | compression factor ( <a href="#">Chapter 7</a> )   |
| $\boldsymbol{\mu}$         | direction vector, $\boldsymbol{\mu} \equiv (\mu_1, \mu_2, \mu_3)$ ( <a href="#">Appendix C</a> )   |
| $\xi$                      | nondimensional spatial variable ( <a href="#">Appendix E</a> )   |
| $\pi_{mk}$                 | Levi-Civita pseudotensor ( <a href="#">Appendix A</a> , <a href="#">Appendix H</a> )   |
| $\rho$                     | mass density ( <a href="#">Chapter 2</a> , <a href="#">Chapter 5</a> , <a href="#">Chapter 6</a> , <a href="#">section 5.1</a> , <a href="#">Appendix E</a> , <a href="#">Appendix F</a> ) |
| $\rho$                     | distance parameter ( <a href="#">Appendix C</a> )  |
| $\rho_0$                   | nominal mass density ( <a href="#">Chapter 7</a> )   |
| $\tilde{\rho}$             | average cell density ( <a href="#">section 6.2</a> , <a href="#">section 8.9</a> , <a href="#">Chapter 9</a> )   |
| $\bar{\rho}$               | advection (cell boundary) density ( <a href="#">section 5.6</a> , <a href="#">Appendix E</a> )   |
| $\rho_T$                   | tabular density (SESAME) ( <a href="#">section 7.7</a> )   |
| $\sigma_{ik}$              | Cauchy stress tensor ( <a href="#">section 15.1</a> , <a href="#">section 15.3</a> )   |
| $\tau$                     | PTW flow-stress ( <a href="#">subsection 15.4.4</a> )  |
| $\phi$                     | scalar function ( <a href="#">Chapter 4</a> )  |
| $^{(m)}\phi$               | volume fraction of material (m) ( <a href="#">section 3.1</a> , <a href="#">Appendix B</a> )   |
| $\chi$                     | yield function argument ( <a href="#">section 15.3</a> )   |
| CONTINUED ON THE NEXT PAGE |  |

| Term          | Meaning   |
|---------------|---|
| $\psi$        | arbitrary hydrodynamic variable ( <a href="#">Chapter 3</a> , <a href="#">Chapter 5</a> )                       |
| $\omega$      | JWL EOS constant ( <a href="#">section 7.5</a> )  |
| $\omega_i$    | axial rotation vector ( <a href="#">Chapter 2</a> , <a href="#">Appendix H</a> )                                |
| $\Gamma$      | Grüneisen parameter ( <a href="#">section 7.6</a> )   |
| $\Delta x$    | cell width- $x$ dimension ( <a href="#">Chapter 3</a> )   |
| $\Delta y$    | cell width- $y$ dimension ( <a href="#">Chapter 3</a> )   |
| $\Delta z$    | cell width- $z$ dimension ( <a href="#">Chapter 3</a> )   |
| $\Omega_{ij}$ | rotation rate tensor ( <a href="#">Chapter 2</a> , <a href="#">section 15.3</a> , <a href="#">section H.2</a> ) |

In these equations, dots refer to the time derivative of the variable. The subscripts  $i$ ,  $j$ , and  $k$  can assume the values  $x$ ,  $y$ , or  $z$ . The equations are written in full three-dimensional (3D) Cartesian Cartesian component form, which should give the reader a better understanding of the equations and techniques being used in PAGOSA. To make this document as widely accessible as possible, only a modest mathematical background is presumed – essentially, a thorough understanding of calculus and vector analysis. The equations are almost always written in their 3D Cartesian component form. More elaborate technical issues are reserved for the many appendices.

# Chapter 1

## Introduction

*In the beginning, the Universe was created. This has made a lot of people very angry and been widely regarded as a bad move.*

– Douglas Adams, The Hitchhiker's Guide to the Galaxy (1979)

PAGOSA is a computational fluid dynamics program developed at LANL for the study of high-speed compressible flow and high-rate material deformation. PAGOSA is a three-dimensional Eulerian finite-difference code, solving problems with a wide variety of EOS, material strength, and explosive modeling options.

This document presents the finite difference equations that are used in the PAGOSA continuum mechanics computer code. This program is especially intended to be used for the numerical simulation of the interactions of gases, fluids, and solids.

PAGOSA is used to investigate high-pressure and high strain-rate phenomena associated with explosive driven systems, high velocity impacts, etc., where material pressures range from kilobars to megabars. At these pressures, all materials exhibit considerable volume changes so that incompressibility is not a valid assumption. These types of continuum mechanics computer codes are intended to resolve the behavior of compression and rarefaction waves generated within materials.

In common parlance, PAGOSA is called a hydrocode, wave code, or shock code. These synonyms deserve a brief digression, and the following explanation is given by Zukas[1]:

*What is a hydrocode and where did it get that ridiculous name? Hydrocodes fall into the very large category of computational continuum mechanics. They were born in the late 1950s when, following the development of the particle-in-cell (PIC) method at Los Alamos National (then Scientific) Laboratory, Robert Bjork at the Rand Corporation applied PIC to the problem of steel impacting steel and aluminum impacting aluminum at velocities of 5.5, 20 and 72 km/s. This is cited in the literature as the first numerical investigation of an impact problem. Because such impact velocities produce pressures in the colliding materials exceeding their strength by several orders of magnitude, the calculations were performed assuming hydrodynamic behavior (material strength is not considered) in the materials. Hence, the origin of the term hydrocode – a computer program for the study of very fast, very intense loading on materials and structures. Such calculations are no longer performed in hydrodynamic mode yet the old name has stuck.*

## 1.1 Algorithm

The highlights of the PAGOSA continuum mechanics computer code are:

- PAGOSA was created for simulations running on massively parallel supercomputers
- PAGOSA is a finite difference code with a Cartesian fixed orthogonal Eulerian mesh
- PAGOSA is a multi-material code – an arbitrary number of materials per cell can be easily computed and visualized
- time integration is fully explicit, with a timestep controlled by the Courant condition – the time integration is second-order accurate
- the Eulerian mesh is staggered, with cell-centered quantities (e.g., density and internal energy) and vertex-centered quantities (e.g., velocity) to increase accuracy
- a standard von Neumann artificial viscosity may be used to spread hydrodynamic shocks over several cells
- the upstream weighted, monotonicity-preserving advection scheme is conservative (total energy is not necessarily conserved during advection) – the donor cell (first-order), van Leer

(second-order), and Youngs/van Leer (third order) methods are automatically selected, depending on the local conditions and

- PAGOSA uses an efficient material interface reconstruction algorithm so that all the interfaces within a cell can be easily represented.

**Figure 1.1** shows a simplified schematic of the computational cycle. First, the strain rates, EOS, artificial viscosity, sound speeds are computed. On the first cycle, these computations are based on the initial conditions. The Courant condition (i.e., a stable timestep) for the next cycle is computed.

The Lagrangian phase integrates the equations for a single timestep. A flowchart showing the details of the integration process is shown in **Figure 1.2**. The equations of motion are solved explicitly in time.

The advection phases remap the Lagrangian variables back onto the original Eulerian mesh. A flowchart of the remap process is shown in **Figure 1.3**.

If trouble is encountered during a computational cycle, the cycle is completed, during which print and restart files are written. The error handling occurs inside the diagnostics computational block as shown in **Figure 1.1**.

**Chapter 6** presents the predictor-corrector integration scheme used for the hydrodynamics variables in the Lagrangian phase. The integration scheme consists of two parts – the predictor and the corrector. Consider the initial value problem

$$\frac{dy}{dx} = f(x, y) \quad ; \quad y(x_0) = y_0$$

The numerical solution of this differential equation is divided into intervals, or steps  $x_i$ . Given a timestep  $h$ , the predictor step creates an approximation  $y_{i+1/2}$  at the halfway point  $x_i + h/2$ . The corrector step is then applied:

$$\begin{aligned} y_{i+1/2} &= y_i + \frac{1}{2}hf(x_i, y_i) && \text{predictor} \\ y_{i+1} &= y_i + hf(x_i + h/2, y_{i+1/2}) && \text{corrector} \end{aligned}$$

This sequence completes one timestep in the PAGOSA simulation.

Conceptually, the Lagrangian phase creates a distorted mesh, which is remapped onto the original Eulerian mesh. This remap results in a transport of mass, energy, and momentum through each face of each cell of the Eulerian mesh. After the transport is complete in all three directions, new material mass densities, energies, and pressures are computed. A new velocity field is computed for the entire mesh.

Next, the boundary conditions are applied to the exterior surface of the Eulerian mesh. Symmetries in the simulation can be exploited by using reflective (symmetry) boundary conditions. In this way the computational cost of a problem can be reduced.

At the end of the Lagrangian and advection phases, all of the materials with strength are subjected to the yield criteria. Materials that have deformed beyond their elastic regime have “yielded” and flow plastically. The elastic-plastic von Mises yield criteria are described in **Chapter 15**.

The governing equations representing the well-known conservation laws of mass, momentum, and energy are given in **Chapter 2**. The complete sets of equations solved by PAGOSA are presented

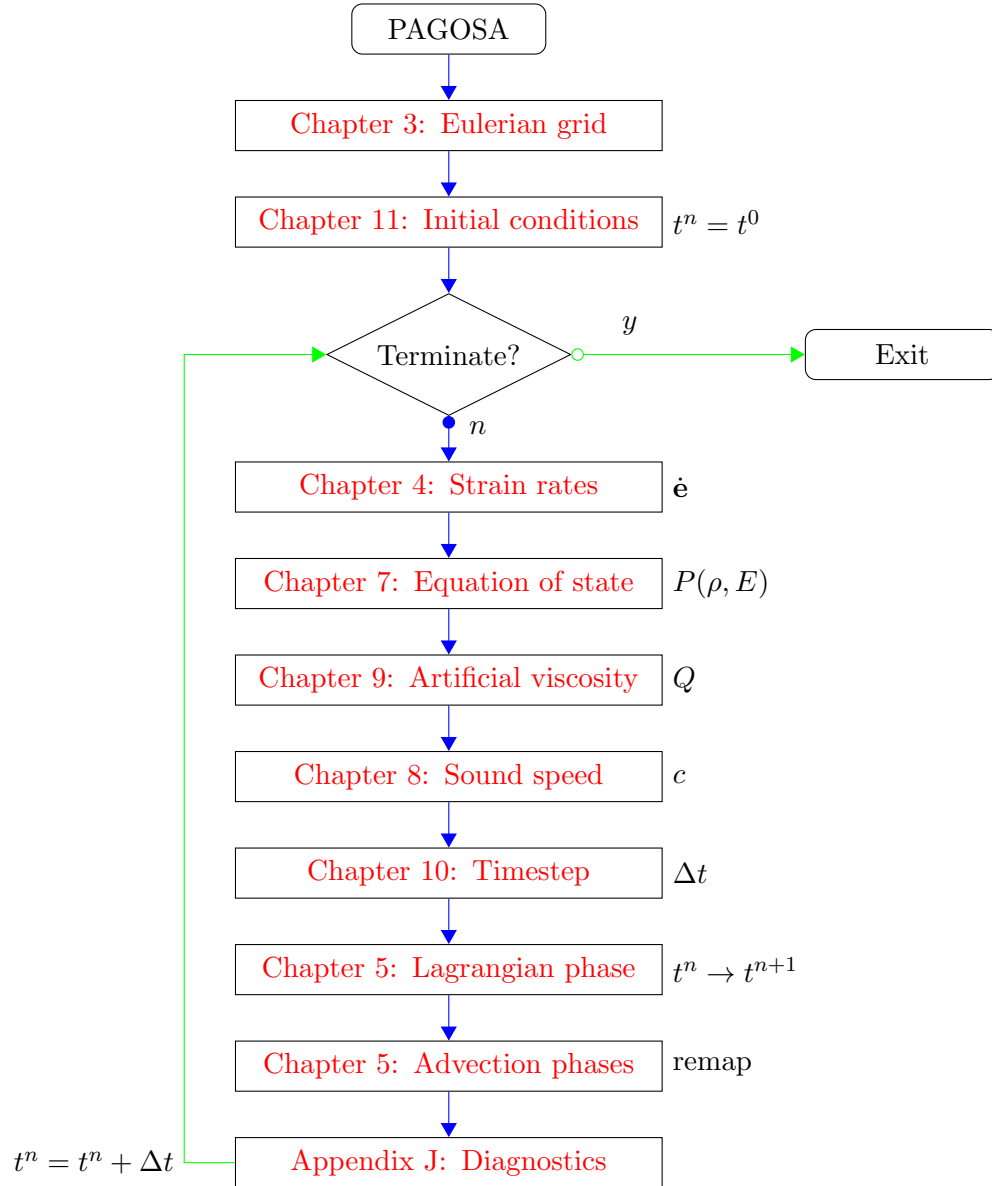


Figure 1.1: Flowchart showing an overview of the PAGOSA algorithm. Chapters and sections containing the relevant physics are hyperlinked.



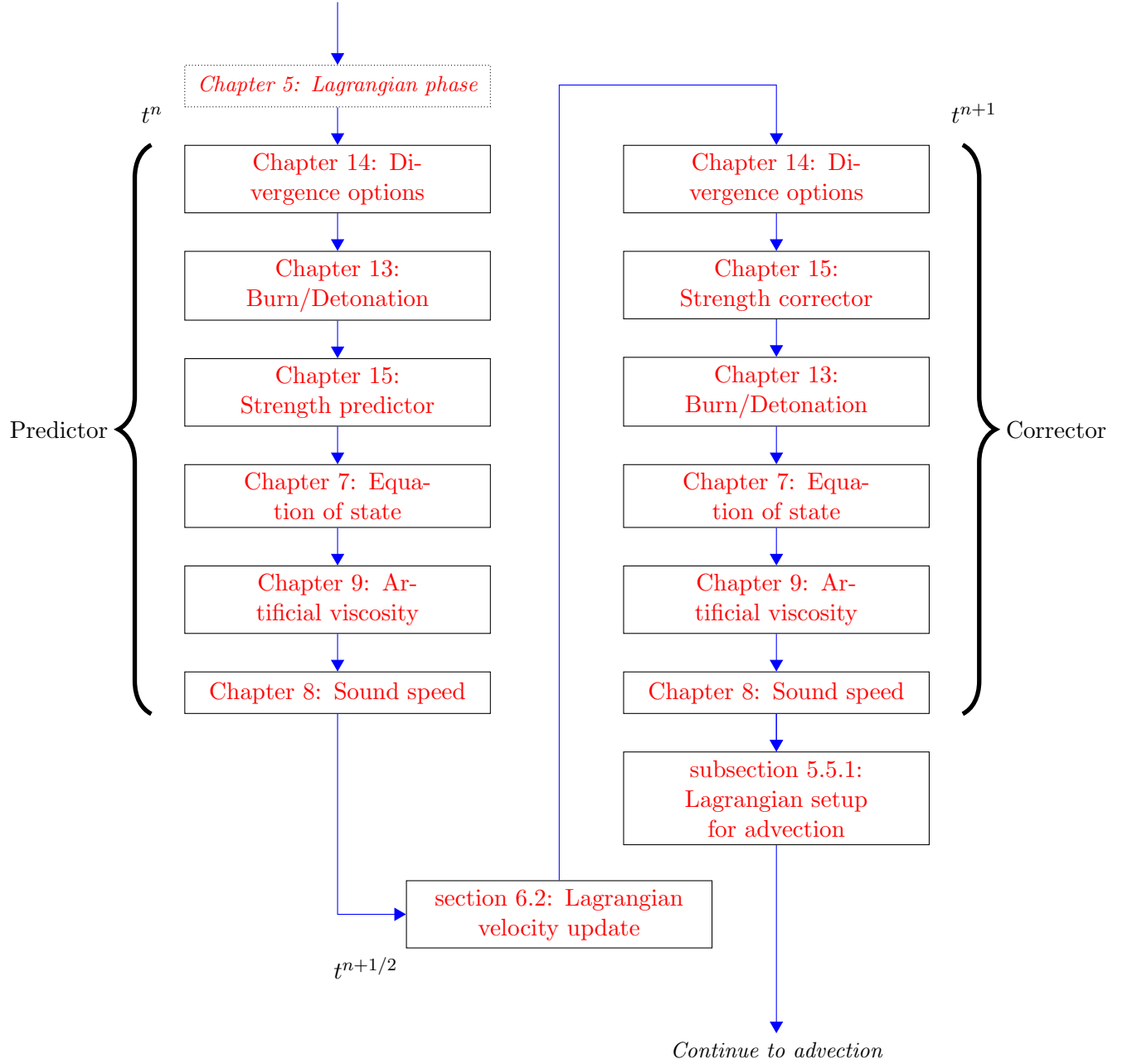


Figure 1.2: Flowchart showing the Lagrangian phase of the PAGOSA algorithm. Chapters and sections containing the relevant physics are hyperlinked.

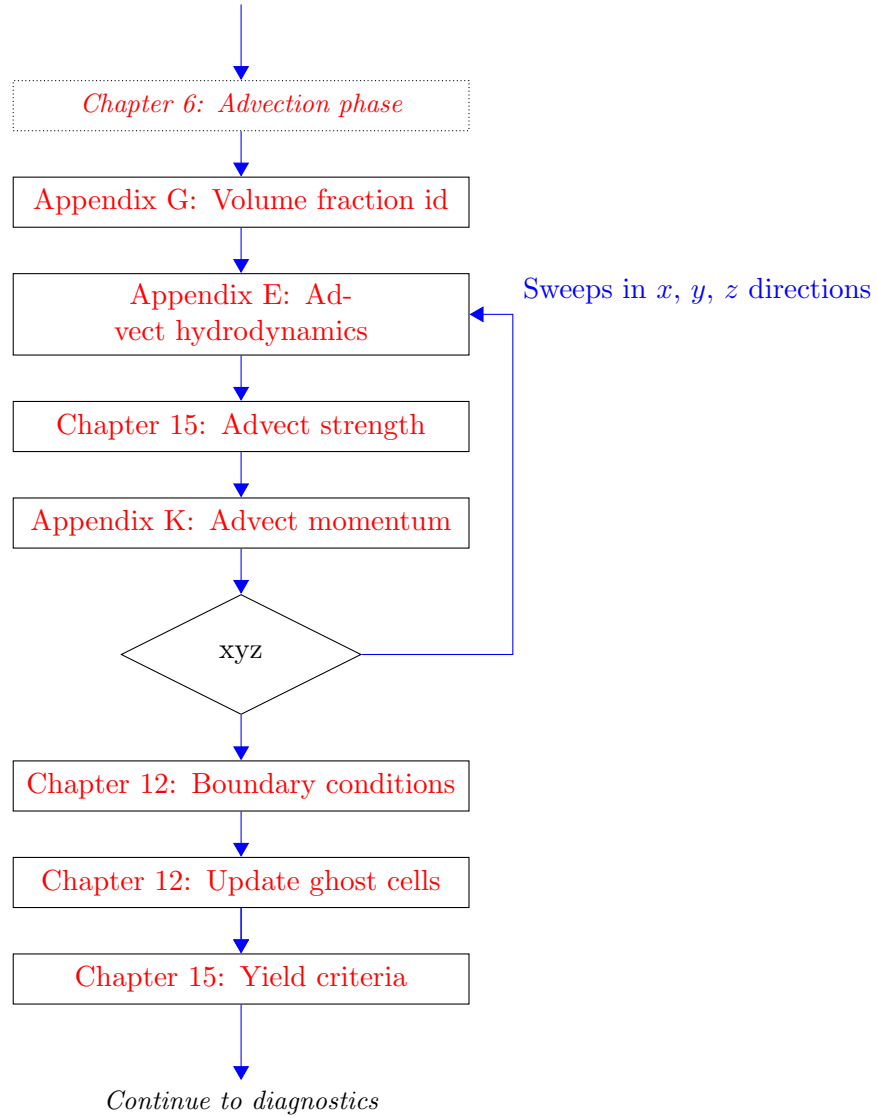


Figure 1.3: Flowchart showing the advection phase of the PAGOSA algorithm. Chapters and sections containing the relevant physics are hyperlinked.

there. The Navier-Stokes equations are written, and no derivation of those equations is presented. The user may consult any number of textbooks for the derivation.[2]

The construction of the Eulerian grid is presented in [Chapter 3](#). The Eulerian mesh is the computational domain of the simulation.

[Chapter 4](#) introduces the concept of strain rates and the numerical discretization of those rates. The basic numerical differencing techniques used in PAGOSA are detailed here. In [Chapter 5](#) the Strang operator-splitting technique is applied to the governing equations of [Chapter 2](#). The resulting Lagrangian- and advection-phase equations are numerically solved by the methods developed in [Chapter 4](#).

The integration of the basic hydrodynamic variables is presented in [Chapter 6](#). The predictor-corrector technique used in PAGOSA is second-order accurate in time.

[Chapter 7](#), [Chapter 8](#), and [Chapter 9](#) are concerned with the thermodynamics of the simulation. The EOS provides a closure to the fundamental equations by connecting the density, energy, and pressure.

A stable timestep must be computed for every step of the simulation. The Courant timestep controls are described in [Chapter 10](#).

The initial and boundary conditions for the governing equations are presented in [Chapter 11](#) and [Chapter 12](#). The initial conditions apply to all of the fundamental variables in the simulation in the interior of the Eulerian mesh. The boundary conditions apply to the exterior surface of the Eulerian mesh.

For high-explosive materials, a common method of releasing the chemical energy into the simulation is “programmed burn.” These algorithms are described in [Chapter 13](#).

The various divergence options are described in [Chapter 14](#). Because PAGOSA has only one velocity field, choices exist regarding how that velocity field is applied in every cell of the simulation.

[Chapter 15](#) describes the algorithms for materials possessing strength, including the algorithm for elastic-plastic yield, as well as the various models for shear and yield moduli available in PAGOSA.

[Chapter 17](#) describes the algorithms for materials possessing damage or fracture models.

[Chapter 18](#) describes the algorithms for materials possessing a crush model.

[Appendix A](#) – [Appendix P](#) contain detailed information on the derivations, as well as other additional information that supplements the development of the PAGOSA algorithms. The information in these appendices is not crucial to the understanding of the main points in the presentation; however, a more complete view of PAGOSA can be had by a careful reading of them.



## Chapter 2

# Governing equations

*Great laws are not divined by flashes of inspiration, whatever you may think. It usually takes the combined work of a world of scientists over a period of centuries.*

– Isaac Asimov, Nightfall (1941)

The partial differential equations solved in PAGOSA are presented. Many equivalent forms of the system of differential equations characterize the flow of inviscid<sup>1</sup> fluids and solid materials in Eulerian coordinates, but certain formulations lead to considerably more accurate difference approximations than do others. These equations express the laws of conservation of mass, momentum, and energy locally. When these equations are combined with a material model relating stress to deformation, an EOS, and a set of initial and boundary conditions, they give a complete description of the motion of a continuum. The difference approximations have proven (empirically) to be quite accurate and generally most satisfactory for a wide range of three-dimensional problems.

In the current formulation, density and the three components of velocity are considered to be fundamental variables; it is quite important to carry this notion over to the difference equations.

The first condition, the equation of continuity, expresses the conservation of mass [3] as

$$\frac{\partial \rho}{\partial t} + U \frac{\partial \rho}{\partial x} + V \frac{\partial \rho}{\partial y} + W \frac{\partial \rho}{\partial z} = -\rho \nabla \cdot \mathbf{u} \quad (2.1)$$

where  $\mathbf{u} = (U, V, W)$  is the velocity vector. This equation defines the time evolution of density.

The Navier-Stokes equations [3] express the conservation of linear momentum as

$$\frac{\partial U}{\partial t} + U \frac{\partial U}{\partial x} + V \frac{\partial U}{\partial y} + W \frac{\partial U}{\partial z} = \frac{F_x}{\rho} - \frac{1}{\rho} \frac{\partial P}{\partial x} + \frac{1}{\rho} \left[ \frac{\partial S_{xx}}{\partial x} + \frac{\partial S_{xy}}{\partial y} + \frac{\partial S_{xz}}{\partial z} \right] \quad (2.2a)$$

$$\frac{\partial V}{\partial t} + U \frac{\partial V}{\partial x} + V \frac{\partial V}{\partial y} + W \frac{\partial V}{\partial z} = \frac{F_y}{\rho} - \frac{1}{\rho} \frac{\partial P}{\partial y} + \frac{1}{\rho} \left[ \frac{\partial S_{yx}}{\partial x} + \frac{\partial S_{yy}}{\partial y} + \frac{\partial S_{yz}}{\partial z} \right] \quad (2.2b)$$

$$\frac{\partial W}{\partial t} + U \frac{\partial W}{\partial x} + V \frac{\partial W}{\partial y} + W \frac{\partial W}{\partial z} = \frac{F_z}{\rho} - \frac{1}{\rho} \frac{\partial P}{\partial z} + \frac{1}{\rho} \left[ \frac{\partial S_{zx}}{\partial x} + \frac{\partial S_{zy}}{\partial y} + \frac{\partial S_{zz}}{\partial z} \right] \quad (2.2c)$$

where  $\mathbf{S}$  is the symmetric and traceless deviatoric stress tensor and is the difference between the total stress tensor and the isotropic pressure<sup>2</sup>  $P$ . The total stress tensor is never computed in PAGOSA and therefore is omitted in this overview. These three equations define the time evolution of the velocity field.

The deviatoric stress tensor,<sup>3</sup> a symmetric tensor,<sup>4</sup> expresses the relationship between stress and strain as

$$\dot{S}_{xx} = 2G \left( \dot{\epsilon}_{xx} - \frac{1}{3} \nabla \cdot \mathbf{u} \right) \quad (2.3a)$$

$$\dot{S}_{yy} = 2G \left( \dot{\epsilon}_{yy} - \frac{1}{3} \nabla \cdot \mathbf{u} \right) \quad (2.3b)$$

$$\dot{S}_{zz} = 2G \left( \dot{\epsilon}_{zz} - \frac{1}{3} \nabla \cdot \mathbf{u} \right) \quad (2.3c)$$

$$\dot{S}_{xy} = 2G(\dot{\epsilon}_{xy}) \quad (2.3d)$$

$$\dot{S}_{xz} = 2G(\dot{\epsilon}_{xz}) \quad (2.3e)$$

$$\dot{S}_{yz} = 2G(\dot{\epsilon}_{yz}) \quad (2.3f)$$

---

<sup>1</sup>Inviscid is defined as having no viscosity

<sup>2</sup>It should be mentioned that the mechanical pressure cannot always be identified with the thermodynamic pressure, but the difference is usually of little consequence from an engineering point of view.

<sup>3</sup>This constitutive relation has many names: Hooke's law, the linear stress-strain equations, etc. A simple derivation is given in [Appendix A](#)

<sup>4</sup>The symmetry of the tensor is a consequence of the conservation of angular momentum. See [Appendix N](#) for a derivation

The shear modulus,  $G$ , is evaluated using one of several available flow-stress models (e.g., Elastic-Perfectly-Plastic, Steinberg-Cochran-Guinan, Kospall, and Johnson-Cook). It contains the material information about melting, pressure, and density dependencies and the material-specific constants. These flow-stress models are described in [section 15.4](#).

The terms in brackets in [Equation 2.2a](#) – [Equation 2.2c](#) are computed only for materials with strength. [Equation 2.3a](#) – [Equation 2.3f](#) are not computed for purely hydrodynamic materials. This concept applies to all the optional physics (e.g., burn, fracture, and crush). The physics is computed only for a material when appropriate. In this way, the computational overhead is reduced to what is necessary to satisfy the physics.

The stress deviators are further adjusted for material rotation, plasticity, fracture, damage, and spall and are described in [Chapter 15](#). This second-order tensor  $\mathbf{S}$  has three invariants<sup>5</sup>:

$$J_1 = \text{Tr}(\mathbf{S}) = S_{xx} + S_{yy} + S_{zz} \quad (2.4a)$$

$$J_2 = \frac{1}{2} \text{Tr}(\mathbf{S}^2) = \frac{1}{2} (S_{xx}^2 + S_{yy}^2 + S_{zz}^2) + S_{xy}^2 + S_{xz}^2 + S_{yz}^2 \quad (2.4b)$$

$$J_3 = \det(\mathbf{S}) \quad (2.4c)$$

The invariants of tensors is an important concept in continuum mechanics. The second invariant  $J_2$  will become important when we consider the yield stress of a material.

The spatial velocity gradient tensor can be decomposed into a symmetrical part and an antisymmetrical (also called skew-symmetric) part. The symmetrical part of this tensor can be identified with the strain rate tensor  $\dot{\mathbf{e}}$  in the limit of small strains<sup>[4]</sup>. In this limit, the strain rate tensor can be written as

$$\dot{e}_{xx} = \frac{\partial U}{\partial x} \quad (2.5a)$$

$$\dot{e}_{yy} = \frac{\partial V}{\partial y} \quad (2.5b)$$

$$\dot{e}_{zz} = \frac{\partial W}{\partial z} \quad (2.5c)$$

$$\dot{e}_{xy} = \frac{1}{2} \left( \frac{\partial U}{\partial y} + \frac{\partial V}{\partial x} \right) \quad (2.5d)$$

$$\dot{e}_{xz} = \frac{1}{2} \left( \frac{\partial U}{\partial z} + \frac{\partial W}{\partial x} \right) \quad (2.5e)$$

$$\dot{e}_{yz} = \frac{1}{2} \left( \frac{\partial V}{\partial z} + \frac{\partial W}{\partial y} \right) \quad (2.5f)$$

The trace of the strain rate tensor is the divergence of the velocity vector, given as

$$\dot{e}_{xx} + \dot{e}_{yy} + \dot{e}_{zz} = \frac{\partial U}{\partial x} + \frac{\partial V}{\partial y} + \frac{\partial W}{\partial z} = \nabla \cdot \mathbf{u} \quad (2.6)$$

The trace of the strain tensor (without the time derivative) is called the dilatation. The dilatation represents the contraction or expansion of a material element. Mathematically, it is simply

$$\text{dilatation} = e_{xx} + e_{yy} + e_{zz} \quad (2.7)$$

---

<sup>5</sup>The values of  $J_1$ ,  $J_2$ ,  $J_3$  are the same (invariant), regardless of the orientation of the coordinate system.

In fluid mechanics, a flow is called incompressible if the divergence of the velocity field is identically zero. This flow corresponds to a material element having no change in volume (contraction or expansion). In PAGOSA, which solves the equations for compressible flow, a material cannot be truly incompressible. However, a material can have a very large value for a bulk compression modulus<sup>6</sup>. The excursions from incompressible flow can be made arbitrarily small from an engineering point of view.

The antisymmetrical (skew-symmetric) part of the spatial velocity gradient tensor is the vorticity tensor, the components of which are:

$$\Omega_{xy} = -\Omega_{yx} = \frac{1}{2} \left( \frac{\partial U}{\partial y} - \frac{\partial V}{\partial x} \right) = -\frac{1}{2} \omega_z \quad (2.8a)$$

$$\Omega_{xz} = -\Omega_{zx} = \frac{1}{2} \left( \frac{\partial U}{\partial z} - \frac{\partial W}{\partial x} \right) = -\frac{1}{2} \omega_y \quad (2.8b)$$

$$\Omega_{yz} = -\Omega_{zy} = \frac{1}{2} \left( \frac{\partial V}{\partial z} - \frac{\partial W}{\partial y} \right) = -\frac{1}{2} \omega_x \quad (2.8c)$$

where  $\boldsymbol{\omega}$  is the axial vector<sup>7</sup> associated with the vorticity tensor.

In matrix form,

$$\boldsymbol{\Omega} = \begin{bmatrix} 0 & \Omega_{xy} & \Omega_{xz} \\ -\Omega_{xy} & 0 & \Omega_{yz} \\ -\Omega_{xz} & -\Omega_{yz} & 0 \end{bmatrix} = \frac{1}{2} \begin{bmatrix} 0 & -\omega_z & \omega_y \\ \omega_z & 0 & -\omega_x \\ -\omega_y & \omega_x & 0 \end{bmatrix}$$

The pressure is assumed to be related to the density and internal energy by the equation:

$$P = P(\rho, E) \quad \text{EOS} \quad (2.9)$$

The EOS can be analytic or tabular and includes phase transitions for each material. The EOS must be solved in conjunction with the equation for specific internal energy as

$$\begin{aligned} \rho \left[ \frac{\partial E}{\partial t} + U \frac{\partial E}{\partial x} + V \frac{\partial E}{\partial y} + W \frac{\partial E}{\partial z} \right] = & -P \boldsymbol{\nabla} \cdot \mathbf{u} \\ & + S_{xx} \dot{e}_{xx} + S_{yy} \dot{e}_{yy} + S_{zz} \dot{e}_{zz} \\ & + 2(S_{xy} \dot{e}_{xy} + S_{xz} \dot{e}_{xz} + S_{yz} \dot{e}_{yz}) \end{aligned} \quad (2.10)$$

The internal energy is further divided into an elastic distortional energy and plastic work. The difference is that the plastic work results in raising the internal energy of the material, whereas the elastic distortional energy is recoverable by the system. These details will be discussed in [Chapter 15](#).

The above development is for a single material. The above equations are applied to every material in PAGOSA. In the following algorithm descriptions, the fundamental variables are scaled by a volume fraction representing the amount of each material in a particular region of space. The material interface treatment is a unique and powerful feature in PAGOSA.

<sup>6</sup>See [section 7.3](#), Polynomial equation of state, for an example

<sup>7</sup>Mathematically the axial vorticity vector is the curl of the velocity vector. For example, if  $\boldsymbol{\nabla} \times \mathbf{u} = 0$ , the flow is called irrotational



Remarkably, these equations capture the flow and deformation of gases, fluids, and solids and the interactions between them, when formulated for multifield[5] flow. The history of these equations is a fascinating story in its own right. The history of modern physics is intimately tied to these equations because originally the luminiferous aether was believed to behave as an elastic solid.[6]

The first step in numerically solving the above equations is to create a computational grid. The creation of the Eulerian grid is discussed in the next chapter.



## Chapter 3

# Eulerian grid

*Every cubic inch of space is a miracle.*

– Walt Whitman, Miracles (1871)

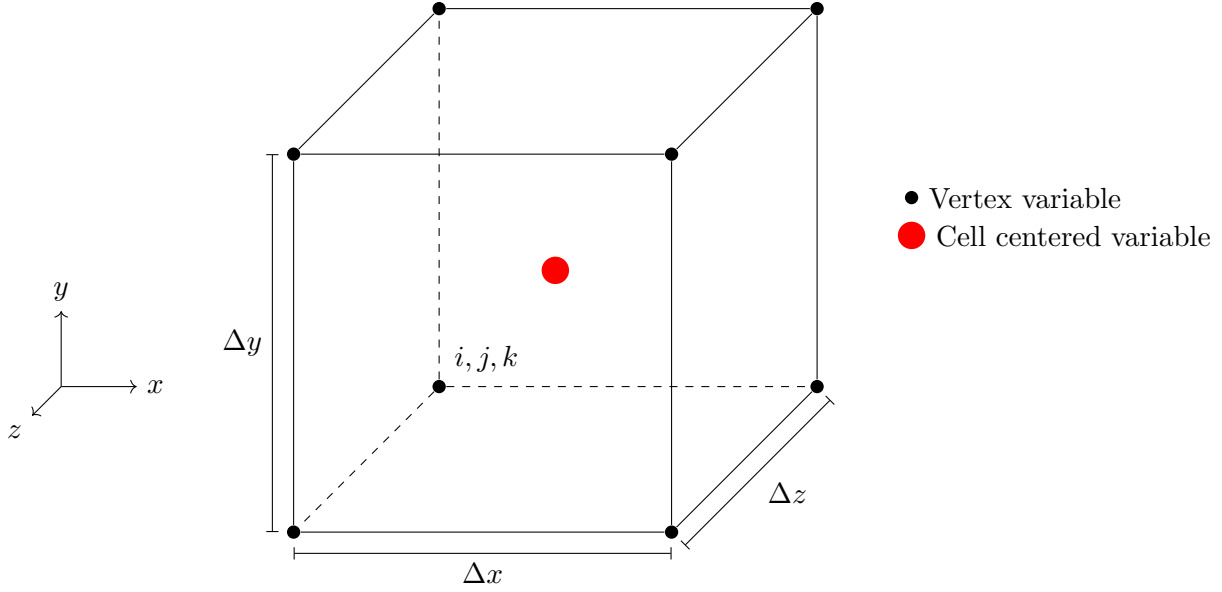


Figure 3.1: A single Eulerian cell in the computational domain

The computational domain is a box (mathematically it is a cuboid<sup>1</sup> or rectangular parallelepiped). The user chooses the computational range of interest by choosing the coordinate ranges

$$[x_{\min} : x_{\max}] \otimes [y_{\min} : y_{\max}] \otimes [z_{\min} : z_{\max}]$$

The governing equations are solved numerically with the appropriate initial and boundary conditions. The computational domain is divided into cells<sup>2</sup> bounded by the surfaces:

$$\begin{aligned} x_i &= x_{\min} + (i - 1)\Delta x & ; & \quad i = 1, 2, \dots, i_{\max} \\ y_j &= y_{\min} + (j - 1)\Delta y & ; & \quad j = 1, 2, \dots, j_{\max} \\ z_k &= z_{\min} + (k - 1)\Delta z & ; & \quad k = 1, 2, \dots, k_{\max} \end{aligned}$$

where  $\Delta x$ ,  $\Delta y$ , and  $\Delta z$  are the grid spacings and the dimensions of a single Eulerian cell. The cell dimensions are shown in [Figure 3.1](#).

The coordinates of the lower left corner of the cell with the indices  $(i, j, k)$  correspond to  $(x_i, y_j, z_k)$ . The cell is the basic spatial discretization in the solution of the partial differential equations. The cell and the entire mesh are fixed in space. Materials move through the grid (also referred to as a mesh) subject to the governing equations and initial and boundary conditions. As time progresses, the variables are computed at fixed points of the grid. In the Eulerian formulation, the volume of the cell is invariant, and changes in density are due to changes in the mass of a material in a particular cell.

The important geometric properties of the Eulerian cell include:

<sup>1</sup>A cuboid is defined as a closed box with three pairs of rectangular faces. The black monolith with side lengths of 1, 4, and 9 in the book and film version of *2001: A Space Odyssey* is an example of a cuboid.

<sup>2</sup>The terms “cell” and “zone” are used interchangeably in the text.

|             |  |             |
|-------------|--|-------------|
| Cell widths | $\Delta x, \Delta y, \Delta z$             |             |
| Cell volume | $\Delta x \times \Delta y \times \Delta z$ |             |
| Face areas  | Area x = $\Delta y \times \Delta z$        | x-component |
|             | Area y = $\Delta x \times \Delta z$        | y-component |
|             | Area z = $\Delta x \times \Delta y$        | z-component |

The numerical solution of partial differential equations[7, 818-849] involves a two-step process:

1. Create a finite difference scheme (a difference approximation to the partial differential equations on a grid)
2. Solve the difference equations; the solution is written in the form of a high-order system of linear and/or nonlinear algebraic equations

The numerical treatment of the original partial differential equations requires that the variables be discretized temporally and spatially.

In PAGOSA, a staggered grid is used, where some variables are centered on the cell vertices, whereas others are cell centered. The discretization begins with the basic cell-centered hydrodynamic variables, as shown in **Figure 3.1**.

|                 |                    |                                |                      |
|-----------------|--------------------|--------------------------------|----------------------|
| Density         | $\rho(t; x, y, z)$ | $\rho_{i+1/2, j+1/2, k+1/2}^n$ |                      |
| Internal energy | $E(t; x, y, z)$    | $E_{i+1/2, j+1/2, k+1/2}^n$    | <b>CELL CENTERED</b> |
| Pressure        | $P(t; x, y, z)$    | $P_{i+1/2, j+1/2, k+1/2}^n$    |                      |

The superscript refers to a discrete time (  $n$  ), and the subscripts refer to a discrete position in space (in this case, the center of the cell). *Note: The superscript (n) is not an exponent or a power-law index, but simply a time index.*

The cell centers are located at the geometric center of the cell; the center coordinates are

$$x_{i+1/2} = \frac{1}{2}(x_i + x_{i+1})$$

and similarly for the other coordinates.

The velocity vector is defined at the cell vertices:

|            |                 |                     |                        |
|------------|-----------------|---------------------|------------------------|
| x velocity | $U(t; x, y, z)$ | $U_{i,j,k}^{n+1/2}$ |                        |
| y velocity | $V(t; x, y, z)$ | $V_{i,j,k}^{n+1/2}$ | <b>VERTEX CENTERED</b> |
| z velocity | $W(t; x, y, z)$ | $W_{i,j,k}^{n+1/2}$ |                        |

The superscript in this case refers to a half-timestep (  $n + 1/2$  ), and the subscript refers to a vertex located at (  $i, j, k$  ). The time centering of the above equations is only an example. The exact time centering [i.e., (  $n$  ), (  $n + 1/2$  ), or (  $n + 1$  ) as superscripts] will be deferred until the discussion in **Chapter 6**, Integration of the Hydrodynamic Variables.

The variables from the original partial differential equations (e.g.,  $U, \rho$ ) are continuous functions of space and time. This statement is not true of the finite difference representation described above. In the literature of finite difference equations, the two functions are often denoted differently to distinguish between the continuous and discrete functions.[8] For example, the discrete functions and their solutions will depend on the choice of grid spacing (zone size). In this text, the same symbols will be used for both descriptions.

In PAGOSA, the choice of placing the velocity vector at the cell vertices is not universal. Some Eulerian hydrodynamics codes locate the velocities on the cell faces [9] whereas others locate them at the cell center with the other variables.[10] The exact placement of variables on a mesh is an active area of research, and the choice of discretization is an art. The advantage of having eight velocity vectors associated with each cell is that complex velocity fields can be represented accurately in PAGOSA.

### 3.1 Mixed cells

Some cells in the computational domain will contain more than one material.<sup>3</sup> These mixed cells present one of the central challenges for Eulerian hydrocodes. Multi-material cells computationally represent the interface between materials.

The volume fractions[11] are defined as

$$^{(m)}\phi_{i+1/2,j+1/2,k+1/2} \equiv \text{fraction of cell volume occupied by material } (m)$$

For a cell, the volume fractions must sum to unity by definition as

$$\sum_m ^{(m)}\phi_{i+1/2,j+1/2,k+1/2} = 1$$

where the summation is over all the materials defined in the simulation. As the simulation progresses, the volume fractions are recomputed for each new timestep. The question is how to compute the initial volume fractions. These fractions are computed using a variation of a Monte-Carlo technique.[7, 155-158] Each cell is sampled with a regular array of “particles,” and the resulting statistics are used to compute the initial volume fractions. A more detailed discussion is given in [Appendix B](#).

Most cells in a simulation are pure cells. The single-material governing equations shown in [Chapter 2](#) apply directly in this case. For example, cell average pressures are identical to the material pressures. No interfaces exist in these cells.<sup>4</sup>

On the other hand, mixed cells provide a richness and complexity to the solution of the governing equations. In a mixed cell, each material possesses its own density, internal energy, and pressure. In general, no attempt is made to force a pressure or temperature equilibrium between the individual materials (see [Chapter 14](#) for a more complete explanation). The cell average pressure is the volume fraction average of each material pressure. Each material in a mixed cell has its own interface represented by a plane; in this way, the materials can be localized within the cell.

<sup>3</sup>A cell containing only one material is called a pure cell. All other cells are called mixed cells.

<sup>4</sup>The only pathological exception is when two adjacent pure cells have different materials. The material interface coincides with the cell face.

### 3.2 Finite differences

It is natural to divide the simulation time interval  $[0, T]$  into short subintervals, with a step denoted  $\Delta t$ . In general, the time intervals will change as the simulation progresses [i.e., the time interval (also called the timestep) will change, depending on the exact physical state at that time]. The simulation time after  $N$  steps is

$$t^N = t_0 + \sum_{n=1}^N \Delta t^n, \text{ the simulation time at cycle } N$$

The finite difference method is a numerical technique for approximating the solution of partial differential equations. A partial derivative is replaced with a finite difference as, for example, the partial time derivative of an arbitrary function

$$\frac{\partial \Psi}{\partial t} \rightarrow \frac{\Psi_{i+1/2, j+1/2, k+1/2}^{n+1} - \Psi_{i+1/2, j+1/2, k+1/2}^n}{\Delta t^n} \quad (3.1)$$

where we have used the standard notation  $\psi(t^{n+1}, x_{i+1/2}, y_{j+1/2}, z_{k+1/2}) \rightarrow \psi_{i+1/2, j+1/2, k+1/2}^{n+1}$

Now suppose we wish to create a finite difference approximation for the equation

$$\frac{\partial \Psi}{\partial t} = F(t, x) \quad (3.2a)$$

$$\frac{\Psi_{i+1/2, j+1/2, k+1/2}^{n+1} - \Psi_{i+1/2, j+1/2, k+1/2}^n}{\Delta t^n} = F_{i+1/2, j+1/2, k+1/2}^n \quad ; \quad \Delta t^n = t^{n+1} - t^n \quad (3.2b)$$

Solving these yields the following algebraic equation:

$$\Psi_{i+1/2, j+1/2, k+1/2}^{n+1} = \Psi_{i+1/2, j+1/2, k+1/2}^n + \Delta t^n F_{i+1/2, j+1/2, k+1/2}^n \quad (3.3)$$

This technique will be used repetitively in the following chapters. The finite difference approximations[12] to the governing equations will be developed in the following chapters.

### 3.3 Momentum control volume

The momentum control volume, or dual mesh, surrounds the vertex. This volume is staggered with respect to the original Eulerian mesh, which is created by connecting the centroids of the Eulerian cells and therefore is identical to the Eulerian mesh, but translated by half a cell in each dimension, as shown in [Figure 3.2](#). In three dimensions, each vertex is surrounded by eight Eulerian cells.

The mass of a single Eulerian cell is computed by

$$m_{i+1/2, j+1/2, k+1/2} = \sum_j^{(j)} \phi_{i+1/2, j+1/2, k+1/2}^{(j)} \rho_{i+1/2, j+1/2, k+1/2}^{(j)} \text{Vol}_{i+1/2, j+1/2, k+1/2}$$

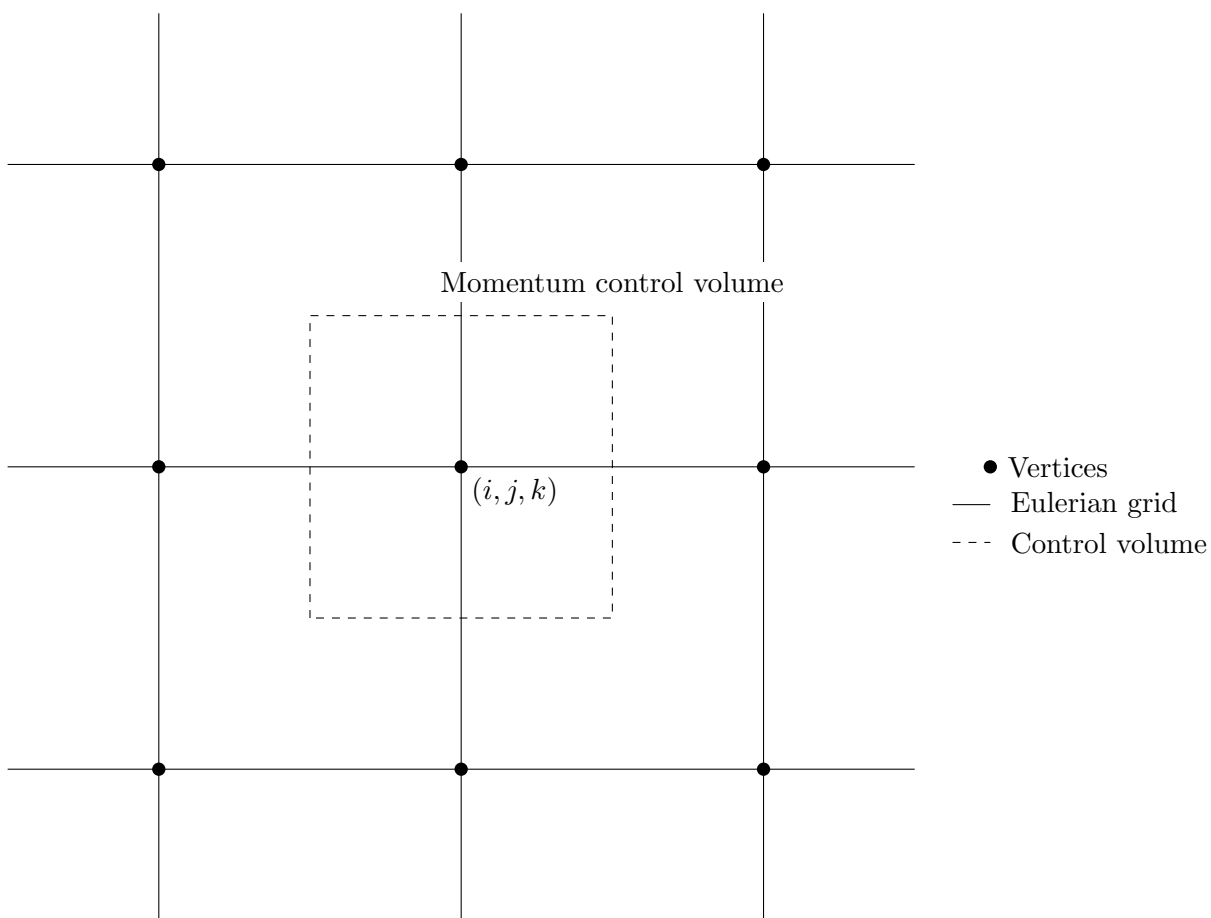


Figure 3.2: A cross section of the momentum control volume. The two-dimensional cut of this control volume passes through the vertex  $(i, j, k)$ .



where the summation is over all materials ( $j$ ). The mass associated with the vertex is computed by

$$\text{Mass}_{i,j,k} = \frac{1}{8} (m_{i+1/2,j+1/2,k+1/2} + m_{i+1/2,j+1/2,k-1/2} + m_{i+1/2,j-1/2,k+1/2} + m_{i+1/2,j-1/2,k-1/2} \\ m_{i-1/2,j+1/2,k+1/2} + m_{i-1/2,j+1/2,k-1/2} + m_{i-1/2,j-1/2,k+1/2} + m_{i-1/2,j-1/2,k-1/2}) \quad (3.4)$$

and the  $x$ -component momentum associated with the vertex is

$$\text{Momentum}_{i,j,k} = \text{Mass}_{i,j,k} U_{i,j,k}$$

The momentum control volume becomes important in the discussion of solving the momentum [Equation 2.2a](#) – [Equation 2.2c](#).

### 3.4 Ghost cells

An extra layer of cells is added to the outside of the computational grid to aid in the construction and implementation of the boundary conditions. In the literature on Eulerian hydrodynamics codes, these “extra” cells are called ghost cells or guard cells. The addition of the external cells is used to extend the grid so that the solver need not be directly aware of its computational boundary.

Two types of boundary conditions are implemented in PAGOSA – reflective and transmissive boundaries. These conditions are discussed in [Chapter 12](#).

The boundary conditions are applied to all six exterior faces of the computational grid. Each face of the Eulerian mesh can have a different boundary condition. Other boundary conditions may be added in the future.

### 3.5 Grid decomposition

The solution of three-dimensional problems requires large amounts of memory and processing power to produce mesh-converged results in a reasonable time. The orthogonality of the grid allows for a straightforward spatial decomposition, as illustrated in [Figure 3.3](#).

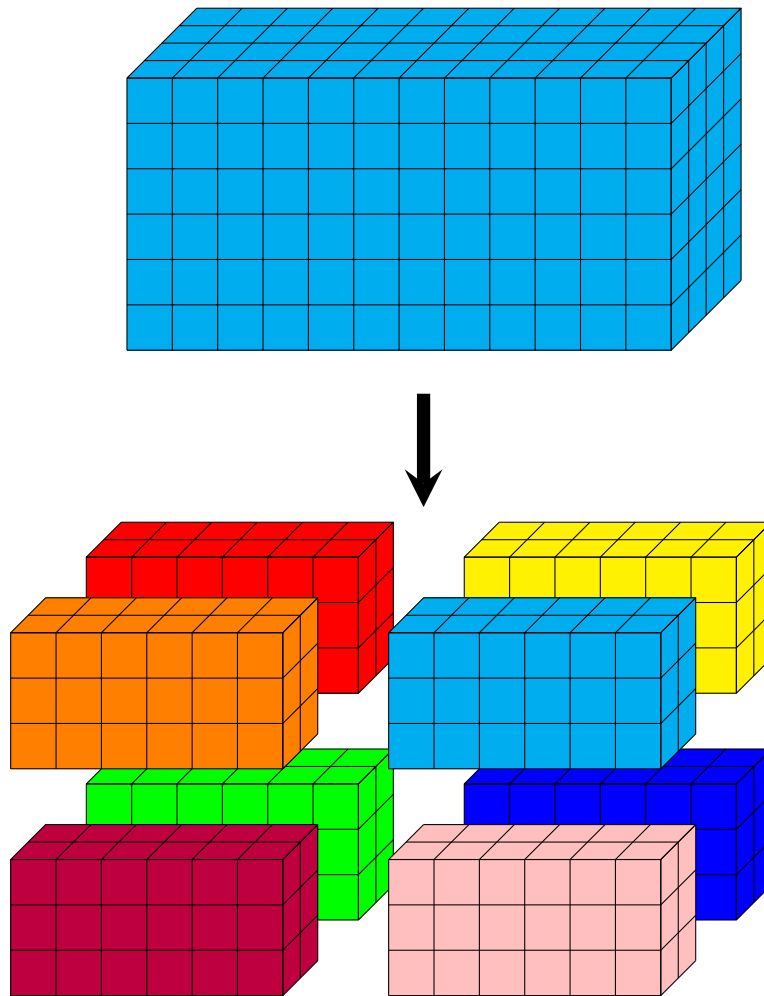


Figure 3.3: Domain decomposition of an Eulerian grid. The example shows the grid being decomposed onto eight processors. The size and shape of the decomposed grid are the same on each processor.

## Chapter 4

# Strain rates

*I have no satisfaction in formulas unless I feel their numerical magnitude.*

– Lord Kelvin, Life of Sylvanus Thompson

The strain rate calculation in PAGOSA requires the evaluation of all the derivatives of the velocity vector  $\mathbf{u} = (U, V, W)$ . Specifically, the derivatives that need to be evaluated are

$$\left[ \frac{\partial U}{\partial x}, \frac{\partial U}{\partial y}, \frac{\partial U}{\partial z} \right], \left[ \frac{\partial V}{\partial x}, \frac{\partial V}{\partial y}, \frac{\partial V}{\partial z} \right], \text{ and } \left[ \frac{\partial W}{\partial x}, \frac{\partial W}{\partial y}, \frac{\partial W}{\partial z} \right]$$

Before we can construct a numerical approximation to the above partial derivatives, we need to take a mathematical detour. Start with the divergence theorem [13, 37 – 39]

$$\int_V \nabla \cdot \mathbf{F} d^3x = \int_S \mathbf{F} \cdot \hat{\mathbf{n}} d^2x \quad (4.1)$$

Let  $\mathbf{F} = \phi \mathbf{c}$ , where  $\mathbf{c}$  is a constant vector  $\neq \mathbf{0}$ , and  $\phi$  is a scalar that is a function only of position. Then we have

$$\int_V \nabla \cdot \mathbf{F} d^3x = \mathbf{c} \cdot \hat{\mathbf{n}} \int_S \phi d^2x \quad (4.2)$$

However, the divergence produces

$$\nabla \cdot \mathbf{F} = \nabla \cdot (\phi \mathbf{c}) = \phi \nabla \cdot \mathbf{c} + \mathbf{c} \cdot \nabla \phi = \mathbf{c} \cdot \nabla \phi \quad (4.3)$$

because  $\mathbf{c}$  is a constant vector. In this case, the divergence theorem reduces to

$$\mathbf{c} \cdot \left( \int_V \nabla \phi d^3x - \int_S \phi \hat{\mathbf{n}} d^2x \right) = 0 \quad (4.4)$$

Because  $\mathbf{c}$  is nonzero and arbitrary, the dot product cannot be zero unless the quantity inside the brackets is zero.

Next, take the limit of the volume as it approaches zero. In this limit, we assume that the gradient is uniform and constant over the volume or has a mean value<sup>1</sup> of

$$\lim_{\Delta \text{Vol} \rightarrow 0} \int_V \nabla \phi d^3x \simeq \lim_{\Delta \text{Vol} \rightarrow 0} \nabla \phi \int_V d^3x = \lim_{\Delta \text{Vol} \rightarrow 0} \int_S \phi \hat{\mathbf{n}} d^2x \quad (4.5)$$

where

$$\int_V d^3x = \Delta \text{Vol}$$

Then under these circumstances,

$$\nabla \phi = \lim_{\Delta \text{Vol} \rightarrow 0} \frac{1}{\Delta \text{Vol}} \int_S \phi \hat{\mathbf{n}} d^2x \quad (4.6)$$

Apply this new definition of the gradient to a single cell in the Eulerian mesh. The volume element is  $\Delta \text{Vol} = \Delta x \Delta y \Delta z$ , the unit normals  $\hat{\mathbf{n}}$  are the Cartesian unit vectors, and the surface areas are those of the cell.

---

<sup>1</sup>In the sense of given by the mean value theorem for integration.

The gradient of a scalar field, in this case the x component of the velocity,  $U$ , can be computed from the surface integral of the velocity field

$$\frac{\partial U}{\partial x} = \lim_{\Delta \text{Vol} \rightarrow 0} \frac{\oiint U dy dz}{\Delta x \Delta y \Delta z} \rightarrow \frac{1}{\Delta x} \left[ \frac{\oiint U dy dz}{\Delta y \Delta z} \right] = \frac{\bar{U}_i - \bar{U}_{i-1}}{\Delta x} \quad (4.7)$$

The term in the square brackets is the integral average of the velocity over the relevant surface area. Evaluating the integrals at the limits of the integration produces the final result<sup>2</sup> in Equation 4.7.  $\bar{U}_i$  is the area-averaged velocity on the  $x$ -face of the cell. The value of  $\bar{U}_i$  is computed as the arithmetic average of the corner vertex velocities<sup>3</sup>

$$\bar{U}_i = \frac{1}{4} (U_{i,j,k} + U_{i,j+1,k} + U_{i,j,k+1} + U_{i,j+1,k+1}) \quad (4.8)$$

The scheme is shown in Figure 4.1. The other gradients are handled similarly.

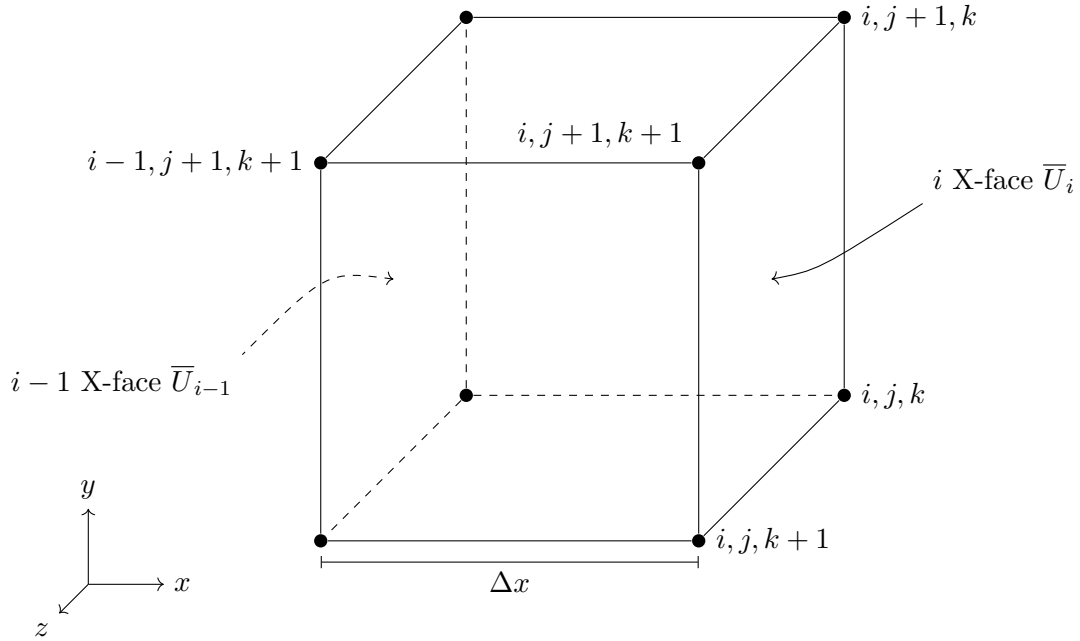


Figure 4.1: The gradient finite difference computation

<sup>2</sup>The difference scheme presented is spatially second-order accurate.

<sup>3</sup>The integral average is approximated by the arithmetic average of the four corner velocities. However, the same answer is arrived at if it is assumed that the velocity is a bilinear function of position on the face.

The strain rates are defined as:

$$\dot{e}_{xx} = \frac{\partial U}{\partial x} \quad (4.9a)$$

$$\dot{e}_{yy} = \frac{\partial V}{\partial y} \quad (4.9b)$$

$$\dot{e}_{zz} = \frac{\partial W}{\partial z} \quad (4.9c)$$

$$\dot{e}_{xy} = \frac{1}{2} \left[ \frac{\partial U}{\partial y} + \frac{\partial V}{\partial x} \right] \quad (4.9d)$$

$$\dot{e}_{xz} = \frac{1}{2} \left[ \frac{\partial U}{\partial z} + \frac{\partial W}{\partial x} \right] \quad (4.9e)$$

$$\dot{e}_{yz} = \frac{1}{2} \left[ \frac{\partial V}{\partial z} + \frac{\partial W}{\partial y} \right] \quad (4.9f)$$

and the finite difference approximations are:

$$\dot{e}_{xx} \Big|_{i-1/2, j+1/2, k+1/2} \rightarrow \frac{\bar{U}_i - \bar{U}_{i-1}}{\Delta x} \quad (4.10a)$$

$$\dot{e}_{yy} \Big|_{i+1/2, j-1/2, k+1/2} \rightarrow \frac{\bar{V}_j - \bar{V}_{j-1}}{\Delta y} \quad (4.10b)$$

$$\dot{e}_{zz} \Big|_{i+1/2, j+1/2, k-1/2} \rightarrow \frac{\bar{W}_k - \bar{W}_{k-1}}{\Delta z} \quad (4.10c)$$

$$\dot{e}_{xy} \Big|_{i-1/2, j-1/2, k+1/2} \rightarrow \frac{1}{2} \left[ \frac{\bar{U}_j - \bar{U}_{j-1}}{\Delta y} + \frac{\bar{V}_i - \bar{V}_{i-1}}{\Delta x} \right] \quad (4.10d)$$

$$\dot{e}_{xz} \Big|_{i-1/2, j+1/2, k-1/2} \rightarrow \frac{1}{2} \left[ \frac{\bar{U}_k - \bar{U}_{k-1}}{\Delta z} + \frac{\bar{W}_i - \bar{W}_{i-1}}{\Delta x} \right] \quad (4.10e)$$

$$\dot{e}_{yz} \Big|_{i+1/2, j-1/2, k-1/2} \rightarrow \frac{1}{2} \left[ \frac{\bar{V}_k - \bar{V}_{k-1}}{\Delta z} + \frac{\bar{W}_j - \bar{W}_{j-1}}{\Delta y} \right] \quad (4.10f)$$

Note that the strain rates are cell-centered quantities, whereas the velocities are vertex centered. In mathematical terms, the difference operator maps vertex quantities to cell-centered quantities.

Finally, the divergence is computed as:

$$\nabla \cdot \mathbf{u} = \dot{e}_{xx} + \dot{e}_{yy} + \dot{e}_{zz} \quad (4.11)$$

and the finite difference approximation is:

$$\nabla \cdot \mathbf{u} \Big|_{i-1/2, j-1/2, k-1/2} \rightarrow \left[ \frac{\bar{U}_i - \bar{U}_{i-1}}{\Delta x} \right] + \left[ \frac{\bar{V}_j - \bar{V}_{j-1}}{\Delta y} \right] + \left[ \frac{\bar{W}_k - \bar{W}_{k-1}}{\Delta z} \right] \quad (4.12)$$

## Chapter 5

# Operator splitting

*No need to ask. He's a smooth operator.*

– Sade, Diamond Life (1984)

Operator-splitting methods<sup>1</sup> are mathematical techniques used for solving partial differential equations. These methods are commonly used to reduce the computational effort required to solve the complex governing equations into a simpler set of equations. We begin with the three-dimensional (3D) Euler equations:<sup>2</sup>

$$\frac{\partial \rho}{\partial t} + U \frac{\partial \rho}{\partial x} + V \frac{\partial \rho}{\partial y} + W \frac{\partial \rho}{\partial z} + \rho \nabla \cdot \mathbf{u} = 0 \quad \text{Conservation law} \quad \text{Mass} \quad (5.1)$$

$$\frac{\partial U}{\partial t} + U \frac{\partial U}{\partial x} + V \frac{\partial U}{\partial y} + W \frac{\partial U}{\partial z} + \frac{1}{\rho} \frac{\partial P}{\partial x} = 0 \quad \text{Momentum (X)} \quad (5.2)$$

$$\frac{\partial V}{\partial t} + U \frac{\partial V}{\partial x} + V \frac{\partial V}{\partial y} + W \frac{\partial V}{\partial z} + \frac{1}{\rho} \frac{\partial P}{\partial y} = 0 \quad \text{Momentum (Y)} \quad (5.3)$$

$$\frac{\partial W}{\partial t} + U \frac{\partial W}{\partial x} + V \frac{\partial W}{\partial y} + W \frac{\partial W}{\partial z} + \frac{1}{\rho} \frac{\partial P}{\partial z} = 0 \quad \text{Momentum (Z)} \quad (5.4)$$

$$\frac{\partial E}{\partial t} + U \frac{\partial E}{\partial x} + V \frac{\partial E}{\partial y} + W \frac{\partial E}{\partial z} + \frac{P}{\rho} \nabla \cdot \mathbf{u} = 0 \quad \text{Internal energy} \quad (5.5)$$

where the velocity vector is defined as  $\mathbf{u} \equiv (U, V, W)$ .

A variety of approaches exists for the differencing of the equations. The method used in PAGOSA is based on the ‘‘Strang operator-splitting’’ technique.<sup>[14]</sup> The above equations all have the form

$$\frac{\partial \psi}{\partial t} + (L_1 + L_2 + L_3)\psi = 0 \quad (5.6)$$

where  $\psi$  is any of the variables (i.e.,  $\rho, U, V, W, E$ ). The operators  $L_1, L_2, L_3$  are linear (spatial) partial difference operators. If  $D_1$  is a finite-difference approximation to  $L_1$ , then the finite-difference equivalent<sup>3</sup> of the above operator equation is simply

$$\psi^{n+1} = (1 - D_1 \Delta t - D_2 \Delta t - D_3 \Delta t) \psi^n \quad (5.7)$$

This equation can be rewritten to within a second-order approximation as

$$\psi^{n+1} = (1 - D_1 \Delta t)(1 - D_2 \Delta t)(1 - D_3 \Delta t) \psi^n + \mathcal{O}(\Delta t^2) \quad (5.8)$$

The time operator is split in the specific sequence

$$\frac{\partial \psi'}{\partial t} = -L_1 \psi' \quad ; \quad \frac{\partial \psi''}{\partial t} = -L_2 \psi'' \quad ; \quad \frac{\partial \psi'''}{\partial t} = -L_3 \psi''' \quad ; \quad \frac{\partial \psi}{\partial t} = \frac{\partial \psi'}{\partial t} + \frac{\partial \psi''}{\partial t} + \frac{\partial \psi'''}{\partial t} \quad (5.9)$$

or in finite difference form:

$$\begin{aligned} \psi' &= (1 - D_1 \Delta t) \psi^n \\ \psi'' &= (1 - D_2 \Delta t) \psi' \\ \psi^{n+1} &= (1 - D_3 \Delta t) \psi'' \end{aligned} \quad (5.10)$$

<sup>1</sup>See [Appendix O](#) for an alternate introduction

<sup>2</sup>The body forces and stress deviators are unnecessary for this discussion.

<sup>3</sup>A variation of [Equation 3.3](#)



which will provide a second-order accurate solution of the original equations.<sup>4</sup> The attraction of operator splitting is clear.[15] The operator splitting replaces a complex set of equations with three much simpler equations.[16]

The PAGOSA version of this operator-splitting technique results in the following equations.

## 5.1 Lagrangian phase

|   | <u>Conservation law</u> |        |
|---|-------------------------|--------|
| $\frac{\partial \rho}{\partial t} + \rho \nabla \cdot \mathbf{u} = 0$ | Mass                    | (5.11) |

|  |              |        |
|--|--------------|--------|
| $\frac{\partial U}{\partial t} + \frac{1}{\rho} \frac{\partial P}{\partial x} = 0$ | Momentum (X) | (5.12) |
|--|--------------|--------|

|  |              |        |
|--|--------------|--------|
| $\frac{\partial V}{\partial t} + \frac{1}{\rho} \frac{\partial P}{\partial y} = 0$ | Momentum (Y) | (5.13) |
|--|--------------|--------|

|  |              |        |
|--|--------------|--------|
| $\frac{\partial W}{\partial t} + \frac{1}{\rho} \frac{\partial P}{\partial z} = 0$ | Momentum (Z) | (5.14) |
|--|--------------|--------|

|  |                 |        |
|--|-----------------|--------|
| $\frac{\partial E}{\partial t} + \frac{P}{\rho} \nabla \cdot \mathbf{u} = 0$ | Internal energy | (5.15) |
|--|-----------------|--------|

The equations in the Lagrangian phase are simply the 3D Lagrangian hydrodynamic equations, the difference properties and behaviors of which are well understood from decades of experiences with Lagrangian hydrocodes. The remainder of the technique results in three additional sets of equations associated with the three Cartesian axes.

## 5.2 X-advective phase

|   | <u>Conservation law</u> |        |
|---|-------------------------|--------|
| $\frac{\partial \rho}{\partial t} + U \frac{\partial \rho}{\partial x} = 0$ | Mass                    | (5.16) |

|   |              |        |
|---|--------------|--------|
| $\frac{\partial U}{\partial t} + U \frac{\partial U}{\partial x} = 0$ | Momentum (X) | (5.17) |
|---|--------------|--------|

|   |              |        |
|---|--------------|--------|
| $\frac{\partial V}{\partial t} + U \frac{\partial V}{\partial x} = 0$ | Momentum (Y) | (5.18) |
|---|--------------|--------|

|   |              |        |
|---|--------------|--------|
| $\frac{\partial W}{\partial t} + U \frac{\partial W}{\partial x} = 0$ | Momentum (Z) | (5.19) |
|---|--------------|--------|

|   |                 |        |
|---|-----------------|--------|
| $\frac{\partial E}{\partial t} + U \frac{\partial E}{\partial x} = 0$ | Internal energy | (5.20) |
|---|-----------------|--------|

---

<sup>4</sup>The second-order accuracy is described in [Chapter 6](#) (Integration of the Hydrodynamic Variables).

### 5.3 Y-advective phase

|   | Conservation law |        |
|---|------------------|--------|
| $\frac{\partial \rho}{\partial t} + V \frac{\partial \rho}{\partial y} = 0$ | Mass             | (5.21) |

|   |              |        |
|---|--------------|--------|
| $\frac{\partial U}{\partial t} + V \frac{\partial U}{\partial y} = 0$ | Momentum (X) | (5.22) |
|---|--------------|--------|

|   |              |        |
|---|--------------|--------|
| $\frac{\partial V}{\partial t} + V \frac{\partial V}{\partial y} = 0$ | Momentum (Y) | (5.23) |
|---|--------------|--------|

|   |              |        |
|---|--------------|--------|
| $\frac{\partial W}{\partial t} + V \frac{\partial W}{\partial y} = 0$ | Momentum (Z) | (5.24) |
|---|--------------|--------|

|   |                 |        |
|---|-----------------|--------|
| $\frac{\partial E}{\partial t} + V \frac{\partial E}{\partial y} = 0$ | Internal energy | (5.25) |
|---|-----------------|--------|

### 5.4 Z-advective phase

|   | Conservation law |        |
|---|------------------|--------|
| $\frac{\partial \rho}{\partial t} + W \frac{\partial \rho}{\partial z} = 0$ | Mass             | (5.26) |

|   |              |        |
|---|--------------|--------|
| $\frac{\partial U}{\partial t} + W \frac{\partial U}{\partial z} = 0$ | Momentum (X) | (5.27) |
|---|--------------|--------|

|   |              |        |
|---|--------------|--------|
| $\frac{\partial V}{\partial t} + W \frac{\partial V}{\partial z} = 0$ | Momentum (Y) | (5.28) |
|---|--------------|--------|

|   |              |        |
|---|--------------|--------|
| $\frac{\partial W}{\partial t} + W \frac{\partial W}{\partial z} = 0$ | Momentum (Z) | (5.29) |
|---|--------------|--------|

|   |                 |        |
|---|-----------------|--------|
| $\frac{\partial E}{\partial t} + W \frac{\partial E}{\partial z} = 0$ | Internal energy | (5.30) |
|---|-----------------|--------|

These equations are the Eulerian-, remap-, or advection-phase equations.

The advection phase essentially forms a three-stage remapping procedure from the distorted Lagrangian grid (produced by the Lagrangian phase) back to the original Eulerian grid.<sup>5</sup> The Lagrangian phase may be regarded as a sequence of computations based on the (fictitious) Lagrangian grid, which coincides with the Eulerian mesh at the beginning of the phase. The advection phases conduct the transport of mass and material quantities between cells and may be viewed as a remapping of the distorted Lagrangian grid back onto the fixed Eulerian grid. In the Lagrangian phase, the density has a constant value and is adjusted at each new timestep by the mass transport of the advection phases.

---

<sup>5</sup>Methods that perform the advection in a single conservative step are collectively called unsplit advection methods. Although unsplit methods have a theoretical advantage over operator-splitting methods, the advantage remains largely theoretical.

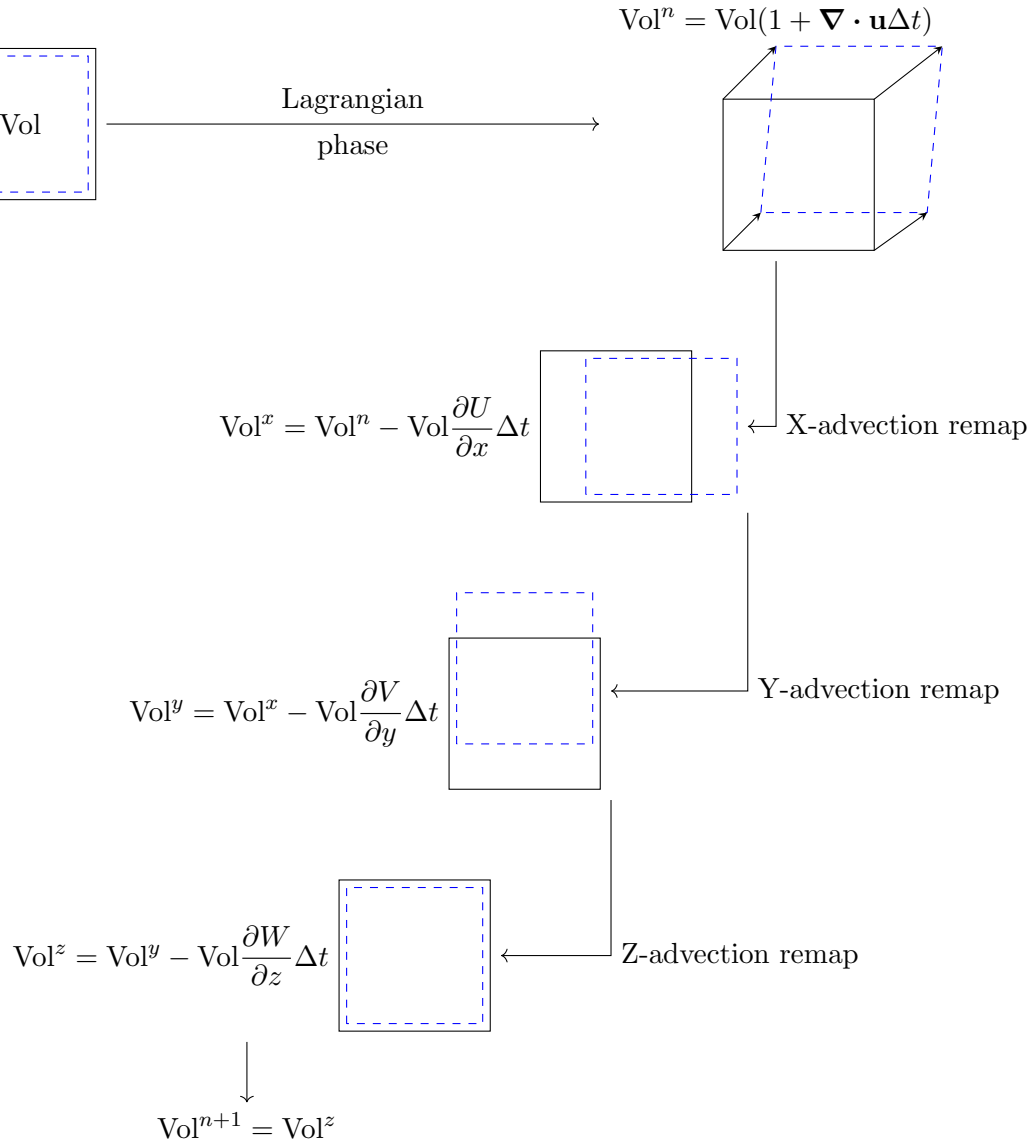


Figure 5.1: A typical sequence of Lagrangian and advection steps

Figure 5.1 illustrates the situation where the x-advection remap is executed first. However, the three 1D advection phases in the orthogonal coordinate directions should alternate (permute) in sequence in successive timesteps to achieve overall second-order accuracy in time. The advection remap permutation tends to mitigate any directional bias in each computational cycle. The choices of how to start the permutation cycle and which permutations to use are outstanding research issues. In PAGOSA, all six spatial permutations are used, beginning with the  $x$  direction. In PAGOSA, the advection order is permuted as:

| Timestep | Advection order   |
|----------|-------------------|
| 1        | X-Y-Z             |
| 2        | Z-X-Y             |
| 3        | Y-Z-X             |
| 4        | X-Z-Y             |
| 5        | Y-X-Z             |
| 6        | Z-Y-X             |
| 7        | X-Y-Z (same as 1) |
| etc.     |                   |

Next, we examine the procedures that PAGOSA uses to solve the individual phases – the Lagrangian phase and the three advection phases.

Notice that the variables  $\rho, U, V, W, E$  have been split into two. For example, a density  $\rho$  is associated with the Lagrangian phase, and another is associated with the Eulerian (remap) phase. During a computational timestep, both sets of variables are computed and used.

## 5.5 Lagrangian phase

The solution of the Lagrangian mass conservation, Equation 5.11, in our finite-difference form is<sup>6</sup>

$$\text{Vol}^{n+1} = \text{Vol}^n [1 + (\nabla \cdot \mathbf{u})\Delta t] \quad (5.31a)$$

$$\rho^{n+1} = \rho^n \left( \frac{\text{Vol}^n}{\text{Vol}^{n+1}} \right) \quad (5.31b)$$

If all of the materials within the zone are assumed to undergo uniform compression (or expansion) during the timestep, then all of the individual volume fractions remain unchanged. This assumption is clearly poor for cells containing mixtures of solids and liquids or gases.

The actual integration of the Lagrangian phase, Equation 5.31, is discussed in Chapter 6 Integration of the Hydrodynamic Variables. The time centering of the divergence and timestep is also discussed in this chapter.<sup>7</sup>

Finally, notice that the product of the divergence and the timestep is a dimensionless quantity that “controls” the fractional change in volume for that single timestep. This observation implies that the timestep should be limited by the inverse of the divergence of the velocity: one of several limits placed on the timestep. These timestep controls are discussed in Chapter 10.

<sup>6</sup>See Appendix D for the complete derivation of this expression

<sup>7</sup>The complete spatial and time indices have been omitted in Chapter 6 for clarity.

The Lagrangian momentum equations [Equation 5.12, Equation 5.13, and Equation 5.14] are the next to be solved. The components of the pressure gradient can be put in a finite-difference form using the same methodology developed in Chapter 4. However, because the velocity is spatially vertex centered, the relevant volume is the momentum control volume surrounding the vertex.<sup>8</sup> The gradient<sup>9</sup> is

$$\frac{\partial P}{\partial x} = \lim_{\Delta \text{Vol} \rightarrow 0} \frac{\oint P dy dz}{\Delta x \Delta y \Delta z} \rightarrow \frac{(\tilde{P}_{i+1/2} - \tilde{P}_{i-1/2}) \text{Area}_i}{\Delta x \Delta y \Delta z} \quad (5.32)$$

where  $\text{Area}_i$  is the relevant surface area of the momentum control volume and the volume in the denominator is the momentum control volume associated with the vertex located at  $(i, j, k)$ . The average cell-centered pressure  $\tilde{P}$  is used to compute the gradient.

The finite-difference form of Equation 5.12 is

$$\frac{U_i^{n+1} - U_i^n}{\Delta t^n} = - \frac{(\tilde{P}_{i+1/2}^n - \tilde{P}_{i-1/2}^n) \text{Area}_i}{\tilde{\rho}_i \Delta x \Delta y \Delta z} \quad (5.33)$$

Notice that the denominator on the right-hand side of the equation is simply the mass of the momentum control volume. One modification is necessary for this equation. The artificial viscosity is an additional “pressure” that can contribute to the acceleration. With the artificial viscosity term,  $Q$ , added, the equation is

$$U_i^{n+1} = U_i^n - \left[ \frac{(\tilde{P}_{i+1/2}^n + Q_{i+1/2}^n) \text{Area}_i - (\tilde{P}_{i-1/2}^n + Q_{i-1/2}^n) \text{Area}_i}{\text{Mass}_i^n} \right] \Delta t^n \quad (5.34)$$

The term inside the brackets is the  $x$  component of the acceleration. All components of accelerations are limited so that “numerical” noise is suppressed in the simulation. A user cutoff parameter is used to suppress small accelerations.

The  $Q$  term will contribute only in a few cells around shock locations. Otherwise, it has a value of zero away from shocks.<sup>10</sup> The artificial viscosity is added for purposes of numerical stability, entropy production at shocks, and energy conservation. Equation 5.34 is the  $x$ -momentum finite-difference solution of the Lagrangian-phase equations.<sup>11</sup>

For vertices surrounded by cells of void, the velocities are zero. The vertex mass ( $\text{Mass}_i$ ) is computed from the eight surrounding Eulerian cells as

$$\text{Mass}_i^n = \frac{1}{8} \sum \tilde{\rho}_i^n \text{Vol}^n \quad (5.35)$$

where the mass is computed from the average cell density and the Eulerian cell volumes.

This velocity equation is used in the predictor-corrector integration of the Lagrangian equations (Equation 5.11 – Equation 5.15). The integration algorithm is discussed in Chapter 6. The Lagrangian energy equation Equation 5.15 is solved in the same manner as Equation 5.11.

<sup>8</sup>See section 3.3 for a description of the momentum control volume.

<sup>9</sup>The gradient is computed as in Equation 4.6; however, in this case, the areas and volumes are computed with respect to the vertex-centered momentum control volume.

<sup>10</sup>See Chapter 9 for details

<sup>11</sup>The gravitational body forces are included by simply adding  $g_x \Delta t$  to the right-hand side of Equation 5.34

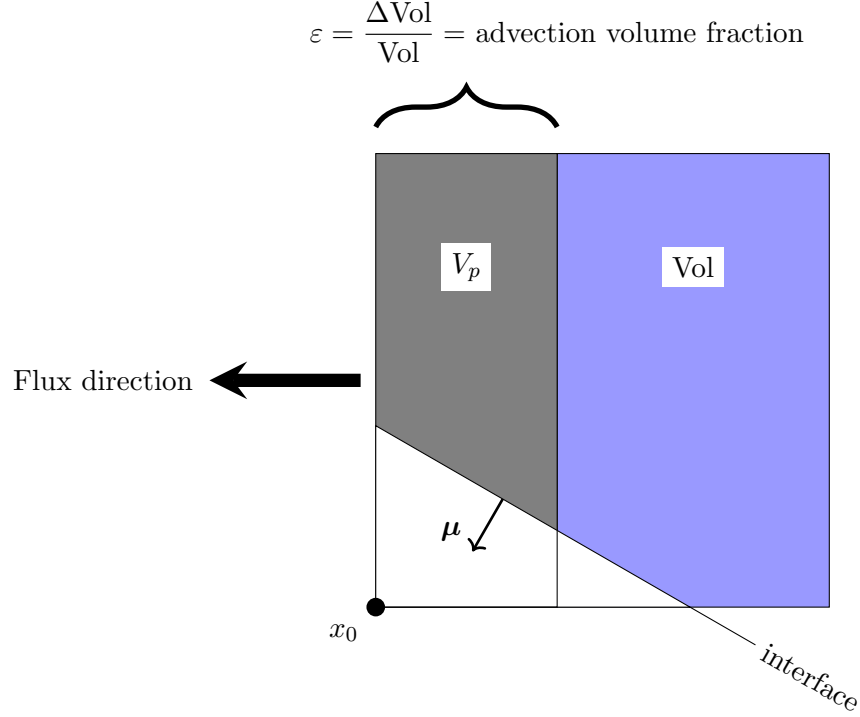


Figure 5.2: A cross section of an Eulerian cell showing a material interface with a direction vector  $\mu$ , a volume fraction to be advected  $\varepsilon$  (relative to the full cell volume  $\text{Vol}$ ), and the volume fraction of the advected portion of the material  $V_p$ .

### 5.5.1 Lagrangian setup for advection

The last step in the Lagrangian phase is to compute the volume fractions that will be advected in the advection phases.

The idea is to compute the volume fraction of the advected portion of a material on one side of a plane that passes through the Eulerian cell, as shown in Figure 5.2.

In this case, we know the volume of the cell ( $\text{Vol}$ ), we know the direction vector associated with the interface  $\mu$ <sup>12</sup>, and we know that this vector points out of the material that lies “behind” the plane. The volume fraction of the advected portion of the material is what is to be computed.

The derivation of the algorithm used to calculate the advection volumes is given in Appendix G.<sup>13</sup> The advected portion of material ( $m$ ) is given by

$$v_p = \varepsilon v'(\mu, \rho') \quad (5.36)$$

where

$$\rho' = \rho |\mu| + \frac{1}{2}(1 - \varepsilon)[\mu_1 - |\mu_1|] \quad (5.37)$$

and  $v'$  is the volume fraction of material within a unit cube, which is behind the interface plane. Note that if  $\rho' < 0$ , then the plane lies entirely outside the advection volume and  $v_p = 0$ . Conversely, if  $\rho' \geq \rho_{\max}$ , then  $v' = 1$  and  $v_p = \varepsilon$ .

<sup>12</sup>The algorithm for finding  $\mu$  is given in Appendix P

<sup>13</sup>The definitions of the variables in Equation 5.36 and Equation 5.37 are detailed in Appendix G.

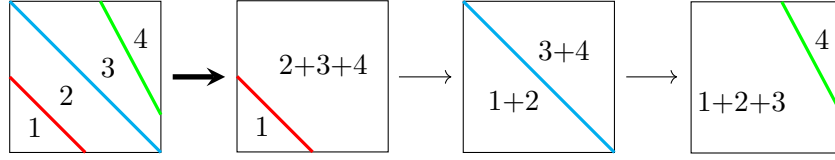


Figure 5.3: An Eulerian cell containing four materials separated by three distinct interfaces (left) is simplified into a sequence of three separate two-material (one-interface) representations (right) by accumulating materials at each step in the sequence. The accumulation order depends on the specific material priorities [e.g., the priority 1 material is treated first (second left); the priority 2 material is accumulated next (third left), followed by the priority 3 material]. The numbers refer to the priority number.

The algorithm described above is based on the Los Alamos National Laboratory publication LA-UR-07-2274.[17]

The complete derivation is presented in that document. The interface reconstruction is an integral part of the advection process.

An example is shown in Figure 5.3. Four materials exist in a single Eulerian cell at a moment in time. A priority number is associated with each material. The priority number provides an ordering to the material advection sequence. This “onion skin” method [18] is used in PAGOSA to provide a systematic reconstruction for the multi-material, multiple interface cells (mixed cells). The last material is computed separately so that material masses and volume fractions are conserved.

The order of material advection has not been addressed. PAGOSA uses a scheme whereby each material is given a priority. The advection order starts with priority 1 through the maximum number of materials. There are several potential problems with this algorithm. The priorities for each material are in general spatially and temporally dependent, but are instead arbitrarily specified as constants by the user.[19]

Nothing precludes the intersection of interfaces within a cell (resulting in negative volume fluxes).<sup>14</sup> Intersections of material (T and Y junctions) cannot be properly represented.[20] In addition, a poor normal ( $\mu$ ) estimation can lead to misrepresentations in the interface topology. An excellent review article on the volume of fluid interface treatments is given by Pilliod and Puckett.[21]

## 5.6 Advection phases

In the advection phase (also called the remap phase), the hyperbolic advection equation

$$\frac{\partial \psi}{\partial t} + a \frac{\partial \psi}{\partial x} = 0 \quad (5.38)$$

is integrated forward in time, where the variable  $\psi$  represents any advected (usually conserved) quantity, such as the mass, momentum, specific internal energy, and stress deviator. The characteristic speed  $a$  is the local time-centered fluid velocity in that cell. A variant of van Leer’s[22] monotonic upwind scheme proposed by Youngs[18] is currently used in PAGOSA.

**Advection:** The horizontal flow of water or air  
Webster’s college dictionary, 1991

<sup>14</sup>The probability of this occurrence increases with the number of materials in a cell.

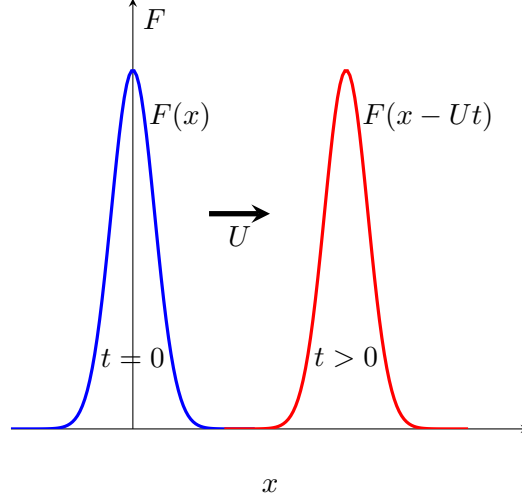


Figure 5.4: The solution of the advection equation.

Consider the 1-D  $x$ -advection equation for the conservation of mass [as shown in Equation 5.16 repeated below]. The partial differential equation is:

$$\frac{\partial \rho}{\partial t} + U \frac{\partial \rho}{\partial x} = 0 \quad (5.39)$$

The general solution of this equation is

$$\rho(x, t) = F(x - Ut) \quad (5.40)$$

where  $F$  is an arbitrary differentiable function. In this case, the function represents a density wave traveling to the right with speed  $U$ , which has a shape that does not change as it moves. The initial wave profile is given by  $\rho(x, 0) = F(x)$ , which is d'Alembert's solution to the advection equation. An example of the solution is shown in Figure 5.4 for a Gaussian pulse as an initial condition.

Integrating the linear advection equation above, Equation 5.39, over an appropriate cell control volume, we have

$$\int_{x_{i-1}}^{x_i} \frac{\partial \rho}{\partial t} dx + \int_{x_{i-1}}^{x_i} U \frac{\partial \rho}{\partial x} dx = 0$$

where the second integral can be easily evaluated to yield

$$\int_{x_{i-1}}^{x_i} \frac{\partial \rho}{\partial t} dx + U[\rho(x_i) - \rho(x_{i-1})] = 0$$

Define the densities at the cell boundaries as  $\bar{\rho}_i = \rho(x_i)$ . A finite difference approximation for the time derivative yields

$$\frac{\rho_{i-1/2}^{n+1} - \rho_{i-1/2}^n}{\Delta t} \Delta x + U[\bar{\rho}_i^n - \bar{\rho}_{i-1}^n] = 0$$

where  $\Delta x = x_i - x_{i-1}$ . The finite difference approximation of the linear advection can now be written as

$$\frac{\rho_{i-1/2}^{n+1} - \rho_{i-1/2}^n}{\Delta t} + U \frac{\bar{\rho}_i^n - \bar{\rho}_{i-1}^n}{\Delta x} \quad (5.41)$$



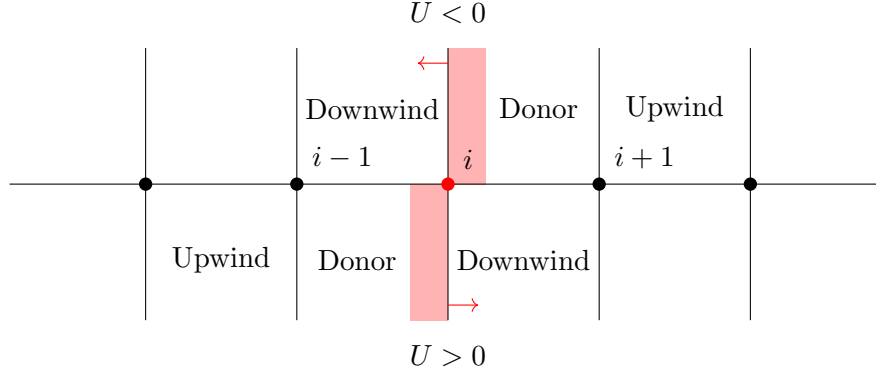


Figure 5.5: Diagram of the advection cells involved in Equation 5.34. For a positive velocity ( $U > 0$ ), the lower portion of the diagram defines the downwind, donor, and upwind cells. The negative velocity case is shown on top. The shaded area is the advection volume.

The precise finite-difference form of Equation 5.16, as derived above, depends on the sign of the velocity  $U$ . The differences are always on the “upwind” (or upstream) side of the cell at which the gradient is being evaluated. Mathematicians often refer to difference equations just with positive coefficients [23] and therefore obscure the issue. In PAGOSA, the finite-difference equation is most generally written as

$$\frac{\rho_{i-1/2}^{n+1} - \rho_{i-1/2}^n}{\Delta t} + U \frac{\bar{\rho}_i^n - \bar{\rho}_{i-1}^n}{\Delta x} ; \quad \text{if } U > 0 \quad (5.42a)$$

$$\frac{\rho_{i-1/2}^{n+1} - \rho_{i-1/2}^n}{\Delta t} + U \frac{\bar{\rho}_{i+1}^n - \bar{\rho}_i^n}{\Delta x} ; \quad \text{if } U < 0 \quad (5.42b)$$

where  $\bar{\rho}_i$  is the density at the  $i$  cell boundary. The cells used in constructing the gradient depend on the sign of the velocity, as shown in Figure 5.5.<sup>15</sup>

Rewriting Equation 5.42a for the case  $U > 0$ , we have

$$\rho_{i-1/2}^{n+1} = \rho_{i-1/2}^n - \eta(\bar{\rho}_i^n - \bar{\rho}_{i-1}^n) \quad (5.43)$$

where  $\eta$  is the Courant number,<sup>16</sup> defined as

$$\eta \equiv U \frac{\Delta t}{\Delta x}$$

The Courant number is important in establishing the stability limitations of the specific numerical method. A necessary condition for the stability of the above scheme is

$$0 \leq |\eta| \leq 1$$

The mass flowing across the cell boundary  $i$  during a timestep is simply  $\bar{\rho}_i U \Delta t$ , where the advection density  $\bar{\rho}_i$  evaluated at the boundary is given by<sup>17</sup>

$$\bar{\rho}_i^n = \rho_{i-1/2}^n + \frac{1}{2}(1 - \eta)\Delta x D_i \quad (5.44)$$

<sup>15</sup>As pointed out by Dr. Philip L. Roe from the College of Engineering at the University of Michigan, the choice of advection cell stencil cannot be arbitrary. The constraints on the stencil are detailed in an article by Iserles and Strang. [24]

<sup>16</sup>The term is named after Richard Courant (1888 – 1972), a mathematician whose work in the analysis of numerical methods laid much of the groundwork for modern computational fluid dynamics.

<sup>17</sup>The detailed derivation is given in Appendix E

Physically, this means that information cannot transit a cell in less than a single timestep. This restriction is discussed more fully in [Chapter 10](#) on timestep controls.

The variable  $D_i$  is a finite-difference approximation of the cell boundary density gradient (i.e.,  $D_i \approx \partial\rho/\partial x$ ). In PAGOSA, the possible choices for  $D_i$  are:

$$\text{First order: } D_i = 0 \tag{5.45a}$$

$$\text{Second order: } D_i = \frac{\rho_{i+1/2}^n - \rho_{i-1/2}^n}{\Delta x}, \text{ and} \tag{5.45b}$$

$$\text{Third order: } D_i = \frac{(2-\eta)}{3} \frac{\rho_{i+1/2}^n - \rho_{i-1/2}^n}{\Delta x} + \frac{(1+\eta)}{3} \frac{\rho_{i-1/2}^n - \rho_{i-3/2}^n}{\Delta x} \tag{5.45c}$$

The first-order method, sometimes called the donor cell method, is diffusive and often produces poor results. The second- and third-order methods are much less diffusive but suffer from nonphysical oscillations and occasionally negative densities. These deficiencies are corrected by limiting the density gradients in the following manner:

$$D_i = S \min \left\{ D_i, 2 \frac{|\rho_{i+1/2}^n - \rho_{i-1/2}^n|}{\Delta x}, 2 \frac{|\rho_{i-1/2}^n - \rho_{i-3/2}^n|}{\Delta x} \right\} \tag{5.46}$$

where

$$S = \begin{cases} -1 & \rho_{i+1/2}^n < \rho_{i-1/2}^n \\ 0 & \text{sign}(\rho_{i+1/2}^n - \rho_{i-1/2}^n) \neq \text{sign}(\rho_{i-1/2}^n - \rho_{i-3/2}^n) \\ +1 & \rho_{i+1/2}^n > \rho_{i-1/2}^n \end{cases} \tag{5.47}$$

which is the Youngs/van Leer gradient limiter method.[\[18\]](#) Details of the methodology are given in [section E.4](#).

The above discussion applies to the density equations [[Equation 5.16](#), [Equation 5.21](#), and [Equation 5.26](#)] and the internal energy equations [[Equation 5.20](#), [Equation 5.25](#), and [Equation 5.30](#)]. The actual integration of the advection phase equations is discussed in [Chapter 6](#), [Integration of the hydrodynamics variables](#).

### 5.6.1 Advection of momentum

The final equations to be solved [[Equation 5.17 – Equation 5.19](#), [Equation 5.22 – Equation 5.24](#), and [Equation 5.27 – Equation 5.29](#)] describe the evolution of the velocity field. For example [as shown in [Equation 5.17](#) repeated below],

$$\frac{\partial U}{\partial t} + U \frac{\partial U}{\partial x} = 0$$

is the  $x$ -momentum update for the  $x$ -advection phase.

The momentum advection proceeds in exactly the same way as that previously described in [section E.4](#), with two important differences. The control volume of interest in this case is the momentum control volume centered on the cell vertex. The fundamental variable in this case is momentum instead of velocity.

From the cell-centered advection described previously, we know the mass in the advection control volume before and after the three advection phases. Upwind, downwind, and donor cells are identified by the amount of mass crossing the surface of the control volume. Downwind is assumed to be a positive mass flux in the positive coordinate direction. Imagine the indices in [Figure 5.5](#) shifted half a cell to the right:

$$U_i^{n+1} = \frac{\text{Mass}_i^n U_i^n + \text{Flux}_{\text{in}} - \text{Flux}_{\text{out}}}{\text{Mass}_i^{n+1}} \quad (5.48)$$

where the Flux is the momentum flux at the surface of the momentum control volume. It is simply a statement of the conservation of linear momentum.[\[25\]](#) In this way, the linear momentum is conserved by construction. The momentum flux is computed as

$$\text{Flux}_{i+1/2}^n = \Delta \text{Mass}_{i+1/2}^n \left[ U_i^n + \frac{1}{2}(1 - \eta) D_i \right] \quad (5.49)$$

where the mass increment is computed in the direction of the advection [ $W$  in the case of [Equation 5.27](#) shown above]. Just as with the cell-centered advection, three advection sweeps are performed after the Lagrangian phase occurs. All of the advection sweeps happen in concert, as shown in [Figure 1.3](#).

The fluxes are computed at cell centers using the variable  $D_i$ , which in this case is a finite-difference approximation of the vertex velocity gradient (i.e.,  $D_i \approx \partial \rho / \partial x$ ). In PAGOSA, the possible choices for  $D_i$  are:

$$\text{First order: } D_i = 0 \quad (5.50a)$$

$$\text{Second order: } D_i = \frac{U_i^n - U_{i-1}^n}{\Delta x}, \text{ and} \quad (5.50b)$$

$$\text{Third order: } D_i = \frac{(2 - \eta)}{3} \frac{U_{i+1}^n - U_i^n}{\Delta x} + \frac{(1 + \eta)}{3} \frac{U_i^n - U_{i-1}^n}{\Delta x} \quad (5.50c)$$

These gradient limiters are again used to suppress oscillations and enforce a consistency with the cell-centered advection

$$D_i = S \min \left\{ D_i, 2 \frac{|U_{i+1}^n - U_i^n|}{\Delta x}, 2 \frac{|U_i^n - U_{i-1}^n|}{\Delta x} \right\} \quad (5.51)$$

where

$$S = \begin{cases} -1 & U_i^n < U_{i-1}^n \\ 0 & \text{sign}(U_{i+1}^n - U_i^n) \neq \text{sign}(U_i^n - U_{i-1}^n) \\ +1 & U_i^n > U_{i-1}^n \end{cases} \quad (5.52)$$

and

$$\eta = W_i^n \frac{\Delta t}{\Delta x} = \frac{\Delta \text{Mass}_{i+1/2}^n}{\Delta \text{Mass}_i^n} \quad (5.53)$$

See [Appendix E](#) for the motivation of this expression.

### 5.6.2 Energy advection

The internal energy advection equations [Equation 5.20, Equation 5.25, and Equation 5.30] are solved in a slightly different manner from that shown for the densities. Start with the internal energy equation [as shown in Equation 5.20, which is repeated below]

$$\frac{\partial E}{\partial t} + U \frac{\partial E}{\partial x} = 0$$

Then, apply the substitution  $E \rightarrow \rho E$  in the above equation. The result is

$$\begin{aligned} \frac{\partial(\rho E)}{\partial t} + U \frac{\partial(\rho E)}{\partial x} &= \rho \left[ \frac{\partial E}{\partial t} + U \frac{\partial E}{\partial x} \right] + E \left[ \frac{\partial \rho}{\partial t} + U \frac{\partial \rho}{\partial x} \right] \\ &= \rho[0] + E[0] = 0 \end{aligned} \quad (5.54)$$

Thus, the conservation law applies equally well to the product of density and internal energy. The finite-difference form of this new equation is

$$\frac{\rho_{i-1/2}^{n+1} E_{i-1/2}^{n+1} - \rho_{i-1/2}^n E_{i-1/2}^n}{\Delta t} + U \frac{\bar{\rho}_i \bar{E}_i - \bar{\rho}_{i-1} \bar{E}_{i-1}}{\Delta x} = 0 \quad (5.55)$$

Rewritten in the same style as Equation 5.43, we have

$$\rho_{i-1/2}^{n+1} E_{i-1/2}^{n+1} = \rho_{i-1/2}^n E_{i-1/2}^n - U \frac{\Delta t}{\Delta x} [\bar{\rho}_i \bar{E}_i - \bar{\rho}_{i-1} \bar{E}_{i-1}] \quad (5.56)$$

Now the mass associated with the advection volume is

$$\delta m_i = \bar{\rho}_i U A_i \Delta t \quad (5.57)$$

The first term in the square brackets of Equation 5.56 can be manipulated in the following way:

$$\begin{aligned} U_i \frac{\Delta t}{\Delta x} \bar{\rho}_i \bar{E}_i &= \frac{(\bar{\rho}_i U A_i \Delta t) \bar{E}_i}{\Delta x A_i} = \frac{\delta m_i \bar{E}_i}{V_{i-1/2}} = \frac{\rho_{i-1/2} \delta m_i \bar{E}_i}{\rho_{i-1/2} V_{i-1/2}} \\ &= \frac{\rho_{i-1/2} \delta m_i \bar{E}_i}{m_{i-1/2}} = \frac{\delta m_i}{m_{i-1/2}} \rho_{i-1/2} \bar{E}_i \end{aligned} \quad (5.58)$$

Thus, the internal energy update now appears as

$$\rho_{i-1/2}^{n+1} E_{i-1/2}^{n+1} = \rho_{i-1/2}^n E_{i-1/2}^n - \eta [\rho_{i-1/2}^n \bar{E}_i - \rho_{i-3/2}^n \bar{E}_{i-1}] \quad (5.59)$$

where<sup>18</sup>

$$\eta = \frac{\delta m_i}{m_{i-1/2}} \quad (5.60)$$

The densities at all of the necessary spatial and temporal positions are known, so the internal energy then may be computed with the same advection scheme presented earlier. Multiplying by the updated advection volume, we finally have

$$E_{i-1/2}^{n+1} = \frac{E_{i-1/2}^n \rho_{i-1/2}^n \text{Vol}_{i-1/2}^n + \delta m_{i-1} \bar{E}_{i-1} - \delta m_i \bar{E}_i}{\text{mass}_{i-1/2}^{n+1}} \quad (5.61)$$

Solving this last equation completes all of the advection of all hydrodynamic variables.

---

<sup>18</sup>See Appendix E for details

## Chapter 6

# Integration of the hydrodynamics variables

*Nature laughs at the difficulties of integration.*

– Pierre-Simon Laplace, The Armchair Science Reader (1959)

The integration of the Lagrangian- and Eulerian-phase equations [Equation 5.11 – Equation 5.30] is described in this chapter. The equations follow the form

$$\frac{\partial \psi}{\partial t} = F(t, \psi) \quad (6.1)$$

where  $F$  is a source term in the Lagrangian and Eulerian equations. For simplicity, we consider a scalar variable  $\psi$ , which may be any of the hydrodynamic state variables. Various methods for solving the above equation are possible. The clear candidates for the time discretization are:

- the explicit Euler method (forward scheme)

$$\psi^{n+1} = \psi^n + \Delta t F(t^n, \psi^n) \quad (6.2)$$

- the implicit Euler method (backward scheme)

$$\psi^{n+1} = \psi^n + \Delta t F(t^{n+1}, \psi^{n+1}) \quad (6.3)$$

- the semi-implicit Euler method (trapezoidal scheme)

$$\psi^{n+1} = \psi^n + \frac{1}{2} \Delta t [F(t^n, \psi^n) + F(t^{n+1}, \psi^{n+1})] \quad (6.4)$$

Note that these schemes may be interpreted either as finite-difference approximations of the time derivative or as finite-difference approximations of the time integration of the source term. Indeed,

$$\psi(t^{n+1}) = \psi(t^n) + \int_{t^n}^{t^{n+1}} F dt \quad (6.5)$$

and the various schemes can be viewed as different ways of approximating the integral.

The explicit and implicit Euler methods are first-order accurate, whereas the trapezoidal scheme is second-order accurate.

However, before proceeding, a serious handicap should be noted. The source term  $F$  depends on the unknown variable  $\psi$ , and we face the problem of not being able to calculate  $F^{n+1} = F(t^{n+1}, \psi^{n+1})$  before we know  $\psi^{n+1}$ , which is computed from  $F^{n+1}$ . A vicious circle is created here. We need to circumvent the exact calculation by searching for a good approximation. Such an approximation is possible by using a guess  $\psi^*$  in the  $F$  term at time  $t^{n+1/2}$

$$F^{n+1/2} \approx F(t^{n+1/2}, \psi^*) \quad (6.6)$$

as long as the variable  $\psi^*$  is a sufficiently good estimate of  $\psi^{n+1}$ . The closer  $\psi^*$  is to  $\psi^{n+1}$ , the more faithful the scheme is to the ideal implicit value. If this estimate  $\psi^*$  is provided by a preliminary explicit (forward) step, according to

$$\psi^{n+1/2} = \psi^n + \frac{1}{2} \Delta t F(t^n, \psi^n) \quad \text{predictor} \quad (6.7)$$

$$F^{n+1/2} \equiv \frac{1}{2} (F^n + F^{n+1}) = \frac{1}{2} [F(t^n, \psi^n) + F(t^{n+1}, \psi^{n+1/2})] \quad \text{evaluation, and} \quad (6.8)$$

$$\psi^{n+1} = \psi^n + \Delta t F^{n+1/2} \quad \text{corrector} \quad (6.9)$$

then we obtain a two-step algorithm that is second-order accurate in time. [7, 740 – 744] This second-order method is a particular member of a family of so-called predictor-corrector methods, in which a guess  $\psi^*$  is used as a proxy for  $\psi^{n+1}$  in the computation of the complicated source terms. The integration process begins at time level  $t^n$ , as shown in Figure 6.1

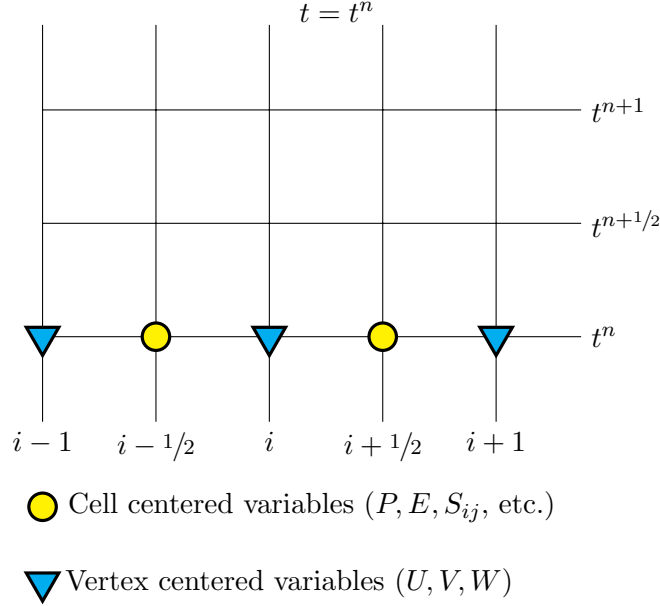


Figure 6.1: The integration step begins with all the variables at a time ( $n$ ). The velocities are shown as triangles and the state variables as circles. The velocities are spatially centered on vertices, whereas the other state variables are cell centered.

## 6.1 Predictor stage

The predictor stage of the integration (see [Figure 6.2](#)) starts with the following steps:

$$\text{Vol}^{n+1/2} = \text{Vol}^n \left[ 1 + (\nabla \cdot \mathbf{u})^n \left( \frac{1}{2} \Delta t^n \right) \right] \quad (6.10a)$$

$$\rho^{n+1/2} = \rho^n \left( \frac{\text{Vol}^n}{\text{Vol}^{n+1/2}} \right) \quad (6.10b)$$

$$E^{n+1/2} = E^n - \left[ \frac{P^n}{\rho^n} + \frac{Q^n}{\tilde{\rho}^n} \right] (\nabla \cdot \mathbf{u})^n \left( \frac{1}{2} \Delta t^n \right) \quad (6.10c)$$

$$P^{n+1/2} = P(\rho^{n+1/2}, E^{n+1/2}) \quad (6.10d)$$

The internal state cell-centered variables are advanced to half-timestep values. The basic hydrodynamic variables are shown above; however, if the material has strength, then the stress deviators, plastic work, and the other strength-related variables are also advanced. This procedure also applies to the various fracture and crush variables that are chosen and initialized in a simulation. The spatial indexing has been omitted for clarity.

Before the corrector stage can be applied, the velocity at the half-timestep must be computed. The velocities are vertex-centered quantities, so the appropriate volume is the momentum control volume, as described in [section 3.3](#). The mass associated with this control volume is the vertex mass.

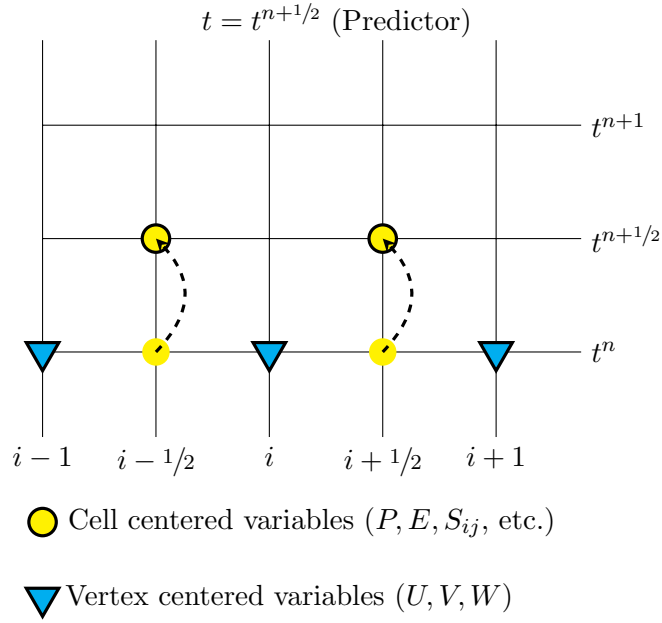


Figure 6.2: The predictor integration step advances the state variables to a time  $(n + 1/2)$ . The velocities are advanced to a time  $(n + 1)$  using the state variables, which are evaluated at a time  $(n + 1/2)$

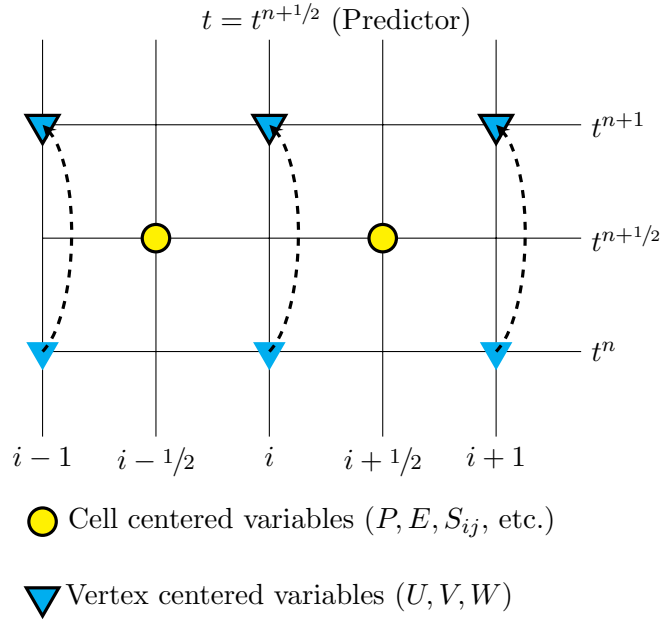


Figure 6.3: The Lagrangian velocity update first integrates the velocities to the time  $(n + 1)$ . It then averages the two velocities to create a temporally centered velocity  $u^{n+1/2}$ .



## 6.2 Lagrangian velocity update

The Lagrangian velocity update (see [Figure 6.3](#)) begins with computing the vertex masses <sup>1</sup>

$$\text{Mass}_i^n = \frac{1}{8} \sum \tilde{\rho}^n \text{Vol}^n \quad (6.11a)$$

$$U_i^{n+1} = U_i^n - \left[ \frac{(\tilde{P}_{i+1/2}^{n+1/2} + Q_{i+1/2}^{n+1/2}) \text{Area}_{i+1/2} - (\tilde{P}_{i-1/2}^{n+1/2} + Q_{i-1/2}^{n+1/2}) \text{Area}_{i-1/2}}{\text{Mass}_i^n} \right] \Delta t^n \quad (6.11b)$$

and similarly for the other components of the velocity vector.<sup>2</sup> The volume in [Equation 6.11a](#) is the original Eulerian cell volume and not the distorted Lagrangian volume. [Equation 6.11b](#) is the finite-difference solution to [Equation 5.12](#). The spatial derivative has been discretized over the momentum control volume in the manner described in [section 5.1](#). The resulting velocity vector is  $\mathbf{u}^{n+1} \equiv (U^{n+1}, V^{n+1}, W^{n+1})$ . The half-timestep velocities and divergences are then computed as

$$\begin{aligned} \mathbf{u}^{n+1/2} &\equiv \frac{1}{2} [\mathbf{u}^n + \mathbf{u}^{n+1}] \\ (\nabla \cdot \mathbf{u})^{n+1/2} &\equiv \frac{1}{2} [(\nabla \cdot \mathbf{u})^n + (\nabla \cdot \mathbf{u})^{n+1}] \end{aligned} \quad (6.11c)$$

An interesting validation for the choice of the time-centered velocity is given in Douglass and Stagg's Los Alamos National Laboratory 2007 report. [\[26, Section 4.1.5\]](#) gives the detailed derivation.] Energy conservation for the Lagrangian predictor-corrector integration timestep can be achieved only by the above choice of velocities.

## 6.3 Corrector stage

The corrector stage (see [Figure 6.4](#)) of the integration uses the updated velocity information to construct the  $(n+1)$  values of the hydrodynamic variables for each material:

$$\text{Vol}^{n+1} = \text{Vol}^n \left[ 1 + (\nabla \cdot \mathbf{u})^{n+1/2} \Delta t^n \right] \quad (6.12a)$$

$$\rho^{n+1} = \rho^n \left( \frac{\text{Vol}^n}{\text{Vol}^{n+1}} \right) \quad (6.12b)$$

$$E^{n+1} = E^n - \left[ \frac{P^{n+1/2}}{\rho^n} + \frac{Q^{n+1/2}}{\tilde{\rho}^n} \right] (\nabla \cdot \mathbf{u})^{n+1/2} \left( \frac{1}{2} \Delta t \right) \quad (6.12c)$$

$$P^{n+1} = P(\rho^{n+1}, E^{n+1}) \quad (6.12d)$$

The corrector completes the integration for a timestep. The procedure is carried out for each material in a cell. Thus, each material in a cell has its own density, internal energy, pressure, etc. No pressure or temperature equilibrium is enforced in this methodology.

In the above discussion, it has been assumed that the divergence of the velocity is applied uniformly to all materials in a cell. Uniform compression for all materials in a mixed cell is only one of the

<sup>1</sup>For the Lagrangian phase, remember that  $\text{Mass}^n = \text{Mass}^{n+1/2} = \text{Mass}^{n+1}$ .

<sup>2</sup>The term inside the brackets of [Equation 6.11b](#) is the acceleration. Acceleration cutoffs are applied to each component of the acceleration terms to suppress numerical “noise” in the simulation.

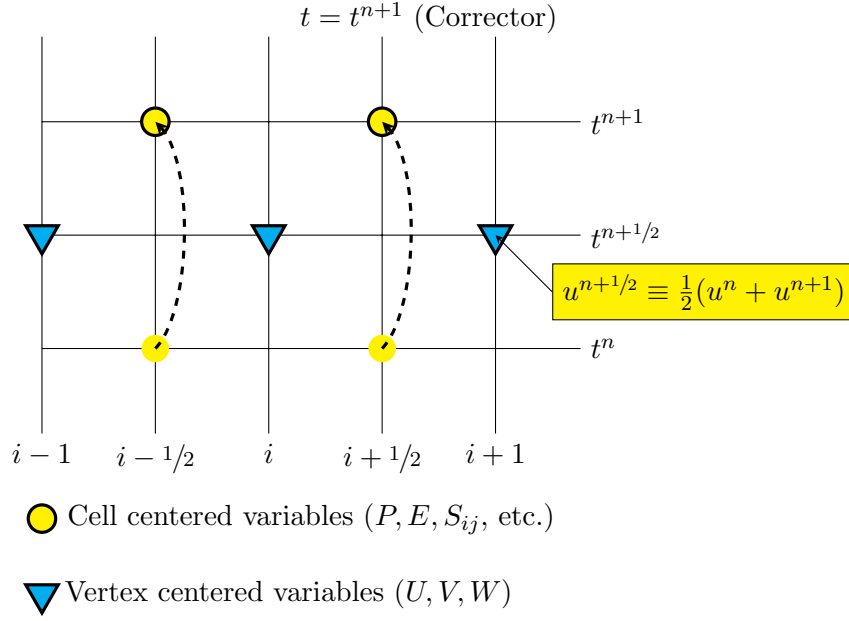


Figure 6.4: The corrector integration step uses the time-centered velocity  $u^{n+1/2}$  to update the state variables from time ( $n$ ) to time ( $n+1$ ).

divergence methods available in PAGOSA. The divergence is related to the compression of the material [see Equation 2.6, Equation 2.7, and Appendix D].

The solution to the basic Navier-Stokes hydrodynamic equations is now complete. Each of the governing equations has been solved. An outline of the equations and solutions is given in Table 6.1. The mass, momentum, and energy conservation laws are completely represented.

The derivations and solutions presented thus far have omitted the stress deviators for brevity. The development of the algorithms dealing with strength is delayed until Chapter 15. The equations and solutions for the various flow-stress models available in PAGOSA are presented in section 15.4. Each component of a multi-material cell carries a complete set of computational variables, including the stress deviators, elastic distortional energy, and plastic strain. Following the current PAGOSA philosophy, each material suffers the same cell strain rate, but the constitutive relations are applied to each material independently of the others.

Table 6.1: A schematic of the hydrodynamic variables, their conservation equations, and their finite-difference solutions

| Variable | Governing equation | Operator split                               | Finite difference solution   |
|----------|--------------------|--|--|
| $\rho$   | 2.1                | 5.11 Lag<br>5.16 Eul<br>5.21 Eul<br>5.26 Eul | 6.12b<br>5.34 $U$<br>5.34 $V$<br>5.34 $W$                                |
| $U$      | 2.2a               | 5.12 Lag<br>5.17 Eul<br>5.22 Eul<br>5.27 Eul | 6.11b $U$<br>5.48<br>5.48<br>5.48  |
| $V$      | 2.2b               | 5.13 Lag<br>5.18 Eul<br>5.23 Eul<br>5.28 Eul | 6.11b $V$<br>5.48<br>5.48<br>5.48  |
| $W$      | 2.2c               | 5.14 Lag<br>5.19 Eul<br>5.24 Eul<br>5.29 Eul | 6.11b $W$<br>5.48<br>5.48<br>5.48  |
| $E$      | 2.10               | 5.15 Lag<br>5.20 Eul<br>5.25 Eul<br>5.30 Eul | 6.12c $E$<br>5.61, section E.4<br>5.61, section E.4<br>5.61, section E.4 |
| $P$      | 2.9                | N/A  | Chapter 7  |

Note: The operator-splitting equations are represented by the one Lagrangian-phase equation (Lag) and three orthogonal Eulerian-phase equations (Eul).



## Chapter 7

# Equation of state

*The ideal gas law is the equation of state of a hypothetical ideal gas. It is a good approximation (...) although it has severe limitations.*

– Max Planck, Treatise on Thermodynamics (1903)

The set of conservation equations solved in PAGOSA contains six dependent variables: velocity (three components), pressure, mass density, and specific internal energy. This system of equations is closed mathematically by specifying an equation of state (EOS) for each material. The EOS specifies the pressure for a given material as a function of the density and specific internal energy<sup>1</sup> as

$$P = P(\rho, E) \quad (7.1)$$

for each material  $m$  in the cell. A few of the forms of this equation are described in the following pages. The average pressure in a cell is simply the volume-fraction-weighted average of all the material pressures in a cell, as defined by

$$\tilde{P} = \sum_m {}^{(m)}\phi {}^{(m)}P \quad (7.2)$$

where  ${}^{(m)}\phi$  is the volume fraction for material  $m$ .

The following notation is used in describing the various EOSs:

|                                      |                                      |
|--------------------------------------|--------------------------------------|
| $\varepsilon \equiv \rho_0 E$        | internal energy per original volume, |
| $\mu \equiv \frac{\rho}{\rho_0} - 1$ | compression / expansion factor, and  |
| $V_0 \equiv \frac{1}{\rho_0}$        | Specific volumes                     |
| $V \equiv \frac{1}{\rho}$            |                                      |

## 7.1 Ideal gas EOS

One of the simplest forms of an EOS is the ideal gas law<sup>2</sup>

$$P = (\gamma - 1)\rho E \quad (7.3)$$

where  $\gamma$  is ratio of specific heats at constant pressure and constant volume. The ideal gas law is favored for monatomic gases at high temperatures and low pressures. This law does not factor in the size of the molecules or intermolecular attractions. However, it is often used in limited regimes, with the value of  $\gamma$  adjusted to fit some data, but only to get a qualitative understanding of how the system will behave using an easily manipulated EOS.

## 7.2 Void EOS

Another commonly used EOS is void. For this EOS, the density, specific internal energy, and pressure are all set to zero

$$\begin{aligned} \rho &= 0 \\ E &= 0 \quad \text{void EOS} \\ P &= 0 \end{aligned} \quad (7.4)$$

---

<sup>1</sup>This type of EOS is denoted “incomplete” because the temperature cannot be calculated unless the specific heat is known.

<sup>2</sup>It is a simply derived alternative to the well-known equation  $PV = nRT$ .

This form has the advantage that no sound speed is computed, and therefore, the material cannot control the timestep in a simulation. The other advantage is void closure. Imagine two materials that are about to collide. The interface reconstruction within a cell allows the three materials to be represented by two planes. If the intervening material is a void, then the void closure model can be invoked. This option allows the two materials to come smoothly into contact without creating bubbles or small densities that are often problematic for any other EOS.

### 7.3 Polynomial EOS

A common analytic EOS is the polynomial EOS, which is often used in fitting experimental EOS data. This EOS has the form

$$P = a_0 + a_1\mu + a_2^*\mu^2 + a_3\mu^3 + \varepsilon(b_0 + b_1\mu + b_2^*\mu^2 + b_3\mu^3) \quad (7.5)$$

The constants  $a_2^*$  and  $b_2^*$  can assume different values in expansion and compression.

$$a_2^* = \begin{cases} a_2^c & \mu \geq 0 \text{ (compression)} \\ a_2^e & \mu < 0 \text{ (expansion)} \end{cases}$$

and similar expressions for  $b_2^*$ .

One clear simple case of the polynomial EOS is a constant pressure. In this case,  $a_0 = P_0 = \text{constant}$ , and the other constants have the value zero. Another special case of the polynomial EOS can be demonstrated by considering the bulk modulus for adiabatic compression, which is defined as

$$\kappa \equiv \rho \left( \frac{\partial P}{\partial \rho} \right)_S = (1 + \mu) \left( \frac{\partial P}{\partial \mu} \right)_S$$

Integrating the expression, the pressure is (for moderate compression/expansion)

$$\begin{aligned} P &= \kappa \ln(1 + \mu) \\ &\approx \kappa\mu - \frac{1}{2}\kappa\mu^2 + \frac{1}{3}\kappa\mu^3 - \frac{1}{4}\kappa\mu^4 + \dots \end{aligned} \quad -1 \leq \mu \leq 1$$

Thus, to first order, the EOS is

$$P = \kappa\mu = \kappa \left( \frac{\rho}{\rho_0} - 1 \right)$$

In terms of the polynomial EOS,  $a_1 = \kappa$ , and all the other constants have a value of zero.

### 7.4 Modified Osborne (or Quadratic) EOS

This form was originally derived by Group T-5 at Los Alamos Scientific Laboratory in the 1950s as a fit between low-pressure Hugoniot data and the high-pressure Thomas-Fermi-Dirac theory.<sup>[27]</sup> One

of the reasons for the particular form of the equation, sometimes called the quadratic EOS,[28, 29] was the small amount of memory of the computers then in use.

$$P = \frac{a_1\mu + a_2^*\mu^2 + (b_0 + b_1\mu + b_2^*\mu^2)\varepsilon + (c_0 + c_1\mu + c_2^*\mu^2)\varepsilon^2}{\varepsilon + \varepsilon_0} \quad (7.6)$$

Many of the original constants found by R. K. Osborne are still in use today.

The constants  $a_2^*$ ,  $b_2^*$ , and  $c_2^*$  assume different values in expansion and compression

$$a_2^* = \begin{cases} a_2^c & \mu \geq 0 \text{ (compression)} \\ a_2^e & \mu < 0 \text{ (expansion)} \end{cases}$$

and similar expressions for  $b_2^*$  and  $c_2^*$ . The traditional Osborne EOS is recovered by setting

$$a_2^e = -a_2^c, \quad b_2^e = b_2^c, \quad c_2^e = 0$$

The constants of the Osborne EOS need to be scaled in the case of an alloy or isotope where the constants are not known. A suggested scaling is given by Lambourn. [30]

|                                |   |
|--------------------------------|---|
| $a_1, a_2$                     | should be scaled with $\rho_0^2$                              |
| $b_0, b_1, b_2, \varepsilon_0$ | should be scaled with $\rho_0$ , and                          |
| $c_0, c_1$                     | should not be scaled (should remain at their original values) |

## 7.5 Jones-Wilkins-Lee (or JWL) EOS

The JWL EOS [31] is often used for computing the EOS of high-explosive detonation products. Its development began with an equation proposed by Jones and Miller [32] and extended by Wilkins.[33] It is therefore now referred to as the JWL EOS. The EOS is written as

$$P = A \left[ 1 - \frac{\omega}{R_1} \frac{\rho}{\rho_0} \right] \exp \left( \frac{-R_1 \rho_0}{\rho} \right) + B \left[ 1 - \frac{\omega}{R_2} \frac{\rho}{\rho_0} \right] \exp \left( \frac{-R_2 \rho_0}{\rho} \right) + \omega \rho E \quad (7.7)$$

where the five constants  $A, B, R_1, R_2, \omega$  are experimentally determined. Note that the constants  $A$  and  $B$  have the units of pressure, whereas the other constants are dimensionless.

If the HE is detonated by the program burn algorithm, the pressure and energy are gradually deposited into a cell over several timesteps. The pressure is scaled by a factor called the burn fraction  $Bf$ . The burn fraction values range between zero and one. A value of zero indicates that the detonation wave has not yet reached the cell, and a value of one indicates a completely burned cell. The program burn algorithm defines a “burn time” for each cell vertex in the simulation.<sup>3</sup> Of the eight cell vertices, the difference between the minimum and maximum burn times is referred to as the burn interval for a cell.

---

<sup>3</sup>In reactive burn models, the burn fraction is evolves according to the physics of the reaction progress.



Mathematically,

$$\begin{aligned}
 t_{\min} &= \min(t_1, t_2, t_3, t_4, t_5, t_6, t_7, t_8) \\
 t_{\max} &= \max(t_1, t_2, t_3, t_4, t_5, t_6, t_7, t_8) \\
 t_{\text{interval}} &= t_{\max} - t_{\min} \\
 Bf &= \begin{cases} 0 & t \leq t_{\min} \\ \frac{t - t_{\min}}{t_{\text{interval}}} & t_{\min} < t < t_{\max} \\ 1 & t \geq t_{\max} \end{cases}
 \end{aligned}$$

This procedure usually results in the cell pressure developing over four or five timesteps. The maximum timestep is adjusted so that a cell cannot burn in fewer steps. Tables of constants for many explosives have been compiled by Brigitta Dobratz.[\[34\]](#)

The constants used in the PAGOSA code have a slightly different form from the original JWL form. The translation between the two forms is:

| PAGOSA             | Dobratz Handbooks |
|--------------------|-------------------|
| $W$                | $\omega$          |
| $B_1$              | $A$               |
| $C_1 = \rho_0 R_1$ | $R_1$             |
| $B_2$              | $B$               |
| $C_2 = \rho_0 R_2$ | $R_2$             |
| $e_0 = E_0/\rho_0$ | $E_0$             |

The main advantage of the JWL EOS lies in its ability to describe the Chapman-Jouget adiabat accurately. The above parameters have been chosen to satisfy the measured Chapman-Jouget state, the measured expansion of a cylinder test, some asymptotic thermodynamics limitations, and hydrodynamic continuity equations.

## 7.6 Grüneisen (or $U_S - U_P$ ) EOS

The most common description of solids uses the measured Hugoniot curve as a reference and uses the Grüneisen relationship to extrapolate off the reference curve. It is often the case that the Hugoniot curve can be represented over a large range of pressures as a simple linear expression[\[35, 36\]](#) in the  $U_S - U_P$  plane

$$U_S = c_0 + sU_P \tag{7.8a}$$

$$P = P_H + \frac{\Gamma}{V}(E - E_H) \tag{7.8b}$$

$$P_H = P_0 + c_0^2(V_0 - V)[V_0 - s(V_0 - V)]^{-2} \tag{7.8c}$$

$$E_H = E_0 + \frac{1}{2}(P_0 + P_H)(V_0 - V) \tag{7.8d}$$

$$\Gamma = \Gamma_0 + \Gamma_1 \left( \frac{V}{V_0} \right) \tag{7.8e}$$

where  $P_H$  is the pressure on the Hugoniot,  $E_H$  is the energy on the Hugoniot,  $V_0 = \rho_0^{-1}$  is the initial specific volume, and  $V = \rho^{-1}$  is the state-specific volume. In the above expressions,  $c_0$  and  $s$  are constants obtained from the relationship between shock speed  $U_S$  and particle speed  $U_P$ .

The Hugoniot pressure relation contains a simple pole at  $s = V_0/(V_0 - V)$ . This relation puts a limit on the allowable density for this EOS. If a maximum density is not specified, then a maximum is imposed by

$$\rho_{\max} = \max \left[ 99\% \rho_0 \left( \frac{s}{s-1} \right), 2\rho_0 \right]$$

where  $\rho_0$  is the nominal mass density.

This particular EOS is sufficiently different from the others described that a short description of the derivation is warranted. The thermodynamic states off of the Hugoniot curve can be obtained by constructing a Taylor expansion, at constant density, about the reference Hugoniot curve. Mathematically,

$$P(\rho, E) = P_H(\rho) + \left( \frac{\partial P}{\partial E} \right)_\rho [E - E_H(\rho)] + \frac{1}{2} \left( \frac{\partial^2 P}{\partial E^2} \right)_\rho [E - E_H(\rho)]^2 + \dots$$

where  $E - E_H(\rho)$  is the displacement from the Hugoniot curve. The values denoted with the subscript  $H$  are points on the reference Hugoniot curve. The definition of the Grüneisen parameter  $\Gamma$  is

$$\left( \frac{\partial P}{\partial E} \right)_\rho \equiv \Gamma \rho = \frac{\Gamma}{V}$$

It is usually assumed that the parameter is a linear function of the compression/expansion, i.e.,  $\Gamma = \Gamma_0 + \Gamma_1(\rho_0/\rho)$ , so that the higher-order terms in the Taylor expansion vanish. The EOS becomes

$$P(\rho, E) = P_H(\rho) + \frac{\Gamma}{V} [E - E_H(\rho)]$$

Experimentally, it has been found that for many solids, the Hugoniot curve can be represented as a simple linear curve in the  $U_S - U_P$  plane. Contrary to what is usually found in the literature,  $c_0$  is not the bulk sound speed in the ambient state. Rather, it is the value of the intercept of the  $U_S - U_P$  line. [37, pp. 710]

## 7.7 SESAME EOS

A tabular EOS that represents hundreds of materials and experiments is available using the LANL SESAME database.[38, 39] The database contains EOS tables for pressure and internal energy as a function of temperature. The database library has several advantages: it can accurately represent phase transitions, it represents a wide range of temperatures and densities, and it represents the best experimental and theoretical data available at LANL. The data are inverted before they are used in PAGOSA so that the pressure is solely a function of density and internal energy. The SESAME EOS is

$$P = P_{\text{SESAME}}(\rho_T, E_T) \tag{7.9}$$

where  $P_{\text{SESAME}}$  is the tabular EOS. The tabular database is read using the EOS package (EOSPAC) software library.[40]

The library software allows for various ways of interpolating and scaling the tabular data. The relation of “code” input to the tabular EOS is given by

$$\begin{aligned}\rho_T &= (SR)\rho \\ E_T &= (E + ES)/SR\end{aligned}$$

where

$$\begin{aligned}SR &= \text{density scaling ratio and} \\ ES &= \text{energy shift}\end{aligned}$$

The scaling ratio parameter  $SR$  is often useful in modeling isotopic mixtures. For example, if  $A_T$  is the atomic mass for a particular SESAME EOS, an EOS for an atomic mass  $A$  is obtained by setting the scaling ratio

$$SR = \frac{A_T}{A}$$

Suppose we wish to model a gas of hydrogen ( $\text{H}_2$ ). The SESAME identification number for deuterium is 5263. A scaling ratio of  $SR = 2$  scales the SESAME tabular deuterium EOS to hydrogen. Similarly, a scaling ratio of  $SR = 0.8$  scales the SESAME tabular deuterium EOS to a 50%:50% mixture of deuterium and tritium (DT).

The energy shift is defined by

$$ES = -\Delta E(\text{initial} \rightarrow \text{final})$$

where  $\Delta E$  is the energy required to transform the low-density phase to the high-density phase. There are two cases. If the initial phase is stable, then the value of  $ES$  is negative. If the initial phase is metastable, then the value of  $ES$  is positive.

The pressure-density curve at  $T = 0\text{K}$  is commonly called the “cold curve” and was traditionally modeled by empirical formulas (e.g., analytic potentials combined with the Thomas-Fermi-Dirac theory). The modern theory uses relativistic electronic band structure methods to compute the cold curve. The total pressure can be thought of as being the sum of the cold-curve pressure and the thermal pressure (i.e., the pressure due to positive internal energies).

### 7.7.1 Ramp treatment

For the treatment of foams and certain types of phase transitions, it is possible to modify the SESAME EOS by adding a ramp (see [Figure 7.1](#)) that describes the behavior of the material under low stress. The material begins in a porous or low-density state. The EOS in this regime is

$$P_1 = A_1 \left( \frac{\rho}{\rho_0} - 1 \right) \tag{7.10}$$

where  $\rho_0$  is the initial density and  $A_1$  is the bulk modulus. The bulk modulus can be computed from the sound speed as

$$A_1 = \rho_0 a^2$$

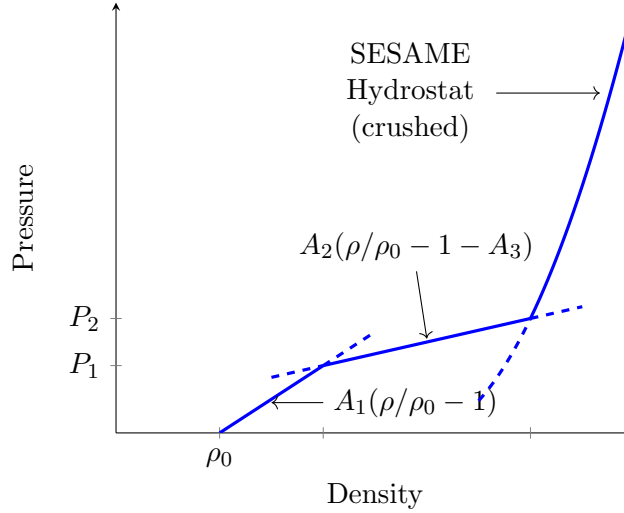


Figure 7.1: SESAME ramp treatment for foams and certain types of phase transitions

where  $a$  is the bulk sound speed. If  $A_1 = 0$ , then no ramp calculation is done. At some value of pressure  $P_1$ , the material begins to crush or transform to a SESAME EOS. The EOS of the “crush curve” is given by

$$P_2 = A_2 \left( \frac{\rho}{\rho_0} - 1 - A_3 \right)$$

If  $A_2 = 0$ , then no crush regime exists and the equation represented by Equation 7.10 is continued until it crosses the SESAME curve. The value of  $A_2$  can be computed from the crossing at the transition pressure  $P_1$ , or it can be guessed at if no other information is available.

$$A_2 = \frac{P_1 A_1}{P_1 - A_1 A_3} \quad \text{if } P_1 \text{ is known}$$

$$A_2 = \frac{A_1}{10} \quad \text{if } P_1 \text{ cannot be measured}$$

The transition pressure for foams is often small ( $< 1$  kbar). On the other hand, for a phase transition, the value of  $P_1$  must be determined from experiments. The value of  $A_3$  can be adjusted to give the appropriate slope for the crush curve. In the absence of any data, the default value of  $A_3 = 0$  should give acceptable results.

However, a better value might be<sup>4</sup>

$$A_3 = P_1 \left[ \frac{1}{A_1} - \frac{1}{A_2} \right]$$

At some pressure  $P_2$ , the crush curve crosses the SESAME curve. At that point the material is “crushed.” Subsequently, the material may behave either reversibly (follow the ramp on expansion) or irreversibly (remain on the high-density phase on expansion). Foams are normally reversible. However, phase transitions may exhibit either behavior. Materials may also behave irreversibly if they melt (i.e., if the melt energy or melt temperature is exceeded).

<sup>4</sup>The value of  $P_1$  should be measured in this case. B.I. Bennett, Los Alamos National Laboratory, private communication, October 22, 1984.

### 7.7.2 SESAME body internal energy iteration<sup>5</sup>

In some cases the initial conditions for a particular SESAME material are not completely known. For example, the user may know the initial density and a desired initial pressure but not know the corresponding initial internal energy. PAGOSA provides a solution to this dilemma by providing a mechanism for setting the initial density and pressure within a body specification. PAGOSA and EOSPAC together then iterate until the appropriate initial internal energy is found.

Given the density and the desired initial pressure, the EOS is

$$P = P(\rho, E)$$

If the desired initial pressure is  $P_0$  and the desired initial density is  $\rho_0$ , then the EOS can be written as

$$P_0 = P(\rho_0, E^*)$$

The problem is finding the value of internal energy  $E^*$  that satisfies this relation. The algorithm for finding  $E^*$  starts with the Newton-Raphson method.[7, pp. 254 – 259] The method is often written as

$$x_{n+1} = x_n - \frac{f(x_n)}{f'(x_n)} \quad n = 1, 2, 3, \dots, n_{\max}$$

To apply this method to our problem, we first start with an approximation for the derivative:

$$\left(\frac{\partial P}{\partial E}\right)_\rho = \frac{P_0 - P}{E_0 - E}$$

The EOSPAC derivatives are with respect to the logarithm of density and energy, so

$$\left(\frac{\partial P}{\partial \ln E}\right)_\rho = E \left(\frac{\partial P}{\partial E}\right)_\rho$$

The equation now can be cast in the Newton-Raphson form

$$E_{n+1} = E_n + \frac{P_0 - P_n}{\left(\frac{\partial P}{\partial E}\right)_\rho}$$

and

$$E_{n+1} = E_n \left[ 1 + (P_0 - P_n) \left(\frac{\partial P}{\partial \ln E}\right)_\rho^{-1} \right] \quad n = 1, 2, 3, \dots, n_{\max}$$

The iteration process completes when the pressure is within an acceptable range of  $P_0$ . The convergence criterion used in PAGOSA is

$$\left| 1 - \frac{P_n}{P_0} \right| < \text{tolerance}$$

Occasionally, the resulting initial internal energy has a small negative value. Some of the SESAME tables have “poor” data in particular regions or the interpolation scheme is not sufficient for the data provided. The user is always responsible for checking the results of the PAGOSA-generated initial conditions.

---

<sup>5</sup>Never use the SESAME body iteration option with the ramp treatment. The results are often wrong.

## 7.8 Exponential EOS

The exponential EOS is unique in PAGOSA in that it specifies a pressure as a function of time. Mathematically,

$$P(t) = P_0 \exp(\alpha t) \quad (7.11)$$

where  $P_0$  is the pressure at  $t = 0$  and  $\alpha$  is the decay constant (with units of inverse time). This analytic form of the EOS provides a simple time-dependent pressure that can be used in certain test problems for validation and verification.[\[41\]](#)

## 7.9 Davis EOS

The Davis EOS acts on both the solid reactants and the gaseous products of a high explosive. It is a complete equation of state that is able to operate over wide ranges of thermodynamic states, including over-driven regimes. Using thermal and mechanical properties of the HE, a Mie-Grüneisen form is used for both products and reactants. Details on its development can be found in the canonical paper by Wescott et al. [\[42\]](#)

With PAGOSA providing material density  $Dm$ , material specific internal energy  $Em$ , and material burn fraction  $Bfm$ , a Pressure-Temperature ( $P$ - $T$ ) equilibration scheme is employed to back out ratio of specific volumes,  $V_p/V_r$ , or  $\phi$ . An enhanced secant method algorithm using the previous timestep's converged  $\phi$  values as initial guesses, provides a speedy root finding technique. If there are issues with convergence, the code switches to the slower, but safer, bisection method to ensure a solution. Once a solution for  $\phi$  is found, it is used subsequently to calculate pressures, sound speeds, and temperatures for the products, reactants, and mixtures of the two.

### 7.9.1 Davis-Reactants

The following equations make heavy use of Aslam's article. [\[43\]](#) The pressure and energy of the reactants can be represented by the standard Mie-Grüneisen form

$$p_r(e, \rho) = p_r^s(\rho) + \rho \Gamma_r(\rho) [e - e_r^s(\rho)] \quad (7.12)$$

$$e_r(p, \rho) = e_r^s(\rho) + \frac{p - p_r^s(\rho)}{\rho} \Gamma_r(\rho) \quad (7.13)$$

where  $r$  indicates reactants and the  $s$  superscript is an isentrope. The reference isentrope of the reactants is

$$p_r^s(\rho) = \begin{cases} \hat{p}[\exp(4By) - 1] & \rho < \rho_0 \\ \hat{p} \left[ \sum_{j=1}^3 \frac{(4By)^j}{j!} + C \frac{(4By)^4}{4!} + \frac{y^2}{(1-y)^4} \right] & \rho \geq \rho_0 \end{cases} \quad (7.14)$$

where  $y = 1 - \rho_0/\rho$  and  $\hat{p} = \rho_0 A^2/4B$ .  $A$  is the bulk sound speed,  $B$  is related to the derivative of the bulk modulus at zero pressure, and  $C$  helps determine the behaviour at high shock strengths.

The above reference pressure along the isentrope can then be integrated to obtain the reference energy along the isentrope

$$e_r^s(\rho) = \int_{\rho_0}^{\rho} \frac{p_r^s}{\rho^2} d\bar{\rho} + E_0 \quad (7.15)$$

where  $E_0$  (or  $q$ ) is an integration constant, equivalent to the stored chemical potential energy of the explosive. The Grüneisen parameter is taken to be

$$\Gamma_r(\rho) = \begin{cases} \Gamma_r^0 & \rho < \rho_0 \\ \Gamma_r^0 + Zy & \rho \geq \rho_0 \end{cases} \quad (7.16)$$

where  $Z$  ( $Z_{solid}$ ) is a constant used to describe the changes to  $\Gamma_r$  with respect to density.

The reactant's temperature,  $T_r$ , can be represented as

$$T_r(e, \rho) = T_r^s(\rho) \left\{ \frac{1 + \alpha}{C_{VR} T_r^s(\rho)} [e - e_r^s(\rho)] + 1 \right\}^{1/1 + \alpha} \quad (7.17)$$

where  $T_r^s(\rho)$  is the temperature along the reference isentrope

$$T_r^s(\rho) = T_0 \exp(-Zy) \left( \frac{\rho}{\rho_0} \right)^{(\Gamma_r^0 + Z)} \quad (7.18)$$

Here,  $C_{VR}$  is the reactant specific heat at constant volume at reference temperature  $T_0$ , and  $\alpha$  determines how the specific heat changes with respect to temperature.

### 7.9.2 Products

The pressure and energy of the products can also be represented by a standard Mie-Grüneisen form

$$p_p(e, \rho) = p_p^s(\rho) + \rho \Gamma_p(\rho) [e - e_p^s(\rho)] \quad (7.19)$$

$$e_p(p, \rho) = e_p^s(\rho) + \frac{p - p_p^s(\rho)}{\rho} \Gamma_p(\rho) \quad (7.20)$$

where  $p$  indicates products.

The pressure on the principal Chapman-Jouget isentrope is given by

$$p_p^s(\rho) = p_c \frac{\left[ \frac{(\rho v_c)^{-n}}{2} + \frac{(\rho v_c)^n}{2} \right]^{\frac{a}{n}}}{(\rho v_c)^{-(k+a)}} \frac{k - 1 + F(\rho)}{k - 1 + a} \quad (7.21)$$

where

$$F(\rho) = \frac{2a(\rho v_c)^n}{(\rho v_c)^{-n} + (\rho v_c)^n} \quad (7.22)$$

The energy along the isentrope is given by

$$e_p^s(\rho) = e_c \frac{\left[ \frac{(\rho v_c)^{-n}}{2} + \frac{(\rho v_c)^n}{2} \right]^{\frac{a}{n}}}{(\rho v_c)^{-(k-1+a)}} \quad (7.23)$$

where

$$e_c = \frac{p_c v_c}{k - 1 + a} \quad (7.24)$$

The Grüneisen parameter is given by

$$\Gamma_p(\rho) = k - 1 + (1 - b)F(\rho) \quad (7.25)$$

The parameters (obtained for the gas phase)  $p_c$ ,  $v_c$ ,  $a$ ,  $b$ ,  $k$ , and  $n$  define the principal CJ isentrope, while parameter  $b$  sets  $\Gamma_p$ , and the off-isentrope behavior.

The temperature of the products are given by

$$T_p(e, \rho) = T_p^s(\rho) = T_p^s(\rho) + \frac{e - e_p^s(\rho)}{C_{vp}} \quad (7.26)$$

where the temperature on the principal isentrope is given by

$$T_p^s(\rho) = T_c \frac{\left[ \frac{(\rho v_c)^{-n}}{2} + \frac{(\rho v_c)^n}{2} \right]^{\left(\frac{a}{n}\right)(1-b)}}{(\rho v_c)^{-(k-1+a(1-b))}} \quad (7.27)$$

$$T_c = \frac{2^{\frac{-ab}{n}}}{k - 1 + a} \frac{p_c v_c}{C_{vp}} \quad (7.28)$$

### 7.9.3 Davis Mixing

With the forms presented above for pressure and temperature of both products and reactants, the pressures, soundspeeds and temperatures for a cell that is fully product or fully reactant is simply computed. When a cell is partially burned, the value  $\Phi$  is used to properly calculate the gas and solid densities, which in turn can be used to calculate the thermodynamic quantities from the equations described above.

### 7.9.4 AWSD Reactive Burn Model

The thermodynamic closure of the Davis equation of state was originally coupled with a reactive burn model, the union of which was known as the WSD model. The AWSD burn rate model is a departure from the original pressure-based burn model. It takes advantage of the temperatures calculated in the Davis EOS in order to update the burn fraction as a function, primarily, dependent upon shock temperature.

Calculation of burn rate as a function of temperature can be advantageous because the sensitivity of a high-explosive's initial temperature is substantial. The difference between a high-explosives with an initial temperature of 218 K vs 348 K translates to a 2-3 times slower burn rate for the colder material. The AWSD model deals with this sensitivity to initial temperatures, with a single set of parameters, thus preventing the need for calibrations of parameters for different initial temperatures.

The burncons are:



|                  |   |
|------------------|---|
| $B_{min}$        | burncon(1), Minimum allowed burn fraction                 |
| $B_{max}$        | burncon(2), Maximum allowed burn fraction                 |
| $p_s$            | burncon(3), Calibrated parameter, Equation 7.31           |
| $n_p$            | burncon(4), Pressure exponential, Equation 7.31           |
| $k_1$            | burncon(5), $F_1$ term multiplier, Equation 7.32          |
| $T_1$            | burncon(6), Activation Temperature 1, Equation 7.32       |
| $k_2$            | burncon(7), $F_2$ term multiplier, See a in Equation 7.33 |
| $T_2$            | burncon(8), Temperature 2, See k in Equation 7.33         |
| $a_1$            | burncon(9), Calibrated parameter, Equation 7.32           |
| $b_1$            | burncon(10), Calibrated parameter, Equation 7.32          |
| $b_2$            | burncon(11), Depletion factor, Equation 7.33              |
| $f_s$            | burncon(12), Rate scaling factor, Equation 7.34           |
| $\lambda_c$      | burncon(13), Calibrated parameter, Equation 7.34          |
| $\delta_\lambda$ | burncon(14), Characteristic scale, Equation 7.34          |
| $T_c$            | burncon(15), $T^*$ exponent, Equation 7.37                |
| $a_T$            | burncon(16), $T^*$ multiplier, Equation 7.37              |
| $p_\zeta$        | burncon(17), Reference shock pressure, Equation 7.35      |
| $k_\zeta$        | burncon(18), Zeta rate, Equation 7.35                     |

The AWSO burn rate is described in Aslam's article, [43] along with the parameters for PBX 9502. The rate  $R$  is a function of shock temperature  $T_{SH}$ , local pressure  $p$ , and burn fraction  $\lambda$

$$\frac{D\lambda}{Dt} = R(T_{SH}, p, \lambda). \quad (7.29)$$

The rate is

$$R = F_p(F_1 + F_2)F_\lambda, \quad (7.30)$$

where

$$F_p = \begin{cases} \exp(-(\frac{p_s}{p})^{n_p}) & \text{if } p > p_\zeta \\ 0 & \text{otherwise} \end{cases} \quad (7.31)$$

The  $F_p$  term above is the primary way that the pressure influences the burn rate. Note that if the pressure is below a certain threshold pressure  $P_\zeta$ , the burn rate will be zero. The next two terms portray the model's temperature dependence. Note that the pressure sensitive and shock temperature sensitive terms are multiplicative, indicating that if either one is low the rate will be low.

$$F_1 = k_1 \exp\left(\frac{-T_1}{T_{SH}}\right) (\lambda + a_1 F_p)(1 - \lambda)^{b_1} \quad (7.32)$$

$$F_2 = k_2 \exp\left(\frac{-T_2}{T_{SH}}\right) (1 - \lambda)^{b_2} \quad (7.33)$$

The  $F_1$  and  $F_2$  terms above are Arrhenius in terms of the shock temperature  $T_{SH}$ , where  $T_1$  and  $T_2$  are activation temperatures. The intent of the  $F_1$  term primarily captures the shock-to-detonation transition sensitivity associated with hot-spots and is dominant at lower shock temperatures. The

role of  $F_2$  is to capture the sensitivities at detonation conditions that are under more homogenous volumetric burn, and is dominant at higher shock temperatures.

$$F_\lambda = f_s + \frac{1}{2}(1 - f_s) \left( 1 - \tanh \left( \frac{\lambda - \lambda_c}{\delta_\lambda} \right) \right) \quad (7.34)$$

The final term  $F_\lambda$  is utilized to lower the rate from its nominal value for the treatment of the long reaction zones observed in the detonation of TATB explosives.

The previously defined burn rates are only calculated when the local pressure exceeds some threshold shock pressure  $p_\zeta$  at which the voids in the HE are compressed. Similarly, a shock timer  $\zeta$  is advanced by a rate  $k_\zeta$  when  $p > p_\zeta$  to ensure that the calculation of the shock temperature  $T_{SH}$  only occurs in the vicinity of a shock.

$$\dot{\zeta} = k_\zeta H(p - p_\zeta) \quad (7.35)$$

where  $H$  is the Heaviside function.

Under the aforementioned conditions, the shock temperature is calculated as

$$T_{SH} = \begin{cases} \max(T_{SH}, T^*) & \text{if } \lambda > \frac{1}{2} \text{ and } \zeta < 1 \\ T_{SH} & \text{otherwise} \end{cases} \quad (7.36)$$

where  $T^*$  is an approximation of the shock temperature given by

$$T^*(T, \lambda) = T \left[ 1 - a_T \lambda \exp \left( \frac{T_c}{T} \right) \right] \quad (7.37)$$

Both  $T_{SH}$  and  $\zeta$  are state variables that are advected throughout the simulation. For an unburned material,  $T_{SH}$  and  $\zeta$  will be set to zero. For a more in depth explanation of the parameters in the equations above see the article by Aslam. [\[43\]](#)

## 7.10 Becker-Kistiakowsky-Wilson High-Explosive (BKW-HE) EOS

The BKW-HE EOS combines the solid Grüneisen form and a BKW gaseous form to model a shock-initiated HE. This form is usually used to model a shock-initiated explosive as it transitions from an undetonated solid to a fully burned detonation product. The discussion follows the one given in Mader.[\[44\]](#), pp. 308 – 311. Mader calls this his Hell Of a Mess (HOM) EOS.]

The EOS computes the pressure, internal energy, specific volume, temperature, and burn fraction for solids, gases, and mixtures of the two. The following subscripts are used in this discussion:

- $g$     gaseous component
- $H$     Hugoniot
- $i$     isentrope
- $S$     solid component

### 7.10.1 Solid components

The solid undetonated HE begins with a solid Mie-Grüneisen EOS with a Walsh-Christian temperature [45] fit to a fourth-degree polynomial. The solid component uses the Grüneisen form described above.

$$\begin{aligned}
 U_s &= c_0 + sU_P \\
 P_H &= P_0 + \frac{c_0^2(V_0 - V_S)}{[V_0 - s(V_0 - V_S)]^2} \\
 E_H &= \frac{1}{2}(P_0 + P_H)(V_0 - V_S) \\
 P_S &= P_H + \frac{\Gamma}{V_S}(E_S - E_H)
 \end{aligned}$$

where

$$\begin{aligned}
 \Gamma &\equiv \Gamma_0 + \Gamma_1 \frac{V_S}{V_0} \\
 \ln T_H &= F + G \ln V_S + H(\ln V_S)^2 + I(\ln V_S)^3 + J(\ln V_S)^4 \\
 T_S &= T_H + \frac{23890}{C_v(\text{solid})}(E_S - E_H)
 \end{aligned}$$

The constant in the last equation is a conversion factor involving the mechanical equivalent of heat. The units of heat capacity  $C_v$  are ( $\text{cal g}^{-1} \text{ deg}^{-1}$ ) and the units of internal energy are ( $\text{Mbar cm}^3 \text{ g}^{-1}$ ). Constants for various explosives are given in Mader's book [44] and the accompanying data CD-ROM.

### 7.10.2 Gaseous components

The detonation products are computed using the BKW EOS.[44]

$$\begin{aligned}
 \ln P_i &= A + B \ln V_g + C(\ln V_g)^2 + D(\ln V_g)^3 + E(\ln V_g)^4 \\
 \ln(E_i - Z) &= K + L \ln P_i + M(\ln P_i)^2 + N(\ln P_i)^3 + O(\ln P_i)^4 \\
 \ln T_i &= Q + R \ln V_g + S(\ln V_g)^2 + T(\ln V_g)^3 + U(\ln V_g)^4 \\
 -\beta^{-1} &= R + 2S \ln V_g + 3T(\ln V_g)^2 + 4U(\ln V_g)^3 \\
 P_g &= P_i + \frac{1}{\beta V_g}(E_g - E_i) \\
 T_g &= T_i + \frac{23890}{C'_v(\text{gas})}(E_g - E_i)
 \end{aligned}$$

The parameter  $Z$  is a constant used to change the gas standard state to be consistent with the solid explosive standard state (which in PAGOSA requires the value  $Z > 0$ ).

The final case is when a material is a combination of the solid and gaseous states. The burn fraction  $Bf$  controls the mixture. For mixed components  $0 < Bf < 1$ .

### 7.10.3 Mixed components

The specific volumes and internal energies are partitioned as a linear combination of the solid and gaseous components. The “burning” cells are assumed to be in pressure and temperature equilibrium and are given by

$$\begin{aligned} V &= Bf V_g + (1 - Bf)V_s \\ E &= Bf E_g + (1 - Bf)E_s \\ P &= P_g = P_s \\ T &= T_g = T_s \end{aligned}$$

Substituting these equations into the ones above results in an equation representing the temperature difference between the solid and gas. The secant method[7, 248 – 251] is used to solve the resulting nonlinear algebraic equation. Limits are set at every cycle of the iteration to prevent the solution from becoming unbounded or unphysical. Convergence is achieved when the temperature difference between the solid and gaseous components is less than  $t_{del}$  (usually  $\sim 10$  K).

The solid component BKW-HE parameters are

|            |   |
|------------|---|
| $c_0$      | intercept of the $U_s/U_p$ line         |
| $s$        | slope of the $U_s/U_p$ line             |
| $\Gamma_0$ | the first Grüneisen ratio               |
| $\Gamma_1$ | the second Grüneisen ratio              |
| $P_0$      | initial pressure                        |
| $d_{max}$  | maximum allowable density (solid)       |
| $F$        | polynomial temperature coefficient      |
| $G$        | polynomial temperature coefficient      |
| $H$        | polynomial temperature coefficient      |
| $I$        | polynomial temperature coefficient      |
| $J$        | polynomial temperature coefficient      |
| $C_v$      | heat capacity (solid)                   |
| $\alpha$   | linear coefficient of thermal expansion |

The gaseous state parameters are

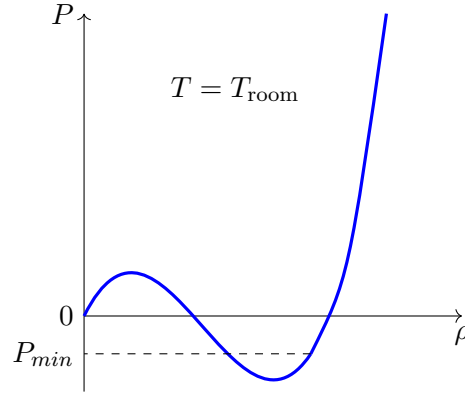


Figure 7.2: Example of the use of  $P_{\min}$  in an EOS with a van der Waals loop.

|               |  |
|---------------|--|
| $A$           | HOM polynomial coefficient for the isentropic pressure               |
| $B$           | HOM polynomial coefficient for the isentropic pressure               |
| $C$           | HOM polynomial coefficient for the isentropic pressure               |
| $D$           | HOM polynomial coefficient for the isentropic pressure               |
| $E$           | HOM polynomial coefficient for the isentropic pressure               |
| $K$           | HOM polynomial coefficient for the isentropic internal energy        |
| $L$           | HOM polynomial coefficient for the isentropic internal energy        |
| $M$           | HOM polynomial coefficient for the isentropic internal energy        |
| $N$           | HOM polynomial coefficient for the isentropic internal energy        |
| $O$           | HOM polynomial coefficient for the isentropic internal energy        |
| $Q$           | HOM polynomial coefficient for the isentropic temperature            |
| $R$           | HOM polynomial coefficient for the isentropic temperature            |
| $S$           | HOM polynomial coefficient for the isentropic temperature            |
| $T$           | HOM polynomial coefficient for the isentropic temperature            |
| $U$           | HOM polynomial coefficient for the isentropic temperature            |
| $C'_V$        | heat capacity (gas)  |
| $Z$           | a constant used to offset (shift) the gas standard state ( $Z > 0$ ) |
| $\rho_{\max}$ | maximum allowable density (gas)                                      |
| $\rho_{\min}$ | minimum allowable density (gas)                                      |

The mixed state uses both the solid and gaseous parameters and the following convergence criteria

|                  |   |
|------------------|---|
| $\text{maxit}$   | maximum number of iterations for the mixed component solver |
| $t_{\text{del}}$ | temperature difference convergence value.                   |

## 7.11 $P_{\min}$

It is often necessary to limit the pressures resulting from the EOS evaluation. Regions of the EOS are suppressed for many reasons, which fall into three major categories.

The first category is demonstrated in [Figure 7.2](#). The plot illustrates a van der Waals loop in the EOS at room temperature. Problems arise when the material density falls below some critical value. Material sound speeds become unphysical.<sup>6</sup> A value of  $P_{min}$  is chosen to suppress the offending portion of the EOS.

A second way that  $P_{min}$  often is used is as a simple-minded spall model. When the material pressure drops below  $P_{min}$ , the pressure is held at  $P_{min}$ , regardless of the density and internal energy. This application of  $P_{min}$  is an awkward attempt to approximate the physics of the material in a state exceeding its dynamic tensile strength. No change is made to the stress deviators  $\mathbf{S}$  while the material is in this state.<sup>7</sup>

The third way that  $P_{min}$  is used in PAGOSA is as a floor or cutoff to the EOS. For example, if it is desired that a material never go into tension during the simulation, then setting  $P_{min}$  to a value of zero will allow the material to experience only compression.

---

<sup>6</sup>The sound speed is related to the slope of the adiabat at a given point.

<sup>7</sup>Every hydrocode implements  $P_{min}$  in a different and unique manner. Reducing complicated physics to a single parameter is at best a poor scheme.

## Chapter 8

# Sound speed

*There is more to life than increasing its speed.*

– Mahatma Gandhi (1869 – 1948)

When a material is perturbed, the net result is a wave propagating away from the disturbed region into the undisturbed region. The speed at which the wave travels in a given medium under specified conditions is known as the speed of sound. The speed of sound does not explicitly appear in the hydrodynamics equations. However, it is used to calculate the Courant timestep (see [Chapter 10](#)). It also can be used to check the thermodynamics properties of materials in a cell. The isentropic sound speed is defined as [\[2, pp. 246\]](#), [\[37, pp. 7\]](#)

$$c^2 \equiv \left( \frac{\partial P}{\partial \rho} \right)_S \quad (8.1)$$

at constant entropy  $S$ . This form is not convenient for computation, so it is necessary to recast the expression in terms of partial derivatives at constant density and constant internal energy. The pressure is a function of density and internal energy

$$P = P(\rho, E) \quad (8.2)$$

The differential is

$$dP = \left( \frac{\partial P}{\partial \rho} \right)_E d\rho + \left( \frac{\partial P}{\partial E} \right)_\rho dE \quad (8.3)$$

The pressure also can be written as a function of density and entropy

$$P = P(\rho, S) \quad (8.4)$$

The differential is

$$dP = \left( \frac{\partial P}{\partial \rho} \right)_S d\rho + \left( \frac{\partial P}{\partial S} \right)_\rho dS \quad (8.5)$$

For an isentropic process, these two forms reduce to

$$\left( \frac{\partial P}{\partial \rho} \right)_E d\rho + \left( \frac{\partial P}{\partial E} \right)_\rho dE = \left( \frac{\partial P}{\partial \rho} \right)_S d\rho \quad (8.6)$$

The internal energy as a function of density and entropy

$$E = E(\rho, S) \quad (8.7)$$

The differential is

$$dE = \left( \frac{\partial E}{\partial \rho} \right)_S d\rho + \left( \frac{\partial E}{\partial S} \right)_\rho dS \quad (8.8)$$

Combining [Equation 8.6](#) and [Equation 8.8](#) yields

$$\left( \frac{\partial P}{\partial \rho} \right)_E + \left( \frac{\partial P}{\partial E} \right)_\rho \left( \frac{\partial E}{\partial \rho} \right)_S = \left( \frac{\partial P}{\partial \rho} \right)_S \quad (8.9)$$

Thus, given the definition of sound speed ([Equation 8.1](#)), we have

$$c^2 \equiv \left( \frac{\partial P}{\partial \rho} \right)_S = \left( \frac{\partial P}{\partial \rho} \right)_E + \left( \frac{\partial P}{\partial E} \right)_\rho \left( \frac{\partial E}{\partial \rho} \right)_S \quad (8.10)$$



Using the first law of thermodynamics for a single component system with one reversible work mode we have

$$\begin{aligned}
 dE &= \delta Q - \delta W \\
 &= TdS - pdV \\
 &= TdS + \frac{P}{\rho^2}d\rho
 \end{aligned} \tag{8.11}$$

The coefficient of the second differential (density) now can be identified with the corresponding differential in [Equation 8.8](#). If we substitute into [Equation 8.10](#), the sound speed is computed for each material as

$$c^2 = \left( \frac{\partial P}{\partial \rho} \right) + \frac{P}{\rho^2} \left( \frac{\partial P}{\partial E} \right)_\rho \tag{8.12}$$

The sound speed is used in various other parts of the computation cycle. For example, the sound speed is used to establish the proper timestep for each computational step.<sup>1</sup>

## 8.1 Ideal gas EOS sound speed

For the ideal gas equation of state (EOS), the pressure and sound speed are simply

$$\begin{aligned}
 P &= (\gamma - 1)\rho E \\
 c^2 &= \left( \frac{\partial P}{\partial \rho} \right)_E + \frac{P}{\rho^2} \left( \frac{\partial P}{\partial E} \right)_\rho \\
 &= (\gamma - 1)E + \frac{P}{\rho^2}(\gamma - 1)\rho \\
 &= \gamma \frac{P}{\rho} = \gamma(\gamma - 1)E
 \end{aligned} \tag{8.13}$$

## 8.2 Void EOS sound speed

A void material has no sound speed, so the value is deliberately set to zero:

$$\begin{aligned}
 P &= 0 \\
 c^2 &= 0
 \end{aligned} \tag{8.14}$$

## 8.3 Polynomial EOS sound speed

The polynomial EOS is written as

$$P = a_0 + a_1\mu + a_2^*\mu^2 + a_3\mu^3 + E(b_0 + b_1\mu + b_2^*\mu^2 + b_3\mu^3)$$

---

<sup>1</sup>See [Chapter 10](#) for more details.

where

$$\mu \equiv \frac{\rho}{\rho_0} - 1$$

The partial derivatives for the sound speed calculation are

$$\begin{aligned} \left( \frac{\partial P}{\partial \rho} \right)_E &= \left( \frac{\partial P}{\partial \mu} \right)_E \left( \frac{\partial \mu}{\partial \rho} \right)_E \\ &= \frac{1}{\rho_0} [a_1 + 2a_2^* \mu + 3a_3 \mu^2] + \frac{E}{\rho_0} [b_1 + 2b_2^* \mu + 3b_3 \mu^2] \\ \frac{P}{\rho^2} \left( \frac{\partial P}{\partial E} \right)_\rho &= \frac{P}{\rho^2} [b_0 + b_1 \mu + b_2^* \mu^2 + b_3 \mu^3] \end{aligned}$$

such that the sound speed is

$$\begin{aligned} c^2 &= \frac{1}{\rho} [a_1 + 2a_2^* \mu + 3a_3 \mu^2] \\ &\quad + \frac{E}{\rho_0} [b_1 + 2b_2^* \mu + 3b_3 \mu^2] \\ &\quad + \frac{P}{\rho^2} [b_0 + b_1 \mu + b_2^* \mu^2 + b_3 \mu^3] \end{aligned} \tag{8.15}$$

## 8.4 Modified Osborne (or quadratic) EOS sound speed

The Osborne EOS is written as

$$P = \frac{a_1 \mu + a_2^* \mu^2 + (b_0 + b_1 \mu + b_2^* \mu^2) \varepsilon + (c_0 + c_1 \mu + c_2^* \mu^2) \varepsilon^2}{\varepsilon + \varepsilon_0}$$

The partial derivatives for the sound speed calculation are

$$\begin{aligned} \left( \frac{\partial P}{\partial \rho} \right)_E &= \left( \frac{\partial P}{\partial \mu} \right)_E \left( \frac{\partial \mu}{\partial \rho} \right)_E \\ &= \left( \frac{a_1 + 2a_2^* \mu + \varepsilon(b_1 + 2b_2^* \mu) + \varepsilon^2(c_1 + 2c_2^* \mu)}{\varepsilon + \varepsilon_0} \right) \frac{1}{\rho_0} \\ \frac{P}{\rho^2} \left( \frac{\partial P}{\partial E} \right)_\rho &= \frac{P}{\rho^2} \frac{(b_0 + b_1 \mu + b_2^* \mu^2 + 2(c_0 + c_1 \mu + c_2^* \mu^2) \varepsilon) - P}{\varepsilon + \varepsilon_0} \end{aligned}$$

Accordingly,

$$\begin{aligned} c^2 &= \left( \frac{a_1 + 2a_2^* \mu + \varepsilon(b_1 + 2b_2^* \mu) + \varepsilon^2(c_1 + 2c_2^* \mu)}{\varepsilon + \varepsilon_0} \right) \frac{1}{\rho} \\ &\quad + \frac{P}{\rho^2} \frac{(b_0 + b_1 \mu + b_2^* \mu^2 + 2(c_0 + c_1 \mu + c_2^* \mu^2) \varepsilon) - P}{\varepsilon + \varepsilon_0} \end{aligned} \tag{8.16}$$

## 8.5 Jones-Wilkins-Lee (JWL) EOS sound speed

The JWL EOS,

$$P = A \left[ 1 - \frac{\omega}{R_1} \frac{\rho}{\rho_0} \right] \exp \left( \frac{-R_1 \rho_0}{\rho} \right) + B \left[ 1 - \frac{\omega}{R_2} \frac{\rho}{\rho_0} \right] \exp \left( \frac{-R_2 \rho_0}{\rho} \right) + \omega \rho E$$

is similarly evaluated in [Equation 8.12](#). The corresponding terms are

$$\begin{aligned} \left( \frac{\partial P}{\partial \rho} \right)_E = & -\frac{A\omega}{R_1} \frac{1}{\rho_0} \exp \left( \frac{-R_1 \rho_0}{\rho} \right) + \frac{AR_1 \rho_0}{\rho^2} \left[ 1 - \frac{\omega}{R_1} \frac{\rho}{\rho_0} \right] \exp \left( \frac{-R_1 \rho_0}{\rho} \right) \\ & -\frac{B\omega}{R_2} \frac{1}{\rho_0} \exp \left( \frac{-R_2 \rho_0}{\rho} \right) + \frac{BR_2 \rho_0}{\rho^2} \left[ 1 - \frac{\omega}{R_2} \frac{\rho}{\rho_0} \right] \exp \left( \frac{-R_2 \rho_0}{\rho} \right) + \omega E \end{aligned}$$

and

$$\frac{P}{\rho^2} \left( \frac{\partial P}{\partial E} \right)_\rho = P \frac{\omega}{\rho}$$

Therefore,

$$\begin{aligned} c^2 = & -\frac{A\omega}{R_1} \frac{1}{\rho_0} \exp \left( \frac{-R_1 \rho_0}{\rho} \right) + \frac{AR_1 \rho_0}{\rho^2} \left[ 1 - \frac{\omega}{R_1} \frac{\rho}{\rho_0} \right] \exp \left( \frac{-R_1 \rho_0}{\rho} \right) \\ & -\frac{B\omega}{R_2} \frac{1}{\rho_0} \exp \left( \frac{-R_2 \rho_0}{\rho} \right) + \frac{BR_2 \rho_0}{\rho^2} \left[ 1 - \frac{\omega}{R_2} \frac{\rho}{\rho_0} \right] \exp \left( \frac{-R_2 \rho_0}{\rho} \right) + \omega E + P \frac{\omega}{\rho} \end{aligned} \quad (8.17)$$

The above sound speed is for the detonation products of the explosive. Before and during the detonation, the pressure in the undetonated explosive is zero and the sound speed is set as follows:

$$c^2 = \begin{cases} D^2 & Bf = 0 \\ 9D^2 & 0 < Bf < 1 \\ c_{\text{JWL}}^2 & Bf = 1 \end{cases} \quad (8.18)$$

where  $D$  is the detonation velocity, and  $Bf$  is the burn fraction.

## 8.6 Grüneisen (or $U_S - U_P$ ) EOS sound speed

The Grüneisen EOS is

$$P = P_H + \frac{\Gamma}{V} [E - E_H]$$

Differentiation according to [Equation 8.12](#) is provided with added complexity, where

$$\begin{aligned} P_H &= P_0 + c_0^2 (V_0 - V) [V_0 - s(V_0 - V)]^{-2} \\ E_H &= E_0 + \frac{1}{2} (P_0 + P_H) (V_0 - V) \\ \Gamma &= \Gamma_0 + \Gamma_1 \frac{V}{V_0} \end{aligned}$$

where the specific volume is defined at

$$V \equiv \frac{1}{\rho}$$

such that

$$\begin{aligned} \left( \frac{\partial P_H}{\partial \rho} \right)_E &= \left( \frac{\partial P_H}{\partial V} \right)_E \left( \frac{\partial V}{\partial \rho} \right)_E \\ &= \frac{c^2}{\rho^2} \left[ (V_0 - s(V_0 - V))^{-2} + 2s(V_0 - V)(V_0 - s(V_0 - V))^{-3} \right] \\ \left( \frac{\partial}{\partial \rho} \left( \frac{\Gamma}{V} \right) \right)_E &= \left( \frac{\partial}{\partial V} \left( \frac{\Gamma}{V} \right) \right)_E \left( \frac{\partial V}{\partial \rho} \right)_E \\ &= \Gamma + \frac{\Gamma_1}{\Gamma_0} \left( \frac{1}{V} \right) \left( \frac{-1}{\rho^2} \right) \\ \left( \frac{\partial}{\partial \rho} (E - E_H) \right)_E &= \left( \frac{\partial}{\partial V} (E - E_H) \right)_E \left( \frac{\partial V}{\partial \rho} \right)_E \\ &= \frac{1}{2} \left[ \left( \frac{\partial P_H}{\partial \rho} \right)_E (V_0 - V) + \left( \frac{P_0 + P_H}{\rho^2} \right) \right] \end{aligned}$$

Thus,

$$\left( \frac{\partial P}{\partial \rho} \right)_E = \left( \frac{\partial P_H}{\partial \rho} \right)_E + \left( \frac{\partial}{\partial \rho} \left( \frac{\Gamma}{V} \right) \right)_E (E - E_H) + \frac{\Gamma}{V} \left( \frac{\partial}{\partial \rho} (E - E_H) \right)_E$$

and

$$\begin{aligned} \frac{P}{\rho^2} \left( \frac{\partial P}{\partial E} \right)_\rho &= \frac{P}{\rho^2} \left( \frac{\Gamma}{V} \right) \\ c^2 &= \left( \frac{\partial P_H}{\partial \rho} \right)_E + \left( \frac{\partial}{\partial \rho} \left( \frac{\Gamma}{V} \right) \right)_E (E - E_H) \\ &\quad + \frac{\Gamma}{V} \left( \frac{\partial}{\partial \rho} (E - E_H) \right)_E + \frac{P}{\rho^2} \left( \frac{\Gamma}{V} \right) \end{aligned} \tag{8.19}$$

## 8.7 SESAME EOS sound speed

The EOS package (EOSPAC) utility software package[\[40\]](#) extracts the pressure from the Los Alamos National Laboratory (LANL) SESAME database. The EOSPAC software also supplies the partial derivatives of pressure with respect to density and internal energy. The sound speed is computed directly from these numerical derivatives.

The EOSPAC derivatives are with respect to the logarithm of density and energy, so

$$\begin{aligned} \left( \frac{\partial P}{\partial \rho} \right)_E &= \frac{1}{\rho} \left[ \left( \frac{\partial P}{\partial \ln \rho} \right)_E \right]_{\text{SESAME}} \\ \left( \frac{\partial P}{\partial E} \right)_\rho &= \frac{1}{E} \left[ \left( \frac{\partial P}{\partial \ln E} \right)_\rho \right]_{\text{SESAME}} \end{aligned}$$

and the appropriate substitutions then are made into [Equation 8.12](#). The EOSPAC software allows the tabular data to be interpolated in various ways [e.g., biquadratic (six-point) interpolation]. The choice of interpolation method will influence the results of the partial derivatives and therefore the sound speed.

An additional point, not referred to earlier, concerns SESAME materials that melt during the simulation. Two SESAME tables can be loaded by PAGOSA, one for the unmelted state and one for the melted state. Certainly, the sound speeds are very different for these two states of the material. However, not every SESAME material has a corresponding SESAME melt table. Compromises and engineering approximations immediately become significant considerations. It is always important to understand and investigate the assumptions and limitations in any EOS, including the SESAME EOS.

## 8.8 Exponential EOS sound speed

The exponential EOS is

$$P(t) = P_0 \exp(\alpha t)$$

In this case, pressure is not a function of either density or internal energy, so

$$c^2 = 0 \tag{8.20}$$

The exponential EOS is intended to be a pressure (normal stress boundary condition) for particular simulations. As a consequence, the thermodynamics of this material should play little or no role in the simulation.

## 8.9 PAGOSA sound speed

The internal sound speed computed by PAGOSA is altered in an attempt to find the largest possible “wave” velocity. The goal is to eventually compute a stable timestep for the simulation. The total sound speed,

$$c^2 = c_{EOS}^2 + \frac{4G}{3\rho} + \frac{2Q}{\tilde{\rho}} \tag{8.21}$$

is composed of three parts. The first term is the sound speed corresponding to the EOS  $P \equiv P(\rho, E)$ , the second term converts the sound speed to a longitudinal elastic wave speed for elastic-plastic materials, and the third term ensures the stability in the presence of shocks ( $Q$  terms).

The diagnostic information in PAGOSA returns only the isentropic sound speed. However, it is important to understand that internal to PAGOSA, the sound speed has additional terms. It is hoped that in the future, these terms can be computed individually and their influence on the timestep can be evaluated individually.

The term  $2Q/\tilde{\rho}$  helps to keep the square of the sound speed positive. It has been suggested that since  $Q$  has the dimensions of pressure, the last term can be thought of as an adiabatic wave speed with  $\gamma = 2$ .



## Chapter 9

# Artificial viscosity

*The equations of hydrodynamics are modified by the inclusion of additional terms which greatly simplify the procedures needed for stepwise numerical solution of the equations in problems involving shocks.*

– J. von Neumann and R.D. Richtmyer (1950)

The mathematical basis for all PAGOSA algorithms is the assumption that we are dealing with a continuum. This assumption precludes the presence of shock waves because, in this formalism, shocks are mathematical discontinuities. Although it is possible to devise mathematical methods that create internal floating boundaries connecting regions of continuous flow, the complexity for three-dimensional (3D) flows becomes numerically intractable. To complicate the matter further, shocks often interact in complicated ways.

Typical shock widths are very narrow and require extremely small cell dimensions to resolve properly. The computer memory and time requirements are prohibitive.

A solution to this dilemma was discovered by von Neumann and Richtmyer in 1950. They introduced the concept of an artificial viscous pressure (often imprecisely called the artificial viscosity) that, when added to the pressure, had the effect of smearing out the shock wave over several cells, thus converting the discontinuity to a steep gradient. The form of this artificial viscosity implemented in PAGOSA is discussed next. The artificial viscosity is added to convert the kinetic energy into internal energy within the shock.

For shock wave calculations, an artificial viscosity is necessary in the difference equations to represent the shock discontinuities properly. The classical quadratic artificial viscosity,  $Q_2$ , is computed as<sup>[46]</sup>

$$Q_2 = \begin{cases} C_2 L^2 \tilde{\rho} [\nabla \cdot \mathbf{u}]^2 & \text{if } \nabla \cdot \mathbf{u} \leq 0 \\ 0 & \text{if } \nabla \cdot \mathbf{u} > 0 \end{cases} \quad (9.1)$$

where  $C_2$  is a constant ( $\sim 2.0$  for many Eulerian hydrodynamic codes),  $L$  is a length appropriate to the cell in which the artificial viscosity is calculated, and  $\tilde{\rho}$  is the cell average density.

The linear artificial viscosity is<sup>[47]</sup>

$$Q_1 = \begin{cases} -C_1 L \tilde{\rho} \tilde{c} \nabla \cdot \mathbf{u} & \text{if } \nabla \cdot \mathbf{u} \leq 0 \\ 0 & \text{if } \nabla \cdot \mathbf{u} > 0 \end{cases} \quad (9.2)$$

where  $C_1$  is a constant and  $\tilde{c}$  is the cell-average sound speed. The linear artificial viscosity is used to damp out oscillations behind the shock waves.<sup>1</sup> Both coefficients ( $C_1$  and  $C_2$ ) and the length scale  $L$  are user selectable.

These equations incorporate a suggestion by Rosenbluth<sup>[12, pp. 313, footnote 11]</sup> that the artificial viscosity should have a value of zero when the fluid is undergoing an expansion (the divergence of the velocity field is positive).

The total artificial viscosity,  $Q$ , is

$$Q = Q_1 + Q_2 \quad (9.3)$$

The artificial viscosity acts to spread the shock over a few cells in such a way that the variables vary continuously through the region of the shock and satisfy the Rankine-Hugoniot conservation relations. The shock will be spread over several zones, regardless of the cell size. A few cells away from the shock, the artificial viscosity is zero.

The effect of artificial viscosity is very much cell size dependent. Simulations at very fine mesh resolutions may not need any artificial viscosity. Further, in simulations where extreme gradients do

---

<sup>1</sup>The coefficients used in Lagrangian hydrodynamics codes are different from the ones listed above.



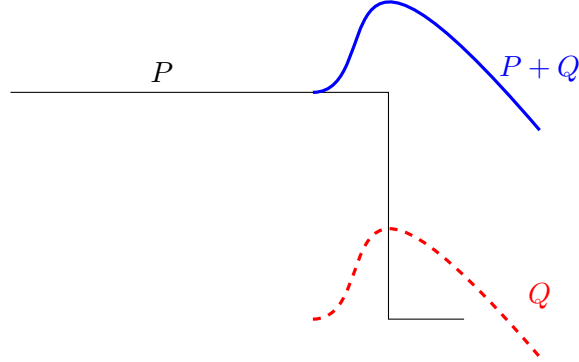


Figure 9.1: A typical pressure and artificial viscosity in the region of a shock.

not exist, the artificial viscosity may need to be suppressed entirely. The excessive use of artificial viscosity often damps out the solution. It is said that experience is the key to success.

Shock artificial viscosities introduce problems and errors of their own. In strong shocks, “wall heating” and “shock-less heating” can occur, leading to errors in the internal energy surrounding the shock.[48] Errors in internal energy lead to errors in density and the shock speed. Many of these effects are seen in the so-called Noh problem.[49] The densities at symmetry boundaries are usually severely reduced, and the internal energies are significantly overpredicted. All of these anomalies are sensitive to mesh resolution.

Treating the artificial viscosity as a pressure term in the momentum and energy finite-difference equations allows the work done by the viscosity to be identified with the thermodynamic irreversibility of the shock. When we compare the energy equation with the first law of thermodynamics

$$\begin{aligned} dE &= -(P + Q)dV \\ TdS &= dE + PdV \\ \rightarrow TdS &= -QdV \end{aligned}$$

The entropy increase  $dS$  is being generated by the artificial viscosity.

The entropy is not computed in PAGOSA; however, it is a useful conceptual explanation of the physical and numerical processes involved in the solution of the Navier-Stokes equations.

An interesting problem is in the choice of the length parameter  $L$ . The Wilkins’ form[50] of the artificial viscosity, the default for PAGOSA, uses a length calculated across the cell in the direction of the maximum pressure gradient. The length scale adapts in each zone, depending on the local pressure gradients.

On the other hand, in 2D problems, the length scale could be computed in several different ways. The appropriate length scale might be the diagonal distance across the cell. The length scale computation is selected by the user.

In 1D problems, only  $\Delta x$  would be an appropriate length scale choice.

For an ideal shock, the pressure is a square wave. When the artificial viscosity is computed and added to the pressure, the result is shown in [Figure 9.1](#). The shock is spread out over several cells, and the artificial viscosity is a fraction of the amplitude of the pressure in the region of the shock and is nonexistent away from the shock.

## Chapter 10

# Computing a timestep

*I am not discouraged, because every wrong attempt discarded is another step forward.*

– Thomas A. Edison (1847 – 1931)

The timestep in any simulation must be smaller than that given by the Courant-Friedrichs-Lewy (CFL) condition. [51]<sup>1</sup> This condition is necessary for the stability of the numerical solution of the partial differential equations. Physically, the timestep restriction [12, pp. 9 – 16, 45 – 48, and 83 – 90] prevents information from moving beyond a cell in a single step.

A timestep for each component of the velocity is computed as follows:

$$\Delta t_U = safeu \cdot \min \left( \frac{\Delta x}{|U|} \right) \quad (10.1)$$

$$\Delta t_V = safeu \cdot \min \left( \frac{\Delta y}{|V|} \right) \quad (10.2)$$

$$\Delta t_W = safeu \cdot \min \left( \frac{\Delta z}{|W|} \right) \quad (10.3)$$

$$\Delta t_{UC} = safec \cdot \min \left( \frac{\Delta x}{[|\tilde{U}| + c]} \right) \quad (10.4)$$

$$\Delta t_{VC} = safec \cdot \min \left( \frac{\Delta y}{[|\tilde{V}| + c]} \right) \quad (10.5)$$

$$\Delta t_{WC} = safec \cdot \min \left( \frac{\Delta z}{[|\tilde{W}| + c]} \right) \quad (10.6)$$

where *safeu* and *safec* are safety factors (between 0 and 1) used to reduce the timestep further and ensure numerical stability. The velocity components  $\tilde{U}$ ,  $\tilde{V}$ , and  $\tilde{W}$  are evaluated at the cell centers.<sup>2</sup> The location of the controlling timestep is also computed and displayed for each cycle of the integration. This information is useful in understanding what is controlling the timestep and where that control is specifically located. Occasionally, a material can move into an equation-of-state (EOS) regime where the calculated sound speed can be quite large. If the sound speed is large enough, it will control the simulation with very small timesteps. In these cases, knowing the location and state of the material can aid the user in setting appropriate density and pressure cutoffs. The question reduces to knowing if the timestep control falls within a region of interest.

In addition, the divergence also has an associated timestep given by

$$\Delta t_{DIV} = safed \cdot \min \left( \frac{1}{|\nabla \cdot \mathbf{u}|} \right) \quad (10.7)$$

The safety factor *safed* is related to the amount that the cell can expand (or contract) during the Lagrangian phase. This timestep condition helps keep distortions small during a single timestep.

In simulations involving the detonation of explosives with the programmed burn algorithm, the timestep is limited so that the detonation wave traverses a cell in a few steps (approximately four by default<sup>3</sup>). In the timestep computation, to ensure the stability during the high-explosive burn, a value of three times the detonation velocity is used in place of the sound speed for cells containing

<sup>1</sup>An English language translation of the original German paper appears in “On the Partial Difference Equations of Mathematical Physics,” IBM Journal, pp. 215 – 234 (March 1967).

<sup>2</sup>Ensuring that the sound speed and velocities are spatially centered in the same manner.

<sup>3</sup>The default user parameter is *safec* = <sup>3</sup>/<sub>4</sub>, so the detonation requires a minimum of four steps to traverse a cell.

Table 10.1: The timestep controls in PAGOSA hydrodynamics (the controls include the standard CFL stability restrictions, as well as controls set at the user's discretion)

| CODE | CONTROL          | EQUATION                            |
|------|------------------|-------------------------------------|
| Div  | $\Delta t_{DIV}$ | Equation 10.7                       |
| Fin  | $\Delta t^n$     | $(t_{\text{final}} - \Delta t)$     |
| G    | –                | $\Delta t = \text{growth} \Delta t$ |
| I    | $\Delta t^0$     | Initial timestep                    |
| Max  | $\Delta t_{MAX}$ | User selectable                     |
| Min  | $\Delta t_{MIN}$ | User selectable                     |
| U    | $\Delta t_U$     | Equation 10.1                       |
| V    | $\Delta t_V$     | Equation 10.2                       |
| W    | $\Delta t_W$     | Equation 10.3                       |
| U+c  | $\Delta t_{UC}$  | Equation 10.4                       |
| V+c  | $\Delta t_{VC}$  | Equation 10.5                       |
| W+c  | $\Delta t_{WC}$  | Equation 10.6                       |

undetonated or partially detonated explosive. This restriction allows the pressure in the cell to build slowly as the energy is deposited into the cell:

$$\Delta t_D = \text{safec} \frac{\min(\Delta x, \Delta y, \Delta z)}{3D} \quad (10.8)$$

where  $D$  is the detonation velocity of the explosive.

The calculation timestep is the minimum of all the various controls, as shown in Table 10.1

$$\Delta t = \min(\Delta t_U, \Delta t_V, \Delta t_W, \Delta t_{UC}, \Delta t_{VC}, \Delta t_{WC}, \Delta t_{DIV}, \Delta t_D, \Delta t_{MAX}) \quad (10.9)$$

where  $\Delta t_{MAX}$  is a user-specified maximum timestep for the simulation.

The timesteps can be adjusted in other ways. The timestep can grow under certain circumstances and is allowed to grow by a small factor for each new step. Typically this increase is 5% to 10% in step size from cycle to cycle.

However, the timestep can shrink dramatically at any point in the simulation. For example, if a detonation begins or if two shocks collide, then the timestep will adjust to reflect the new physics in the simulation. The timestep will be computed subject to the restrictions described above and subject to the minimum and maximum timestep values.

The timestep is also limited by minimum value. If the value of the timestep drops below a specified minimum value ( $\Delta t_{MIN}$ ), then the simulation is stopped. This situation can occur when a calculation has difficulty with an EOS with unrealistic densities or internal energies. If the timestep becomes too small, it is usually indicative of some problem in the simulation.

In certain simulations, when an exact final simulation time is wanted, the timestep is adjusted for the last integration step. If the normally computed timestep would overshoot the desired time, a fraction of the timestep is used. This option is useful when simulations are to be compared with experiments, for example.

The initial timestep,  $\Delta t^0$ , is either set by the user or computed by trial and error from the initial conditions. The user is encouraged to compute the initial timestep manually. Appendix F provides a few important ideas for computing an initial timestep ( $\Delta t^0$ ).

In cases where the timestep is too large for the Lagrangian or advection phases,<sup>4</sup> the PAGOSA algorithm “backs up” to the last simulation time and attempts a smaller timestep. This backup capability is an important feature in PAGOSA and provides a robust method of continuing a simulation when the CFL conditions vary significantly over the course of the complete simulation.

The safety factors, growth factors, minimum timesteps, and maximum timesteps all have default values in PAGOSA. These factors have been fine tuned and adjusted over many years for typical problems of interest.

---

<sup>4</sup>For example, if the Lagrangian-phase volume consumes the entire Eulerian cell volume. Another common occurrence is when the Lagrangian-phase volume is negative.

## Chapter 11

# Initial conditions

*These mysteries are heightened when we reflect how surprising it is that the laws of nature and the initial conditions of the universe should allow for the existence of beings who could observe it.*

– Steven Weinberg, Scientific American (October 1994)

The solution of the partial differential equations presented in [Chapter 2](#) requires a set of initial conditions for the fundamental variables at the beginning of the simulation ( $t = t_0$ ). For every material and every cell, the following initial conditions are needed:

|                          |                         |
|--------------------------|-------------------------|
| $\rho(t = t_0; x, y, z)$ | initial density         |
| $\phi(t = t_0; x, y, z)$ | initial volume fraction |
| $U(t = t_0; x, y, z)$    | initial $x$ -velocity   |
| $V(t = t_0; x, y, z)$    | initial $y$ -velocity   |
| $W(t = t_0; x, y, z)$    | initial $z$ -velocity   |
| $E(t = t_0; x, y, z)$    | initial internal energy |

The pressures can be derived from the densities and internal energies. Similarly, the cell masses can be derived from the densities, volume fractions, and cell sizes.

On the other hand, the stress deviators are initially zero

$$S_{ij}(t = t_0; x, y, z) = 0 \quad ; \forall i, j \in (x, y, z)$$

There are no initial material stresses; this fact may be incompatible with the other initial conditions specified by the user. It is important to ensure that all initial conditions are consistent and compatible.

In the case of programmed burn explosives, the vertex-centered burn times are required initial conditions. The “simple” programmed burn algorithms are detailed in [Chapter 13](#). The general three-dimensional programmed burn algorithm[\[52\]](#) allows for more complicated geometries, shadow regions, and multiple high-explosive materials.

$$Bt(x, y, z) \quad \text{programmed burn times (vertex centered)}$$



## Chapter 12

# Boundary conditions

*The cube which you will generate will be bounded by six sides, that is to say, six of your insides.*

– Edwin A. Abbott, Flatland (1884)

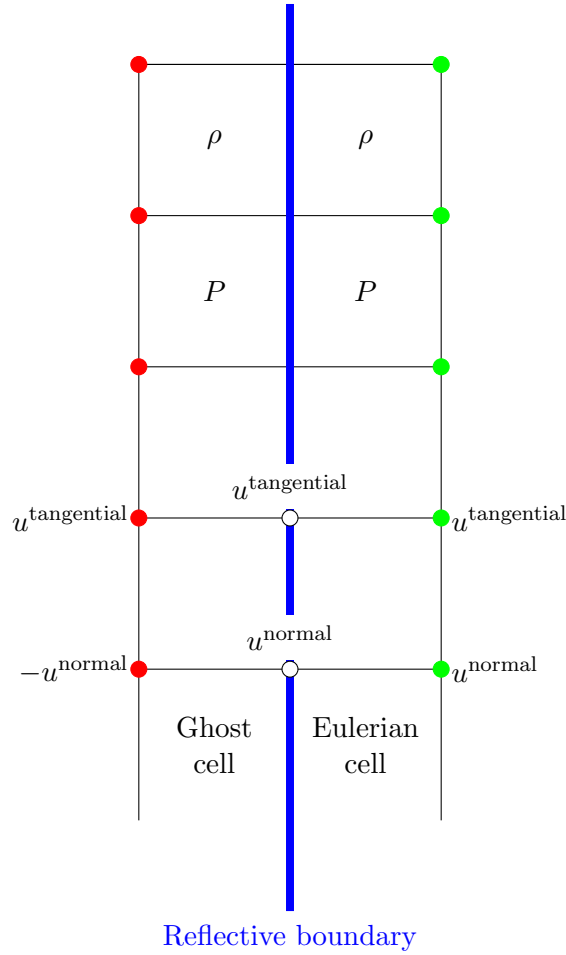


Figure 12.1: The reflective (symmetry) boundary conditions

Boundaries on which the boundary conditions are set form the exterior surface of the Eulerian computational domain. The two types of boundary conditions available in PAGOSA are reflective (symmetry) and transmissive.

## 12.1 Reflective boundary conditions

The reflective boundary conditions, sometimes called the symmetry boundary conditions, represent a boundary of the Eulerian mesh where the interior is a mirror image of the other side. No motion is possible normal to the boundary; only motion tangential to the boundary is allowed. In the current implementation of PAGOSA, materials contacting a reflective (symmetry) boundary cannot subsequently pull away from it.

At a reflective (symmetry) boundary, the ghost cells are the mirror image of their “real” neighbors.

For example, on the  $x_{\min}$  boundary surface, the boundary conditions would be

$$\begin{aligned} U_{0,j,k}^n &= -U_{2,j,k}^n \\ V_{1,j,k}^n &= 0 \\ W_{0,j,k}^n &= -W_{2,j,k}^n \end{aligned}$$

and

$$\begin{aligned} \phi_{1/2,j+1/2,k+1/2}^n &= \phi_{3/2,j+1/2,k+1/2}^n \\ \rho_{1/2,j+1/2,k+1/2}^n &= \rho_{3/2,j+1/2,k+1/2}^n \\ E_{1/2,j+1/2,k+1/2}^n &= E_{3/2,j+1/2,k+1/2}^n \\ P_{1/2,j+1/2,k+1/2}^n &= P_{3/2,j+1/2,k+1/2}^n \end{aligned}$$

The general prescription is shown in [Figure 12.1](#). The cell-centered portion of the ghost cells is simply copied from the adjacent Eulerian cells. However, the velocities are handled differently. The normal component of the velocity is zero at the reflective (symmetry) boundary, whereas the tangential component is computed in the same manner as every “interior” cell. The above situation is complicated at the intersection of two or three reflecting boundaries. The row of ghost cells must be set appropriately in these cases.

## 12.2 Transmissive boundary conditions

The transmissive boundary conditions allow material to flow out of the computational domain by absorbing all incident waves without generating any signals back into the Eulerian mesh that might perturb the solution. Achieving this boundary condition is very difficult, and implementations are generally poor in most Eulerian hydrocodes.

The transmissive boundary conditions (see example in [Figure 12.2](#)) provide a way to anticipate the flow behavior at the very limit of the computational domain. The flow properties at the boundary must derive from the knowledge of the flow inside the computational domain, coupled with some approximations of the outside flow

$$\begin{aligned} U_{0,j,k}^n &= U_{1,j,k}^n = U_{2,j,k}^n \\ V_{0,j,k}^n &= V_{1,j,k}^n \\ W_{0,j,k}^n &= W_{1,j,k}^n \end{aligned}$$

and

$$\begin{aligned} \phi_{1/2,j+1/2,k+1/2}^n &= \phi_{3/2,j+1/2,k+1/2}^n \\ \rho_{1/2,j+1/2,k+1/2}^n &= \rho_{3/2,j+1/2,k+1/2}^n \\ E_{1/2,j+1/2,k+1/2}^n &= E_{3/2,j+1/2,k+1/2}^n \\ P_{1/2,j+1/2,k+1/2}^n &= P_{3/2,j+1/2,k+1/2}^n \end{aligned}$$

Some small amount of information is reflected off of the transmissive boundary back into the simulation. It is always important to choose the position of a transmissive boundary so that it has only a minimal effect on the results of the simulation.

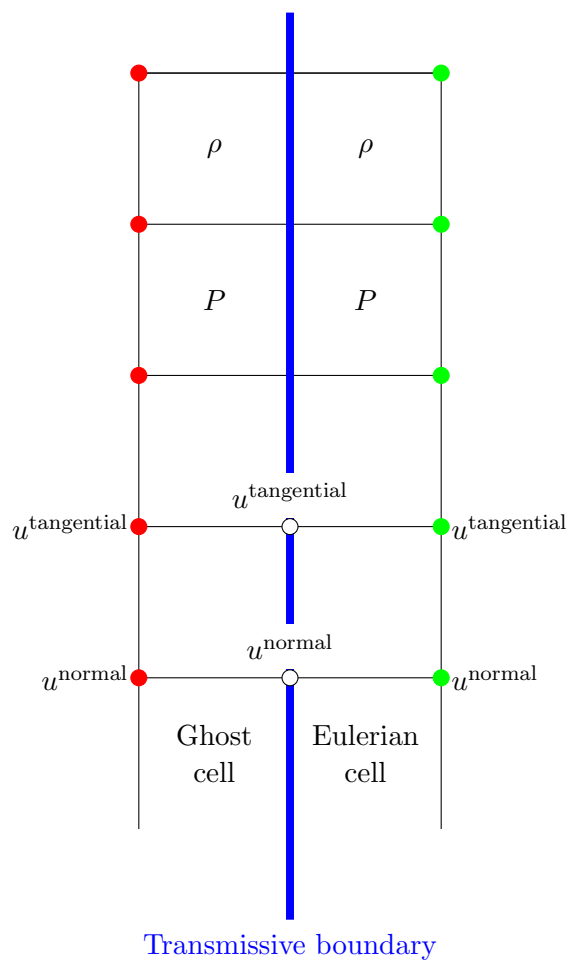


Figure 12.2: The transmissive boundary conditions

## 12.3 Other boundary conditions

Other types of boundary conditions are possible and under consideration:

- inflow
- periodic, and
- pinned, no slip, or no velocity.



## Chapter 13

# Programmed burn

*Double, double toil and trouble; fire burn and caldron bubble.*

– William Shakespeare, Macbeth (1603 – 1607)

The programmed burn technique<sup>1</sup> is used in PAGOSA to simulate the detonation of explosives when the properties of that particular explosive are well known and its behavior is not the focus of the study. The basic assumption is that the detonation wave front travels in all directions at the Chapman-Jouget detonation[53, pp. 116 – 121, 127] velocity. The position of the detonation front is predicted based on the initial configuration of the explosive.

The detonation burn times,  $Bt$ , are defined at the cell vertices. For simulations using the programmed burn technique, the burn times are computed as part of the initial conditions. The burn times are computed from a user-selected detonator type and the explosive detonation velocity  $D$ . For vertices in no way connected to the explosive, the burn times are set to a large value, `btlim`. For cells that contain any explosive, the burn time is computed for every vertex. The propagation of the detonation is modeled by a simple line-of-sight approximation to a complicated Huygen's construction. The detonation wave is regarded as a propagating energy deposition front in the explosive.

The difference between the minimum and maximum burn times of the eight cell vertices is referred to as the burn interval for a cell. Mathematically, we have

$$\begin{aligned} t_{\min} &= \min(t_1, t_2, t_3, t_4, t_5, t_6, t_7, t_8) \\ t_{\max} &= \max(t_1, t_2, t_3, t_4, t_5, t_6, t_7, t_8) \\ t_{\text{interval}} &= t_{\max} - t_{\min} \\ Bf &= \begin{cases} 0 & \text{if } t \leq t_{\min} \\ \frac{t - t_{\min}}{t_{\text{interval}}} & \text{if } t_{\min} < t < t_{\max} \\ 1 & \text{if } t \geq t_{\max} \end{cases} \end{aligned}$$

The burn fraction,  $Bf$ , is used in the Jones-Wilkins-Lee (JWL) equation of state (EOS) (See [section 7.5](#)) to allow a gradual deposition of pressure/energy into a cell. The energy starts to deposit proportionally from the time when the detonation front first arrives at the cell. This energy deposition, combined with the EOS of the explosive material, produces a finite pressure in the cell, which then begins to affect other portions of the problem. Detonation points normally occur on the surface of explosive regions. The available simple (i.e., line-of-sight) detonator types are **Point**, **Line**, **Plane**, **Cylinder**, **Sphere**, and **Ring**. These types are described in the following sections.

## 13.1 Simple point

If the initiation point of detonation is at  $(x_d, y_d, z_d)$ , then the arrival time of the detonation front to the cell vertex  $(i, j, k)$  is given by

$$\begin{aligned} Bt_{i,j,k} &= t_d + \frac{R}{D} \\ R &\equiv \sqrt{(x_{i,j,k} - x_d)^2 + (y_{i,j,k} - y_d)^2 + (z_{i,j,k} - z_d)^2} \end{aligned} \tag{13.1}$$

---

<sup>1</sup>Programmed burn is not the only technique for handling explosives in PAGOSA. Several reactive burn models are available for a more detailed study of explosive behavior.



where each detonation point has a detonation time,  $t_d$ , and the explosive has a detonation velocity  $D$ . The detonation will sweep out from the point spherically and cover the entire mesh containing explosive.<sup>2</sup>

## 13.2 Simple line

If the initiation surface is a line and the line is aligned along one of the Cartesian axes, then the arrival time of the detonation front to the cell vertex  $(i, j, k)$  is given by

$$Bt_{i,j,k} = t_d + \frac{R}{D} \quad (13.2)$$

$R \equiv$  perpendicular distance from the vertex to the line

where each detonation point has a detonation time,  $t_d$ , and the explosive has a detonation velocity  $D$ .

## 13.3 Simple plane

If the initiation surface is a plane and the plane<sup>3</sup> is located at  $([-\infty : +\infty], y_d, [-\infty : +\infty])$ , then the arrival time of the detonation front to the cell vertex  $(i, j, k)$  is given by

$$Bt_{i,j,k} = t_d + \frac{R}{D} \quad (13.3)$$

$R \equiv |y_{i,j,k} - y_d|$

where each detonation point has a detonation time,  $t_d$ , and the explosive has a detonation velocity  $D$ . In general, both sides of the plane will have detonation times. The detonation waves themselves will be planes parallel to the detonation plane.

## 13.4 Simple cylinder

If the initiation surface is a cylinder and the cylinder axis is aligned along one of the Cartesian axes, then the arrival time of the detonation front to the cell vertex  $(i, j, k)$  is given by

$$Bt_{i,j,k} = t_d + \frac{R}{D} \quad (13.4)$$

$R \equiv$  radial distance from the vertex to the cylinder surface

where each detonation point has a detonation time,  $t_d$ , and the explosive has a detonation velocity  $D$ . In general, both sides of the cylindrical surface will have detonation times. The detonation waves themselves will be cylinders concentric to the cylindrical detonation surface.

---

<sup>2</sup>Any cell that has a non-zero volume fraction for the explosive material has eight vertex burn times.

<sup>3</sup>This is an example for the  $XZ$  plane. The other two cases are also available.

### 13.5 Simple sphere

If the initiation surface is a sphere, then the arrival time of the detonation front to the cell vertex  $(i, j, k)$  is given by

$$Bt_{i,j,k} = t_d + \frac{R}{D} \quad (13.5)$$

$R \equiv$  radial distance from the vertex to the spherical surface

where each detonation point has a detonation time,  $t_d$ , and the explosive has a detonation velocity  $D$ . In general, both sides of the spherical surface will have detonation times. The center coordinates and radius of the detonation surface must be specified by the user. The detonation waves themselves will be spheres concentric to the spherical detonation surface.

### 13.6 Simple ring

If the initiation surface is a ring, then the arrival time of the detonation front to the cell vertex  $(i, j, k)$  is given by

$$Bt_{i,j,k} = t_d + \frac{R}{D} \quad (13.6)$$

$R \equiv$  minimum distance from the vertex to the ring surface

where each detonation point has a detonation time,  $t_d$ , and the explosive has a detonation velocity  $D$ . If the inner radius of the ring detonator is zero, then the surface is a circle. In addition, if the outer radius is larger than the computational mesh, this case reduces to a simple plane detonator.

### 13.7 Limitations of simple detonators

In some cases, the line-of-sight approach is a poor approximation to the physics in the simulation. Situations exist where portions of the material are not within the line of sight. These shadow regions can be important in a simulation. In these cases, other detonation methods should be used.

Consider the complicated explosive geometry in [Figure 13.1](#). The detonation point, located on the left, has a limited line of sight to most of the explosive material. The demarcation between the line-of-sight regions and the shadow regions is shown by the dotted lines. The distance calculations for the lines  $\beta$  and  $\lambda$  will clearly be in error. A contour plot of the burn times is one of the best methods of checking the computation.

The programmed burn methodology is most often used in conjunction with the JWL EOS (See [section 7.5](#)) The combination ignores many physical properties that could be important in a simulation. For example, the detonation front contains a reaction zone[54, pp. 275 – 298] of a finite width. In the simple model of detonation, we treat the reaction zone as if it had zero width. The detonation velocity varies as a function of the local shock curvature.[55, 56] The detonation velocity  $D$  in the line-of-sight programmed burn method is a constant.

The programmed burn algorithm is a geometric construction approximating many complicated nonlinear processes. This algorithm can be a very good approximation to reality if the questions driving the simulation are not about details of the high-explosive detonation.[52]

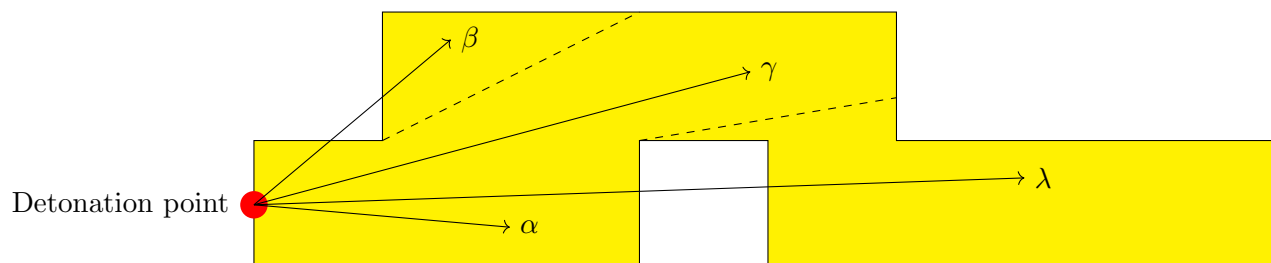


Figure 13.1: An explosive is to be detonated at the point shown. The lines  $\alpha$  and  $\gamma$  point to regions that are directly within the line of sight of the detonator. The lines  $\beta$  and  $\lambda$  point to the shadow regions. The distance calculation assumptions are violated because the line-of-sight path crosses another material.

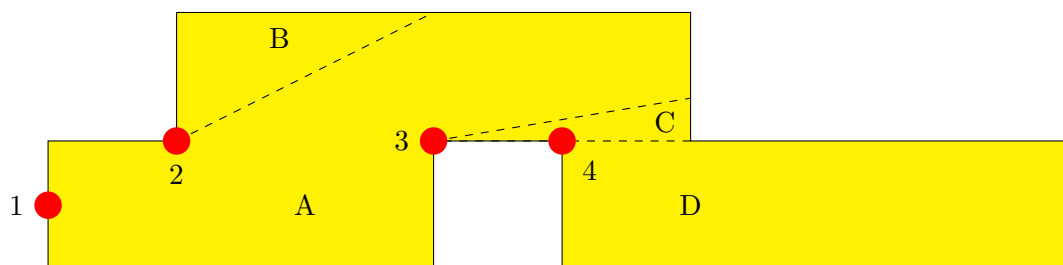


Figure 13.2: An explosive, shown in the previous figure, is to be detonated with four distinct detonation points. Region A is the line-of-sight region, which will be detonated with detonator 1 (the original detonator). Region B is a shadow region, detonated by detonator 2. Region C is the second shadow region, detonated by detonator 3. The remaining explosive material, D, will be detonated by detonator 4. The four regions A, B, C, and D have the same material properties.

One way of avoiding the difficulties with shadow regions is for the user to construct a series of connected regions, each with a single individual detonator. In the case shown in **Figure 13.2**, the explosive has been divided into four regions. The first region, **A**, is the line-of-sight region. The original detonation point is now designated as detonator 1 and corresponds to region **A**. Regions **B**, **C** and **D** are shadow regions.

The detonation times for the four detonation points are

$$\begin{array}{ll}
 t_1 = t_d & \text{material A} \\
 t_2 = t_1 + \frac{R_{12}}{D} & \text{material B} \\
 t_3 = t_1 + \frac{R_{13}}{D} & \text{material C} \\
 t_4 = t_3 + \frac{R_{34}}{D} & \text{material D}
 \end{array}$$

where  $R_{ik}$  is defined as the minimum distance between points  $i$  and  $k$ . Each region would need to have a unique material number for this method to work properly.

## 13.8 Other detonation methods

Several other options exist in PAGOSA for the release of energy from an explosive, including reactive burn models (SURF, MATCH, CJ Volume, DynaBurn, Forest Fire, AWSO, and Multi-Shock Forest Fire). The description of these models is beyond the scope of this work and therefore is not discussed here.

## Chapter 14

# Divergence options

*One cannot escape the feeling that these mathematical formulas have an independent existence and an intelligence of their own, that they are wiser than we are, wiser even than their discoverers.*

– Heinrich Hertz (1857 – 1894)

The implementation of material models in PAGOSA is made somewhat difficult because of the use of a single velocity field for all materials. Under certain circumstances, mixed cell components can behave nonphysically if they possess very different compressibilities or shear moduli. Various divergence models have been developed to handle these situations.

To understand why divergence is central to this issue, consider the Lagrangian equation [Equation 5.1] developed in Chapter 5

$$\frac{\partial \rho}{\partial t} + \rho \nabla \cdot \mathbf{u} = 0 \quad (14.1)$$

Rewriting this equation with the reference density explicitly included, we find

$$\nabla \cdot \mathbf{u} = - \left( \frac{\rho}{\rho_0} \right)^{-1} \frac{\partial}{\partial t} \left( \frac{\rho}{\rho_0} \right) \quad (14.2)$$

If the compression and the rate of compression are increasing, then the divergence is negative.

## 14.1 Uniform

All materials in a mixed cell are uniformly compressed (or expanded) at the same rate using the same value of divergence. No distinction is made between gases, liquids, metals, or voids within a single Eulerian cell. The differences in compressibility between materials are ignored, and all materials are treated with the same value.

Consider the right-hand side of Equation 14.2. Using this uniform compression model, all materials in a mixed cell would be subject to the same divergence.

## 14.2 Void Closure

Void closure is a phenomenon that occurs when a void material is sandwiched between two nonvoid materials. For the uniform case described above, all the materials in mixed cells under compression will be squeezed in proportion to their material volume fraction.

This squeezing leads to over-compression of the nonvoid materials, which is clearly nonphysical. In reality, the voids would be squeezed out before any compression of the materials occurred. In practice, the void closure model in PAGOSA allows the void to be squeezed out between two objects that are colliding. Without the model, a small amount of void would remain forever sandwiched between the two objects.

The details of the void closure model are as follows.<sup>1</sup> During both the predictor and corrector steps of the Lagrangian phase in PAGOSA, the velocity divergence is examined in each mixed cell. If the divergence is negative (i.e., the cell is contracting), the cell is inspected for the presence of void materials. If void material is found, then the minimum and maximum priorities of all materials present in the surrounding twenty-six neighboring cells are determined. If the priority of the void

---

<sup>1</sup>K.S. Holian [Los Alamos National Laboratory (LANL)], D.J. Cagliostro (LANL), T.F. Adams (LANL), and B. Parker [Atomic Weapons Research Establishment (AWRE), United Kingdom], private communication, November 9, 1990.

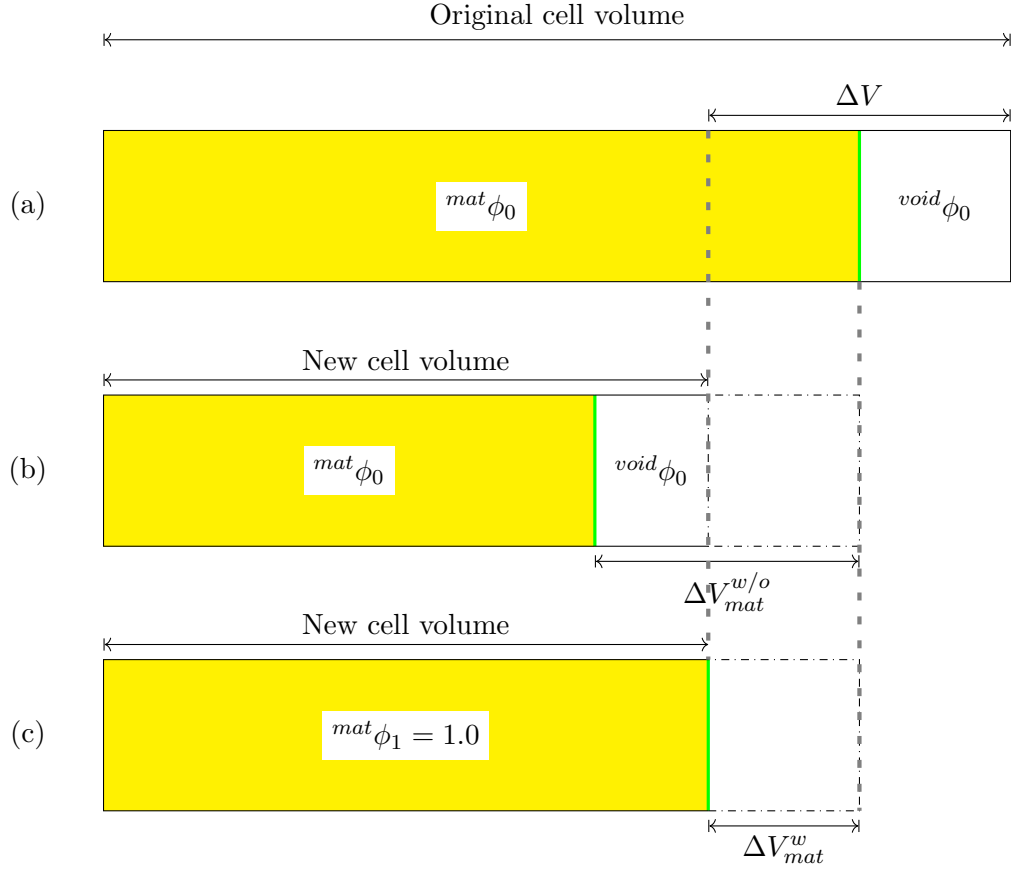


Figure 14.1: Schematic showing two different methods of contracting void in a mixed cell. At the beginning of the Lagrangian phase (a), the mixed cell contains solid material and void. If the contraction is apportioned between solid and void according to volume fractions, then the solid is preferentially compressed (b). If the void contracts before the solid is allowed to contract, then the result is (c).

to be closed is between the minimum and maximum priorities of the neighboring cells, then that void will be contracted preferentially. That is, the void will take up any contraction of the cell before any other materials are allowed to compress. If the volume of the void is insufficient to use the contraction entirely, then the other materials in the cell will share the remaining contraction according to their individual volume fractions. If the priority of a closeable void does not occur between the minimum and maximum priorities of the neighboring nonvoid materials, it may still be allowed to close if no neighboring cells are pure void cells.

In PAGOSA, when a void is preferentially contracted in a mixed cell, the contributions to the energy change from the nonvoid materials are multiplied by a scalar factor.

Figure 14.1 shows a diagram of the derivation of this factor for a mixed cell containing one solid material and a void.

At the start of the Lagrangian phase, we have

$mat \phi_0$  = the volume fraction of the material and

$void \phi_0$  = the volume fraction of the void

After the contraction occurs during the predictor portion of the Lagrangian phase, we have

$$\begin{aligned} {}^{\text{mat}}\phi_1 &= \text{the volume fraction of the material and} \\ {}^{\text{void}}\phi_1 &= \text{the volume fraction of the void} \end{aligned}$$

Figure 14.1(a) shows the partitioning of material and void in the cell before contraction. The whole cell will contract by  $\Delta V$  (which has a negative value) during the predictor portion of the Lagrangian phase.

Figure 14.1(b) illustrates the case where the contraction is apportioned between material and void according to their individual volume fractions. In this case, the volume change of the solid material after the predictor phase is given by

$$\Delta V_{\text{mat}}^{\text{w/o}} = {}^{\text{mat}}\phi_0 \Delta V \quad (14.3)$$

Figure 14.1(c) illustrates the case in which void closure occurs, and the void contracts before the solid material is allowed to contract. In this case, the volume change of the material is given by

$$\Delta V_{\text{mat}}^{\text{w}} = {}^{\text{mat}}\phi_1 (V + \Delta V) - {}^{\text{mat}}\phi_0 V \quad (14.4)$$

The factor that multiplies the contribution to the energy change by the contraction of the material then is the change in volume of the material with void closure divided by the change in volume of the material without void closure, as

$$f = \frac{{}^{\text{mat}}\phi_1 (V + \Delta V) - {}^{\text{mat}}\phi_0 V}{{}^{\text{mat}}\phi_0 V} \quad (14.5)$$

The densities of the nonvoid material components of the mixed cell are clearly modified by this preferential contraction of the void.

### 14.3 Pressure relaxation<sup>2</sup>

The pressure relaxation algorithm is designed to reduce, but not eliminate, pressure differences among materials in a mixed cell. It is more general than the void-closure algorithm but is still expected to produce good results for a void closure.

A relaxation method was chosen over an equilibrium method for two reasons. The waves that reduce pressure differences within the zone have finite speeds that may be too small to produce equilibrium within the timestep, and forced equilibrium can result in unphysical behavior. Consider the simple problem of gas expanding into a void. [57, pp. 5 – 12, Blowoff] Forcing equilibrium during the Lagrangian phase would put all of the cell volume change into the gas and result in the gas moving through the mesh at the rate of one cell per timestep.

Consider a material-dependent compression that consists of the usual uniform compression followed by a relaxation of the material pressure  ${}^{(m)}P$  toward a common cell pressure  $P_{eq}$  with a material-dependent time constant  ${}^{(m)}\tau$ .

The resulting Lagrangian equation for a material pressure  ${}^{(m)}P$  is

$$\frac{D^{(m)}P}{Dt} = -{}^{(m)}\rho {}^{(m)}c^2 \nabla \cdot {}^{(m)}\mathbf{u} = -{}^{(m)}\rho {}^{(m)}c^2 \nabla \cdot \mathbf{u} - \frac{{}^{(m)}P - P_{eq}}{{}^{(m)}\tau} \quad (14.6)$$

---

<sup>2</sup>This section was adapted from the writings of James W. Painter, Los Alamos National Laboratory (1994).



Subtracting the effect of uniform compression produces a Lagrangian equation for the material volume fraction as

$$\frac{1}{^{(m)}\phi} \frac{D^{(m)}\phi}{Dt} = \nabla \cdot ^{(m)}\mathbf{u} - \nabla \cdot \mathbf{u} = \frac{^{(m)}P - P_{eq}}{^{(m)}\rho^{(m)}c^2^{(m)}\tau} \quad (14.7)$$

Requiring the sum of the changes in volume fraction to be zero for the cell gives

$$P_{eq} = \frac{\left( \sum_m \frac{^{(m)}\phi^{(m)}P}{^{(m)}\rho^{(m)}c^2^{(m)}\tau} \right)}{\left( \sum_m \frac{^{(m)}\phi}{^{(m)}\rho^{(m)}c^2^{(m)}\tau} \right)} \quad (14.8)$$

The form of the relaxation algorithm is determined by the choice of the time constant  $^{(m)}\tau$ . Some possible choices are  $^{(m)}\tau = \Delta t$ , which produces the “equilibrium” form of the algorithm, and  $^{(m)}\tau = ^{(m)}\phi L / ^{(m)}c$ , which produces the Riemann-like form of the algorithm. In the Riemann-like form,  $L$  is a measure of the cell thickness and  $^{(m)}\tau$  is the estimated time for the wave to traverse material  $(m)$  and change the material pressure from  $^{(m)}P$  to  $P_{eq}$ . In the equilibrium form,  $P_{eq}$  takes on the well-known form

$$P_{eq} = \frac{\left( \sum_m \frac{^{(m)}\phi^{(m)}P}{^{(m)}\rho^{(m)}c^2} \right)}{\left( \sum_m \frac{^{(m)}\phi}{^{(m)}\rho^{(m)}c^2} \right)} \quad (14.9)$$

and the volume fraction equation becomes

$$\frac{1}{^{(m)}\phi} \frac{D^{(m)}\phi}{Dt} = \frac{^{(m)}P - P_{eq}}{^{(m)}\rho^{(m)}c^2\Delta t} \quad (14.10)$$

When the left-hand side of Equation 14.10 is differenced,  $\Delta t$  cancels from the equation. To first approximation, the changes in volume fractions will tend to equilibrate the material pressures within a timestep  $\Delta t$ .

In the Riemann-like form,  $P_{eq}$  takes on the form

$$P_{eq} = \frac{\left( \sum_m \frac{^{(m)}P}{^{(m)}\rho^{(m)}c} \right)}{\left( \sum_m \frac{1}{^{(m)}\rho^{(m)}c} \right)} \quad (14.11)$$

and the volume fraction equation becomes

$$\frac{D^{(m)}\phi}{Dt} = \frac{^{(m)}P - P_{eq}}{^{(m)}\rho^{(m)}cL} \quad (14.12)$$

For a two-material cell, this form is similar to the methods developed by David Youngs<sup>3</sup> and Ransom and Hicks.[58] For PAGOSA, a variation of the Riemann-like method was chosen. Modifications were required to handle some of the difficulties with the basic method, such as  $^{(m)}\tau \ll \Delta t$  and a potential instability associated with the artificial pressure  $Q$ .

The differenced equation for  $^{(m)}\phi$ ,

$$^{(m)}\phi^* = ^{(m)}\phi \left( 1 + \frac{^{(m)}P - P_{eq}}{^{(m)}\rho^{(m)}c^2} \frac{\delta t}{^{(m)}\tau} \right) \quad (14.13)$$

---

<sup>3</sup>David L. Youngs (AWRE, United Kingdom), private communication, January 15, 1992.

requires a stability and accuracy condition on the integration timestep  $\delta t$ , where  $\delta t \leq t$ .  $\delta t$  must be  $\leq^{(m)} \tau$  to prevent overshoots of  $P_{eq}$ , and it must be small enough to produce a good approximation to the exponential correction of  $\phi$ . If  $\delta t < \Delta t$ , relaxation subcycling is required. For stability, the definition of  $^{(m)}\tau$  is replaced with  $^{(m)}\tau = \max [L/^{(m)}c, 1.1\Delta t/(1-f)]$ , where  $f = \max(\text{safeu}, \text{safec})$  is a safety factor between 0 and 1. This definition guarantees that  $\delta t <^{(m)} \tau$ .

For accuracy and stability, the fractional change in  $^{(m)}\phi$  for any single material in a cell is allowed to be no larger than the maximum allowable fractional change in the cell volume.

For the case  $^{(m)}P < P_{eq}$ , the singularity at  $^{(m)}c = 0$  is mitigated by replacing  $^{(m)}c$  with  $^{(m)}c + ^{(m)}U_p$ , where  $^{(m)}U_p$  is estimated from

$$^{(m)}c + ^{(m)}U_p = \frac{^{(m)}c}{2} + \sqrt{\left(\frac{^{(m)}c}{2}\right)^2 + \left(\frac{P_{eq} - ^{(m)}P}{^{(m)}\rho}\right)} \quad (14.14)$$

Equation 14.14 is obtained by applying a linear  $U_s - U_p$  approximation<sup>4</sup> with  $s \rightarrow 1$  to a two-material, one-dimensional planar boundary.

When  $^{(m)}\phi^*$  has been evaluated, the density and internal energy are updated according to

$$^{(m)}\rho^* = ^{(m)}\rho \frac{^{(m)}\phi}{^{(m)}\phi^*} \quad (14.15)$$

and

$$^{(m)}E^* = ^{(m)}E - \frac{^{(m)}P}{^{(m)}\rho_0} \left( \frac{^{(m)}\phi^* - ^{(m)}\phi}{^{(m)}\phi_0} \right) (1 + \nabla \cdot \mathbf{u} \Delta t) - \frac{Q}{\rho_0} \left( ^{(m)}F^* - ^{(m)}F \right) \nabla \cdot \mathbf{u} \Delta t \quad (14.16)$$

where

$$0 \leq ^{(m)}F \equiv 1 + \left( \frac{^{(m)}\phi - ^{(m)}\phi_0}{^{(m)}\phi_0} \right) \left( \frac{1 + \nabla \cdot \mathbf{u} \Delta t}{\nabla \cdot \mathbf{u} \Delta t} \right) \leq 1 \quad (14.17)$$

In the above equations, the subscript 0 indicates a value at the beginning of the hydrodynamic timestep.  $^{(m)}\phi^*$  and  $^{(m)}\phi$  are the values of the volume fraction for successive relaxation subcycles. The last term in Equation 14.16 is required to partially correct the defect in the relaxation process related to the artificial pressure  $Q$ . Without it, the relaxation process tends to overexpand materials significantly to compensate for the introduction of internal energy by  $Q$ . The current limits on  $F$  are imposed for stability and may be relaxed in the future. The introduction of the last term in Equation 14.16 requires that the cell-averaged  $Q$  in the momentum equation be replaced with

$$\frac{Q}{\rho} \sum_m \left( ^{(m)}F^* \right) \cdot \left( ^{(m)}\phi_0 \right) \cdot \left( ^{(m)}\rho \right) \quad (14.18)$$

The approach described above works reasonably well if material strength effects are insignificant compared with the basic hydrodynamics. However, if strength effects are significant, the algorithm must be properly adjusted to avoid anomalous results. In particular, instead of relaxing just the pressure  $^{(m)}P$  toward equilibrium, it is necessary to relax  $^{(m)}P - \mathbf{n} \cdot ^{(m)}\mathbf{S} \cdot \mathbf{n}$ , where  $^{(m)}\mathbf{S}$  is the material-dependent, deviatoric stress tensor and  $\mathbf{n}$  is the average unit interface normal vector for

---

<sup>4</sup>See section 7.6, Grüneisen EOS.

the mixed cell. The algorithm obtains the average value for  $\mathbf{n}$  by volume averaging the individual surface normals obtained by interface reconstruction in the mixed cell.<sup>5</sup>

We therefore make the replacements

$$^{(m)}P \leftarrow ^{(m)}P - \mathbf{n} \cdot ^{(m)}\mathbf{S} \cdot \mathbf{n} \quad (14.19)$$

and

$$^{(m)}c^2 \leftarrow ^{(m)}c^2 + \frac{4}{3} \frac{^{(m)}G}{^{(m)}\rho} \quad (14.20)$$

Here  $^{(m)}G$  is the material-dependent shear modulus. In addition, the zone strain-rate tensor  $\bar{\dot{\mathbf{e}}}$  used to update  $^{(m)}\mathbf{S}$  is replaced with the material-dependent, strain-rate tensor  $^{(m)}\dot{\mathbf{e}}$ , which is approximated by

$$^{(m)}\dot{\mathbf{e}} = \bar{\dot{\mathbf{e}}} + \frac{1}{^{(m)}\phi} \frac{D^{(m)}\phi}{Dt} \mathbf{n}\mathbf{n} \quad (14.21)$$

---

<sup>5</sup> subsection 5.5.1 and Appendix C.



## Chapter 15

# Strength

*People do not lack strength, they lack will.*

– Victor Hugo (1802 – 1885)

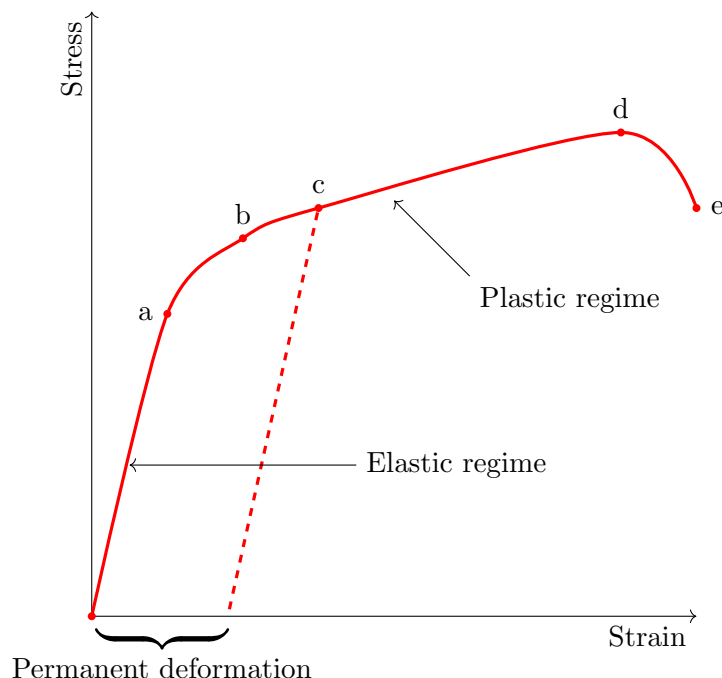


Figure 15.1: The elastic-plastic behavior of a typical ductile material (e.g., copper). Point **a** is the proportional limit, point **b** is the yield point, point **c** is a state in the plastic regime, point **d** is the ultimate tensile strength of the material, and point **e** is the fracture point.

This chapter is concerned with materials that can support a shear without continuous deformation. These elastic (and plastic) materials are different from the hydrodynamic materials studied up to this point.[59, See Volume II, Chapters 38 and 39 on elasticity] The stress deviators  $\mathbf{S}$  will be fully described.

Consider the stress-vs-strain curve of a typical solid material. During the first portion of the curve (up to a strain of less than  $\sim 1\%$ ), the stress and strain are proportional. This proportionality holds until point **a** in Figure 15.1, the proportional limit, is reached. We know that stress and strain are proportional because this segment of the line is straight. Hooke's Law, named after physicist Robert Hooke (1635 – 1703), is applicable in the region in which stress and strain are proportional.

Every material has a unique elastic modulus value (the slope of the line segment **0a** in Figure 15.1. That is, the stress required to produce a given strain depends on the nature of the material under stress.

From points **a** to **b** on the figure, stress and strain are not proportional; nevertheless, if the stress is removed at any point between **0** and **b**, the curve will be retraced in the opposite direction and the material will return to its original shape and length. In other words, the material will snap back into shape in a reverse order to the way it snapped out of shape to begin with. In region **0b** the material is said to be elastic or to exhibit elastic behavior and point **b** is called the yield point or elastic limit.

If the material is stressed further, the strain increases rapidly; but when the stress is removed at some point beyond **b**, say **c**, the material does not come back to its original shape but returns along a different path to a different point, shown along the dashed line in Figure 15.1. The length of the material at zero stress is now greater than the original length, and the material is said to

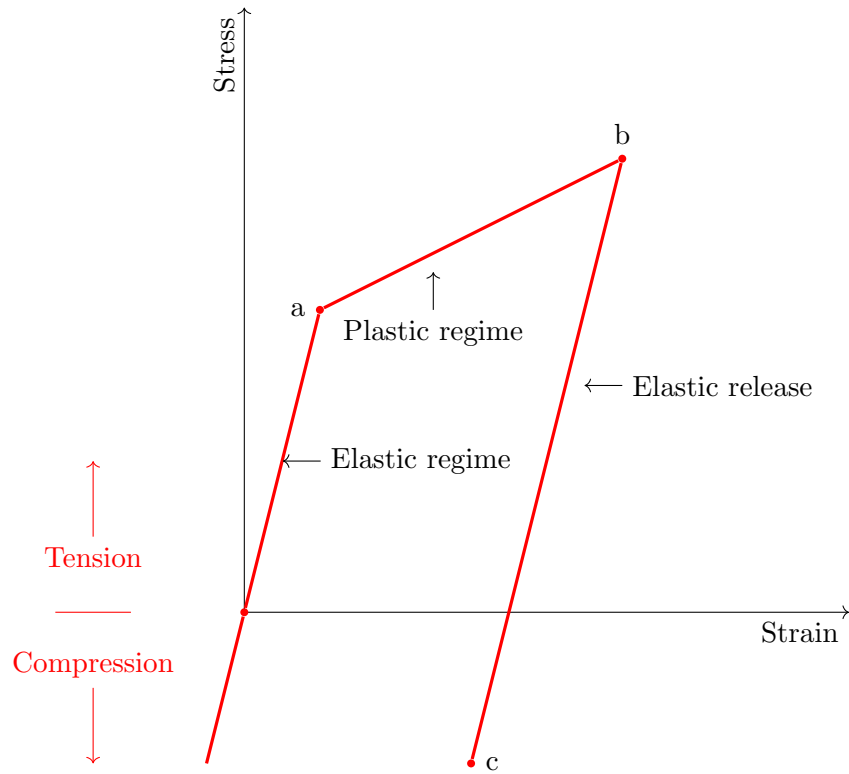


Figure 15.2: The elastic-plastic behavior of a PAGOSA material with strength.

have a permanent deformation.

A further increase of stress beyond **c** produces a large increase in strain until point **e** is reached, at which point fracture takes place. Between points **c** and **e**, the stress increases until point **d**, the maximum or ultimate tensile strength of the material. From points **b** to **e**, the metal is said to undergo plastic deformation. If large plastic deformation takes place between the elastic limit and the fracture point the metal is said to be *ductile*. However, if fracture occurs soon after the elastic limit is passed the metal is said to be *brittle*.

In PAGOSA, the stress strain curve is idealized as shown in Figure 15.2. Point **a** is the yield point of the material. From points **a** to **b**, the material is in the plastic regime. At some point **b** the loading stops and the material releases elastically. After the material has unloaded elastically (point **c**) the material can still unload plastically until it reaches an equilibrium state.

In the figure, the elastic release is a reversible process. The elastic release is essentially parallel to the initial elastic loading. The plastic regime shows a positive slope which represents work hardening in the material during plastic deformation. The empirical formula used to model this process is described in section 15.5

*Up to this point, the stress tensor and tensor notation have been avoided. However, to progress forward, explicit use of the Cauchy stress tensor and tensor notation is necessary and essential.*

## 15.1 Cauchy stress tensor

A second-order tensor, the Cauchy stress tensor, completely describes the state of stress of a material body. In previous chapters the stress tensor had been decomposed into its dilatational and deviatoric parts: [60]<sup>1</sup>

$$\sigma_{ij} = -P\delta_{ij} + S_{ij} \quad (15.1)$$

The Cauchy stress tensor is symmetric in its indices. If the stress deviator  $S_{ij} = 0$ , then the stress has the form  $\sigma_{ij} = -P\delta_{ij}$ . This form is called a pure hydrostatic state of stress, and  $P$  is the hydrostatic pressure. The negative sign arises because, by convention, we regard pressure, which causes compression, as positive, but we define compressive stress as negative.

The stress deviator  $\mathbf{S}$  in PAGOSA is associated with materials with a shear modulus  $G$ . The constitutive relations are given in Chapter 2, Equation 2.3a – Equation 2.3f. These constitutive relations connect the stress deviator and the material strain rates. The strain rates act differently depending on the state of the material: elastic regime or plastic regime. The next section describes the decomposition of the strains into their elastic and plastic parts.

Unlike finite elasticity, this model of elastic response does not carry the initial unstressed state as a reference state and thus is more suited to elastic-plastic modeling, where the plastic deformation continuously changes the zero-stress reference state.

## 15.2 Strain rate splitting

To separate the elastic and plastic flow behavior, the total linear strain is assumed to be linearly separable into an elastic component and a plastic component:

$$e_{ij} = e_{ij}^e + e_{ij}^p \quad (15.2)$$

It is found experimentally that, to a good approximation, the purely plastic component of the deformation of most materials[61] under hydrostatic loading should involve no volume change (dilatation). In other words, the plastic state of the material is incompressible. Therefore,

$$e_{kk}^p = e_{xx}^p + e_{yy}^p + e_{zz}^p = 0 \quad (15.3)$$

which expresses the property for the plastic strain. It follows that the divergence is

$$\nabla \cdot \mathbf{u} = \dot{e}_{kk} = \dot{e}_{kk}^e + \dot{e}_{kk}^p = \dot{e}_{kk}^e \quad (15.4)$$

For plastic behavior, the elastic component  $e_{ij}^e$  does not vanish in general. It is assumed that any changes in the stress state in the plastic regime are an elastic response to the elastic strain rates.

The details of the elastic-plastic response flow follow the Prandtl-Reuss treatment for fully compact ductile metals as presented in Freudenthal and Geiringer.[62] The second assumption in the Prandtl-Reuss treatment is that the plastic strain is proportional to the current stress deviator

$$e_{ij}^p = \lambda S_{ij} \quad \lambda > 0 \quad (15.5)$$

---

<sup>1</sup>It is a physically convenient decomposition for materials that exhibit plastic incompressibility.



where  $\lambda$  is the proportionality function between the plastic strain and the elastic-plastic response flow rule.

The changes in the deviatoric stress tensor are given by

$$\dot{S}_{ij} = 2G(\dot{e}_{ij} - \dot{e}_{ij}^p) \quad (15.6)$$

A derivation of this constitutive relation is given in [Appendix A](#)

In PAGOSA the elastic response of the material is decoupled from its thermodynamics. Thus, for the elastic regime in the absence of shocks, the material response should be isentropic. In particular, the isentropic part of the response should follow an adiabat of the equation of state (EOS).

The basic elastic-plastic algorithm is shown in [Table 15.1](#)

### 15.3 Yield criterion

The plastic behavior of a metal is a reflection of modifications of the internal material structure. At the macroscopic level, this behavior produces a material flow. This flow results in permanent local deformations and energy dissipation, which contributes to the local specific internal energy of the material.

The basic assumption is that there exists a scalar function of stress and strain,  $F(\boldsymbol{\sigma}, \boldsymbol{\varepsilon})$ , that characterizes the elastic and plastic states of the material.<sup>2</sup> When the scalar function is negative, the state is elastic. When the scalar function is zero, the state is plastic; that is, when  $F(\boldsymbol{\sigma}, \boldsymbol{\varepsilon}) = 0$  is reached, plastic deformations will develop. The case for which the scalar function is positive is physically unreachable. Any tendency in the state variables toward a positive scalar value is compensated by the plastic deformation such that the zero scalar function value is maintained. The scalar value of zero is called the “yield criterion.”

For isotropic materials, the yield criterion should be independent of the coordinate system. In PAGOSA, this yield criterion is a function of the stress deviator invariants. In particular, the second invariant is chosen.<sup>3</sup>

It is customary to relate the yield criterion to the yield stress  $Y_0$  for the material in a simple tension test. In the one-dimensional uniaxial stress configuration (simple tension), yield occurs when

$$\sigma_{xx} = Y_0 \quad \text{and all other components } \sigma_{ij} = 0$$

so that

$$P \equiv \frac{1}{3}Y_0$$

and the stress deviators are

$$S_{xx} = \frac{2}{3}Y_0 \quad ; \quad S_{yy} = -\frac{1}{3}Y_0 \quad ; \quad S_{zz} = -\frac{1}{3}Y_0$$

---

<sup>2</sup>The functional form of  $F(\boldsymbol{\sigma}, \boldsymbol{\varepsilon})$  is termed the yield surface

<sup>3</sup>See [Equation 2.4](#) in [Chapter 2](#) for the three tensor invariants

Table 15.1: The PAGOSA elastic-plastic algorithm at a glance

|     |   |                                      |
|-----|---|--------------------------------------|
| 1.  | $\dot{e}_{ij} \equiv \frac{1}{2} \left( \frac{\partial u_i}{\partial x_j} + \frac{\partial u_j}{\partial x_i} \right) \begin{cases} \text{if predictor,} & u = u^n \\ \text{if corrector,} & u = u^{n+1/2} \end{cases}$ | linear strain rate tensor            |
| 2.  | $\dot{e}_{ij} \equiv \dot{e}_{ij} - \frac{1}{3} \delta_{ij} \dot{e}_{kk}$   | linear deviatoric strain rate tensor |
| 3.  | $\Omega_{ij} = \frac{1}{2} \left( \frac{\partial u_i}{\partial x_j} - \frac{\partial u_j}{\partial x_i} \right)$  | linear spin (or rotation) tensor     |
| 4.  | Compute $Y$ and $G$   | flow-stress and shear modulus        |
| 5.  | $R_{ij} = \Omega_{im} S_{mj}^{old} - S_{im}^{old} \Omega_{mj}$  | rotation term                        |
| 6.  | $S_{ij}^* = S_{ij}^{old} + 2G \dot{e}_{ij} \Delta t - R_{ij} \Delta t$  | elastic prediction (trial stress)    |
| 7.  | $f(plastic) = \max \left( \frac{3S_{ij}^* S_{ji}^*}{2Y^2}, 1 \right) \quad \text{for } f \geq 1$  | radial return correction             |
|     | $f(elastic) = 1 \quad \text{for } f < 1$  |                                      |
| 8.  | $S_{ij}^{new} = \frac{S_{ij}^*}{\sqrt{f}}$  | new stress deviator                  |
| 9.  | $R_{ij} = \frac{1}{2} \left[ \Omega_{im} (S_{mj}^{old} + S_{mj}^{new}) - (S_{im}^{old} + S_{im}^{new}) \Omega_{mj} \right]$   | rotation update                      |
| 10. | $\Delta e_{ij}^p = \dot{e}_{ij} \Delta t - \frac{1}{2G} (S_{ij}^{new} - S_{ij}^{old} + R_{ij} \Delta t)$  | linear plastic strain tensor         |
| 11. | $\Delta e_{eq}^p = \sqrt{\frac{2}{3} e_{ij}^p e_{ji}^p}$  | change in equivalent plastic strain  |
| 12. | $\dot{e} = \sqrt{\frac{2}{3} \dot{e}_{ij} \dot{e}_{ji}}$  | deviatoric strain rate               |
| 13. | $\Delta W^p = S_{ij}^{old} \Delta e_{ji}^p$   | change in plastic work               |
| 14. | $e_{new}^p = e_{old}^p + \Delta e_{eq}^p$   | equivalent plastic strain            |
| 15. | $E_{new} = E_{old} + \frac{\Delta W^p}{\rho}$   | specific internal energy             |

and all the other stress deviators are zero.

The second invariant of the stress deviator tensor is related to the yield criterion by the classic von Mises yield criterion [63]

$$\begin{aligned} J_2 &= \frac{1}{2}(S_{xx}^2 + S_{yy}^2 + S_{zz}^2) + S_{xy}^2 + S_{xz}^2 + S_{yz}^2 \\ &= \frac{1}{2}\left(\frac{4}{9}Y_0^2 + \frac{1}{9}Y_0^2 + \frac{1}{9}Y_0^2\right) + 0 + 0 + 0 \\ &= \frac{1}{3}Y_0^2 \end{aligned}$$

This equation is the relation between the second deviatoric stress invariant and the yield stress: the classical von Mises yield criterion. This form is generalized in PAGOSA by replacing  $Y_0$  by the yield function

$$J_2 = \frac{1}{2}S_{ij}S_{ji} = \frac{1}{3}[Y(\chi_1, \chi_2, \dots)]^2 \quad (15.7)$$

The forms of the yield function  $Y$  available in PAGOSA are given in [subsection 15.4.1](#) – [subsection 15.4.7](#). The arbitrary arguments  $\chi_n$  are the dependencies of the yield function.

The yield limiting algorithm in PAGOSA can be understood best in a nine-dimensional stress deviator space.<sup>4</sup> In this space a stress deviator is represented by a vector  $\mathbf{S}$ , where its elements are the tensor components of  $\mathbf{S}$ . The Euclidian norm of the vector  $\mathbf{S}$  is given as

$$J_2 = \frac{1}{2}S_{ij}S_{ji} = \frac{1}{2}\|\mathbf{S}\| \quad (15.8)$$

The classical von Mises yield criterion is

$$Y = \sqrt{\frac{3}{2}S_{ij}S_{ji}} \quad (15.9)$$

which represents a hyper-sphere with a radius of  $\sqrt{2/3}Y$ , where the specific value depends on the current state variables influencing the yield function  $Y$ . States inside the hyper-sphere are elastic, and states on the surface of the hyper-sphere are plastic

$$\text{Elastic: } \|\mathbf{S}\| < \sqrt{\frac{2}{3}}Y \quad (15.10a)$$

$$\text{Plastic: } \|\mathbf{S}\| = \sqrt{\frac{2}{3}}Y \quad (15.10b)$$

If components of the  $\mathbf{S}$  vector are referred to the material (co-rotational) frame, the strain rate deviator  $\mathbf{e}$  can be represented in this space by a vector  $2G\mathbf{e}$  where the elements are scaled by  $2G$  where  $G$  is the current shear modulus.

The elastic-plastic distortions are shown in [Figure 15.3](#) and [Figure 15.4](#). Suppose the stress deviator vector at time  $t$  is  $\mathbf{S}^0$  and the vector at time  $t + \Delta t$  is  $\mathbf{S}^1$ . The yield criterion are shown as

---

<sup>4</sup>The style and mathematical structure of this exposition is primarily credited to Ian N. Gray, Atomic Weapons Research Establishment (AWRE), Aldermaston, Berkshire, UK.

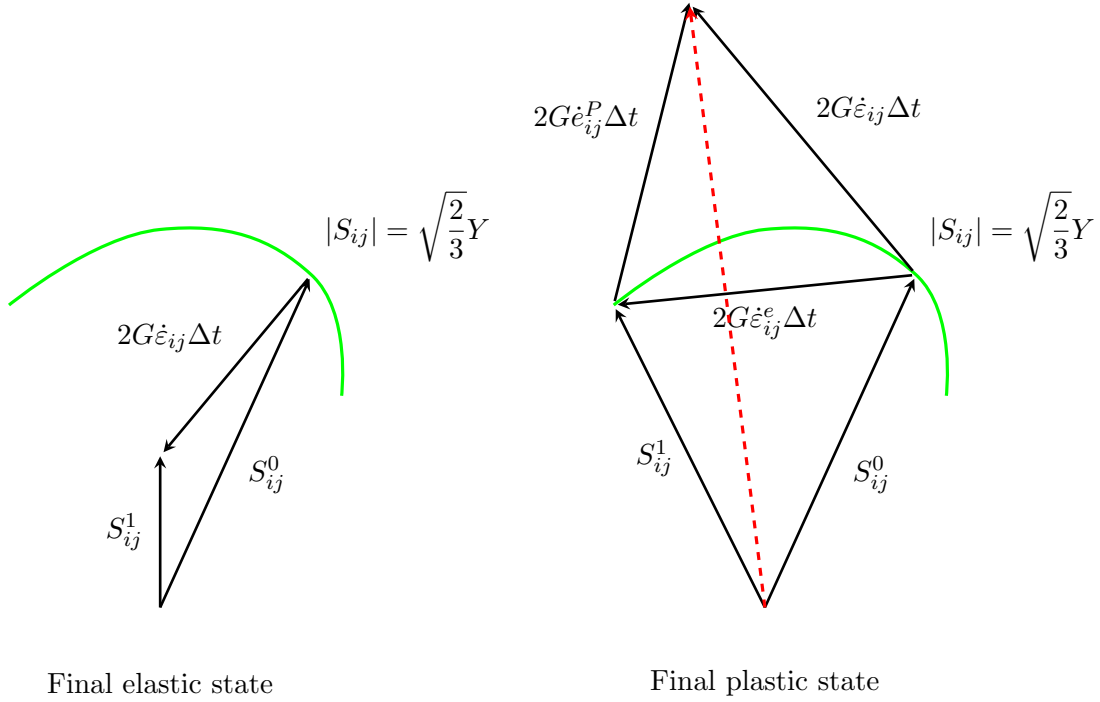


Figure 15.3: The two possible final states for a single timestep  $\Delta t$ . In the case where the transition to a final state is elastic the strain rate deviator is all elastic. On the other hand, if the transition is to a final plastic state the strain rate deviator splits into two parts: elastic and plastic. The plastic contribution must lie on the yield surface. The elastic part cannot exceed the yield surface under these circumstances. The vector  $\mathbf{S}^*$  is called the elastic predictor and has the value of the stress deviator if the total strain rate deviator was all elastic. The conditions do not uniquely determine  $\mathbf{S}^1$  when the final state is plastic. The condition used in PAGOSA that provides a unique solution is given by the mathematical expression  $\dot{\epsilon}_{ij}^p \Delta t = \lambda S_{ij}^1$

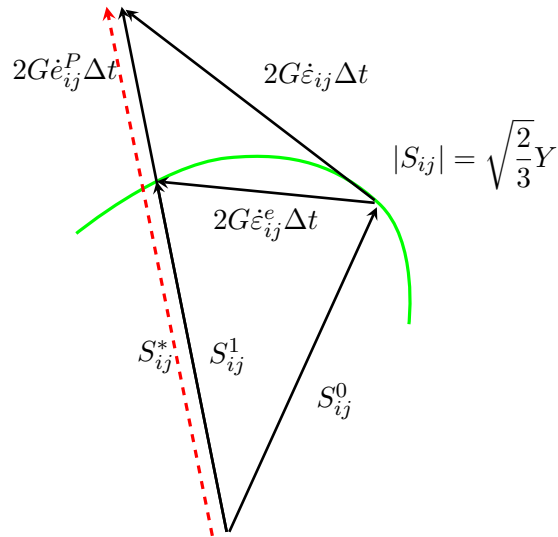


Figure 15.4: The vector components of an elastic-plastic state.

Now with the above condition the values of  $\mathbf{S}^1$  and  $e_{ij}^p$  can be determined by (not including the rotation terms):

(I) Elastic prediction

$$\mathbf{S}^* = \mathbf{S}^0 + 2G\dot{\epsilon}\Delta t \quad (15.11)$$

(II) Yield limiting

$$\mathbf{S}^1 = \begin{cases} \mathbf{S}^* & |\mathbf{S}^*| \leq \sqrt{\frac{2}{3}}Y \\ \frac{\sqrt{2/3}Y}{|\mathbf{S}^*|} \mathbf{S}^* & |\mathbf{S}^*| > \sqrt{\frac{2}{3}}Y \end{cases} \quad (15.12)$$

(III) Strain rate deviator splitting

$$\dot{\mathbf{e}}^p = \dot{\epsilon} - \frac{\mathbf{S}^1 - \mathbf{S}^0}{2G\Delta t} \quad (15.13)$$

The above algorithm provides a first-order (backward) difference approximation to  $\mathbf{S}^1$  and  $\mathbf{e}^p$ . It also has the virtue of automatically handling the elastic-plastic transitions, as shown in [Figure 15.3](#) and [Figure 15.4](#)

The stress deviator is updated so that the elastic predictor contains the rotation correction terms

$$S_{ij}^* = S_{ij}^0 + 2G\dot{\epsilon}_{ij}\Delta t - (\Omega_{ik}S_{kj} - S_{ik}\Omega_{kj})\Delta t \quad (15.14)$$

where all variables are appropriately time centered.

The plastic strain is computed as

$$e_{ij}^p = \varepsilon_{ij} - \frac{S_{ij}^1 - S_{ij}^0}{2G\Delta t} + \frac{\Omega_{ik}S_{kj} - S_{ik}\Omega_{kj}}{2G} \quad (15.15)$$

Remember that in general,  $G$  and  $Y$  are functions of density, pressure, and internal energy. The specific forms are described in [subsection 15.4.1](#) – [subsection 15.4.7](#)

The velocity field at the start of a timestep (time  $t^n$ ) is used to evaluate the divergence,  $\dot{\epsilon}_{ik}$ , and  $\Omega_{mn}$ . Using these values, a forward differencing of the stress deviator equations, together with the yield-limiting algorithm, gives a first-order prediction of the stress deviator at a half timestep  $t^{n+1/2}(t^n + 1/2\Delta t)$ . For multi-material cells, the cell strain rate is applied to each material component separately, regardless of its compressibility,<sup>5</sup> and no attempt is made to force any equilibrium between the various components. Using the velocity divergence to update the specific volume (and density) and forward differencing the internal energy equation, using plastic strain rates from the yield-limiting algorithm, allows a first-order EOS prediction of pressure at time  $t^{n+1/2}(t^n + 1/2\Delta t)$ . Again, a uniform cell value of velocity divergence is applied to components of multi-material cells.

Straightforward spatial differencing of pressures and stress deviators at  $t^{n+1/2}(t^n + 1/2\Delta t)$  allows the acceleration equations to give a second-order update of the velocity field from time  $t^n$  to  $t^n + \Delta t$ .

From the velocity fields at times  $t^n$  and  $t^n + \Delta t$ , the divergence,  $\dot{\epsilon}_{ik}$ , and  $\Omega_{mn}$  are evaluated at the half timestep  $t^{n+1/2}(t^n + 1/2\Delta t)$  and used in a second-order differencing of the stress deviator and

<sup>5</sup>As in the case of the “uniform” divergence option [section 14.1](#)

energy equations to update the remaining quantities at time  $t^n + \Delta t$ . See [Chapter 6](#) on Integration for more details.

The Lagrangian phase passes cell velocities at half timesteps to the advection phases. To avoid problems in consistency with the yield surface following advection, the last Lagrangian step passes its elastic prediction (not yield-limited) value of the stress deviator to the advection phases. The post-advection deviators are considered to be elastic predictions and are yield limited according to the post-advection values of plastic strain, pressure, and internal energy.

## 15.4 Flow stress models

The flow-stress models give specific functional forms to the shear and yield moduli. In situations where very high hydrodynamic pressures or large strains are created, the constitutive relations may generate unrealistically large values for  $G$  and  $Y$ . To avoid this problem, the user can supply a maximum permitted shear modulus  $G_{max}$  and a maximum permitted yield modulus  $Y_{max}$ . In PAGOSA these limits are implemented as

$$G = \min(G, G_{max}) \quad (15.16)$$

$$Y = \min(Y, Y_{max}) \quad (15.17)$$

If the yield modulus is set to a large value, then the material behavior is completely elastic and no plastic deformation occurs. This flow-stress model can be useful in some test problems and cases where the deformation is expected to be purely elastic.

### 15.4.1 Elastic perfectly plastic

The elastic-perfectly plastic model is an idealized material and the easiest to understand. The shear and yield moduli are simply constants. The shear and yield moduli are

$$G = G_0 \quad \text{and} \quad Y = Y_0 \quad (15.18)$$

In this case, the plastic regime (shown in [Figure 15.5](#)) is a horizontal line. The stress in the plastic regime would be independent of the strain. The effects of thermal softening and work hardening are absent from this model.

The class of elastic-perfectly plastic materials is an idealization to keep the constitutive equations simple. The idealization is reasonable for materials that do not show significant work hardening. The adequacy of this idealization depends on the purpose and requirement of the specific application.

### 15.4.2 Modified Steinberg-Cochran-Guinan

The Modified Steinberg-Cochran-Guinan model[[64](#)] is applicable for high-strain-rate materials (usually metals). The shear modulus and yield strength are functions of equivalent plastic strain, pressure, and internal energy.

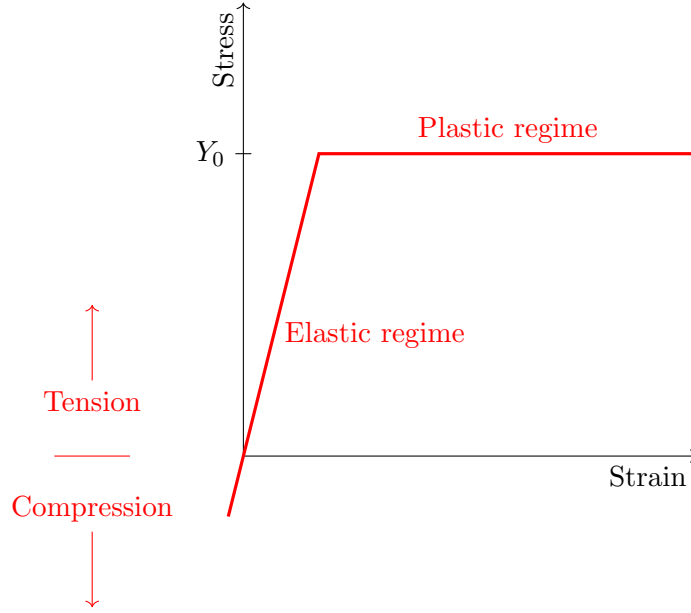


Figure 15.5: An elastic-perfectly plastic material.

The shear modulus is

$$G = G_0 P'_{cor} F_{melt} \quad (15.19)$$

$$P'_{cor} = 1 + \gamma' P \left( \frac{\rho_0}{\rho} \right)^{1/3} \quad (15.20)$$

$$F_{melt} = \begin{cases} 0 & E \geq E_m \\ \exp \left( -\frac{\delta E}{E_m - E} \right) & E < E_m \end{cases} \quad (15.21)$$

Equation 15.20 is a pressure correction term, and Equation 15.21 is a thermal softening term. The yield strength is given by

$$Y = Y_0 [1 + \alpha(e_0^p + e^p)]^\beta P_{cor} F_{melt} \quad (15.22)$$

$$P_{cor} = 1 + \gamma P \left( \frac{\rho_0}{\rho} \right)^{1/3} \quad (15.23)$$

The pressure correction terms are different for shear and yield. However, the thermal softening term is the same for Equation 15.19 and Equation 15.22. The time-integrated equivalent plastic strain is denoted  $e^p$ .

This model requires seven user-supplied inputs:  $\alpha, \beta, \gamma, \gamma', \delta, e_0^p$ , and  $E_m$ . A single melt energy  $E_m$  is specified for the material. If the internal energy is greater than this value, then both  $G$  and  $Y$  are set to a value of zero. The thermal softening is discussed in subsection 15.4.8

### 15.4.3 Steinberg-Cochran-Guinan

The Steinberg-Cochran-Guinan model is a full-temperature version of the Modified Steinberg-Cochran-Guinan model. The material temperatures ( $\theta$ ) are obtained from the SESAME database via the EOSPAC library (see Chapter 7, section 7.7).

The shear modulus is

$$G = G_0(P'_{cor} - F'_{melt}) \quad (15.24)$$

$$P'_{cor} = 1 + \gamma' P \left( \frac{\rho_0}{\rho} \right)^{1/3} \quad (15.25)$$

$$F'_{melt} = \gamma'_T(\theta - \theta_{room}) \quad (15.26)$$

The yield strength is given by

$$Y = Y_0[1 + \alpha(\varepsilon_0^p + \varepsilon^p)]^\beta (P_{cor} - F_{melt}) \quad (15.27)$$

$$P_{cor} = 1 + \gamma P \left( \frac{\rho_0}{\rho} \right)^{1/3} \quad (15.28)$$

$$F_{melt} = \gamma_T(\theta - \theta_{room}) \quad (15.29)$$

The pressure and thermal softening terms are different for the shear and yield equations. The time-integrated equivalent plastic strain is denoted  $\varepsilon^P$ . It is computed simply as

$$\varepsilon^p = \int_0^t \sqrt{\frac{2}{3} \dot{\varepsilon}_{ik}^p \dot{\varepsilon}_{ik}^p} dt \quad (15.30)$$

This model requires nine user-supplied inputs:  $\alpha, \beta, \gamma, \gamma', \gamma_T, \gamma'_T, \delta, \varepsilon_0^p, \theta_{room}$  and  $\theta_{melt}$ .

The pressure correction terms [Equation 15.25 and Equation 15.28] are set to a value of one in the case where  $P < 0$  (i.e., tension). In the case where the material temperature exceeds the melt temperature ( $\theta \geq \theta_{melt}$ ), both  $G$  and  $Y$  are set to a value of zero.

#### 15.4.4 Johnson-Cook (JC)

The Johnson-Cook (JC) model[65] is an empirical flow-stress model. The shear modulus and yield strength are functions of equivalent plastic strain, pressure, and internal energy.

The shear modulus is

$$G = G_0 P_{cor} [1 - \max(0, T^*)^m] \quad (15.31)$$

$$P_{cor} = 1 + \gamma' P \quad (15.32)$$

The yield strength is given by

$$Y = (Y_0 + B\varepsilon^p)(1 + C \ln \dot{\varepsilon}^*) [1 - \max(0, T^*)^m] \quad (15.33)$$

where the homologous temperature  $T^*$  is given by:

$$T^* \equiv \frac{E - E_{room}}{E_{melt} - E_{room}} \quad (15.34)$$

and the dimensionless plastic strain rate is

$$\dot{\varepsilon}^* = \frac{\dot{\varepsilon}^p}{\dot{\varepsilon}_0} \quad \text{and } \dot{\varepsilon}_0 = 1.0\text{s}^{-1} \quad (15.35)$$



This model requires seven user-supplied inputs:  $B, C, n, m, E_{melt}, E_{room}$ , and  $\gamma'$ .

**NOTE:** The homologous temperature, in PAGOSA, is computed as the homologous internal energy. The assumption is that the two are not much different. For example, if the heat capacity  $C_v$  is only weakly dependent on temperature, then the homologous temperature is

$$T^* = \frac{E - E_{room}}{E_{melt} - E_{room}} \approx \frac{T - T_{room}}{T_{melt} - T_{room}}$$

### 15.4.5 Preston-Tonks-Wallace (PTW)

The Preston-Tonks-Wallace (PTW) yield model is a physically based constitutive model. The following have been taken from several sources: a published paper by PTW[66] and a memorandum by Zocher and Flower-Maudlin.<sup>6</sup>

The shear modulus is

$$G = G_0(1 - \alpha\hat{T}) \quad (15.36)$$

where  $G_0$  is the initial shear modulus at 0 K and is a user-defined parameter and  $\alpha$  is also a user-defined dimensionless material constant. The normalized temperature in the above equation is defined to be

$$\hat{T} = \frac{T}{T_{melt}} \quad (15.37)$$

where  $T_{melt}$  is either a user-defined melt temperature from data or the melt temperature field generated by a SESAME melt model. The flow-stress (also known as yield strength  $Y$ ) for PTW is, as a function of the stress tensor  $\sigma$ ,

$$\sigma = 2\tau \quad (15.38)$$

or, in terms of normalized stress,

$$\sigma = 2\hat{\tau}G \quad (15.39)$$

The normalized stress is defined to be:

$$\hat{\tau} = \hat{\tau}_s + \frac{1}{p}(S_0 - \hat{\tau}_y) \ln \left[ 1 - W \exp \left\{ - \frac{p\theta_0\psi}{(S_0 - \hat{\tau}_y) \left[ \exp \left( p \frac{\hat{\tau}_s - \hat{\tau}_y}{S_0 - \hat{\tau}_y} \right) - 1 \right]} \right\} \right] \quad (15.40)$$

where the equivalent plastic strain  $\psi$  is calculated from the code. The parameter  $W$  is defined as

$$W \equiv 1 - \exp \left( -p \frac{\hat{\tau}_s - \hat{\tau}_y}{S_0 - \hat{\tau}_y} \right) \quad (15.41)$$

The user-defined dimensionless parameters in the above and following equations are  $p, S_0$ , and  $\theta_0$ . The yield stress  $\hat{\tau}_y$  and saturation stress  $\hat{\tau}_s$  equations are defined as follows

---

<sup>6</sup>M.A. Zocher and E.C. Flower-Maudlin, "The Implementation of Plasticity into CHAD," Los Alamos National Laboratory, X-4 memorandum to L.S. Bennett, M.B. Prime, M.W. Burkett, and R. Mason (January 29, 1999).

The yield stress is

$$\hat{\tau}_y = \max \left\{ y_0 - (y_0 - y_\infty) \operatorname{erf} \left[ \kappa \hat{T} \ln \left( \frac{\gamma \dot{\xi}}{\dot{\psi}} \right) \right], \min \left[ y_1 \left( \frac{\dot{\psi}}{\gamma \dot{\xi}} \right)^{y_2}, S_0 \left( \frac{\dot{\psi}}{\gamma \dot{\xi}} \right)^\beta \right] \right\} \quad (15.42)$$

and the saturation stress is

$$\hat{\tau}_S = \max \left\{ S_0 - (S_0 - S_\infty) \operatorname{erf} \left[ \kappa \hat{T} \ln \left( \frac{\gamma \dot{\xi}}{\dot{\psi}} \right) \right], S_0 \left( \frac{\dot{\psi}}{\gamma \dot{\xi}} \right)^\beta \right\} \quad (15.43)$$

The “erf” in the yield stress and saturation stress equations is the error function. The equivalent plastic strain  $\psi$  and equivalent plastic strain rate  $\dot{\psi}$  are used in the above equations. The strain-rate scaling factor used in the equations above is defined to be

$$\dot{\xi} = \frac{1}{2} \left( \frac{4\pi\rho}{3M} \right)^{1/3} \sqrt{\frac{G}{\rho}} \quad (15.44)$$

where  $M \equiv 1.6605387 \times 10^{-24} \text{A}$  is the atomic mass of an atom. Clearly,  $\rho$  is the material mass density. This strain-rate scaling factor is the reciprocal of the time required for a shear wave to traverse a unit cell (atomic vibration frequency).

The flow-stress  $\sigma$  and the shear modulus  $G$  are set to zero when the temperature is greater than the melt temperature. The form requires both the maximum yield strength and initial and maximum shear modulus. A von Mises yield criterion is used that results in a “radial return” to the yield surface. This model requires 14 user-supplied inputs:  $\theta_0, p, S_0, S_\infty, \kappa, \gamma, y_0, y_\infty, y_1, y_2, \beta, \alpha, T_{melt}$ , and  $A$ .

#### 15.4.6 Mechanical threshold stress (MTS)

The mechanical threshold stress (MTS) yield model is a physically based constitutive model founded on dislocation mechanics.<sup>[67]</sup> The accumulative flow-stress, also known as yield strength  $Y$ , is calculated as

$$\sigma = \hat{\sigma}_a + \frac{\mu}{\mu_0} \sum_{i=1}^N \hat{\sigma}_i S_i \quad (15.45)$$

where  $\hat{\sigma}_a, \mu_0, N$  are user-defined parameters. Currently, three terms are used in the above equation. The summed product in the above equation separates the contribution from interaction  $i$  into a structure evolution term  $\hat{\sigma}_i$  modified with a constant-structure deformation  $S_i$  that is mainly a function of temperature and strain rate. The index  $i$  can assume the values 1, 2, or 3, where they represent dislocation, interstitial atomic, and solute atomic terms, respectively. The athermal threshold stress  $\hat{\sigma}_a$  represents dislocation interactions with long-range barriers, such as boundaries, and is assumed to be constant. The shear modulus is

$$G = \left( b_1 - \frac{b_2}{\exp(b_3/T) - 1} \right) (1 + p_{hard} P) \quad (15.46)$$

where  $b_1, b_2, b_3$ , and  $p_{hard}$  are user-defined parameters. The pressure and temperature,  $P$  and  $T$ , are calculated from the EOS. Generally,  $p_{hard}$  has a value of 0.7 for copper and 0.0 (zero) for most other materials.

The  $\hat{\sigma}_i$  described above is obtained from the structure evolution equation, which is a differential hardening law

$$\frac{\partial \hat{\sigma}_i}{\partial \varepsilon} = \theta_0 [1 - F(X_i)] \quad (15.47)$$

where the expression  $\partial \varepsilon$  is just  $\dot{\varepsilon} \partial t$ , with  $\varepsilon$  and  $\dot{\varepsilon}$  being the total strain and total strain rate, respectively. The equation for the dislocation rate  $\theta_0$  varies according to the material.

The five different possibilities are:

|       |   |         |
|-------|---|---------|
| idmts | Theta equation  |         |
| (1)   | $\theta_0 = a_1 - a_2 \frac{kT}{\mu b^3} \ln \frac{\dot{\varepsilon}_{s0}}{\dot{\varepsilon}}$          |         |
| (2)   | $\theta_0 = a_1 + a_2 \ln \dot{\varepsilon} + a_3 \dot{\varepsilon}$                                    |         |
| (3)   | $\theta_0 = a_1 + a_2 \ln \dot{\varepsilon} + a_3 \sqrt{\dot{\varepsilon}}$                             | (15.48) |
| (4)   | $\theta_0 = a_1 - a_2 T$  |         |
| (5)   | $\theta_0 = \theta_{0s} \left( \frac{\dot{\varepsilon}_{s0}}{\dot{\varepsilon}} \right)^{-kT/A\mu b^3}$ |         |

where  $a_1, a_2$ , and  $a_3$  are the three user-defined parameters. The  $F(X_i)$  and  $X_i$  are defined as

$$F(X_i) = \frac{\tanh(\alpha X_i)}{\tanh \alpha} \quad (15.49)$$

and

$$X_i = \frac{\hat{\sigma}_i}{\hat{\sigma}_s} \quad (15.50)$$

respectively. The saturation threshold stress at 0 K is

$$\hat{\sigma}_s = \hat{\sigma}_{s0} \left( \frac{\dot{\varepsilon}_{s0}}{\dot{\varepsilon}} \right)^{-kT/A\mu b^3} - \hat{\sigma}'_a \quad (15.51)$$

In this equation,  $\hat{\sigma}_{s0}, \dot{\varepsilon}_{s0}, b_3$ , and  $A$  are user-defined parameters, and  $k$  is the Boltzmann constant. The last term in the above equation,  $\hat{\sigma}'_a$ , is usually nonzero for copper and zero for all other materials. It should be noted that the relationships for  $\theta_0, F(X_i), \hat{\sigma}_{s0}$ , and  $\alpha$  are material specific. A constant-structure deformation term  $S_i$ , which is a function of temperature and strain rate, is defined to be

$$S_i = \left[ 1 - \left( \frac{kT \ln(\dot{\varepsilon}_i / \dot{\varepsilon})}{\mu b^3 g_i} \right)^{1/q_i} \right]^{1/p_i} \quad (15.52)$$

where  $b$  is the magnitude of Burgers Vector (the inter-atomic distance in the slip direction) and  $g_i$  is a normalized activation energy for a given dislocation/obstacle interaction.

The flow-stress  $\sigma$  and the shear modulus  $G$  are set to zero when the temperature is greater than the melt temperature. If the SESAME melt model is specified for the associated material, MTS uses the melt temperature field generated by the SESAME melt model instead of the user-defined  $T_{melt}$ .

Currently, the SESAME EOS database must be used with this yield model. The form requires both the maximum yield strength and the maximum shear modulus. A von Mises yield criterion is used, which results in a “radial return” to the yield surface.

The dislocation rate equation must be chosen by specifying  $idmts = 1, 2, 3, 4$ , or  $5$ . This constant specifies which dislocation rate equation  $\theta_0$  is used in the model.

This model requires 35 user-supplied inputs:  $b_1, b_2, b_3, p_{hard}, \dot{\epsilon}_{0d}, g_{0d}, \dot{\epsilon}_{0i}, g_{0i}, \dot{\epsilon}_{0s}, g_{0s}, 1/p_d, 1/q_d, 1/p_i, 1/q_i, 1/p_s, 1/q_s, \hat{\sigma}_a, \hat{\sigma}_d, \hat{\sigma}_i, \hat{\sigma}_s, b, boltz, T_{melt}, T_{room}, G_{min}, \epsilon_{min}, A, \hat{\sigma}'_a, \hat{\sigma}_0, \alpha, a_1, a_2, a_3, \dot{\epsilon}_{s0}$ , and  $idmts$ .

### 15.4.7 Kospall

The Kospall model[68] is closely related to the Steinberg-Cochran-Guinan model. The shear modulus contains two thermal softening terms and a pressure correction term:

$$G = G_0(P'_{cor} - F'_{melt})H'_{melt} \quad (15.53)$$

$$P'_{cor} = 1 + bP\left(\frac{\rho_0}{\rho}\right)^{1/3} \quad (15.54)$$

$$F'_{melt} = |h|(\theta - \theta_{room}) \quad (15.55)$$

$$H'_{melt} = \begin{cases} 0 & E \geq E_m \\ \exp\left(-\frac{gE}{E_m - E}\right) & E < E_m \end{cases} \quad (15.56)$$

Note that the input parameter  $h$  is taken as an absolute value to avoid confusion with other hydrodynamics codes using the Kospall model.

Similarly, the yield modulus has two thermal softening terms:

$$Y = Y_0[1 + \alpha \exp(p)]^\beta (P_{cor} - F_{melt})H_{melt} \quad (15.57)$$

$$P_{cor} = 1 + bqP\left(\frac{\rho_0}{\rho}\right)^{1/3} \quad (15.58)$$

$$F_{melt} = |h|(\theta - \theta_{room}) \quad (15.59)$$

$$H_{melt} = \begin{cases} 0 & E \geq E_m \\ \exp\left(-\frac{fE}{E_m - E}\right) & E < E_m \end{cases} \quad (15.60)$$

The first thermal softening term is based on temperature, and the second is based on internal energy. The temperatures are found from the SESAME database for the material of interest.

This model requires eight user-supplied inputs:  $\alpha, \beta, b, f, g, h, q$ , and  $\theta_{room}$ .

### 15.4.8 Thermal softening

The shear and yield moduli degrade (soften) as a function of the degree of melt. The term

$$F_{melt} = \exp\left(-\delta \frac{E}{E_m - E}\right) \quad (15.61)$$

is used in many of the flow-stress models to approximate this melt behavior.

The expression provides a crude model for the diminishing strength upon melting. The parameter  $E_m$  specifies the specific internal energy for melting. In some strength forms, it is a user-specified input; in others, it is obtained from the SESAME EOS database.

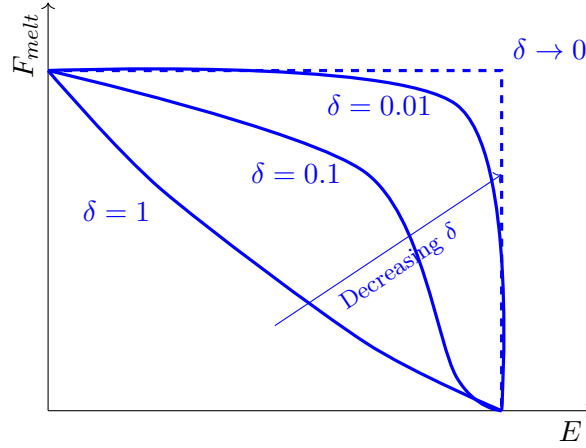


Figure 15.6: The thermal softening function  $F_{melt}$  as a function of the specific internal energy. In the limit  $\delta \rightarrow 0$ , the term becomes a step function.

If  $E < E_m$ , then the term is evaluated. If  $E \geq E_m$ , the term and thus the yield strength are set to zero. The melt term has no physical significance. It is simply a convenient functional expression that provides a smooth transition to zero strength at melting.

The thermal softening coefficient  $\delta$  controls the shape of the melt function. Typical values for  $\delta$  are in the range of  $10^{-2}$  to  $10^{-3}$  dimensionless units. A value of zero results in a step function, as illustrated in [Figure 15.6](#)

The thermal softening function is based on internal energy. PAGOSA is energy based as distinct from temperature based.

## 15.5 Work hardening

Work hardening, also known as strain hardening, is the strengthening of a material by plastic deformation. Work hardening is a consequence of plastic deformation, a permanent change in shape. The associated elastic deformation is reversible. Most materials do not exhibit only one or the other, but rather a combination of the two deformations. Work hardening is most common in ductile materials such as metals.

If the material is work hardened, then some initial hypersurface represents the primary yield. Further plastic straining alters the shape of the current yield surface. For example, if  $Y_0$  is the primary yield surface, then the distance to the von Mises yield surface is  $Y_0 \sqrt{2/3}$ . Suppose that the straining continues beyond  $Y_0$  to  $Y_1$  and that the material is then completely unloaded. The material now possesses a yield surface at a distance  $Y_1 \sqrt{2/3}$ . The new surface surrounds and is “concentric” with the primary yield surface. The implication here is that the material has been isotropically work hardened. This result can be represented by a yield surface, which expands with stress and strain history, retaining the same shape throughout.

Several empirical mathematical descriptions of the work-hardening phenomenon exist. Holloman’s equation[69] is a power law relationship between the stress and the plastic strain:

$$\sigma = A(e^p)^n \quad (15.62)$$

where  $\sigma$  is the stress,  $A$  is the strength hardening coefficient,  $e^p$  is the plastic strain, and  $n$  is the strain hardening index.[70] Ludwik's equation[71] is similar but includes the yield stress

$$\sigma - Y = A(e^p)^n \quad (15.63)$$

If the material has a history of deformation, then the yield stress will be increased by a term, which depends on the initial plastic strain  $e_0^p$  as:

$$\sigma = Y + A(e_0^p + e_{ij}^p)^n \quad (15.64)$$

The strain-hardening index can be evaluated by

$$n = \frac{e}{\sigma} \frac{d\sigma}{de} = \frac{d \ln \sigma}{d \ln e} \quad (15.65)$$

The index can be evaluated by examining the slope on a log-log plot of the data.

Work hardening is an important feature in correctly modeling the deformation of materials in the plastic regime. The work-hardening term in many of the flow-stress models has the form

$$Y[1 + \alpha(e_0^p + e^p)]^\beta \quad (15.66)$$

which is a generalization of [Equation 15.63](#). The material specific inputs are  $\alpha$ ,  $\beta$ , and  $e_0^p$ .

## Chapter 16

# MATCH

*I am building a fire, and everyday I train, I add more fuel. At just the right moment, I light the match.*

– Mia Hamm (1972 – )

## 16.1 MATCH and DEFLAGRATE Physics Description

MATCH is the “Mechanically Activated Thermal Chemistry ” (MATCH) explosives model. MATCH has two key sub-models: a mechanics model called VPS and an ignition model called Hotspot. DEFLAGRATE involves reactive burn physics. The Equation of State (EOS) models used for the reactants, products, and burning mixtures exist already within Pagosa.

## 16.2 MATCH-VPS

- **Viscoelasticity:** The explosives modeled by MATCH are Plastic Bonded eXplosives (PBX), and the binder in these materials is typically polymeric. Even though the binder concentration may be as little as 5 weight percent, as in the case of PBX 9501, the binder is responsible for the significant strain rate and temperature dependences observed in the small strain regime of the stress-strain curves. A generalized Maxwell Model, using a set of viscoelastic shear moduli and relaxation times, is used to model viscoelastic effects. The temperature dependence enters through a tabulated shift function. The viscoelastic model is thermo-mechanically consistent and thus not restricted to isothermal events. The model is described in Chapters 2 and 3, and examples for fitting the model are provided in Chapters 4 and 5 of the MATCH-PAGOSA Manual.[\[72\]](#)
- **Shear Crack Damage:** Damage is known to influence both explosive ignition and the following violence resulting from a deflagration. Thus, the continuum damage field calculated in MATCH determines the explosives stress-strain behavior, but is also used in the Hotspot ignition model. It is also passed to the DEFLAGRATE algorithm. The underlying physics of the damage model is explained in Chapter 2 and the procedure for fitting the model is provided in Chapters 4 and 5 of the MATCH-PAGOSA Manual.
- **Plastic Flow:** Certain explosives show yield-like behavior at the macroscopic level, for example, in the stress-strain behavior. A typical example is the explosive PBX 9502, where the graphitic crystalline structure of the TATB explosive is known to have easily accessed slip planes. A generalization to a Bodner-Partom visco-plasticity model is used in MATCH. A discussion of the model is provided in Chapter 2 and the procedure for fitting the flow model to PBX 9502 is given in Chapter 5 of the MATCH-PAGOSA Manual.

## 16.3 MATCH-Hotspot

- **Sub-scale Ignition Model:** MATCH uses a sub-scale model, Hotspot, to determine the ignition threshold arising from localized heating of an explosive due to grain-scale phenomena like frictional heating of micro-cracks. It is based on the Frank-Kamenetskii (FK) thermal explosion model. The Hotspot ignition criterion is based on the micro-burn fraction reaching a user-specified value, *bf\_crit*. Hotspot also contains an approximate method for including the effects of phase transformation (for example, the solid-solid HMX phase transformations in PBX 9501). The ignition theory is described in Chapter 6 of the MATCH-PAGOSA Manual[\[72\]](#). The formalism linking the sub-scale model to the macroscopic Pagosa element level is described in Chapter 7 of the MATCH-PAGOSA Manual[\[72\]](#). At the present time, the chemical kinetics of the explosive is captured by a single Arrhenius exponential. Future releases of MATCH will include the full Henson-Smilowitz chemical kinetics model, briefly



summarized in Chapter 10 of the MATCH-PAGOSA Manual[72]. After *bf\_crit* is reached, Hotspot is no longer called for that Lagrangian point.

## 16.4 DEFLAGRATE

- Deflagration Model: Upon Hotspot ignition threshold *bf\_crit* being reached, a damage-modified pressure-dependent deflagration model, DEFLAGRATE, is called. The VPS calculated damage, reflecting the increased surface area of a cracked explosive, is passed by MATCH to DEFLAGRATE. Damage enhances the burn rate, consistent with experimental observations. DEFLAGRATE returns the deflagration macro-burn fraction. If the user is concerned with ignition only, then a call to DEFLAGRATE can be effectively disabled by setting the fifth burncon entry to zero (*P\_prefct=0*). DEFLAGRATE is a full explosive reactive burn calculation requiring a call to JWL-HE.

## 16.5 MATCH-BURN-DEFLAGRATE-SURF (future PAGOSA release)

- Detonation Model: According to the physics from which the SURF[73] model is based, for a detonation to occur a shock of significant strength is first required. This shock can arise directly from a high velocity impact of an explosive by an inert impactor (for example) or from sympathetic detonation of adjacent explosives (one detonating). It can also arise in the region of the unburnt explosive from the compression wave caused by a rapidly expanding deflagrating explosive, *via* the shocking-up process, *i.e.* DDT. MATCH must anticipate all these processes as being possible. IF statements in the MATCH-BURN Fortran attempt to properly assign these possibilities. According to SURF, if the shock is weak, the explosive will desensitize, and will not detonate upon being re-shocked, thus prohibiting future calls to SURF. However, a desensitized explosive may still deflagrate, and thus MATCH and MATCH-BURN must be called in subsequent cycles. SURF, described elsewhere[73], has two components: the shock detector and surf-burn algorithms. In MATCH-BURN each of these algorithms are called. The necessity to bundle SURF and Deflagrate in MATCH-BURN is that Pagosa only allows a single call to a HE burn model for each material explosive. A flow chart containing MATCH and MATCH-BURN is provided in Chapter 8 of the MATCH-PAGOSA Manual.



## Chapter 17

# Fracture and damage

*“I lose my temper, but it’s all over in a minute,” said the student. “So is the hydrogen bomb,” I replied. “But think of the damage it produces!”*

– Spencer Tracy (1900 – 1967)

The main objectives when modeling fracture/damage are to predict where the fracture/damage will occur (see Rinehart and Pearson[74] for an introduction of fracture under impulsive loading).

The fracture and damage models are able to describe the initiation and propagation of these properties. PAGOSA possesses two models for fracture and damage: (1) the Johnson spall model for investigating the ductile hole growth for materials under tensile stresses and (2) The Johnson-Cook (J-C) damage model for investigating the fracture characteristics of metals under impulsive loads. The J-C damage model predicts fracture from dynamic loading conditions. The formulation is similar in form to the flow-stress model described in subsection 15.4.4

The Johnson spall model predicts the growth of porosity (distension) in a material. One of the simplest forms of mechanical spalling is the plate impact: two waves of compression are reflected on the free-surfaces of the plates; they then interact to generate a region of high-tension stress inside one of the plates. Voids are not created by PAGOSA. However, the region of spallation and its volume can be estimated.

## 17.1 Johnson spall[75]

The amount of spall with this model is described by a distention ratio  $\alpha$ . If the solid volume of a material (with all the pores removed) is defined as  $V_0$  and the actual volume of the material (with pores) is  $V$ , then the distention ratio is defined as

$$\alpha \equiv \frac{V}{V_0} \quad (17.1)$$

In terms of porosity, we have

$$\phi = \frac{\alpha - 1}{\alpha} \quad (17.2)$$

The ductile void growth can be described by a model that relates the pressure  $P$  and the distention ratio  $\alpha$ . The equilibrium  $P$ - $\alpha$  curve is given by

$$P_{eq} = -\frac{2}{3} \frac{Y}{\alpha} \ln \left( \frac{\alpha}{\alpha - 1} \right) \quad (17.3)$$

If the pressure is negative and below the pressure determined from the equilibrium curve for a given  $\alpha$ , then voids will grow. Otherwise, the distention ratio will not be allowed to increase any further. It is important to note that the value of the distention ratio  $\alpha$  must be greater than or equal to one. Also, for void growth to begin, the initial distention ratio of a material must be slightly greater than one. For example, the initial distention ratio for oxygen-free, high-conductivity (OFHC) copper[75, 2821] has a value of 1.0003.

The time evolution of the distention ratio is given by integrating the rate[75, 2871. Eq. 32] equation as

$$\dot{\alpha} = \begin{cases} 0 & \Delta p \geq 0 \\ -\left(\frac{1}{\eta}\right)(\alpha_0 - 1)^{2/3} \alpha (\alpha - 1)^{1/3} & \Delta p < 0 \end{cases} \quad (17.4)$$

$$\Delta p \equiv P + \frac{\alpha_s}{\alpha} \ln \frac{\alpha}{\alpha - 1} \quad (17.5)$$

where the constant  $\alpha_s$  has replaced  $2/3Y$ ,  $P$  is the material pressure,  $\eta$  is a coefficient relating to the resistance to plastic flow void growth, and  $\alpha_0$  is the initial distention ratio.

The yield and shear moduli are modified to reflect the evolving porosity in the material. The moduli are modified above the threshold stress value of  $\Delta p > 0$ . Then

$$Y \rightarrow \frac{Y}{\alpha} \quad (17.6)$$

$$G \rightarrow G(1 - \phi) \left( 1 - 2\phi \frac{4 - 5\nu}{7 - 5\nu} \right) \quad (17.7)$$

where  $\nu$  is the Poisson ratio of the fracture material. The form of the shear modulus is attributed to Mackenzie.[76]. The Johnson spall model may be used with any flow-stress model described in [Chapter 15 \(subsection 15.4.1 to subsection 15.4.7\)](#)

The Johnson spall model requires four inputs:  $\alpha_0, \alpha_s, \mu$ , and  $\nu$ .

The formulation restricts the Poisson ratio to values of  $1/5 < \nu < 1/2$

## 17.2 Johnson-Cook damage[77]

The damage in the cell is defined as

$$D \equiv \int_{t_0}^t \frac{\varepsilon^n}{\varepsilon^f} dt \rightarrow \sum_{n=0}^N \frac{\Delta \varepsilon^n}{\varepsilon^f} \quad (17.8)$$

where  $\Delta \varepsilon$  is the increment of equivalent plastic strain that occurs in one integration step and  $\varepsilon^f$  is the equivalent strain at fracture. Fracture occurs when  $D = 1.0$ .

The general expression for the strain at fracture is given by Johnson and Cook[77, p. 40, Eq. 3] as

$$\varepsilon^f = [D_1 + D_2 \exp(D_3 \sigma^*)][1 + D_4 \ln \dot{\varepsilon}^*][1 + D_5 T^*] \quad (17.9)$$

where

- $\sigma^*$  the dimensionless stress ratio,  $\sigma^* = \frac{\sigma_m}{\bar{\sigma}}$  for  $\sigma^* \leq 1.5$
- $\sigma_m$  the average of the normal stresses
- $\bar{\sigma}$  the von Mises equivalent stress
- $\dot{\varepsilon}^*$  the dimensionless strain rate,  $\dot{\varepsilon}^* = \frac{\dot{\varepsilon}}{\dot{\varepsilon}_0}$  with  $\dot{\varepsilon}_0 \equiv 1.0\text{s}^{-1}$
- $T^*$  the homologous temperature,  $T^* = \frac{T - T_{room}}{T_{melt} - T_{room}}$

The J-C damage model can be used with any flow-stress model described in [Chapter 15 \(subsection 15.4.1 to subsection 15.4.7\)](#)

The J-C damage model requires 10 material inputs:  $D_1, D_2, D_3, D_4, D_5, e_{room}, e_{melt}, p_{fail}$ , and damage level

The spall stress  $p_{fail}$  is an experimentally determined value for this model. The strain makes a transition ( $\varepsilon_{min}^f$ ) from [Equation 17.9](#) to a linear expression before spalling occurs.[77, p.46, Fig. 15] The damage threshold (damage level) is the value of  $D$  at the onset of damage (usually set to a value of 1.0, as stated above).



## Chapter 18

# Crush

*Obstacles cannot crush me. Every obstacle yields to stern resolve.*

– Leonardo da Vinci (1452 – 1519)

The  $P$ - $\alpha$  crush model is based on the published version in the CTH Eulerian code used at Sandia National Laboratories.[78] The model originally was proposed by Hermann[79] as a simple way to describe the compaction of pores in a material.

The model uses a distention ratio variable, defined as

$$\alpha = \frac{\rho_s}{\rho} \quad (18.1)$$

where  $\rho_s$  is the density of the solid material and  $\rho$  is the macroscopic material density. The equation of state (EOS) of the porous material is determined from the EOS of the regular solid material as

$$P(\rho, E, \alpha) = \frac{1}{\alpha} P_s(\rho_s, E) = \frac{1}{\alpha} P_s(\alpha \rho, E) \quad (18.2)$$

The  $1/\alpha$  factor ensures thermodynamic consistency for the EOS. This improvement in the crushing model was originally suggested by Carroll and Holt.[80] The crushing behavior (that is, the evolution of the distention ratio in time) is dependent on the pressure.

It is assumed that the material starts out at an initial distention ratio  $\alpha_0$ :

$$\alpha_0 = \frac{\rho_{s0}}{\rho_0} \quad (18.3)$$

where  $\rho_{s0}$  is the reference density of the solid matrix and  $\rho_0$  is the initial density of the porous material. An initial elastic region exists up to a pressure  $P_e$ , in which if the pressure is relieved, the distention ratio will return to its initial value.

The actual compaction region starts at the pressure  $P_e$  and all voids are crushed out (that is numerically,  $\alpha = 1$ ) when the pressure reaches  $P_s$ . The maximum allowed distention ratio for a given value of pressure between those two pressures is given by

$$\alpha_{max}(P) = 1 + (\alpha_e - 1) \left( \frac{P_s - P}{P_s - P_e} \right)^2 \quad \text{for } P_e < P < P_s \quad (18.4)$$

Crushing as a function of time follows the pressure history according to

$$\dot{\alpha} = \frac{d\alpha}{dt} = \frac{d\alpha}{dP} \frac{dP}{dt} = \alpha_p \dot{P} \quad (18.5)$$

As the material compacts, if the pressure is suddenly decreased at any point, the material will behave elastically (reversibly) until the pressure again increases to the maximum pressure for a given distention ratio. Release and recompression behaviors are reversible until all pores are crushed out. (The term “reversible” in this case has nothing to do with the strength model; it is only relevant to the behavior of the  $P$ - $\alpha$  model. However, as an aside, a  $P$ - $\alpha$  material may also have strength.)

When material is compacting, the change in distention ratio with respect to pressure is given by

$$\alpha_P = \frac{d\alpha_{max}(P)}{dP} = -2 \frac{(\alpha_0 - 1)(P_s - P)}{(P_s - P_e)^2} \quad \text{for } \alpha = \alpha_{max} \text{ and } \dot{P} > 0 \quad (18.6)$$

In the elastic region, the change in distention ratio with respect to pressure is given by

$$\alpha_P = \alpha^2 \left( 1 - \frac{1}{h^2} \right) \quad \text{for } \alpha < \alpha_{max} \text{ and/or } \dot{P} < 0 \quad (18.7)$$



where

$$h \equiv 1 + \frac{c_e - c_s}{c_s} \frac{\alpha - 1}{\alpha_0 - 1} \quad (18.8)$$

The sound speed for the fully dense solid is given by  $c_s$ , and that for the elastic region of the porous material is  $c_e$ . These values are input constants for the material and model in the code and are generally obtained from experimental data.

The distention ratio parameter must be advanced in time in the Lagrangian phase of the code and must be advected in the advection phase. However, in the advection phase, the distention ratio is converted to porosity, which is then advected and subsequently converted into a distention ratio. The model is fairly sensitive to the timestep. In fact, an internal subcycling occurs to advance the distention ratio in time in the Lagrangian phase in smaller steps. This subcycling can be controlled by the user. However, even the overall timestep may need to be reduced to ensure that a simulation does not go unstable. In addition, to be even more conservative, the user should specify that there be only one Lagrangian cycle per advection step.

A  $P$ - $\alpha$  model requires six material inputs:  $\alpha_0$ ,  $P_e$ ,  $P_s$ ,  $c_e$ ,  $c_s$ , and  $\nu$ , where

- $\alpha_0$  the initial distention ratio
- $P_e$  the pressure at end of the elastic region
- $P_s$  the pressure at which all pores are crushed out
- $c_e$  the sound speed in the elastic region
- $c_s$  the sound speed of the fully dense solid, and
- $\nu$  Poisson's ratio

The shear modulus  $G$  and yield modulus  $Y$  can be modified by the distention ratio. This option modifies the moduli by

$$Y \rightarrow \frac{Y}{\alpha} \quad (18.9)$$

$$G \rightarrow G(1 - \phi) \left( 1 - 2\phi \frac{4 - 5\nu}{7 - 5\nu} \right) \quad (18.10)$$

where the porosity is computed from the distention ratio [i.e.,  $\phi \equiv (\alpha - 1)/\alpha$ ].

The SESAME EOS ramp treatment (see [subsection 7.7.1](#)) *cannot* be used simultaneously with the crush model. The two forms of handling porosity are inconsistent with one another.



## Chapter 19

# FLIP + MPM

*Empty space is a boiling, bubbling brew of virtual particles that pop in and out of existence in a time scale so short that you can't even measure them.*

– Lawrence M. Krauss

## 19.1 Overview

The name FLIP+MPM is an acronym of “FLuid Implicit Particle + Material Point Method.” In this method, Lagrangian particles<sup>1</sup> are added to an Eulerian code (such as PAGOSA), thereby introducing the capability for a full stress history of a material, which in turn allows for tracking the dynamic evolution of damage.

With the introduction of these particles, simulations are said to be carried out in a “mixed frame,” i.e., materials are represented by a combination of Lagrangian particles and the Eulerian cells native to the host code.

By introducing particles within the native Eulerian mesh, advection errors typical in Eulerian simulations may be minimized. The Eulerian mesh is leveraged as a computational scratch pad for calculating gradients, which are then used to update state data on the particles. [81].

Additionally, each marker (or particle) has its own velocity allowing material separation and breakup to be simulated with higher fidelity. Contact between materials is handled using a variety of momentum exchange options that also allow for handling failed material. This type of behaviour cannot be realized with Eulerian codes that typically employ cell averaged velocities, where each cell may be host to several materials.

FLIP+MPM has a history of development in LANL’s Theoretical division, with roots in the particle in cell (PIC) methods, first developed in the 1950’s. Development of the FLIP code by Brackbill [82] was mainly used for fluid dynamics.

An extension of the method to include solid materials was formulated in the 1990’s by Sulsky, [83] and the Material Point Method (MPM) was born. This method carried along with it a stress history, and was adopted as a modeling option within PAGOSA in 2018, largely to make use of the method’s predictive fragmentation capability.

## 19.2 Governing equations

We are solving a subset of the general multifield equations for compressible materials, some of which may be fluids and some of which may be solids, with an arbitrary equation of state, and some history-dependent stress. The numerical method is a combination of the FLIP scheme, [82] the Material Point Method, [83] and the numerical techniques used to solve the Navier-Stokes equations, as outlined in the earlier chapters of this Theory Manual. The physics of FLIP+MPM has been described in great detail in FLIP Recipes, [84] and we summarize the key features here.

In FLIP+MPM terminology, a “field” is a particle type. For example, a simulation of HE + steel casing + target plate could have three different materials, with the HE treated as a purely Eulerian material, and the steel and target plates treated as FLIP materials. In such a simulation, there will be two “fields” of FLIP material, one representing the steel casing, and the other representing the target.

The description of the state at the markers (or particles) of field  $r$  is a collection of state variables representing their masses ( $m_r$ ), positions ( $\mathbf{x}_r$ ), velocities ( $\mathbf{v}_r$ ), internal energies ( $e_r$ ), specific volumes

---

<sup>1</sup>Particles are also referred to as material points, or markers

( $v_r$ ), stresses ( $\sigma_r$ ) and, depending upon the constitutive model, several material-dependent history variables (\*).

The governing equations below, where bold symbols refer to vector quantities, are finite difference update schemes for each Eulerian cell for position (Equation 19.1), velocity update/conservation of momentum (Equation 19.2), conservation of energy (Equation 19.3), conservation of mass (Equation 19.4), and updates of history variables and internal energy (Equation 19.5).

$$\Delta \mathbf{x}_r = \Delta t \mathbf{u}_r \quad (19.1)$$

$$\rho_r \Delta \mathbf{u}_r = \Delta t [-\theta_r \nabla p + \sum_s \mathcal{K}_{rs} (\mathbf{u}_s - \mathbf{u}_r)] + \rho_r \Delta_\rho \mathbf{u}_r \quad (19.2)$$

$$\rho_r (\Delta e_r + p \Delta v_r) = \Delta t [-\nabla_r \cdot \mathbf{j}_r + \sigma_r : \dot{\epsilon}_r] \quad (19.3)$$

$$\rho_r \Delta v_r = (\theta_r \beta_r \Delta T_r - f_r^\theta \sum_s \theta_s \Delta T_s) + \Delta t [f_r^\theta \nabla \cdot \mathbf{u}] \quad (19.4)$$

$$\sigma_i \rightarrow \sigma_i + \Delta t \Psi[\sigma_i, \nabla_i, T_i, *i] \quad (19.5)$$

In these equations,  $\Psi$  is a material model that controls the evolution of stress and the history variables, while  $\mathcal{K}_{rs}$  is the momentum exchange rate between materials (fields)  $r$  and  $s$ . Similarly,  $\theta_r$  is the volume fraction of material  $r$ , while  $\beta_r$  is its expansivity. Finally,  $f_r^\theta$  is defined as the product of material  $r$ 's compressibility and volume fraction divided by the total sum of each material's product of compressibility and volume fraction.

Given a set of initial and boundary values, and the equations of state associated with the material fields  $r$ , the state of the system at the cells is evolved per Equation 19.1 – Equation 19.4.

### 19.3 Algorithm for Mapping/Interpolation

Since FLIP+MPM uses equations that exist on both Eulerian cells and Lagrangian markers, a mapping must exist to connect the two descriptions. This is achieved by the use of tri-linear interpolation<sup>2</sup> involving the use of weighting (or shape) functions  $\mathcal{S}_{ic}$ , such that the following equations hold true:

$$\mathbf{x}_i = \sum_c \mathcal{S}_{ic} \mathbf{x}_c \quad (19.6)$$

$$\sum_c \mathcal{S}_{ic} = 1 \quad (19.7)$$

where the index  $i$  refers to a particle, and  $c$  refers to a cell.

For example, the total mass  $M_{cr}$  of field  $r$  in cell  $c$  can be mapped from the mass  $m_{ir}$  of field  $r$  on markers  $i$  by:

$$M_{cr} = \sum_i \mathcal{S}_{ic} m_{ir} \quad (19.8)$$

---

<sup>2</sup>The word interpolation may be used interchangeably with mapping. Use of the word “interpolation” in this context could be considered an abuse of terminology, but its use can be argued when the mapping between marker and cell are considered in a purely spatial sense.

The inverse mapping, from cell to marker, is also necessary. For instance, temperature from the cells  $c$  of field  $r$  may be mapped to marker  $i$  by:

$$T_{ri} = \sum_c \mathcal{S}_{ic} T_{rc} \quad (19.9)$$

The details of the weighting functions  $\mathcal{S}_{ic}$  depend on the data being mapped. Vertex centered data (e.g. velocity) is mapped from the markers to the vertices using linear interpolants, carrying first-order accuracy and weighting functions. The bulk of the data in PAGOSA, however, is cell-centered. A “Poor-man’s Second Order” approach is employed for the interpolation of these data. In this approach, cell-centered data, such as internal energy, are initially mapped linearly from the markers to the vertices, and then gathered from the vertices to the cell centers, using a second linear mapping. This effectively distributes the marker quantities to cells in their spatial neighborhoods. This is done for cell-centered quantities with the caveat that in the case of a material boundary (where an adjacent cell contains no mass of the marker’s material), a zeroth-order, nearest gridpoint method is imposed (rather than a Poor-man’s Second Order approach), assigning all of that marker quantities to the cell in which it resides.

Figure 19.1 shows a 2-D example of a single marker’s weights being calculated during the mapping to surrounding cells,  $\mathcal{S}_{ic}$ . In this example, a marker coincides exactly with a cell’s center, and the weights are first scattered to the four cell vertices,  $\mathcal{S}_{iv}$ , and then once again from the four vertices to the nine cell centers with weights  $\mathcal{S}_{vc}$ . In the 3D-case, there will be eight vertices and 26 cells to which the weights would be scattered.

Mathematically, the final weights for each cell can be written as the sum of the products the two weights, or:

$$\mathcal{S}_{ic} = \sum_v \mathcal{S}_{vc} \mathcal{S}_{iv} \quad (19.10)$$

This “poor-man’s” approach is used to avoid the computational overheads of a true second-order method, while reducing the noise that is introduced in a zeroth order “nearest gridpoint” approach. While it is technically a first-order method, it has the footprint of a second-order method.<sup>3</sup>

The inverses of the aforementioned mappings are used to map the cell/vertex data back to the markers. These inverse mappings can be thought of as a gathering of grid contributions to the markers, as opposed to the scattering that occurred in the marker-to-vertex-to-cell mapping described above. In the cell-centered case, the cell data is first distributed to the appropriate vertices, and then gathered to the markers. Such mapping schemes are used extensively throughout PAGOSA’s implementation of FLIP+MPM and are fundamental in the bookkeeping that must occur in the symbiotic relationship between the two data structures.

## 19.4 FLIP+MPM Recipe

The main FLIP+MPM algorithm can be broken down into three steps:

---

<sup>3</sup>In this context, “footprint” means the same number of cells used for a second order method, as indicated by the yellow dashed lines in Figure 19.1

$$\mathcal{S}_{ic} = \sum_v \mathcal{S}_{vc} \mathcal{S}_{iv}$$

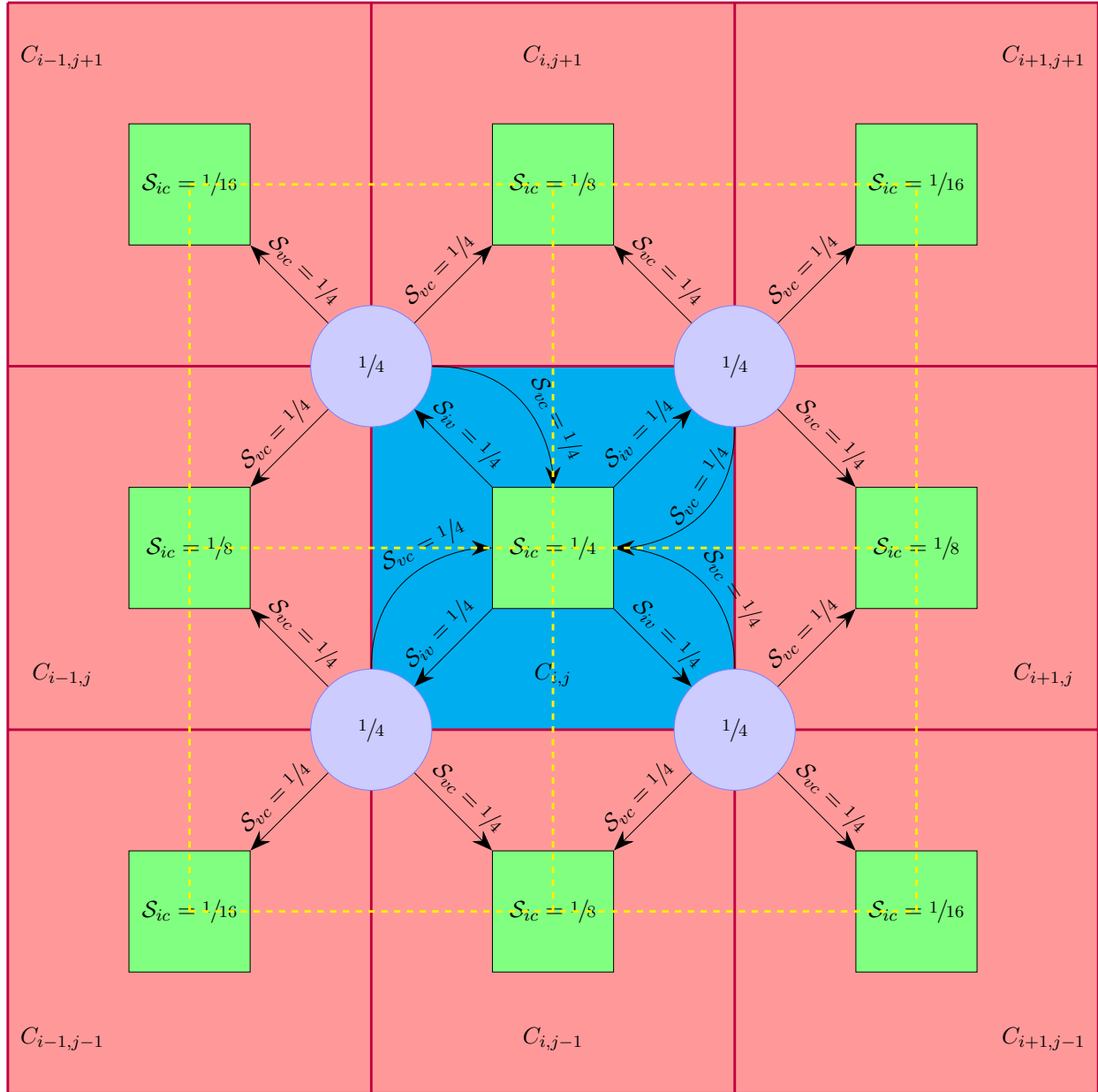


Figure 19.1: Schematic of a poor man's 2<sup>nd</sup> order weighting of a cell centered particle that is scattered to the surrounding cells. While the particle is not shown, it is at the center of the middle cell. The yellow dashed lines refer to the “footprint” discussed in the text.

### 19.4.1 Step I. Map Marker Quantities to Cells and Evaluate EOS

In the first step, *some* of the state data  $\{\rho_r, \mathbf{u}_r, e_r, v_r, p, T_r\}_c$  on markers belonging to field  $r$  markers are mapped to the cells/vertices  $c$  belonging to the Eulerian mesh. This mapping is achieved using the previously described tri-linear interpolation, and update/overwrites the PAGOSA state data stored on the mesh with the marker data. The remaining state data  $\{\sigma_r, *_r\}$  need not be mapped to the grid. The equation of state is evaluated on the cells on a field-wise basis, where the changes in pressure and fieldwise temperature are calculated.

In order to achieve the stress and history variable update, represented by Equation 19.5, it is necessary to map  $p_i$ ,  $T_{ri}$ , and  $\nabla \mathbf{u}_{ri}$  onto the markers, as per equation Equation 19.9.

### Step II. Calculate Changes in State Quantities on the Cells

In the second step, gradients on the Eulerian grid are used to compute the changes in state for Equation 19.1 – Equation 19.4. The changes in internal energy, volume and velocity are calculated, and an update of  $\sigma_i$  and  $*_i$  is done on the markers. PAGOSA also conducts any finite rate momentum exchange that occurs between any pairs of materials that are user-specified for a particular type of momentum exchange. One of these materials must be FLIP material, while the other can be either cell-Eulerian or another FLIP material.

### Step III. Map Changes in State Quantities Back onto Markers and Update State

In the final step, changes in the state variables over time  $\Delta t$  for Equation 19.1 – Equation 19.4 are mapped to the markers, and used to update  $\mathbf{x}_i$ ,  $\mathbf{u}_i$ ,  $e_i$ , and  $v_i$ . Some bookkeeping is conducted which includes migrating a marker to a different processor, as well as the natural coordinates of the marker within the cell, which is used to calculate the weighting functions  $\mathcal{S}_{ic}$ . These three steps are exercised during each time step to update the state data on the particles.

## 19.5 Use within PAGOSA

The particles in a material utilizing FLIP+MPM, herein referred to as a FLIP material, have physics capabilities to represent solids or inviscid fluids in a given simulation. On one end of the spectrum, the user may choose to represent all materials in a simulation as FLIP materials (fully Lagrangian), while on the other end all of the materials may be treated with their native PAGOSA physics (fully Eulerian). Depending on the problem, it is typical to represent some materials as Eulerian and treat the others as FLIP materials — somewhere in the middle of the aforementioned spectrum.

In either of these cases, since the native Eulerian background mesh is utilized, the FLIP materials carry an additional computational expense, both in terms of memory requirements as well as additional computations. The choice of assigning a material as a FLIP material or an Eulerian material is very problem-specific. Typically, users assign FLIP materials as those where large deformations, material damage, or momentum transfer are a key part of the problem, while leaving the others as Eulerian materials.



When a FLIP material is chosen to be part of a PAGOSA simulation there are many modeling options that must be considered. These are covered in detail in the Pagosa Input Reference manual [19]. Some of the crucial modeling options include initial marker density and locations (typically specified on a per-material basis), which materials to treat as FLIP materials, choosing what type of physics (inert, inviscid fluid, or solid with strength) should be exercised on a material's markers, options to handle momentum exchange between pairs of materials, and how to handle a marker that has failed (become fully damaged according to the fracture type chosen).

## 19.6 Additional Features

Besides introducing the FLIP+MPM particle treatment of materials, assigning `DoPlus = .true.` activates several additional significant departures from the standard PAGOSA simulation. For all materials, a tensor viscosity method [85] is used to calculate the changes to internal energies, densities, velocities and viscosities on the cells. This occurs during step II, and overrides any calculations that PAGOSA has made for these updates. Additionally, an MGGB multiple-material closure algorithm [86] is used to update the pressure, avoiding PAGOSA's native closure models. This process is used for all materials when `DoPlus = .true..` This can be found embedded in the governing Equation 19.4, expressing the conservation of mass, where  $f_r^\theta$  is the material's compressibility.

Paramount to FLIP+MPM's purpose in Pagosa is the dynamic evolution of failed and fragmented materials. Because each FLIP field has its own velocity, it is able to separate from other materials, as dictated by their momentum. Furthermore, several novel options are available when a material fails. One option allows the marker, and its mass, to simply be removed from the simulation. Another option allows for the mapping of the marker, along with its mass, to another material, (i.e. a dummy material with no shear strength). Perhaps the most physically accurate option allows the failed marker's mass, along with its thermodynamic and kinematic quantities, to be mapped to the surrounding markers.



# Appendices



# Appendix A

## Constitutive equations

We assume that the deviatoric stress rates are a linear function of the velocity gradients.[\[87, 88\]](#) In tensor notation,

$$\dot{S}_{ij} = A_{ijkn} \frac{\partial u_k}{\partial x_n} \quad i, j, k, n = x, y, z \quad (\text{A.1})$$

where  $A_{ijkn}$  is an arbitrary fourth-order tensor. First decompose the gradient into its symmetrical and antisymmetrical parts:

$$\frac{\partial u_k}{\partial x_n} = \dot{e}_{kn} + \Omega_{kn} = \dot{e}_{kn} - \frac{1}{2} \pi_{knm} \omega_m \quad (\text{A.2})$$

where  $\pi_{knm}$  is the Levi-Civita pseudotensor.[\[89\]](#) Assume that the  $A_{ijkn}$  tensor is isotropic:[\[90\]](#)

$$A_{ijkn} = G \delta_{ik} \delta_{jn} + G' \delta_{in} \delta_{jk} + G'' \delta_{ij} \delta_{kn} \quad (\text{A.3})$$

where  $G, G', G''$  are scalar coefficients. The tensor  $A_{ijkn}$  is symmetrical in the indices  $i$  and  $j$  because the stress deviator is symmetrical in these indices. This symmetry implies that  $G' = G$ . The tensor is also symmetrical in the indices  $k$  and  $n$ . This symmetry results in the antisymmetrical portion of [Equation A.2](#) vanishing (i.e.,  $\pi_{knm} = \mathbf{0}$ ):

$$\dot{S}_{ij} = G \dot{e}_{ij} + G \dot{e}_{ji} + G'' \delta_{ij} \dot{e}_{kk} = 2G \dot{e}_{ij} + G'' \delta_{ij} \dot{e}_{kk} \quad (\text{A.4})$$

The stress deviator tensor is traceless, and its derivative is also traceless. Thus,

$$\dot{S}_{ii} = 2G \dot{e}_{ii} + 3G'' \dot{e}_{ii} = (2G + 3G'') \dot{e}_{ii} = 0 \quad (\text{A.5})$$

Therefore, the isotropic constitutive relation for deviatoric stress and the linearly elastic small strains are

$$\dot{S}_{ij} = 2G \left( \dot{e}_{ij} - \frac{1}{3} \delta_{ij} \dot{e}_{kk} \right) = 2G \left( \dot{e}_{ij} - \frac{1}{3} \delta_{ij} \nabla \cdot \mathbf{u} \right) \quad (\text{A.6})$$

[Equation A.6](#) can be integrated in time. The constant of integration is zero, implying the physical argument that no strains implies no stress.



## Appendix B

# Initial volume fraction calculation

The initial volume fractions  $^{(m)}\phi$  for each material are determined by sampling each Eulerian cell.[91] If a cell contains no interfaces, then the cell is called a pure cell and contains only a single material. The volume fractions are zero for all materials, except for one that has a value of unity. Most of the cells in an Eulerian simulation are pure.

If a cell contains more than one material, then that cell is selected for further sampling. This first sampling pass seeks to identify the multi-material (mixed) cells and is the coarse particle sampling. A second pass of sampling actually determines the numerical approximation for the value of the volume fractions for each material in the mixed cells and is the fine-particle sampling.

Consider the example of a multi-material cell shown in **Figure B.1**. If a  $4 \times 4$  array of sampling particles is distributed<sup>1</sup> in the cell, then the first sampling pass would identify the cell as mixed. The second pass, using the same sampling density, would conclude that the material volume fractions

---

<sup>1</sup>In the original version of PAGOSA (circa 1992), the sampling particles were distributed randomly. However, it was found that symmetries were broken by using this method. A symmetric body would have more mass on one side of the symmetry plane than the other.

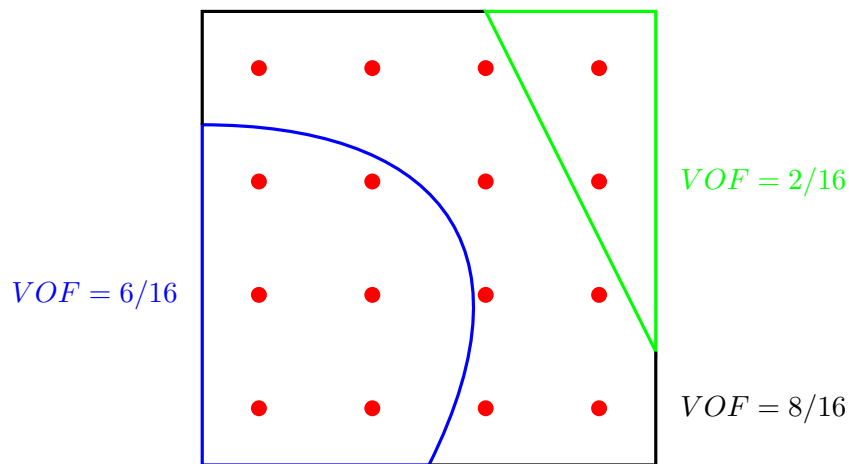


Figure B.1: Volume fractions of a mixed cell containing three materials (four interfaces).

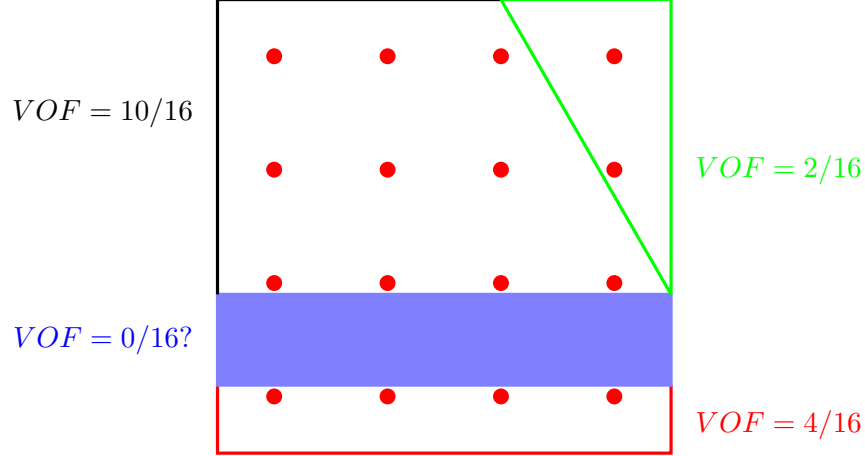


Figure B.2: A pathological case where some materials can go missing from a cell.

are

$$(\text{material1})\phi = \frac{6}{16}, \quad (\text{material2})\phi = \frac{8}{16}, \quad (\text{material3})\phi = \frac{2}{16}$$

A different sampling density would result in different initial volume fractions. The user is responsible for deciding the cell size, coarse- and fine-sampling densities, and what features are important to capture in the initial geometry of the simulation.

Each material in the cell possesses an interface. For example, in Figure B.1, the first material has an interface represented by the blue line. The second material has two interfaces: the green line and the blue curve. The third material has a single interface represented by the green curve. In total, four interfaces are shown in Figure B.1.

The curved surfaces of the input body definitions will be represented by planes in each cell. Each material interface in a cell is represented by a plane (see Appendix C). Therefore, a part of the geometry information is lost in the surface reconstruction algorithm. Small features less than a cell thick can be represented using this technique. However, some pathological cases are of note.

Consider the case shown in Figure B.2, with four materials. In this case, one of the materials has an orientation and a thickness that escape detection by our sampling process. The cell would be identified as mixed during the coarse-particle sampling. However, only three of the four materials would be identified, which requires that the sampling density be chosen with some care and a detailed knowledge of the parts in the simulation.<sup>2</sup> The volume fractions for this sampling density are

$$(\text{material1})\phi = \frac{10}{16}, \quad (\text{material2})\phi = \frac{2}{16}, \quad (\text{material3})\phi = \frac{0}{16}, \quad (\text{material4})\phi = \frac{4}{16}$$

The thin layer of material (material 3) is missing, and the volume fraction for material 4 is also incorrect.

Doubling the fine-particle density (8 instead of 4) would capture part of the missing material and result in a better balance between the representations of materials 3 and 4. Clearly, a tradeoff

<sup>2</sup>The total mass could be numerically correct. However, the mass distribution could be wrong.



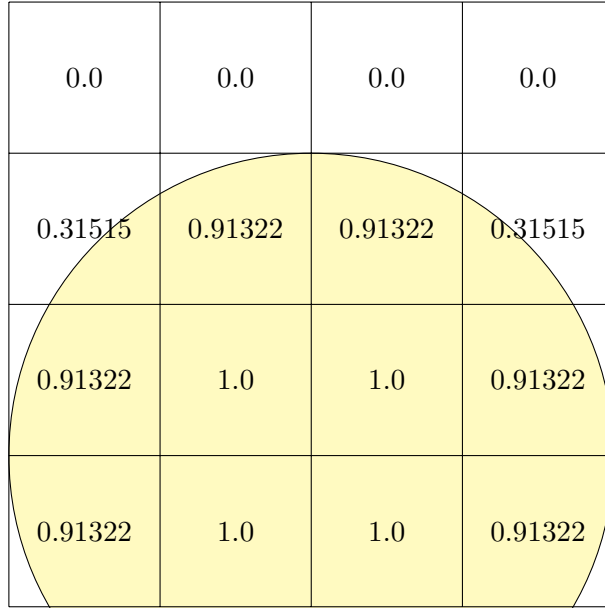


Figure B.3: Exact volume fractions and ideal interfaces. The ideal values for the volume fractions are 0.0%,  $\frac{1}{12}\pi$ ,  $\frac{\sqrt{3}}{4} + \frac{1}{4} \approx 31.51467\%$ ,  $\frac{1}{3}\pi + \frac{\sqrt{3}}{2} - 1 \approx 91.322295\%$ , and 100%.

between computation and simulation fidelity is evident. A higher density of sampling particles means a longer computation. Eventually, the user is faced with the situation of diminishing returns. The extra accuracy is not worth the computational effort.

This Monte Carlo technique is used to compute the initial volume fraction for a simulation. As the simulation proceeds, the volume fractions for each cell are recomputed based on the advection volumes (see [Chapter 5](#) and [Appendix E](#) for details about the advection algorithm).

Finally, a numerical example of the particle sampling technique is shown in [Figure B.3](#) and [Figure B.4](#). An offset circle is placed in a uniform  $4 \times 4$  Eulerian mesh. The exact volume fractions and ideal interfaces are shown in [Figure B.3](#).

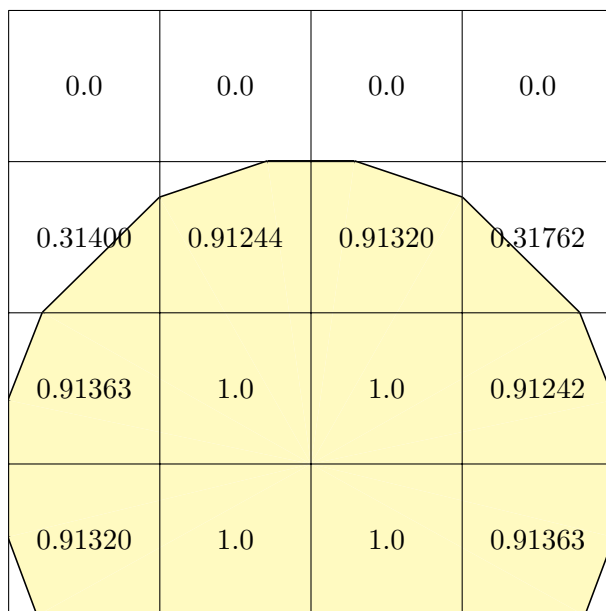


Figure B.4: Reconstructed interfaces and volume fractions based on the PAGOSA initial volume fraction algorithm with a small sampling density.

# Appendix C

## Youngs interface reconstruction

The following is based on publication LA-UR-07-2274.[\[17\]](#) The complete derivation is presented in that document.

### C.1 Analytic geometry

Consider the equation of a plane in Cartesian  $\mathbb{R}^3$  space:

$$\mu_1 x + \mu_2 y + \mu_3 z - \rho = 0 \tag{C.1}$$

Define the following quantities:

direction vector  $\boldsymbol{\mu} \equiv (\mu_1, \mu_2, \mu_3)$ , and  
distance parameter  $\rho$

The sense of  $\boldsymbol{\mu}$  and the sign of  $\rho$  are not defined by the equation. For example, we could say that

$$-\mu_1 x - \mu_2 y - \mu_3 z - (-\rho) = 0$$

so that the direction of  $\boldsymbol{\mu}$  and the sign of  $\rho$  are reversed.

The direction cosines of the normal to the plane are

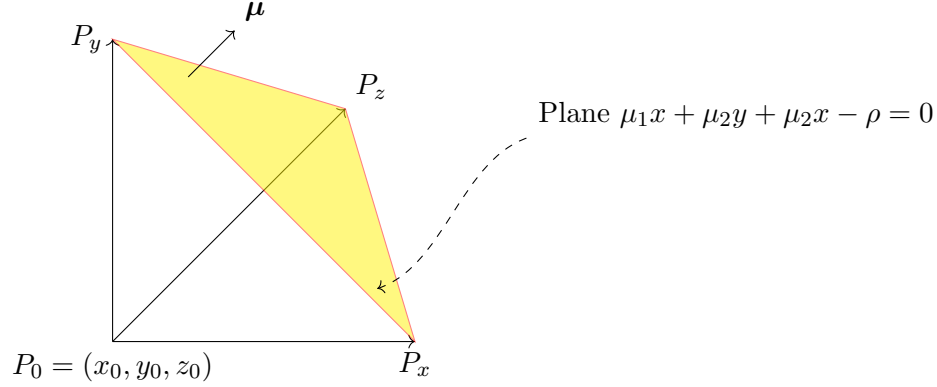
$$\frac{\mu_1}{\sqrt{\mu_1^2 + \mu_2^2 + \mu_3^2}}, \frac{\mu_2}{\sqrt{\mu_1^2 + \mu_2^2 + \mu_3^2}}, \frac{\mu_3}{\sqrt{\mu_1^2 + \mu_2^2 + \mu_3^2}} \tag{C.2}$$

and the distance from the coordinates' origin to the plane is

$$\frac{\rho}{\sqrt{\mu_1^2 + \mu_2^2 + \mu_3^2}} \tag{C.3}$$

**Equation C.1** divides all space into two regions. The direction vector points into the region “in front of the plane” and away from the region “in back of the plane.” Given a point  $\mathbf{x}_0 = (x_0, y_0, z_0)$ , then

- $\mathbf{x}_0$  lies *behind* the plane if  $\mu_1 x_0 + \mu_2 y_0 + \mu_3 z_0 - \rho < 0$
- $\mathbf{x}_0$  lies *in front of* the plane if  $\mu_1 x_0 + \mu_2 y_0 + \mu_3 z_0 - \rho > 0$

Figure C.1: Tetrahedron bounded by the  $(\boldsymbol{\mu}, \rho)$  plane

Suppose that  $\mathbf{x}_0 \equiv (x_0, y_0, z_0)$  is a point and  $(\boldsymbol{\mu}, \rho)$  is a plane. Define a right tetrahedron with vertices  $P_0, P_x, P_y, P_z$  as follows (see Figure C.1):

- Set  $\mathbf{P}_0 = (x_0, y_0, z_0)$
- Draw lines through  $P_0$  parallel to the  $x$ ,  $y$ , and  $z$  axes
- Define  $P_z =$  intersection of the  $z$  line with the plane

If  $P_z = (x, y, z)$ , then  $x = x_0$ ,  $y = y_0$ , and  $\mu_1 x_0 + \mu_2 y_0 + \mu_3 z - \rho = 0$ , so

$$z = \frac{\rho - \mu_1 x_0 - \mu_2 y_0}{\mu_3}$$

and

$$P_z = (x_0, y_0, \frac{\rho - \mu_1 x_0 - \mu_2 y_0}{\mu_3})$$

Similarly,  $P_x, P_y$  are the intersections of the  $x$  line and  $y$  lines into the plane, respectively, and

$$P_x = (\frac{\rho - \mu_2 y_0 - \mu_3 z_0}{\mu_1}, y_0, z_0),$$

$$P_y = (x_0, \frac{\rho - \mu_1 x_0 - \mu_3 z_0}{\mu_2}, z_0),$$

Define

$T_0 = 0$  if  $\mathbf{x}_0$  is in front of the plane

$T_0 =$  volume of the tetrahedron if  $\mathbf{x}_0$  is in the back of the plane

Then for  $\mathbf{x}_0$  in the back of the plane, the volume of the tetrahedron is[92]

$$T_0 = \frac{1}{3!} \overline{P_0 P_x} \times \overline{P_0 P_y} \times \overline{P_0 P_z}$$

or

$$T_0 = \frac{(\rho - \mu_1 x_0 - \mu_2 y_0 - \mu_3 z_0)^3}{|6\mu_1 \mu_2 \mu_3|} \quad (\text{C.4})$$

In this definition,

- $T_0$  is always  $\geq 0$
- $T_0 = +\infty$  if any one of  $\mu_1, \mu_2, \mu_3 = 0$ , which corresponds to the  $(\boldsymbol{\mu}, \rho)$  plane being parallel to one or more of the x, y, and z axes.
- $\mu_1, \mu_2, \mu_3, \rho$  can have any sign, but  $|\mu_1 \mu_2 \mu_3| \geq 0$
- The expression for  $T_0$  is unchanged under a (positive) scaling  $\mu_i \rightarrow \lambda^2 \mu_i, \rho \rightarrow \lambda^2 \rho$

## C.2 Distance parameter $\rho$

Consider a volume fraction  $v$  containing the origin and satisfying the relation

$$0 \leq v \leq \frac{1}{2}$$

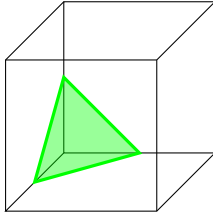
The case where  $1/2 < v \leq 1$  is obtained by symmetry (discussed below). The plane is described by the direction cosines  $(\mu_1, \mu_2, \mu_3)$ , which satisfy

$$0 \leq \mu_1 \leq \mu_2 \leq \mu_3 \quad \text{and} \quad \mu_1^2 + \mu_2^2 + \mu_3^2 = 1$$

The equation for the plane is  $\mu_1 x + \mu_2 y + \mu_3 z = \rho$  and has five different solutions for  $\rho(\boldsymbol{\mu}, v)$  which correspond to the five ways of slicing a cube with a plane.

The variable mask is logically true when a particular following case applies.

### Case 1: Triangular section



Triangular

Mask:

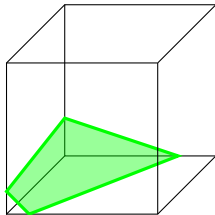
$$0 < v < v_1, \text{ where } v_1 \equiv \frac{\mu_1^2}{6\mu_2\mu_3} \text{ with } \mu_2 \neq 0$$

Solution:

$$\rho = [6\mu_1\mu_2\mu_3v]^{1/3} \quad (\text{C.5})$$

If  $\mu_1 = 0$ , then  $v = 0$ .

### Case 2: Quadrilateral section, type A



Quadrilateral A

Mask:

$$0 < v \leq v_2, \text{ where } v_2 \equiv \frac{\mu_1^2 + 3\mu_2(\mu_2 - \mu_1)}{6\mu_2\mu_3} \text{ with } \mu_2 \neq 0$$

Solution:

$$\rho = \frac{1}{2} \left[ \mu_1 + \sqrt{8\mu_2\mu_3v - \frac{1}{3}\mu_1^2} \right] \quad (\text{C.6})$$

There is no solution if  $\mu_2 = 0$ . And  $\mu_1 = 0$  is acceptable.

### Case 3: Pentagonal section

Mask:

$$\begin{aligned} v_2 < v \leq v_3 & \text{ if } \mu_1 + \mu_2 > \mu_3 \quad (\mu_1 \neq 0) \\ v_2 < v \leq v_4 & \text{ if } \mu_1 + \mu_2 \leq \mu_3 \end{aligned}$$

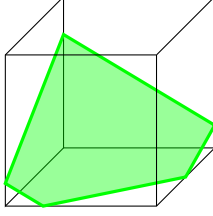
In this last mask, if  $\mu_1 = 0$ , then  $v_2 = v_4$  where

$$\begin{aligned} v_3 &= \frac{\mu_3^3 - (\mu_3 - \mu_1)^3 - (\mu_3 - \mu_2)^3}{6\mu_1\mu_2\mu_3} \\ v_4 &= \frac{\mu_1 + \mu_2}{2\mu_3} \end{aligned}$$

Solution:

$$\begin{aligned} \rho &= \mu_1 + \mu_2 - 2\sqrt{2\mu_1\mu_2} \cos \left[ \frac{\theta - 2\pi}{3} \right] \\ \text{where} \\ \theta &= \cos^{-1} \left[ \frac{3(\mu_1 + \mu_2 - 2\mu_3 v)}{4\sqrt{2\mu_1\mu_2}} \right] \end{aligned} \tag{C.7}$$

**Case 4:** Hexagonal section



Pentagonal

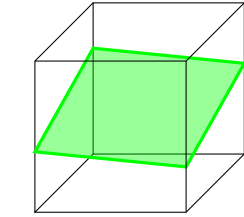
Mask:

$$v_3 < v \leq \frac{1}{2} \quad \text{if } \mu_1 + \mu_2 > \mu_3 \quad (\mu_1 \neq 0)$$

Solution:

$$\begin{aligned} \rho &= \rho_0 - 2\sqrt{\rho_0^2 - 1/2} \cos \left[ \frac{\theta - 2\pi}{3} \right] \\ \rho_0 &= \frac{1}{2}(\mu_1 + \mu_2 + \mu_3) = \rho(v = 1/2) \\ \theta &= \cos^{-1} \left[ \frac{3(\mu_1 + \mu_2 - 2\mu_3 v)}{4\sqrt{2\mu_1\mu_2}} \right] \end{aligned} \tag{C.8}$$

**Case 5:** Quadrilateral section, type B



Quadrilateral B

Mask:

$$v_4 < v \leq \frac{1}{2}, \text{ if } \mu_1 + \mu_2 \leq \mu_3$$

Both  $\mu_1 = 0$  and  $\mu_2 = 0$  are acceptable.

Solution:

$$\rho = \mu_3 v + \frac{1}{2}(\mu_1 + \mu_2) \tag{C.9}$$

### C.3 $\rho$ symmetry

For the case of  $\frac{1}{2} < v \leq 1$ , the solution is obtained by

$$\rho(v) = \rho_{max} - \rho(1 - v) \tag{C.10}$$

where

$$\rho_{max} = \mu_1 + \mu_2 + \mu_3$$

## C.4 Volume $v$

Given a vector  $\boldsymbol{\mu}$  normal to a plane passing through a unit cube and which need not be normalized but which satisfies

$$0 \leq \mu_1 \leq \mu_2 \leq \mu_3 \quad (\text{C.11})$$

and given  $\rho$ , where  $\rho/|\boldsymbol{\mu}|$  is the distance from the origin to the plane and which satisfies

$$0 < \rho \leq \frac{1}{2}\rho_{max} \quad (\text{C.12})$$

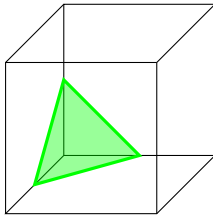
where

$$\rho_{max} \equiv \mu_1 + \mu_2 + \mu_3. \quad (\text{C.13})$$

the case of  $\frac{1}{2}\rho_{max} < \rho \leq \rho_{max}$  is obtained by symmetry (discussed below).

The volume fraction behind the plane that contains the origin has five different solutions corresponding to the five ways of a plane slicing a cube.

### Case 1: Triangular section



Triangular

Mask:

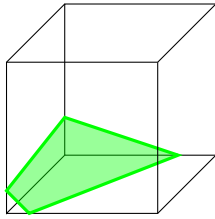
$$0 < \rho \leq \mu_1, \text{ where } \mu_1 > 0$$

Solution:

$$v(\rho) = \frac{\rho^3}{6\mu_1\mu_2\mu_3} \quad (\text{C.14})$$

If  $\mu_1 = 0$ , then  $v = 0$ .

### Case 2: Quadrilateral section, type A



Quadrilateral A

Mask:

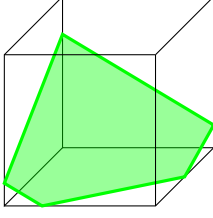
$$\mu_1 < \rho \leq \mu_2, \text{ where } \mu_2 > 0$$

Solution:

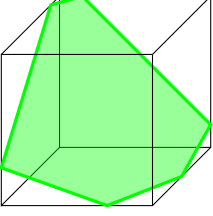
$$v(\rho) = \frac{3\rho^2 - 3\mu_1\rho + \mu_1^2}{6\mu_2\mu_3} \quad (\text{C.15})$$

There is no solution if  $\mu_2 = 0$ . And  $\mu_1 = 0$  is acceptable.

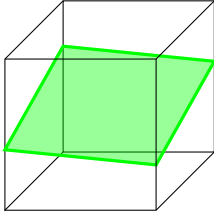
### Case 3: Pentagonal section



Pentagonal

**Case 4:** Hexagonal section

Hexagonal

**Case 5:** Quadrilateral section, type B

Quadrilateral B

Mask:

$$\mu_2 < \rho \leq \min(\mu_1 + \mu_2, \mu_3), \text{ with } \mu_1 > 0$$

Solution:

$$v(\rho) = \frac{\rho^3 - (\rho - \mu_1)^3 - (\rho - \mu_2)^3}{6\mu_1\mu_2\mu_3} \quad (\text{C.16})$$

Mask:

$$\mu_3 < \rho \leq \frac{1}{2}\rho_{\max}, \text{ if } \mu_1 + \mu_2 > \mu_3 \text{ and } (\mu_1 > 0)$$

Solution:

$$v(\rho) = \frac{\rho^3 - (\rho - \mu_1)^3 - (\rho - \mu_2)^3 - (\rho - \mu_3)^3}{6\mu_1\mu_2\mu_3} \quad (\text{C.17})$$

Mask:

$$\mu_1 + \mu_2 < \rho \leq \frac{1}{2}\rho_{\max} \text{ with } \mu_1 + \mu_2 < \mu_3$$

Solution:

$$v(\rho) = \frac{2\rho - (\mu_1 + \mu_2)}{2\mu_3} \quad (\text{C.18})$$

## C.5 $v$ symmetry

For the case of  $\frac{1}{2}\rho_{\max} < \rho \leq \rho_{\max}$ , the solution is obtained by

$$v(\rho) = 1 - v(\rho_{\max} - \rho) \quad (\text{C.19})$$

where

$$\rho_{\max} \equiv \mu_1 + \mu_2 + \mu_3 \quad (\text{C.20})$$



## Appendix D

# Lagrangian phase equation

Consider the expansion of a fluid. Let  $V$  be the volume of the fluid element, bounded by a surface  $S$ . Let  $S$  move with the fluid so that it always contains the same particles (i.e., a Lagrangian surface). Let  $\mathbf{u}$  be the velocity. Then  $\mathbf{u} \cdot \hat{\mathbf{n}}$  is the component of the velocity along the outward normal vector  $\hat{\mathbf{n}}$ . As the fluid moves, a point on the surface is displaced.

The Lagrangian equation for mass continuity<sup>1</sup> is given by

$$\frac{\partial \rho}{\partial t} + \rho(\nabla \cdot \mathbf{u}) = 0. \quad (\text{D.1})$$

The mass within the bounded surface  $S$  is  $m$ . The mass density of the material within the surface  $S$  is simply

$$\rho = m/Vol \quad (\text{D.2})$$

Substituting the expression for density into the continuity equation, we find that

$$-\frac{1}{Vol} \frac{\partial Vol}{\partial t} + \nabla \cdot \mathbf{u} = 0 \quad (\text{D.3})$$

This expression in a finite difference form is

$$\frac{1}{Vol^n} \frac{Vol^{n+1} - Vol^n}{dt} = (\nabla \cdot \mathbf{u})^{n+1/2}, \text{ or} \quad (\text{D.4})$$

$$Vol^{n+1} = Vol^n [1 + (\nabla \cdot \mathbf{u}) dt] \quad (\text{D.5})$$

where the superscripts refer to the  $(n)$  and  $(n + 1)$  timesteps. The cell may contain multiple materials, each with their own individual volumes. The Lagrangian volume is the sum of all those individual volumes. The entire cell volume evolves subject to the expression in [Equation D.5](#).

An alternate way of understanding [Equation D.5](#) is by a first-principles derivation.

Consider the expansion of a fluid element. Let  $V$  be the volume of the fluid bounded by a surface  $S$ . Let  $S$  move with the fluid so that it always contains the same material. Let  $u_i$  be the local fluid

---

<sup>1</sup> See Equation [Equation 2.1](#) in [Chapter 2](#) (Governing Equations).

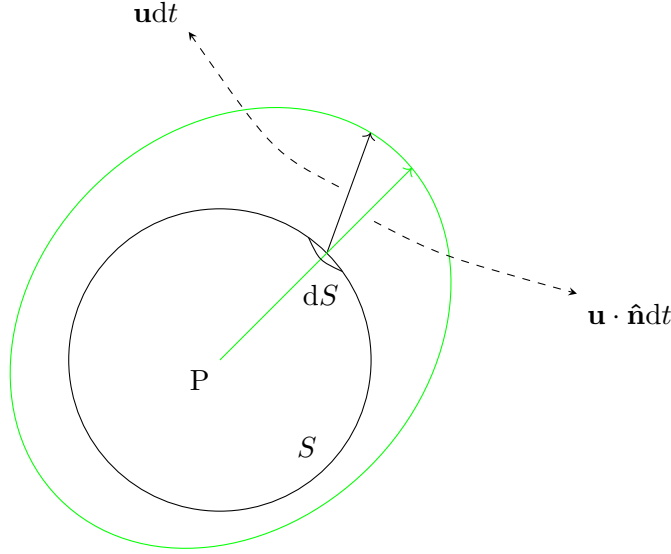


Figure D.1: Lagrangian expansion of a fluid

velocity. Then  $u_i n_i = \mathbf{u} \cdot \hat{\mathbf{n}}$  is the component of velocity in the direction of the outward normal. As the fluid moves, a fluid element on the surface is displaced, as shown in [Figure D.1](#). The normal displacement in an infinitesimal time  $dt$  is  $u_i n_i dt$ . Thus, the volume of the thin shell between the surface  $S$  at time  $t$  and the surface formed later at time  $t + dt$  is

$$\delta \text{Volume} \rightarrow dt \int u_i n_i d^2 x \quad (\text{D.6})$$

However, this volume is an increase in the volume  $V$ , and so we have

$$\frac{\partial \text{Vol}}{\partial t} = \int u_i n_i d^2 x = \int \mathbf{u} \cdot \hat{\mathbf{n}} d^2 x = \int \nabla \cdot \mathbf{u} d^3 x \quad (\text{D.7})$$

by Green's theorem. Partition the volume  $\text{Vol}$ , and consider a sequence of volumes, all enclosing point  $\mathbf{P}$ . Let the volumes shrink to point  $\mathbf{P}$ . Then we have

$$\lim_{\text{Vol} \rightarrow 0} \frac{1}{\text{Vol}} \frac{\partial \text{Vol}}{\partial t} = \lim_{\text{Vol} \rightarrow 0} \frac{1}{\text{Vol}} \int \nabla \cdot \mathbf{u} d^3 x = \nabla \cdot \mathbf{u} \quad (\text{D.8})$$

evaluated at point  $\mathbf{P}$ , exactly as was previously found in [Equation D.3](#). The divergence of the velocity at point  $\mathbf{P}$  is the expansion of the fluid at point  $\mathbf{P}$ .

## Appendix E

# First-, second-, and third-order advection

Consider the  $x$ -advection-phase conservation of mass equation. The one-dimensional equation is

$$\frac{\partial \rho}{\partial t} + U \frac{\partial \rho}{\partial x} = 0. \quad (\text{E.1})$$

If we assume that the velocity  $U$  is a constant, the finite difference form can be written as

$$\frac{\rho_{i-1/2}^{n+1} - \rho_{i-1/2}^n}{\Delta t} + U \frac{\bar{\rho}_i^1 - \bar{\rho}_{i-1}^n}{\Delta x} = 0, \quad (\text{E.2})$$

where the  $\bar{\rho}_i$  densities are evaluated at the cell boundaries, as shown in [Figure E.1](#). Solving for the density at the new time, we have

$$\rho_{i-1/2}^{n+1} = \rho_{i-1/2}^n - U \frac{\Delta t}{\Delta x} (\bar{\rho}_i^n - \bar{\rho}_{i-1}^n) = \rho_{i-1/2}^n - \eta (\bar{\rho}_i^n - \bar{\rho}_{i-1}^n) \quad \eta \equiv \frac{\Delta t}{\Delta x} \quad (\text{E.3})$$

The problem is to find the cell boundary densities  $\bar{\rho}$  in terms of the surrounding cell centered densities. The mass flow through the cell boundary located at index  $i$  is equal to  $\bar{\rho} U A_i \Delta t$ , where  $A_i$  is the cell boundary surface area.

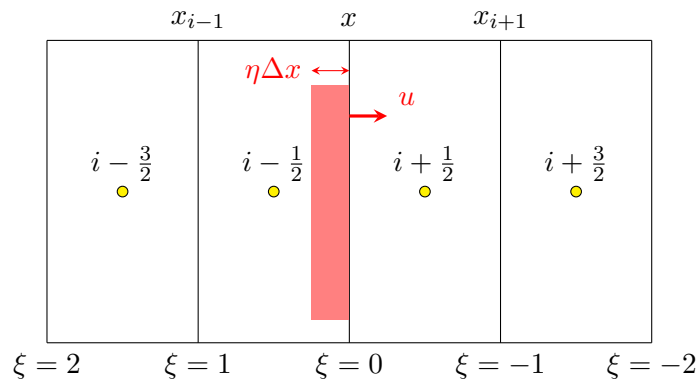


Figure E.1: Cell advection diagram

First we choose a nondimensional spatial variable <sup>1</sup>

$$\xi \equiv (x_i - x)/\Delta x \quad (\text{E.4})$$

The velocity at  $\xi = 0$  is assumed to be positive. <sup>2</sup> The time indices will be dropped for the remaining portion of the derivation.

The density is assumed to be a polynomial function <sup>3</sup> of the dimensionless spatial variable (i.e.,  $\rho = a + b\xi + c\xi^2$ ). The increasing orders of advection correspond to the increasing degrees of the density polynomial. *Note that the degree of the polynomial does not necessarily correspond to a formal order of accuracy.*

## E.1 First-order advection

The density is assumed to be a constant function over the range  $\xi = [0, 1]$  as

$$\rho = a \quad (\text{E.5})$$

The average density of the advection volume ( $\xi = [0, \eta]$ ) is assumed to be the density at the cell boundary. The cell boundary average density is

$$\bar{\rho}_i = \frac{1}{\eta} \int_0^\eta \rho d\xi = a. \quad (\text{E.6})$$

The cell centered density is

$$\rho_{i-1/2} = \int_0^1 \rho d\xi = a. \quad (\text{E.7})$$

The coefficient  $a$  is thus known. First-order advection, also called upwind advection or the donor cell method, is [94]

|   |
|---|
| <div style="display: flex; justify-content: space-between;"> <span>First Order</span> <span><math>\bar{\rho}_i = \rho_{i-1/2}</math> <span style="float: right;">(E.8)</span></span> </div> |
|---|

Upwind differencing is simple but known to be diffusive. The first-order method often gives poor results.

## E.2 Second-order advection

In this case, the density is assumed to be a linear function over the range  $\xi = [-1, 1]$ . The polynomial is

$$\rho = a + b\xi. \quad (\text{E.9})$$

---

<sup>1</sup>For simplicity, assume a constant cell size. Variable zoning requires slight modifications to the equations.

<sup>2</sup>This is only one case of the trichotomy. A negative velocity represents another case and is not derived here. The zero velocity case is trivial.

<sup>3</sup>Reference [93] and [Appendix C](#)

The average density of the advection volume is assumed to be the density at the cell boundary. The advection density is assumed to be constant in the range  $\xi = [0, \eta]$ . The cell boundary average density is

$$\bar{\rho}_i = \frac{1}{\eta} \int_0^\eta \rho d\xi = a + \frac{1}{2}b\eta \quad (\text{E.10})$$

The cell-centered densities are

$$\rho_{i+1/2} = \int_{-1}^0 \rho d\xi = a - \frac{1}{2}b, \text{ and} \quad (\text{E.11})$$

$$\rho_{i-1/2} = \int_0^1 \rho d\xi = a + \frac{1}{2}b \quad (\text{E.12})$$

The coefficients  $a$  and  $b$  are easily evaluated. They are

$$a = \frac{1}{2}(\rho_{i-1/2} + \rho_{i+1/2}), \text{ and} \quad (\text{E.13})$$

$$b = \rho_{i-1/2} - \rho_{i+1/2} \quad (\text{E.14})$$

The cell boundary density is

$$\bar{\rho}_i = \frac{1}{2}(\rho_{i-1/2} + \rho_{i+1/2}) + \frac{1}{2}(\rho_{i-1/2} - \rho_{i+1/2})\eta, \quad (\text{E.15})$$

which can be written as

|  |
|--|
| <p>Second order</p> $\bar{\rho}_i = \rho_{i-1/2} + \frac{1}{2}(1 - \eta)(\rho_{i+1/2} - \rho_{i-1/2}) \quad (\text{E.16})$ |
|--|

**Equation E.16** is second-order advection. This method is less diffusive than the firstorder method, but nonphysical oscillations and negative densities often occur.

It is interesting to note that in the limit as  $\eta \rightarrow 0$ , the second-order method results in the cell boundary average density being just the average of the densities on either side of the boundary.

### E.2.1 Third-Order Advection

In this case, the density is assumed to be of the form of a quadratic function over the range of  $\xi = [-1, 2]$ . The polynomial is

$$\rho = a + b\xi + c\xi^2. \quad (\text{E.17})$$

The cell boundary average density is

$$\bar{\rho}_i = \frac{1}{\eta} \int_0^\eta \rho d\xi = a + \frac{1}{2}b\eta + \frac{1}{3}c\eta^2 \quad (\text{E.18})$$

The cell-centered densities are

$$\rho_{i+1/2} = \int_{-1}^0 \rho d\xi = a - \frac{1}{2}b + \frac{1}{3}c \quad , \quad (\text{E.19})$$

$$\rho_{i-1/2} = \int_0^1 \rho d\xi = a + \frac{1}{2}b + \frac{1}{3}c, \text{ and} \quad (\text{E.20})$$

$$\rho_{i-3/2} = \int_1^2 \rho d\xi = a + \frac{3}{2}b + \frac{7}{3}c \quad (\text{E.21})$$

We have three simultaneous equations with three unknowns. In matrix form, we have

$$\frac{1}{6} \begin{bmatrix} 6 & -3 & 2 \\ 6 & 3 & 2 \\ 6 & 9 & 14 \end{bmatrix} \begin{bmatrix} a \\ b \\ c \end{bmatrix} = \begin{bmatrix} \rho_{i+1/2} \\ \rho_{i-1/2} \\ \rho_{i-3/2} \end{bmatrix} \quad (\text{E.22})$$

The solution of this  $3 \times 3$  matrix equation is

$$\begin{bmatrix} a \\ b \\ c \end{bmatrix} = \frac{1}{6} \begin{bmatrix} 2 & 5 & -1 \\ -6 & 6 & 0 \\ 3 & -6 & 3 \end{bmatrix} = \begin{bmatrix} \rho_{i+1/2} \\ \rho_{i-1/2} \\ \rho_{i-3/2} \end{bmatrix} \quad (\text{E.23})$$

or

$$a = \rho_{i-1/2} + \frac{1}{6} (2\rho_{i+1/2} - \rho_{i-1/2} - \rho_{i-3/2}), \quad (\text{E.24})$$

$$b = \rho_{i-1/2} - \rho_{i+1/2}, \text{ and} \quad (\text{E.25})$$

$$c = \frac{1}{2} (\rho_{i+1/2} - 2\rho_{i-1/2} + \rho_{i-3/2}). \quad (\text{E.26})$$

The cell boundary density is

$$\begin{aligned} \bar{\rho}_i &= \rho_{i-1/2} + \frac{1}{6} (2\rho_{i+1/2} - \rho_{i-1/2} - \rho_{i-3/2}) + \frac{1}{2} (\rho_{i-1/2} - \rho_{i+1/2}) + \frac{1}{6} (\rho_{i+1/2} - 2\rho_{i-1/2} - \rho_{i-3/2}) \eta^2, \\ &= \rho_{i-1/2} + \left( \frac{1}{3} - \frac{1}{2}\eta + \frac{1}{6}\eta^2 \right) (\rho_{i+1/2} - \rho_{i-1/2}) + \left( \frac{1}{6} - \frac{1}{6}\eta^2 \right) (\rho_{i-1/2} - \rho_{i-3/2}) \\ &= \rho_{i-1/2} + \frac{1}{2} (1 - \eta) \left[ \frac{1}{3} (2 - \eta) (\rho_{i+1/2} - \rho_{i-1/2}) + \frac{1}{3} (1 + \eta) (\rho_{i-1/2} - \rho_{i-3/2}) \right] \end{aligned} \quad (\text{E.27})$$

The third-order method yields a cell boundary density of

|   |
|---|
| <p>Third order</p> $\bar{\rho}_i = \rho_{i-1/2} + \frac{1}{6} (1 - \eta) [(2 - \eta)(\rho_{i+1/2} - \rho_{i-1/2}) + (1 + \eta)(\rho_{i-1/2} - \rho_{i-3/2})] \quad (\text{E.28})$ |
|---|

The third-order method is less diffusive than the second-order method but still exhibits some minor problems with negative densities and nonphysical oscillations. These problems can be eliminated by using the gradient limiters discussed next.

The methodology presented here presumably can be extended indefinitely. However, the higher-order advection schemes require increasingly more complexity and more distant cell information.

For all the possible advection methods discussed, the density at the cell boundary can be written following the style of Youngs [18]:

$$\bar{\rho}_i = \bar{\rho}_{i-1/2} + \frac{1}{2} (1 - \eta) \Delta x D_i, \quad (\text{E.29})$$

where  $D_i \approx \partial \rho / \partial x$  has the role of the density gradient. This formalism provides a concise way of understanding the various methods. The gradients are

$$\text{First Order: } D_i = 0 \quad (\text{E.30})$$

$$\text{Second Order: } D_i = \frac{\rho_{i+1/2} - \rho_{i-1/2}}{\Delta x}, \text{ and} \quad (\text{E.31})$$

$$\text{Third Order: } D_i = \frac{2 - \eta}{3} \cdot \frac{\rho_{i+1/2} - \rho_{i-1/2}}{\Delta x} + \frac{(1 + \eta)}{3} \cdot \frac{\rho_{i-1/2} - \rho_{i-3/2}}{\Delta x} \quad (\text{E.32})$$

The higher-order methods require more information to construct an approximation to the density gradient at the cell boundary.

A physical interpretation of the above equations can be gained by considering a simple example. A material of uniform density is moving with a positive velocity through the 1D Eulerian mesh. In this case, all the gradients are zero. First, second, and third orders give the same answer-simple downwind advection (donor cell advection). However, this advection is only first order! First-order advection gives the correct answer in this simple example. The cell boundary densities are the same as the cell-centered densities.

Next consider a square pulse with a uniform density moving with a positive velocity in a 1D Eulerian mesh. The top of the pulse exhibits the same behavior as described in the previous example. Locally, the density gradients are all zero. Again, the result is first order advection. The gradients will be nonzero only near the edge of the pulse. The finite difference gradients can capture the infinite slope at the edge of the pulse only partially. The square pulse will smooth out over many advection steps. The higher-order advection methods become important when the density gradients are large. The numerical advection of a square pulse is shown at the end of this appendix.

Higher order methods, above 3rd order, can be developed in the same manner. See the Los Alamos internal publications by Wayne Weseloh [95, 96] for more information.

### E.3 Gradient limiters and monotonicity

The van Leer [22, 97] choice of advection order depends on the local density gradients. The third-order method is clearly the best choice in most situations. In fact, it is the default advection method used in PAGOSA. However, the third-order method is occasionally nonphysical.

The nonphysical behaviors can be eliminated by choosing  $D_i$  such that [18]

$$D_i = \min \left( \frac{2|\rho_{i+1/2} - \rho_{i-1/2}|}{\frac{2-\eta}{3}|\rho_{i+1/2} - \rho_{i-1/2}| + \frac{1+\eta}{3}|\rho_{i-1/2} - \rho_{i-3/2}|}, \frac{2|\rho_{i-1/2} - \rho_{i-3/2}|}{\frac{2-\eta}{3}|\rho_{i+1/2} - \rho_{i-1/2}| + \frac{1+\eta}{3}|\rho_{i-1/2} - \rho_{i-3/2}|} \right) \cdot \frac{1}{\Delta x} \quad (\text{E.33})$$

The result is that in some cases the density gradient can be first, second, or third order, depending on the exact local density distribution. Figure E.2 shows this option graphically.<sup>4</sup> It is a powerful and convenient way of understanding the various limiters and monotonicity conditions that are needed to realize fully the third-order advection method.

It is important to note that the gradients are limited and not the densities themselves. This gradient limiting ensures that the conservation law is not violated.

In general, the van Leer limiter allows for the largest possible gradient without oscillations and therefore the least amount of diffusion. This choice of nonlinear cutoff of the density gradient also ensures that the new density gradient (at the next timestep,  $\eta+1$ ) will have the following property:

$$\min \left( \rho_{i-1/2}^n, \rho_{i+1/2}^n \right) \leq \rho_{i+1/2}^{n+1} \leq \max \left( \rho_{i-1/2}^n, \rho_{i+1/2}^n \right) \quad (\text{E.34})$$

This condition guarantees that when a monotonic initial value distribution is advected, the resulting distribution is also monotonic.[98]

---

<sup>4</sup> Sean Clancy, Los Alamos National Laboratory, personal communication (June 5, 2008).

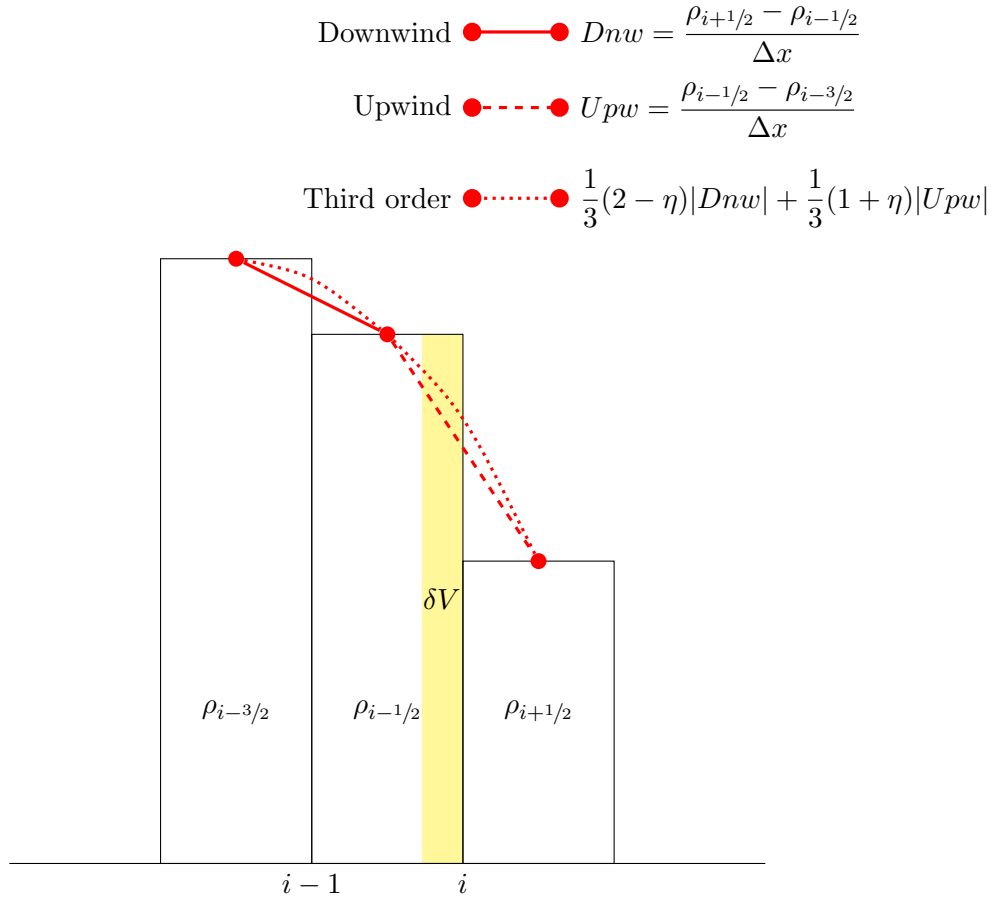


Figure E.2: Upwind, downwind, and third-order gradients



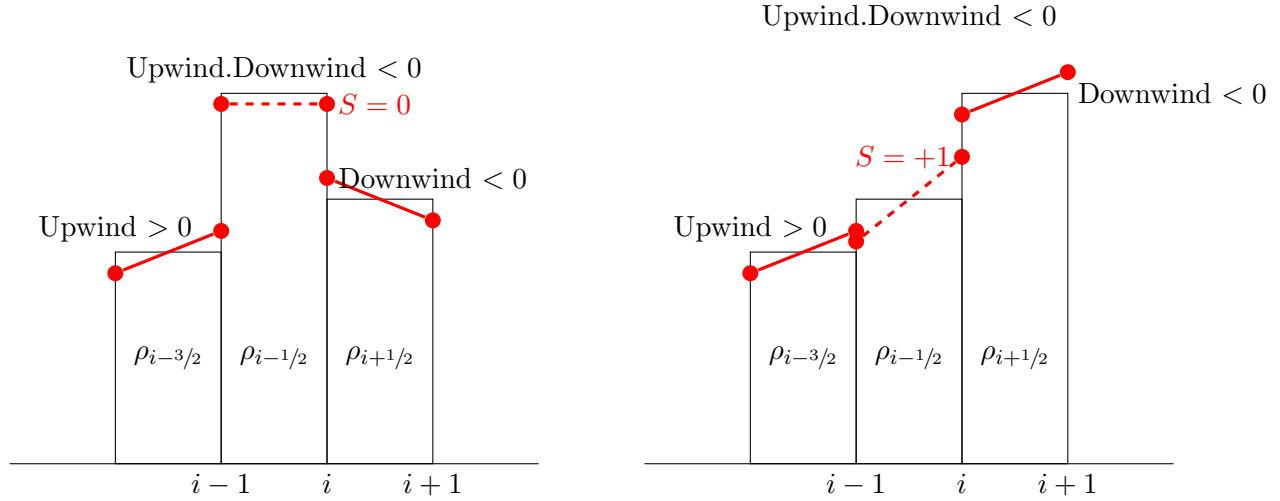


Figure E.3: The Youngs/van Leer gradient limiter. When (a), the gradients are monotonic, or when (b), the gradients indicate that the density has reached a local maximum (minimum).

In highly discontinuous flows, the value of  $D_i$  is modified to prevent undershoots and overshoots. A multiplicative factor is constructed such that, as shown in Figure E.3,

$$S = \text{sign}(\rho_{i+1/2} - \rho_{i-1/2}) \begin{cases} 0 & (\rho_{i+1/2} - \rho_{i-1/2})(\rho_{i-1/2} - \rho_{i-3/2}) \leq 0 \\ 1 & (\rho_{i+1/2} - \rho_{i-1/2})(\rho_{i-1/2} - \rho_{i-3/2}) > 0 \end{cases} \quad (\text{E.35})$$

If the upwind and downwind gradients differ in sign, the factor  $S$  is set to zero.

The sign factor for the value of  $S$  establishes the local sign of the gradient. The Youngs/van Leer gradient limiter suppresses negative densities or reduces the density gradient to zero if an extremum is reached or if the slope does not agree with the trend in density averages.

An example of the effect of the gradient limiter is shown in the last section of this appendix. The negative densities and other nonphysical behaviors readily apparent in the third-order method are suppressed using the Youngs/van Leer gradient limiter.

## E.4 PAGOSA advection

All of these pieces are brought together in PAGOSA. Start with the following definitions:

$$\begin{aligned} Don &\equiv \rho_{i-1/2}^n && \text{donor cell,} \\ Upw &\equiv \rho_{i-1/2}^n - \rho_{i-3/2}^n && \text{upwind gradient, and} \\ Dnw &\equiv \rho_{i+1/2}^n - \rho_{i-1/2}^n && \text{downwind gradient,} \end{aligned}$$

and we define the following coefficients

$$\begin{aligned} \varepsilon_1 &\equiv \delta Vol_{i-1/2}^n / Vol_{i-1/2}^n \\ \varepsilon_2 &\equiv \delta m_{i-1/2} / m_{i-1/2} \\ \varepsilon_3 &\equiv (1 + \varepsilon_1) / 6 \\ \varepsilon_4 &\equiv (2 - \varepsilon_1) / 6 \end{aligned}$$

The value  $\eta$ , defined in Equation E.3, sometimes called the Courant number, can be related to the fractional advection volume. The Courant number is less than unity because the advection volume must be less than the original cell volume. The Courant number, at index  $i$ , is

$$\eta_i \equiv U_i \frac{\Delta t}{\Delta x} = \frac{U_i \Delta t}{\Delta x} \frac{A_i}{A_i} = \frac{\delta V ol_{i-1/2}}{V ol_{i-1/2}} = \frac{\text{advection volume}}{\text{cell volume}} = \varepsilon_1 \quad (\text{E.36})$$

The cell boundary density, with all factors included, is

$$\bar{\rho}_i = Don + S(1 - \varepsilon_1) \min(|Upw|, |Dnw|, \varepsilon_3|Upw| + \varepsilon_4|Dnw|) \quad (\text{E.37})$$

The interface (cell boundary) mass flux is

$$\delta m_i = \delta V ol_{i-1/2} \bar{\rho}_i \quad (\text{E.38})$$

The updated cell mass is

$$mass_{i-1/2}^{n+1} = mass_{i-1/2}^n + \delta m_{i-1} - \delta m_i \quad (\text{E.39})$$

The new cell mass is the old cell mass plus the mass entering from the left boundary minus the mass leaving through the right boundary. Remember that we have assumed that  $U_i > 0$ ; therefore, in every cell we have mass entering from the left and leaving to the right.

The updated cell density is <sup>5</sup>

$$\bar{\rho}_{i-1/2}^{n+1} = mass_{i-1/2}^{n+1} / \left( Vol_{i-1.2}^n + \delta V ol_{i-1/2}^n - \delta V ol_{i+1/2}^n \right). \quad (\text{E.40})$$

The new cell density is the new cell mass divided by the new associated cell volume.

Next, the specific internal energy is advected. The process is basically the same as that described above, with a few exceptions. The specific internal energy is advected by mass and not by volume, as was done previously.[99] Start with the following definitions:

$$\begin{aligned} Don &\equiv E_{i-1/2}^n && \text{donor cell,} \\ Upw &\equiv E_{i-1/2}^n - E_{i-3/2}^n && \text{upwind gradient, and} \\ Dnw &\equiv E_{i+1/2}^n - E_{i-1/2}^n && \text{downwind gradient.} \end{aligned}$$

The cell boundary specific internal energy is

$$\bar{E}_i = Don + S(1 - \varepsilon_2) \min(|Upw|, |Dnw|, \varepsilon_3|Upw| + \varepsilon_4|Dnw|) \quad (\text{E.41})$$

where  $S$  has the same form as before, except that specific internal energy functionally replaces density in Equation E.35.

The updated cell specific internal energy is

$$E_{i-1/2}^{n+1} = \left( E_{i-1/2}^n \rho_{i-1/2}^n V ol_{i-1/2}^n + \delta m_{i-1} \bar{E}_{i-1/2} - \delta m_i \bar{E}_i \right) mass_{i-1/2}^{n+1} \quad (\text{E.42})$$

This equation completes the advection-phase of the basic hydrodynamic variables.

Each of the finite difference equations has stability[12] and convergence considerations, dissipation,[100] dispersion,[101] and phase errors.[102] These analyses and considerations are

---

<sup>5</sup>The temporal indices (n) and (n+1) refer to before and after the advection sweep.

beyond the scope of this work. Please consult the literature. The cell-centered quantities (e.g., strain rates, stress deviators, and elastic distortional energy) are advected by mass in the same way that the specific internal energy is advected. To prevent small values from being advected through the Eulerian mesh, various cutoffs are imposed on the advection algorithm. If the advection volume is too small, then it is set to zero. The final section of this appendix gives a numerical example of advecting a square pulse.

## E.5 Advection example: advection of a square pulse

The results of a test problem using the advection equations are shown in [Figure E.4](#). A square pulse with a uniform constant velocity is propagated through 300 cells. The exact solution is shown in black in each case. The initial square pulse is 20 cells wide, with a density of unity. The Courant number  $\eta = 0.100$ .

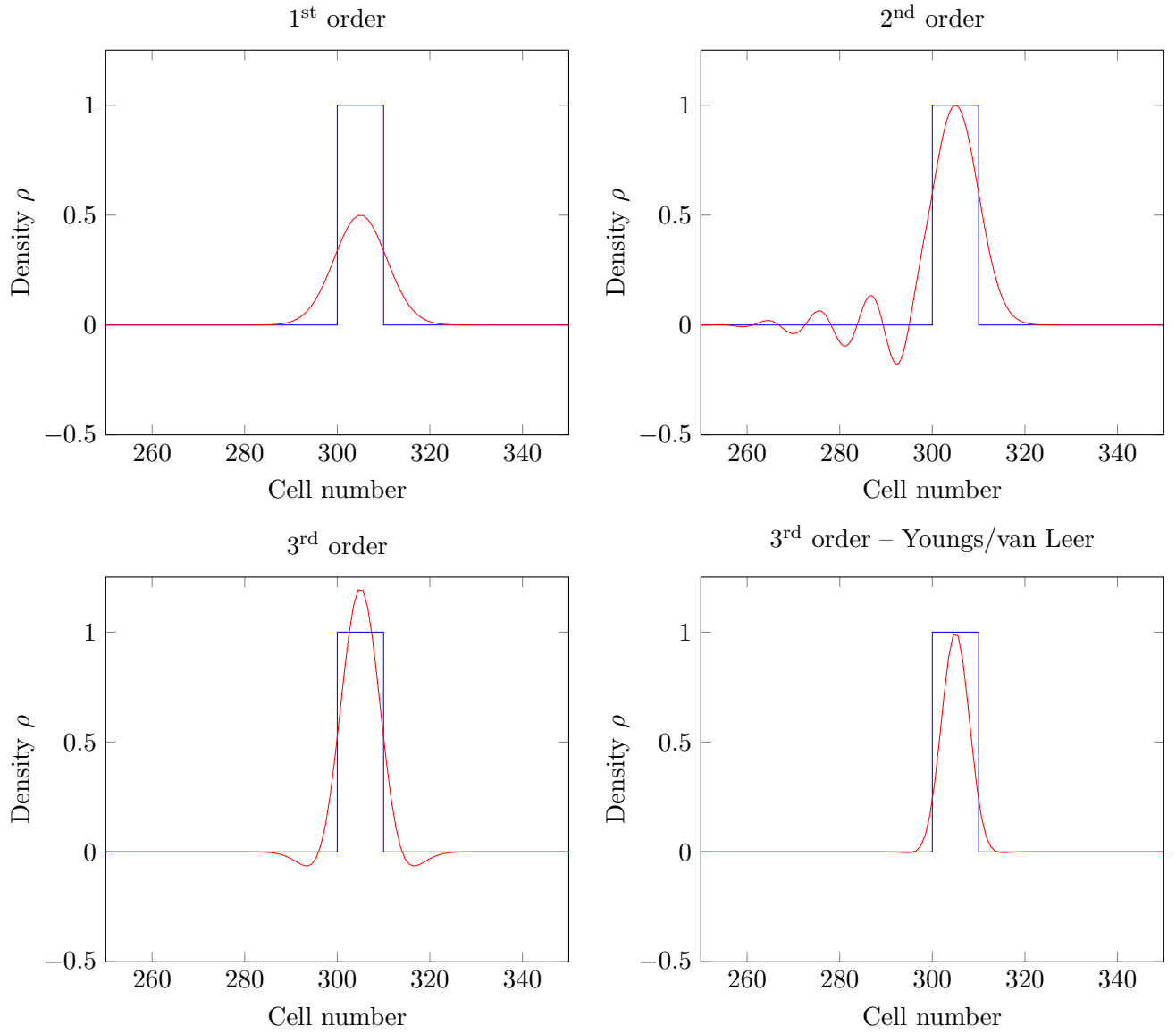


Figure E.4: Advection of a square pulse

## Appendix F

# Initial timestep calculation

The timestep used for each cycle must be less than the maximum stable timestep for each cell in the simulation. The initial timestep can be specified by the user, and must satisfy the following conditions:

$$\Delta t^0 < \min \left( \frac{\Delta x}{\max(|U| + c)}, \frac{\Delta y}{\max(|V| + c)}, \frac{\Delta z}{\max(|W| + c)} \right) \quad (\text{F.1})$$

Two equations that are useful for estimating the initial timestep are the equations for the sound speed of an elastic solid:

$$c_1 = \sqrt{\frac{\kappa}{\rho}} \quad , \quad \text{equivoluminal wave propagation speed, and} \quad (\text{F.2})$$

$$c_2 = \sqrt{\frac{\kappa + \frac{4}{3}G}{\rho}} \quad , \quad \text{irrotational (shear) wave propagation speed,} \quad (\text{F.3})$$

where  $\kappa$  is the bulk modulus,  $G$  is the shear modulus, and  $\rho$  is the mass density. In the case of solid materials, the initial timestep can often be computed by

$$\Delta t^0 < \min \left[ \frac{\min(\Delta x, \Delta y, \Delta z)}{\max(c_1, c_2)} \right] \quad (\text{F.4})$$

When the simulation involves HE, the sound speed for the undetonated explosive is set to  $3 \times D$ , where  $D$  is the explosive detonation velocity. The timestep for the explosive is then given by

$$\Delta t^0 < \textit{safec} \min \frac{\min(\Delta x, \Delta y, \Delta z)}{3D} \quad (\text{F.5})$$

where *safec* is the Courant safety factor described in [Chapter 10](#).

The initial condition should be chosen by the user to be much smaller than any of the above criteria. The timestep should “creep up” to a stable timestep determined from the most restrictive criterion.



## Appendix G

# Multi-material interface reconstruction for advection

### G.1 Reconstruction

For each sweep of the advection phase, it is necessary to compute the volume fractions that will be advected in that sweep.<sup>1</sup> The advection volume may contain several materials, as shown in [Figure G.1](#).

The main objective of this process is to find the advection volume for each material in a cell given the advection volume and the volume fraction of each material in the donor cell and its 26 neighbors. The notation for this appendix is

- $v$  = donor cell volume
- $\Delta v$  = advection volume
- $\Delta v_m$  = advection volume for the material ( $m$ )
- $\varepsilon = \Delta v/v$  advection volume fraction
- $v_m$  = donor cell volume fraction of material ( $m$ )
- $\langle v \rangle_m$  = total volume fraction up to the  $m^{\text{th}}$  interface,
- $\langle v_p \rangle_m$  = portion of  $\langle v \rangle_m$  contained in the advection volume,
- $\boldsymbol{\mu}_m$  = vector normal to the  $m^{\text{th}}$  interface, pointing out of the volume  $\langle v \rangle_m$ , and
- $\langle \Delta v \rangle_m = \langle v_p \rangle_m \Delta v$  total advection volume up to the  $m^{\text{th}}$  interface.

The procedure for calculating the individual material advection volumes is to

- calculate  $\varepsilon$ ,
- initialize all  $\langle v \rangle_m$ ,
- sum over the number of materials ( $m$ ) (except for the last material):
  - increment the sum and obtain  $\langle v \rangle_m$ ,
  - calculate  $\boldsymbol{\mu}_m$  from the gradients of  $\langle v \rangle_m$  (26 neighbors + donor),
  - calculate  $\langle v_p \rangle_m$  (depends on  $\varepsilon$ ,  $\boldsymbol{\mu}_m$ , and  $\langle v \rangle_m$ ),

---

<sup>1</sup>Rick Smith, Los Alamos National Laboratory, personal communication, March 15, 1991.

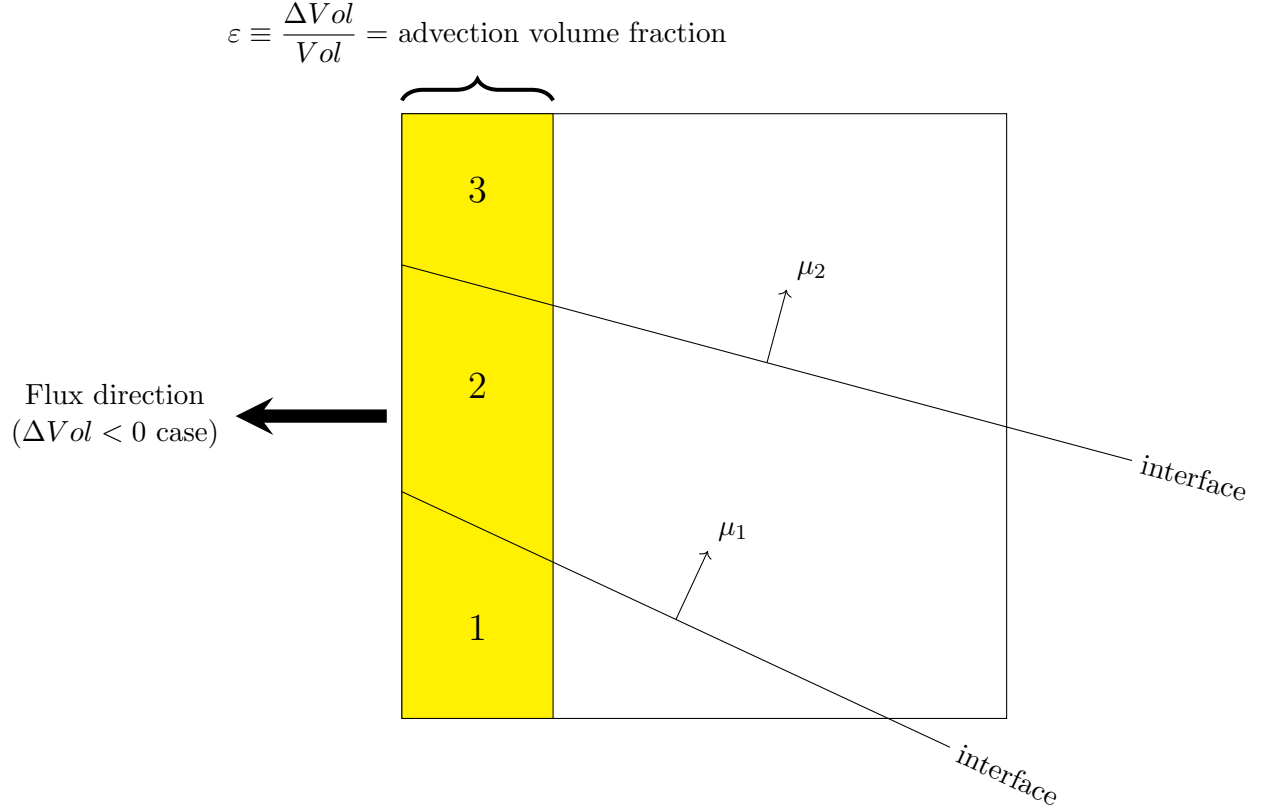


Figure G.1: The advection volume (shown in yellow) contains three materials to be advected. The flux direction in this case is negative.

- calculate  $\Delta v_m = \langle v_p \rangle_m \Delta v - \langle \Delta v \rangle_{m-1}$ , and
- determine a new value of  $\langle \Delta v \rangle_m = \langle v_p \rangle_m \Delta v$ .
- end of material loop ( $m$ ), and
- calculate the last material  $\Delta v_{last(m)} = \Delta v - \langle \Delta v \rangle_{last(m)-1}$

For the  $\Delta v > 0$  cases (i.e., flux through the right face of the cell), we must ensure that the donor cell quantities (in the cell to the left) are used. Also, it is necessary to replace  $\varepsilon \rightarrow 1 - \varepsilon$  and substitute the advection volume fraction with its complement.

## G.2 Volume fraction identifier

The idea is to compute the volume fraction of the advected portion of a material on one side of a plane that passes through the Eulerian cell, as shown in [Figure G.2](#).

In this case we know the volume of the cell ( $Vol$ ), the volume fraction of the materials behind the plane ( $\langle v \rangle$ ), and the direction vector associated with the interface ( $\mu$ ) and which points out of the material that lies “behind” the plane.<sup>2</sup> The volume fraction of the advected portion of the material is what is to be computed ( $\langle v_p \rangle$ ) and is defined relative to the full cell volume.

<sup>2</sup>The direction vector for the interface is computed by a simple finite difference formula using the volume fractions of the surrounding 26 cells.



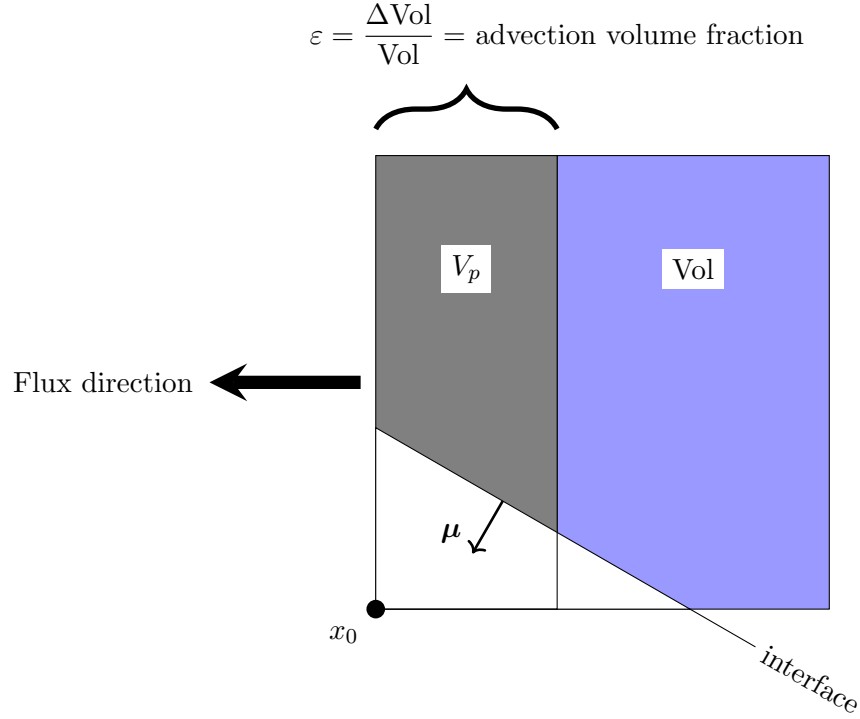


Figure G.2: A cross section of an Eulerian cell showing a material interface with a direction vector  $\mu$ , a volume fraction to be advected  $\varepsilon$  (relative to the full cell volume  $\text{Vol}$ ), and the volume fraction of the advected portion of the material  $V_p$ .

In the derivation, if we assume that the flux direction is for the positive flux, the solution can be obtained by treating the nonadvected portion as the advection volume (see [Figure G.2](#) and [Figure G.3](#)).

The coordinate system used here has  $\mathbf{x}_0$  at the origin (where  $\mathbf{x}_0$  is the vertex with the same indices as the cell). In this derivation, it is assumed that the flux direction is negative (through the face containing  $\mathbf{x}_0$ ).

For the case of positive flux, the solution can be obtained by treating the nonadvected portion as the advection volume, as shown in [Figure G.3](#).

If we denote the solution for positive and negative flux as  $V_p^{(+)}$  and  $V_p^{(-)}$ , respectively, then  $V_p^{(+)}$  is given in terms of  $V_p^{(-)}$  by

$$V_p^{(+)}\varepsilon = \text{Vol} - V_p^{(-)}(1 - \varepsilon) \quad (\text{G.1})$$

where  $\text{Vol}$  is the full cell volume.

The algorithm for the solution of  $V_p^{(-)}$  is obtained in two steps (see [Figure G.4](#)):

**Step 1.** Find the equation of the plane  $\mu \cdot \mathbf{x} = d$ .

**Step 2.** Transform the advection volume into a unit cube, and using the equation for the plane in the transformed frame, find the volume fraction  $V'$  of the material within this cube that is behind the plane (see [Appendix C](#) for details). The solution for  $V_p$  is then given by  $V_p = \varepsilon V'$ .

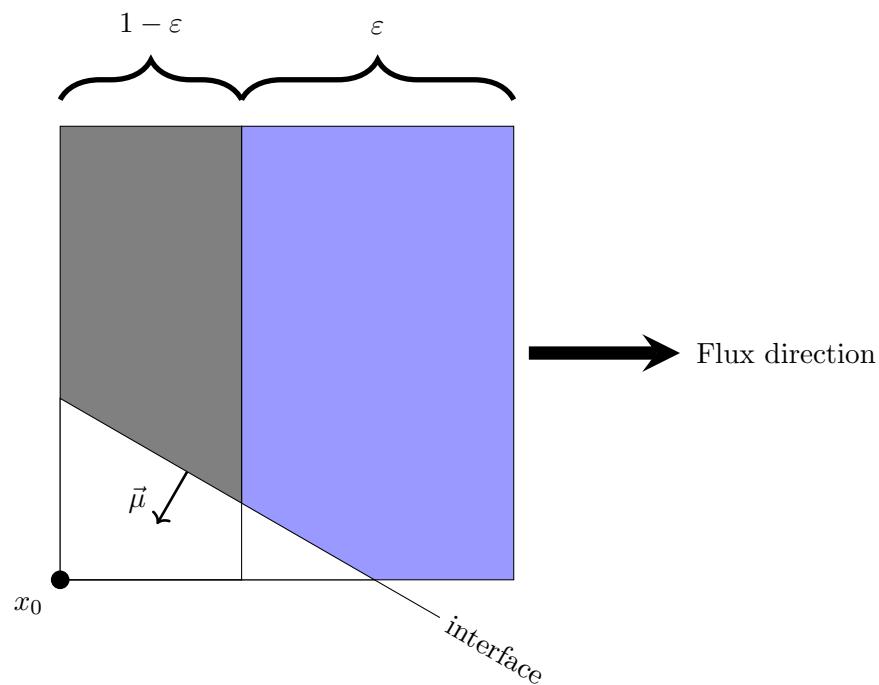


Figure G.3: The case of positive flux is simply the complement of the previous case shown in [Figure G.2](#).

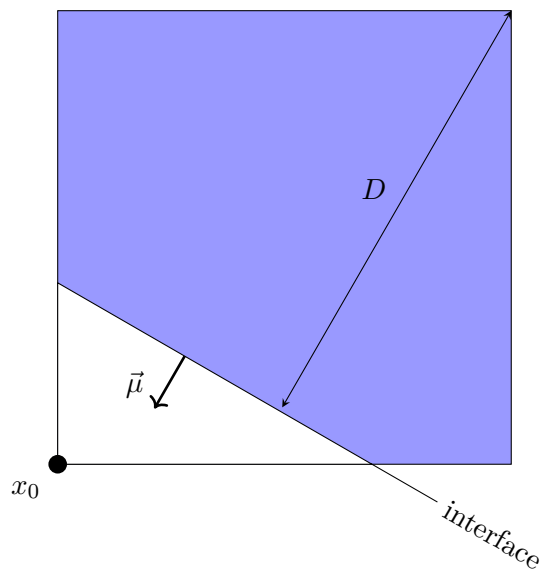


Figure G.4: If we are given the volume behind the plane ( $v$ ) and the unit normal  $\vec{\mu}$ , the algorithm will find the distance parameter  $d$ .

We begin with the detailed procedures for Step 1.

**Step 1.** Find the equation of the plane  $\boldsymbol{\mu} \cdot \mathbf{x} = d$  in the coordinate frame  $\mathbf{x}$ , with  $\mathbf{x}_0$  at the origin.

Let  $\mathbf{x}_m$  be the coordinate of the vertex toward which  $-\boldsymbol{\mu}$  most closely points (i.e.,  $\boldsymbol{\mu} \cdot \mathbf{x}_k$  is a minimum for the vertex  $k = m$ ). Now translate to a frame  $\mathbf{x}'$  with  $\mathbf{x}_m$  at the origin as

$$\mathbf{x}' = \mathbf{x} - \mathbf{x}_m, \quad (\text{G.2})$$

$$\boldsymbol{\mu} \cdot \mathbf{x}' = d - d_m, \quad (\text{G.3})$$

$$d_m \equiv \boldsymbol{\mu} \cdot \mathbf{x}_m = \frac{1}{2} [(\mu_1 - |\mu_1|) + (\mu_2 - |\mu_2|) + (\mu_3 - |\mu_3|)], \quad (\text{G.4})$$

Now normalize  $\boldsymbol{\mu}$  to unity – a unit normal vector. Then

$$\hat{\boldsymbol{\mu}} \cdot \mathbf{x}' = \rho, \quad (\text{G.5})$$

$$\rho = (d - d_m)/|\boldsymbol{\mu}|, \text{ and} \quad (\text{G.6})$$

$$\hat{\boldsymbol{\mu}} \equiv \boldsymbol{\mu}/|\boldsymbol{\mu}| \quad (\text{G.7})$$

By symmetry, the solution  $\rho(\boldsymbol{\mu}, V)$  will not change if we replace

$$\hat{\boldsymbol{\mu}} \rightarrow \mathbf{c} = (|\hat{\mu}_1|, |\hat{\mu}_2|, |\hat{\mu}_3|) \quad (\text{G.8})$$

and reorder the components of  $\mathbf{c}$  such that

$$0 \leq c_1 \leq c_2 \leq c_3 \quad (\text{G.9})$$

The solution then is  $\rho(\hat{\boldsymbol{\mu}}, V) = (\mathbf{c}, V)$ , which is derived in [Appendix C](#) and report LA-UR-07-2274.[\[17\]](#)

The solution is then

$$d = |\boldsymbol{\mu}| \rho + d_m \quad (\text{G.10})$$

Note that  $|d|/|\boldsymbol{\mu}|$  is the distance from the origin  $\mathbf{x}_0$  to the plane. If  $d > 0$ , then  $\mathbf{x}_0$  is behind the plane and thus inside the material; however, if  $d < 0$ , we have the situation where  $\mathbf{x}_0$  is in front of the plane and outside the material. The algorithm proceeds with Step 2.

**Step 2.** Next, transform to a coordinate system  $\mathbf{x}$  in which the advection volume is stretched to a unit cube (see [Figure G.5](#)):

$$\mathbf{x} = (x_1/\varepsilon, x_2, x_3) \text{ and} \quad (\text{G.11})$$

$$\mathbf{g} = (\varepsilon, x_2, x_3) \quad (\text{G.12})$$

Now translate these equations to a new frame  $\mathbf{x}'$  with  $\mathbf{x}_m$  at the origin, where  $\mathbf{x}_m$  is the vertex in the new unit cube representing the advection volume toward which  $-\mathbf{g}$  most closely points (i.e.,  $\mathbf{g} \cdot \mathbf{x}_k$  is a minimum for the vertex  $k = m$ ):

$$\mathbf{x}' = \mathbf{x} - \mathbf{x}_m, \quad (\text{G.13})$$

$$\mathbf{g} \cdot \mathbf{x}' = d - d_m \equiv \rho', \text{ and} \quad (\text{G.14})$$

$$d_m \equiv \mathbf{g} \cdot \mathbf{x}_m = \frac{1}{2} [(g_1 - |g_1|) + (g_2 - |g_2|) + (g_3 - |g_3|)]. \quad (\text{G.15})$$

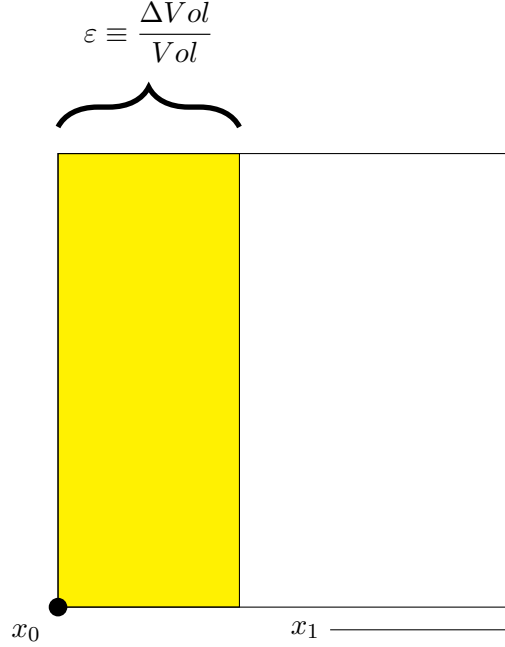


Figure G.5: The advection volume in the new coordinate system stretched to a unit cube.

Now we need to determine the fraction  $v'$  of the advection volume that lies behind the plane. By symmetry, the solution  $v'(g, \rho')$  will not change if we permute the components of

$$0 \leq g_1 \leq g_2 \leq g_3 \quad (\text{G.16})$$

We can again use the results in [Appendix C](#), which derive  $v(g, \rho)$ . The solution for  $v_p$  is then finally given by

$$V_p = \varepsilon V'(\mathbf{g}, \rho') \text{ and} \quad (\text{G.17})$$

$$\rho' = d - d_m = \rho |\mathbf{g}| + \frac{1}{2}(1 - \varepsilon) [g_1 - |g_1|]. \quad (\text{G.18})$$

Note that if  $\rho' < 0$ , then the plane lies entirely outside the advection volume and  $V_p = 0$ . Conversely, if  $\rho' \geq \rho_{\max}$ , then  $V' = 1$  and  $V_p = \varepsilon$ .

This algorithm is applied over all materials in the mixed cell, as described in [Figure 5.3](#) and the associated text. A flowchart of that algorithm is shown at the beginning of this appendix.

## Appendix H

# The Cauchy-Stokes decomposition theorem

The decomposition theorem developed by Cauchy [103] and Stokes [88] states that

An arbitrary instantaneous state of a fluid particle moving along its path may be resolved at each position  $x_i(P, t)$  as a superposition of (1) a translation, (2) a rigid rotation, (3) a dilatation along three mutually perpendicular axes, and (4) a shear motion.

Consider a velocity field  $u_i(x_k, t)$  of a moving fluid particle in a neighborhood of its position  $x_k$  at a time  $t$ . When the velocity field is continuous and differentiable, a Taylor expansion of the velocity function near a point  $P$  exists and takes the form

$$u_i(x_k, t) = u_i(P, t) + \frac{\partial u_i}{\partial x_j} (x_k - P) + \dots \quad (\text{H.1})$$

The gradient can be decomposed into its symmetrical and antisymmetrical parts as

$$\frac{\partial u_i}{\partial x_j} = \dot{e}_{ij} + \Omega_{ij} = \dot{e}_{ij} - \frac{1}{2} \pi_{ijm} \omega_m \quad (\text{H.2})$$

where the symmetrical tensor  $\dot{e}$  is called the strain rate tensor, the antisymmetrical tensor  $\Omega$  is called the vorticity tensor, and  $\omega$  is the axial vector associated with the vorticity tensor. The permutation symbol  $\pi_{ijm}$  is the Levi-Civita pseudotensor, [89] where

$$u_i(x_k, t) = u_i(P, t) + \dot{e}_{ij} x_j - \frac{1}{2} \pi_{ijm} x_j \omega_m + \dots \quad (\text{H.3})$$

The second term can be written as

$$\dot{e}_{ij} x_j = \frac{\partial}{\partial x_k} \left( \frac{1}{2} \dot{e}_{ij} x_j x_k \right) + \dots \quad (\text{H.4})$$

This term represents a velocity field normal at each point to the quadratic surface  $\dot{e}_{ij} x_j x_k = \text{constant}$ , which contains the point  $P$ . Because the symmetric tensor possesses three mutually perpendicular eigenvectors, the eigenvalues of the deformation tensor  $\dot{e}$  measure the rates of extension per unit length of the fluid particle at  $x_k(P, t)$  in the directions of the eigenvectors, which can always be taken as the three basis vectors of the velocity field.

Therefore, Equation H.1 becomes

$$u_i(x_k, t) = u_i(P, t) + \frac{1}{2} \frac{\partial}{\partial x_k} (\dot{e}_{ij} x_j x_k) - \pi_{ijm} x_j (\omega_m/2) + O(x^2) \quad (\text{H.5})$$

Thus, the first term represents a translation. Simple integration of the velocity field gives the three translations. The second term determines the distortion of the fluid element. The distortion consists of a dilatation (the diagonal terms of the tensor  $\dot{e}_{ik}$ ) and a superposition of shear motions (the off-diagonal terms of the tensor  $\dot{e}_{ik}$ ). The vorticity tensor (or vorticity vector) determines the rigid rotation of a fluid particle that keeps its volume and shape the same. The rotation axis is defined by the direction of the vorticity vector and an angular velocity of  $\omega_m/2$ .

This result is profound. Each piece of the deformation can be computed independently, and the results can be combined by linear superposition. Consider the motion of a small mass of an arbitrary shape, such as a cube. The motion of the cube may be divided into two types: a rigid body motion and a deformation motion. The rigid body motion may be divided further into a translation and a rotation. As the mass undergoes its rigid body motion, it can also deform. The deformation of the mass can be completely specified by describing the dilatation (volumetric expansion or contraction) and the shear strains of the mass, as shown in Figure H.1.

## H.1 Translation

The translation is given by integrating the velocity vector  $\mathbf{u}$ , which is closely related to the advection (remap) phase.

## H.2 Rotation

The rotation rate is the angular velocity vector  $\boldsymbol{\omega}$  and is related to the vorticity<sup>1</sup> tensor  $\boldsymbol{\Omega}$ . Rotation may or may not occur in a particular flow/deformation. A flow where the vorticity is zero is known as irrotational flow.

### H.2.1 Dilatation

The dilatation represents the contraction or expansion of an elemental mass. The rate of dilatation is related to the velocity divergence.<sup>2</sup> The numerical value of the dilatation is independent of the coordinate system because it is the first invariant of the strain rate tensor [Equation 2.4].

### H.2.2 Shear Deformation

A shear strain deformation is a strain that acts parallel to the surface of the material upon which it is acting. Thus, in our cubic example, the  $90^\circ$  angles between faces diverge from that value. The strain rate tensor [Equation 2.5 a – c] gives the rate at which the sides close toward each other.

---

<sup>1</sup>See Equation 2.8a – Equation 2.8c.

<sup>2</sup>See Equation 2.6 and Equation 2.7.

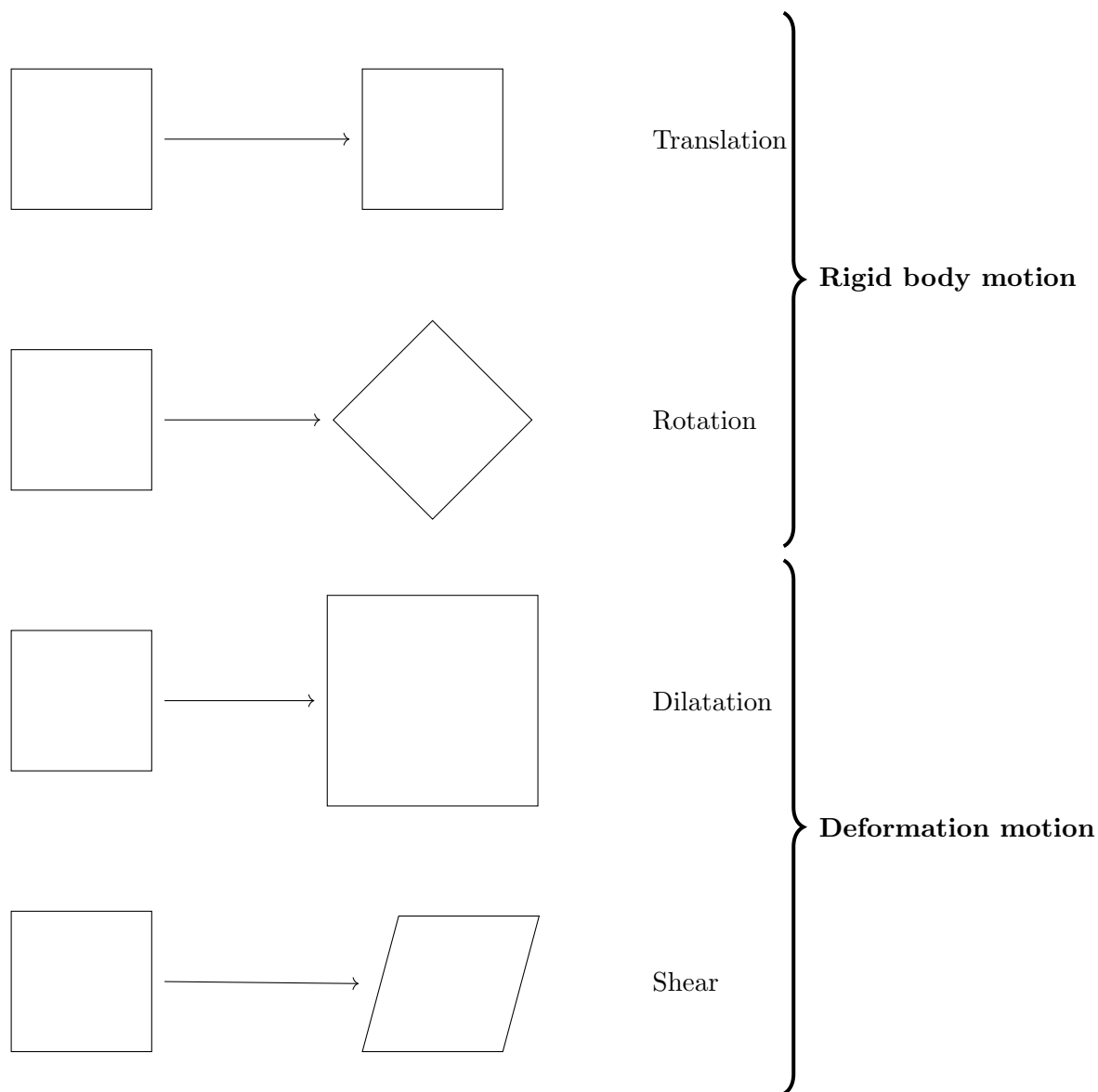


Figure H.1: The types of motion that, when superimposed, completely describes the kinematics of a small elemental mass. The cubical shape is arbitrary.





# Appendix I

## Stress rotation

An important concept in the formulation of constitutive theories in deformations is that of frame indifference, or objectivity.[104] The basic idea is that the constitutive relation between stress and strain should be unaffected by any rigid body rotations the material may undergoing at a particular instant of time. Mathematically we describe this situation by defining an alternative reference frame that is rotating and translating with respect to the original Eulerian coordinate system. For the constitutive relations to be meaningful, the tensor quantities we use (stress, stress rate, strain, and strain rate) should transform according to the laws of tensor calculus. If a given quantity does this transformation, we say it is material frame indifferent; if it does not, we say it is not properly invariant or not objective. The deviatoric stress in the Eulerian (laboratory) frame is  $\mathbf{S}^*$  and is denoted  $\mathbf{S}$  in the material (rotated) frame of reference.[105]

The deviatoric stress tensor transforms as [106]

$$\mathbf{S}_{ij}^* = Q_{ik} S_{km} Q_{mj}, \quad (\text{I.1})$$

where  $Q$  is a proper orthogonal (rotation) tensor that transforms the tensor  $S$ . Because  $Q$  is an orthogonal tensor, the transpose is the inverse. Thus,

$$Q_{ij} Q_{jk} = \delta_{ik}. \quad (\text{I.2})$$

If we take the time derivative of the above equation,

$$\dot{Q}_{ij} Q_{jk} + Q_{ij} \dot{Q}_{jk} = \mathbf{0} \quad \Rightarrow \quad \dot{Q}_{ij} Q_{jk} = -Q_{ij} \dot{Q}_{jk} \quad (\text{I.3})$$

Then we right-and-left multiply both sides of Equation I.1 by orthogonal tensors. Thus,

$$S_{ij} = Q_{ik} S_{km}^* Q_{mj} \quad (\text{I.4})$$

The time derivative of the deviatoric stress tensor, Equation I.1, produces

$$\dot{S}_{ij}^* = \dot{Q}_{ik} S_{km} Q_{mj} + Q_{ik} \dot{S}_{km} Q_{mj} + Q_{ik} S_{km} \dot{Q}_{mj} \quad (\text{I.5})$$

If we substitute Equation I.4 into the above equation,

$$\begin{aligned} \dot{S}_{ij}^* &= \dot{Q}_{ik} (Q_{kn} S_{nl}^* Q_{lm}) Q_{mj} + Q_{ik} \dot{S}_{km} Q_{mj} + Q_{ik} (Q_{kn} S_{nl}^* Q_{lm}) \dot{Q}_{mj} \\ &= \dot{Q}_{ik} Q_{kn} S_{nl}^* \delta_{lj} + Q_{ik} \dot{S}_{km} Q_{mj} + \delta_{in} S_{nl}^* Q_{lm} \dot{Q}_{mj} \text{ and} \\ &= \dot{Q}_{ik} Q_{kn} S_{nj}^* + Q_{ik} \dot{S}_{km} Q_{mj} + S_{il}^* Q_{lm} \dot{Q}_{mj}. \end{aligned} \quad (\text{I.6})$$

If we apply [Equation I.3](#),

$$\dot{S}_{ij} = \dot{Q}_{ik}Q_{kn}S_{nj}^* + Q_{ik}\dot{S}_{kn}Q_{nj} - S_{ik}^*\dot{Q}_{kn}Q_{nj} \quad (\text{I.7})$$

If we introduce a new variable,

$$W_{ij} \equiv \dot{Q}_{ik}Q_{kj}, \quad (\text{I.8})$$

we will find that this rotation is actually related to the vorticity tensor, but for now it is simply a mathematical convenience. [Equation I.7](#) is now written as

$$\dot{S}_{ij}^* = Q_{ik}\dot{S}_{kn}Q_{nj} + W_{in}S_{nj}^* - S_{ik}^*W_{kj} \quad (\text{I.9})$$

$$\text{Laboratory Frame} = \text{Material Frame} + \text{Rotation} \quad (\text{I.10})$$

[Equation I.9](#) is known as the Jaumann derivative,[\[107\]](#) or the Jaumann-Zaremba rate.[\[108\]](#) These objective rates are simply an application of the Lie derivative.[\[109\]](#) What is not generally known or conceded is that Zaremba essentially introduced what is now known as the Jaumann derivative [but commonly referred to as the corotational (sometimes spelled “co-rotational”) derivative]. The rotational portion of [Equation I.9](#) is computed separately as

$$R_{ij} \equiv W_{ik}S_{kj}^* - S_{ik}^*W_{kj} \quad (\text{I.11})$$

Next consider a line segment in the rotated configuration  $dx^*$  referenced to the fixed Eulerian configuration  $dX$ . This vector follows the standard transformation for infinitesimal rotations<sup>1</sup> as

$$dx_i^* = Q_{ij}dX_j \quad (\text{I.12})$$

Left multiply the (transpose/inverse) rotation as

$$Q_{ki}dx_i^* = Q_{ki}Q_{ij}dX_j = \delta_{kj}dX_j = dX_k \quad (\text{I.13})$$

Taking the time derivative of [Equation I.12](#) yields <sup>2</sup>

$$dx_i^* \equiv du_i = \dot{Q}_{ij}dX_j = \dot{Q}_{ij}Q_{jk}dx_k. \quad (\text{I.14})$$

The time derivative of position is the velocity vector  $u$ . Thus, we have

$$\frac{\partial u_i}{\partial x_k} = \dot{Q}_{ij}\dot{Q}_{jk}, \quad (\text{I.15})$$

However, we have previously decomposed the gradients of velocity as the sum of a symmetric tensor and an antisymmetric tensor <sup>3</sup> as

$$\frac{\partial u_i}{\partial x_k} = \dot{e}_{ik} + \Omega_{ik} \quad (\text{I.16})$$

Because [Equation I.15](#) and [Equation I.16](#) are equivalent,

$$W_{ik} = \dot{Q}_{ij}Q_{jk} = \dot{e}_{ik} + \Omega_{ik} \quad (\text{I.17})$$

---

<sup>1</sup>For finite rotations, the derivation is much more complicated and results in many additional terms.

<sup>2</sup>Because the Eulerian reference frame is independent of time, mathematically,  $dX \neq 0$ .

<sup>3</sup>See [Chapter 2](#), Governing Equations, for the definitions.

Substituting the above equation into Equation I.11 produces

$$\begin{aligned}
R_{ij} &= W_{ik}S_{kj}^* - S_{ik}^*W_{kj} \\
&= (\dot{e}_{ik} + \Omega_{ik})S_{kj}^* - S_{ik}^*(\dot{e}_{kj} + \Omega_{kj}) \\
&= \Omega_{ik}S_{kj}^* - S_{ik}^*\Omega_{kj} + (\dot{e}_{ik}S_{kj}^* - S_{ik}^*\dot{e}_{kj}) \\
&= \Omega_{ik}S_{kj}^* - S_{ik}^*\Omega_{kj}
\end{aligned} \tag{I.18}$$

The strain rate tensor  $\mathbf{e}$  and the deviatoric stress tensor  $\mathbf{S}$  are both symmetric in their indices; therefore, the term in the parentheses is zero.

The rigid body rotation must be subtracted out of the deviatoric stress tensor before we can compute the deformation of the material in the cell. The velocity field applies to all materials in a cell; therefore, the rotation also applies to all materials in a given cell.

The complete rotation terms <sup>4</sup> in Equation I.11 are

$$\begin{aligned}
R_{xx} &= -2\Omega_{xy}S_{xy} - 2\Omega_{xz}S_{xz}, \\
R_{yy} &= 2\Omega_{xy}S_{xy} - 2\Omega_{yz}S_{yz}, \\
R_{xy} &= \Omega_{xy}(S_{xx} - S_{yy}) - \Omega_{xz}S_{yz} - \Omega_{yz}S_{xz}, \\
R_{xz} &= \Omega_{xz}(2S_{xx} + S_{yy}) - \Omega_{xy}S_{yz} + \Omega_{yz}S_{xy}, \text{ and} \\
R_{yz} &= \Omega_{yz}(S_{xx} + 2S_{yy}) + \Omega_{xy}S_{xz} + \Omega_{xz}S_{xy}
\end{aligned} \tag{I.19}$$

These rotation terms are used in PAGOSA.

---

<sup>4</sup> The  $R_{zz}$  is not needed because  $S_{zz}$  is not directly computed. Remember that  $\mathbf{S}$  is traceless:  $S_{zz} = -(S_{xx} + S_{yy})$ .



# Appendix J

## Diagnostics

The diagnostics in PAGOSA allow the user to confirm the conservation laws for mass and energy. The following sections detail the calculation of the various diagnostics available.

### J.1 Volume

The total volume of material ( $m$ ) in the simulation is

$$^{(m)}\text{Volume} = \sum_{\text{cells}} \left[ ^{(m)}\phi_{i+1/2,j+1/2,k+1/2} ^{(m)}Vol_{i+1/2,j+1/2,k+1/2} \right] \quad (\text{J.1})$$

where  $Vol$  is the Eulerian cell volume. The summation is over every cell in the Eulerian mesh, excluding the ghost cells.

### J.2 Mass

The total mass of material ( $m$ ) in the simulation is

$$^{(m)}\text{Mass} = \sum_{\text{cells}} \left[ ^{(m)}\phi_{i+1/2,j+1/2,k+1/2} ^{(m)}\rho_{i+1/2,j+1/2,k+1/2} ^{(m)}Vol_{i+1/2,j+1/2,k+1/2} \right] \quad (\text{J.2})$$

As before, the summation is over the entire Eulerian mesh.

### J.3 Internal Energy

The internal energy of material ( $m$ ) in the simulation is

$$^{(m)}\text{IE} = \sum_{\text{cells}} \left[ ^{(m)}\phi_{i+1/2,j+1/2,k+1/2} ^{(m)}\rho_{i+1/2,j+1/2,k+1/2} ^{(m)}E_{i+1/2,j+1/2,k+1/2} ^{(m)}Vol_{i+1/2,j+1/2,k+1/2} \right] \quad (\text{J.3})$$

As before, the summation is over the entire Eulerian mesh.

## J.4 Kinetic Energy

The kinetic energy poses a problem in computation. The mass is a cell-centered variable, whereas the velocities are vertex centered. In PAGOSA, the square of the velocities is averaged at the cell centers. First, the value of  $\mathbf{u} \cdot \mathbf{u}$  is computed for each vertex. Next, the cell-centered velocity is obtained by arithmetically averaging the eight vertex quantities. This average magnitude is used to compute the kinetic energy. The kinetic energy of material  $(m)$  in the simulation is

$${}^{(m)}\text{KE} = \frac{1}{2} \sum_{\text{cells}} \left[ {}^{(m)}\phi_{i+1/2,j+1/2,k+1/2} {}^{(m)}\rho_{i+1/2,j+1/2,k+1/2} {}^{(m)}Vol_{i+1/2,j+1/2,k+1/2} \langle U^2 + V^2 + W^2 \rangle_{i+1/2,j+1/2,k+1/2} \right] \quad (\text{J.4})$$

over the entire Eulerian mesh.

## J.5 Elastic Distortional Energy

The elastic distortional energy is the energy in the material due to elastic distortions.<sup>1</sup> The elastic distortional energy  $W^e$  is computed from the rate equation

$$\rho \dot{W}^e = S_{xx} \dot{e}_{xx}^e + S_{yy} \dot{e}_{yy}^e + S_{zz} \dot{e}_{zz}^e + 2(S_{xy} \dot{e}_{xy}^e + S_{xz} \dot{e}_{xz}^e + S_{yz} \dot{e}_{yz}^e). \quad (\text{J.5})$$

The elastic energy can be recovered in the form of kinetic energy. Think of a spring storing and releasing energy. This energy is computed for each material in the simulation that possesses a deviatoric stress.

## J.6 Plastic Work

The plastic work is the energy in the material due to plastic distortions. The plastic work  $W^p$  is computed from the rate equation

$$\rho \dot{W}^p = S_{xx} \dot{e}_{xx}^p + S_{yy} \dot{e}_{yy}^p + S_{zz} \dot{e}_{zz}^p + 2(S_{xy} \dot{e}_{xy}^p + S_{xz} \dot{e}_{xz}^p + S_{yz} \dot{e}_{yz}^p). \quad (\text{J.6})$$

The plastic work is part of the internal energy of the material and is computed separately for the convenience of the user. The plastic work represents an irreversible process.

## J.7 Mass Melted

Only materials with a flow-stress model have a melt mass computed. First, determine that the material exceeds the melt energy or temperature. The melt factor for material  $(m)$  is computed as

$${}^{(m)}f = \begin{cases} 1 & {}^{(m)}E > E_{\text{melt}} \text{ or } {}^{(m)}\theta > \theta_{\text{melt}} \\ 0 & \text{otherwise} \end{cases} \quad (\text{J.7})$$

---

<sup>1</sup> In PAGOSA the elastic distortional energy is computed separately and is not included in the total internal energy. This point has been and continues to be controversial in hydrocode forums.

Then

$$^{(m)}\text{Mass}(\text{melt}) = \sum_{\text{cells}} \left[ ^{(m)}\phi_{i+1/2,j+1/2,k+1/2} ^{(m)}\rho_{i+1/2,j+1/2,k+1/2} ^{(m)}f_{i+1/2,j+1/2,k+1/2} ^{(m)}Vol_{i+1/2,j+1/2,k+1/2} \right] \quad (\text{J.8})$$

The total mass was melted for material  $(m)$ . If the factor  $f$  has a value of one everywhere, then the entire mass is melted and reduces to [Equation J.2](#). The diagnostic holds for a particular moment in time. The mass can melt, freeze, and melt again during the course of the simulation.

## J.8 Mass Burned

Only materials with a detonation model have a burn mass computed. The burn fraction <sup>2</sup>  $Bf$  ranges from zero to one, as

$$^{(m)}\text{Mass}(\text{burn}) = \sum_{\text{cells}} \left[ ^{(m)}\phi_{i+1/2,j+1/2,k+1/2} ^{(m)}\rho_{i+1/2,j+1/2,k+1/2} ^{(m)}Bf_{i+1/2,j+1/2,k+1/2} ^{(m)}Vol_{i+1/2,j+1/2,k+1/2} \right] \quad (\text{J.9})$$

The total mass was burned (detonated) for material  $(m)$ . If the factor  $Bf$  has a value of one everywhere, then the entire mass is burned and reduces to [Equation J.2](#).

## J.9 Mixed-Cell Statistics

In normal circumstances, only a small percentage of the cells in a simulation is mixed. The vast majority of cells contain a single material (pure cells). The mixed-cell statistics can be useful to the user in several ways. First, the statistics reveal the cell with the maximum number of materials. For example, if the maximum is two, then at least one cell in the simulation contains two materials that share an interface. As this number increases, the ability for the algorithm to represent the geometry accurately is severely compromised. However, if this cell inhabits an unimportant region of the simulation, then the statistic may be safely ignored. The volume fraction determines the type:

$$\text{Mixed cells} \quad 0 < \phi < 1 \quad (\text{J.10})$$

$$\text{Pure cells} \quad \phi = 1 \quad (\text{J.11})$$

## J.10 Minimum and Maximum Statistics

For each of the important simulation variables, the minimum and maximum values for pure and mixed cells are tabulated. These statistics can be useful in determining the extreme states of the materials in question. For example, an unphysical sound speed or temperature may indicate that the equation of state is in a dubious regime.

---

<sup>2</sup>See [Chapter 13](#) for the definition of a burn fraction.





# Appendix K

## Momentum advection

The stress deviators contribute to the velocity fields, as can be seen readily in [Equation 2.2a](#) – [Equation 2.2c](#) individual stress deviators contribute to the momentum in much the same way as the pressure. The  $x$  component of the Navier-Stokes equation ([Equation 2.2a](#)) is

$$\frac{\partial U}{\partial t} = -\frac{1}{\rho} \frac{\partial P}{\partial x} + \frac{1}{\rho} \left[ \frac{\partial S_{xx}}{\partial x} + \frac{\partial S_{xy}}{\partial y} + \frac{\partial S_{xz}}{\partial z} \right] \quad (\text{K.1})$$

The complication arises when we address the question of mixed cells. A mixed cell contains materials of various densities, pressures, and stress deviators. Let us denote the density of material ( $m$ ) by  $^{(m)}\rho$ , the pressure of material ( $m$ ) by  $^{(m)}P$ , etc.

The equation for a particular material in a single Eulerian cell now can be written as

$$^{(m)}\rho \frac{\partial U}{\partial t} = -\frac{\partial ^{(m)}P}{\partial x} + \left[ \frac{\partial ^{(m)}S_{xx}}{\partial x} + \frac{\partial ^{(m)}S_{xy}}{\partial y} + \frac{\partial ^{(m)}S_{xz}}{\partial z} \right]. \quad (\text{K.2})$$

Notice that the velocity  $U$  does not have a material index. The velocity field applies to all materials in a cell.<sup>1</sup> Next, multiply both sides of the equation by the cell volume and the material volume fraction. Then

$$Vol^{(m)}\phi^{(m)}\rho \frac{\partial U}{\partial t} = -Vol^{(m)}\phi \frac{\partial ^{(m)}P}{\partial x} + Vol^{(m)}\phi \left[ \frac{\partial ^{(m)}S_{xx}}{\partial x} + \frac{\partial ^{(m)}S_{xy}}{\partial y} + \frac{\partial ^{(m)}S_{xz}}{\partial z} \right]. \quad (\text{K.3})$$

When we sum over all materials in the momentum control volume and the

$$Mass = \sum_m Vol^{(m)}\phi^{(m)}\rho. \quad (\text{K.4})$$

then [Equation K.3](#) becomes

$$Mass \frac{\partial U}{\partial t} = -\frac{\partial \tilde{P}}{\partial x} + \left[ \frac{\partial \tilde{S}_{xx}}{\partial x} + \frac{\partial \tilde{S}_{xy}}{\partial y} + \frac{\partial \tilde{S}_{xz}}{\partial z} \right] \quad (\text{K.5})$$

where the tildes refer to the cell-averaged quantities. The partial derivatives are constructed in the same manner as described in [Chapter 3](#). However, the momentum control volume covers the eight cells that surround the vertex. The differencing and integration are done in the same way as the other variables described in [Chapter 5](#) and [Chapter 6](#).

---

<sup>1</sup>In theory, a velocity field could exist for each material in a cell.



# Appendix L

## Pin package

The pin diagnostic is used to record arrival times at a particular point in space. The diagnostic is positioned near a material surface, and electrical connections carry the timing signal to a recording device. The pin package in PAGOSA allows the user to emulate this experimental diagnostic tool.

Consider a point in space inside the Eulerian mesh, as shown in [Figure L.1](#). The pin is located at

$$\mathbf{x} \equiv (x_p, y_p, z_p) \tag{L.1}$$

As the simulation proceeds, the material surface of interest will move into the Eulerian cell containing the point  $\mathbf{x}$ . The perpendicular distance of a point  $\mathbf{x}$  to the material plane is given by

$$d = \frac{\mu_1 x_p + \mu_2 y_p + \mu_3 z_p - \rho}{\sqrt{\mu_1^2 + \mu_2^2 + \mu_3^2}} \tag{L.2}$$

where  $\rho$  is the distance parameter associated with the material plane. The material surface is characterized by a direction vector, as described in [Appendix C](#). With each new timestep, a new distance is computed and stored for later use. Typically, the material passes through the cell in a few timesteps, as shown in [Figure L.2](#).

The optimal situation is when four distance data points are recorded—two with positive distances and two with negative distances. Lagrange interpolation[7] is used to find the zero crossing time, which occurs when the pin is on the material surface.

Pathological situations can result in fewer than four data points being available. The crossing algorithm in PAGOSA changes, depending on the number of distance data points available from the simulation. The individual cases are detailed below.

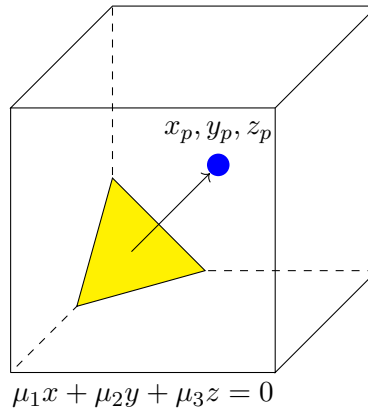


Figure L.1: The material surface, shown as a yellow triangle, is represented as a plane possessing a unique direction vector  $(\mu_1, \mu_2, \mu_3)$  that points to the pin location (shown as a blue dot). If the point  $\mathbf{x}$  lies in front of the plane, the distances are positive. If the point  $\mathbf{x}$  lies behind the plane, the distances are negative.

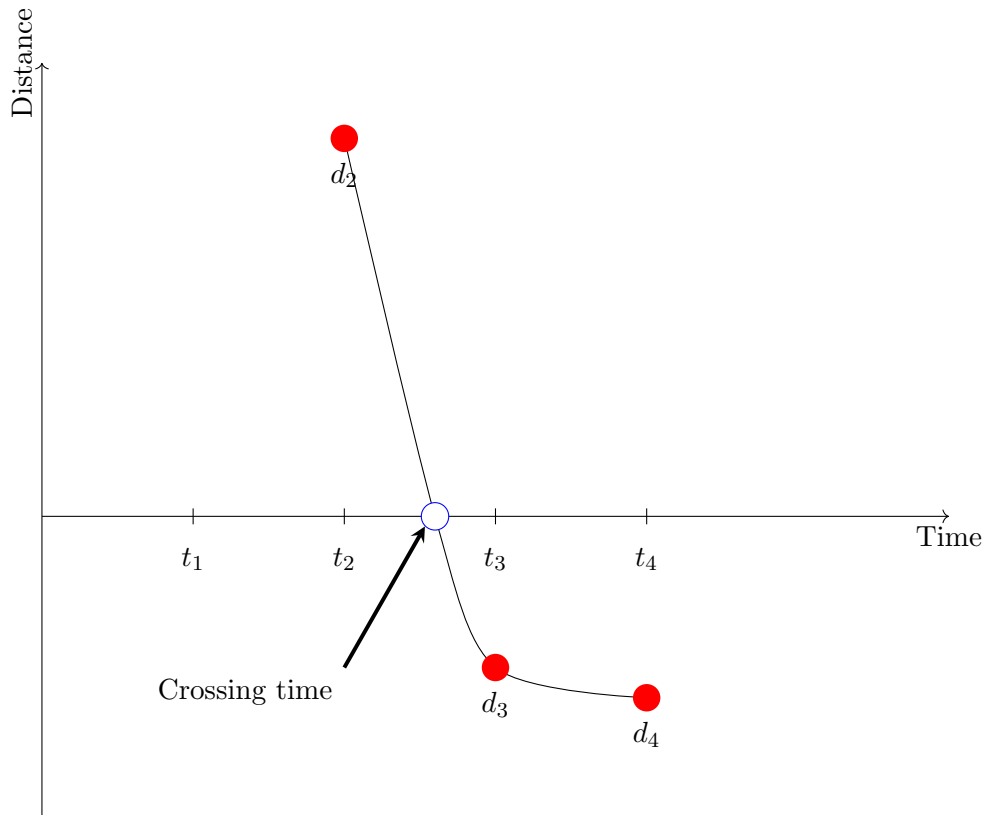


Figure L.2: A typical pin distance vs simulation time plot that points to the pin location (shown as a blue dot). If the point  $\mathbf{x}$  lies in front of the plane, the distances are positive. If the point  $\mathbf{x}$  lies behind the plane, the distances are negative.

## L.1 Four Points

When four data points are available for computing a pin-crossing time, the Lagrange interpolation formula is

$$t_{cross} = \frac{t_1 d_2 d_3 d_4}{(d_2 - d_1)(d_3 - d_1)(d_4 - d_1)} + \frac{t_2 d_1 d_3 d_4}{(d_1 - d_2)(d_3 - d_2)(d_4 - d_2)} + \frac{t_3 d_1 d_2 d_4}{(d_1 - d_3)(d_2 - d_3)(d_4 - d_3)} + \frac{t_4 d_1 d_2 d_3}{(d_1 - d_4)(d_2 - d_4)(d_3 - d_4)} \quad (\text{L.3})$$

Appropriate checks are made to ensure that the denominators are not too small and that the crossing time is within the proper range. These checks prevent extrapolation outside the physical range of interest.

## L.2 Three Points

Three data points allows for a second-order Lagrange interpolation to be used. The crossing time is then

$$t_{cross} = \frac{t_1 d_2 d_3}{(d_2 - d_1)(d_3 - d_1)} + \frac{t_2 d_1 d_3}{(d_1 - d_2)(d_3 - d_2)} + \frac{t_3 d_1 d_2}{(d_1 - d_3)(d_2 - d_3)} \quad (\text{L.5})$$

Appropriate checks are made to ensure that the denominators are not too small and that the crossing time is within the proper range. These checks prevent extrapolation outside the physical range of interest.

## L.3 Two Points

When only two data points are available for a pin diagnostic, we resort to linear interpolation to find the crossing time as

$$t_{cross} = \frac{d_2 t_1 - d_1 t_2}{d_2 - d_1} \quad (\text{L.6})$$

Appropriate checks are made to ensure that the denominator is not too small and that the crossing time is within the proper range. These checks prevent extrapolation outside the physical range of interest.

## L.4 One Point

On rare occasions, the material flow is so complicated that only one distance point is available for computing the pin-crossing time. The crossing time is estimated by linear interpolation based on the maximum velocity allowed by the Courant timestep safety factor *safeu*<sup>1</sup> as

$$t_{cross} = t - t_1(d_1/safeu) \quad (\text{L.7})$$

where  $t$  is the current simulation time.

---

<sup>1</sup>See [Chapter 10](#).

## L.5 Zero Points

This pathological case is used when the material interface jumps over the cell containing the pin diagnostic without ever being in the cell at any time. The pin-crossing time is approximated by taking the average of the simulation times surrounding the event as

$$t_{cross} = \frac{1}{2}(t_1 + t_2), \tag{L.8}$$

where  $t_1$  and  $t_2$  are current and previous simulation times, respectively.

# Appendix M

## Tracers

The tracer particle is an important diagnostic tool in PAGOSA. Massless tracer particles are placed in the computational domain, and information at the particle location is recorded for the benefit of the user.

Two types of tracer particles are available-Eulerian and Lagrangian. The Eulerian tracer particle is fixed in space at its original coordinates. However, the Lagrangian tracer moves with the material following the velocity field. Each tracer type has its own unique uses and capabilities.

For example, if the simulation is given of an experiment that has a probe (sensor) fixed at a particular location, the Eulerian tracer particle is the most appropriate choice to use for modeling this probe. In the Taylor Anvil sample problem,[57] the shape and deformation of the projectile is one of the desired measurements. Placing Lagrangian tracer particles on the surface of the projectile allows the diagnostic to move with the material surface. Many other uses for the tracer diagnostic easily can be imagined.

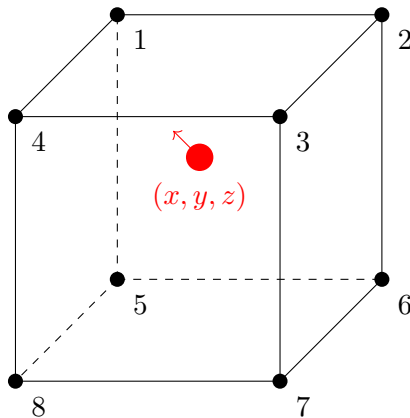


Figure M.1: A tracer particle at  $(x, y, z)$  in an Eulerian cell.

## M.1 Interpolation

The tracer particle begins its life at a point in space within the computational domain and in a single Eulerian cell, as shown in [Figure M.1](#). The velocities are defined at cell vertices ([Chapter 3](#)), and some interpolation is necessary to estimate the velocity at the particle coordinates  $(x, y, z)$ . A tri-linear interpolation formula is used to find the velocity at the tracer location. For the  $U$  velocity, the interpolation appears as

$$U(x, y, z) = a_0 + a_1x + a_2y + a_3z + a_4xy + a_5xz + a_6yz + a_7xyz \quad (\text{M.1})$$

where the coefficients  $a_0 - a_7$  are derived from the eight known velocities at the cell vertices. The other components of velocity are found in the same way.

Once the velocity field is constructed at the point of interest, the Lagrangian tracer particles can be moved by integrating the equations of motion for these massless particles.

## M.2 Integration

The integration applies only to the Lagrangian tracers because the Eulerian tracers are fixed in space and report the changes in quantities as materials sweep past them. The integration scheme follows the same predictor-corrector methodology presented in [Chapter 6](#). The positions of the Lagrangian tracers after one timestep are

$$\mathbf{x}^{n+1/2} = \mathbf{x}^n + \mathbf{u}^n \Delta t / 2 \quad \text{predictor, and} \quad (\text{M.2})$$

$$\mathbf{x}^{n+1} = \mathbf{x}^n + \mathbf{u}^{n+1/2} \Delta t \quad \text{corrector.} \quad (\text{M.3})$$

Because the interpolation point wanders from cell to cell, the interpolated function values change continuously. However, the gradients (velocities and accelerations) of the interpolated function change discontinuously at the boundaries of each cell.

The integration uses the velocity field generated by the Lagrangian-phase integration described in [section 6.1](#), [section 6.2](#), and [section 6.3](#). In theory, it is possible to use the velocity field from the advection-phase solution ([subsection 5.6.1](#)) instead of the Lagrangian-phase solution; some other hydrocodes have this option. PAGOSA uses only the Lagrangian phase velocities.

At the new tracer position, a new interpolation is used to construct the appropriate velocity field and prepare for the next integration step. This process is repeated for the duration of the simulation. Lagrangian tracer particles can fly off the mesh during an integration step. These particles are then lost to the simulation - no further information can be recorded for these particles.

The same tri-linear interpolation is used for all variables of interest associated with the tracer particle. For variables located at cell vertices (e.g.,  $U$ ,  $W$ , and  $Bt$ ), the interpolation coefficients are obtained from the local vertices of the cell containing the tracer particle. For variables located at cell centers (e.g.,  $P$ ,  $Q$ , and  $Bf$ ), the interpolation coefficients are obtained from the cell centers of the vertex volume containing the tracer particle.



## M.3 Comments

The concept of a continuous variable field is useful in constructing a tracer particle diagnostic. However, previously ([Chapter 4](#)) we assumed that the gradients were uniform over the cell volume. No functional form was assumed for the fundamental variables. The tracer diagnostic operates under slightly different assumptions than did the fundamental hydrodynamics.

This concept illustrates an important point. The tracer diagnostic is only a diagnostic tool. For example, a Lagrangian tracer particle placed on a material interface will not exactly follow the movements of that interface. The particle may be in a different cell from the interface. Or the particle may lead or lag the movement of the interface. The interface reconstruction (see [subsection 5.5.1](#), [Appendix C](#), and [Appendix G](#)) is based on a set of algorithms that is different from the algorithms presented in this appendix.

Note that when the material volume fractions in a multi-material cell are adjusted during the Lagrangian phase, a change is implied in the distribution of velocity field in the cell. The movement of the Lagrangian tracer particle depends critically on the sub-cell velocity distribution and needs to be adjusted if the pressure relaxation or void closure divergence options are invoked ([Chapter 14](#)). No adjustments are necessary with the uniform divergence option.



## Appendix N

# Symmetry of the stress tensor

Let the body force in the continuum be specified by  $F_k$  and the stresses by the tensor field  $T_{ij}$ . The body force  $\rho F_k dV$  acting on a volume element with the radius vector  $x_j$  has a moment  $\varepsilon_{ijk} x_j \rho F_k$ <sup>1</sup> with respect to the coordinate origin. The volume element  $dV$  has a surface denoted by  $dS$ , and a unit exterior normal denoted by  $n_r$ . The surface force  $T_{ij} n_i dS$  that is transmitted across  $dS$  on the continuum has a moment  $\varepsilon_{ijk} x_j T_{rk} n_r dS$  with respect to the origin. Assuming that the body forces are in equilibrium with the surface forces in the continuum we must have:

$$\int T_{ij} n_i dS + \int \rho F_j dV = 0 \quad (\text{N.1})$$

Using Gauss' divergence theorem<sup>2</sup>, we find that

$$\int [T_{ij,i} \rho F_j] dV = 0 \quad (\text{N.2})$$

Since the integral must vanish for *any* arbitrary volume, it follows that the integrand must be zero:

$$[T_{ij,i} \rho F_j] = 0 \quad (\text{N.3})$$

The moment must also be in equilibrium, so that

$$\int \varepsilon_{ijk} x_j T_{rk} n_r dS + \int \varepsilon_{ijk} x_j \rho F_k dV = 0 \quad (\text{N.4})$$

Applying Ostrogradsky's formula once again, we find that

$$\begin{aligned} \int \varepsilon_{ijk} x_j T_{rk} n_r dS &= \int (\varepsilon_{ijk} x_j T_{rk})_{,r} dV \\ &= \int \varepsilon_{ijk} x_{j,r} T_{rk} dV + \int \varepsilon_{ijk} x_j T_{rk,r} dV \\ &= \int \varepsilon_{ijk} T_{jk} dV + \int \varepsilon_{ijk} x_j T_{rk,r} dV \end{aligned} \quad (\text{N.5})$$

---

<sup>1</sup>Here  $\varepsilon_{ijk}$  is the permutation symbol

<sup>2</sup>Known to our comrades as Ostrogradsky's formula

The moment equation thus becomes

$$\int [\varepsilon_{ijk}T_{jk} + \varepsilon_{ijk}x_jT_{rk,r} + \varepsilon_{ijk}x_j\rho F_k]dV = 0 \quad (\text{N.6})$$

or

$$\int \varepsilon_{ijk}[T_{jk} + x_j(T_{rk,r} + \rho F_k)]dV = 0 \quad (\text{N.7})$$

The term in the parentheses (...) is zero, so the integral equation becomes

$$\int \varepsilon_{ijk}T_{jk}dV = 0 \quad (\text{N.8})$$

Again, as this applies to *any* volume element, the integrand must vanish:

$$\varepsilon_{ijk}T_{jk}dV = 0 \quad (\text{N.9})$$

Let  $t_i$  be a vector such that

$$t_i = \varepsilon_{ijk}T_{jk} \quad (\text{N.10})$$

Multiply both sides by the Levi-Civita pseudotensor:

$$\begin{aligned} \varepsilon_{irs}t_i &= \varepsilon_{irs}\varepsilon_{ijk}T_{jk} \\ &= (\delta_{rj}\delta_{sk} - \delta_{rk}\delta_{sj})T_{jk} \\ &= T_{rs} - T_{sr} \end{aligned} \quad (\text{N.11})$$

however, since  $t_i = 0$ , we find that the stress tensor is symmetric<sup>3</sup>:

$$T_{ij} = T_{ji} \quad (\text{N.12})$$

The stress tensor can be decomposed into its polar and deviatoric parts as:

$$T_{ij} = -P\delta_{ij} + S_{ij} \quad (\text{N.13})$$

Exchanging the indices of the stress tensor, we find tha

$$T_{ji} = -P\delta_{ji} + S_{ji} \quad (\text{N.14})$$

Since the stress tensor and the Kronecker delta are both symmetric, we deduce that the deviatoric stress tensor is also symmetric:

$$S_{ij} = S_{ji} \quad (\text{N.15})$$

The symmetry of the stress and deviatoric tensors arise from the conservation of angular momentum expresses through the moment equation.

---

<sup>3</sup>This would not be true if a body moment existed, for example, from a dipole of electric charge in the continuum

## Appendix O

# Operator splitting revisited

Consider a homogeneous PDE, similar to [Equation 2.2a](#)

$$\frac{\partial \phi}{\partial t} + U \frac{\partial \phi}{\partial x} + V \frac{\partial \phi}{\partial y} + W \frac{\partial \phi}{\partial z} = 0 \quad (\text{O.1})$$

First, let use expand the function  $\phi$  using a Taylor series:

$$\phi(t + \Delta t, x, y, z) = \phi(t, x, y, z) + \Delta t \frac{\partial \phi}{\partial t} + \frac{1}{2!} \Delta t^2 \frac{\partial^2 \phi}{\partial t^2} + \mathcal{O}(\Delta t^3) \quad (\text{O.2})$$

Differentiating [Equation O.1](#) with respect to time, we get

$$\begin{aligned} \frac{\partial^2 \phi}{\partial t^2} &= -U \frac{\partial^2 \phi}{\partial t \partial x} - V \frac{\partial^2 \phi}{\partial t \partial y} - W \frac{\partial^2 \phi}{\partial t \partial z} \\ &= -U \frac{\partial}{\partial x} \frac{\partial \phi}{\partial t} - V \frac{\partial}{\partial y} \frac{\partial \phi}{\partial t} - W \frac{\partial}{\partial z} \frac{\partial \phi}{\partial t} \\ &\quad - U \frac{\partial}{\partial x} \left[ -U \frac{\partial \phi}{\partial x} - V \frac{\partial \phi}{\partial y} - W \frac{\partial \phi}{\partial z} \right] \\ &\quad - V \frac{\partial}{\partial x} \left[ -U \frac{\partial \phi}{\partial x} - V \frac{\partial \phi}{\partial y} - W \frac{\partial \phi}{\partial z} \right] \\ &\quad - W \frac{\partial}{\partial x} \left[ -U \frac{\partial \phi}{\partial x} - V \frac{\partial \phi}{\partial y} - W \frac{\partial \phi}{\partial z} \right] \\ &= U^2 \frac{\partial^2 \phi}{\partial x^2} + V^2 \frac{\partial^2 \phi}{\partial y^2} + W^2 \frac{\partial^2 \phi}{\partial z^2} \\ &\quad + 2UV \frac{\partial^2 \phi}{\partial x \partial y} + 2UW \frac{\partial^2 \phi}{\partial x \partial z} + 2VW \frac{\partial^2 \phi}{\partial y \partial z} \end{aligned} \quad (\text{O.3})$$

Substituting into Equation O.2 produces

$$\begin{aligned}
\phi(t + \Delta t, x, y, z) = & \phi(t, x, y, z) - \Delta t U \frac{\partial \phi}{\partial x} - \Delta t V \frac{\partial \phi}{\partial y} - \Delta t W \frac{\partial \phi}{\partial z} \\
& + \frac{1}{2} \Delta t^2 U^2 \frac{\partial^2 \phi}{\partial x^2} + \frac{1}{2} \Delta t^2 V^2 \frac{\partial^2 \phi}{\partial y^2} + \frac{1}{2} \Delta t^2 W^2 \frac{\partial^2 \phi}{\partial z^2} \\
& + \Delta t^2 UV \frac{\partial^2 \phi}{\partial x \partial y} + \Delta t^2 UW \frac{\partial^2 \phi}{\partial x \partial z} + \Delta t^2 VW \frac{\partial^2 \phi}{\partial y \partial z} \\
& + \mathcal{O}(\Delta t^3)
\end{aligned} \tag{O.4}$$

Let us define an operator  $L$  such that

$$\begin{aligned}
L(\Delta t) = & 1 - \Delta t \left\{ U \frac{\partial}{\partial x} + V \frac{\partial}{\partial y} + W \frac{\partial}{\partial z} \right\} \\
& + \frac{1}{2} \Delta t^2 \left\{ U^2 \frac{\partial^2}{\partial x^2} + V^2 \frac{\partial^2}{\partial y^2} + W^2 \frac{\partial^2}{\partial z^2} + 2UV \frac{\partial^2}{\partial x \partial y} + 2UW \frac{\partial^2}{\partial x \partial z} + 2VW \frac{\partial^2}{\partial y \partial z} \right\}
\end{aligned} \tag{O.5}$$

so that we can write

$$\phi(t + \Delta t, x, y, z) = L(\Delta t) \phi(t, x, y, z) + \mathcal{O}(\Delta t^3) \tag{O.6}$$

For simplicity, we can split the original PDE into three one-dimensional advection equations:

$$\frac{\partial \phi}{\partial t} + U \frac{\partial \phi}{\partial x} = 0 \tag{O.7a}$$

$$\frac{\partial \phi}{\partial t} + V \frac{\partial \phi}{\partial y} = 0 \tag{O.7b}$$

$$\frac{\partial \phi}{\partial t} + W \frac{\partial \phi}{\partial z} = 0 \tag{O.7c}$$

Following the technique developed for the full 3D operator, we find

$$L_x(\Delta t) = 1 - \Delta t \left\{ U \frac{\partial}{\partial x} \right\} + \frac{1}{2} \Delta t^2 \left\{ U^2 \frac{\partial^2}{\partial x^2} \right\} \tag{O.8a}$$

$$L_y(\Delta t) = 1 - \Delta t \left\{ V \frac{\partial}{\partial y} \right\} + \frac{1}{2} \Delta t^2 \left\{ V^2 \frac{\partial^2}{\partial y^2} \right\} \tag{O.8b}$$

$$L_z(\Delta t) = 1 - \Delta t \left\{ W \frac{\partial}{\partial z} \right\} + \frac{1}{2} \Delta t^2 \left\{ W^2 \frac{\partial^2}{\partial z^2} \right\} \tag{O.8c}$$

$$\tag{O.8d}$$

Consider the operator sequence

$$L_z L_y L_x$$

We wish to show that this sequence is “the same” as  $L$  in Equation O.5, which we know solves the original 3D PDE, Equation O.1. By “the same,” it is enough to show that the difference is an

appropriate order of  $\Delta t$ . Expanding the sequence of operators gives:

$$\begin{aligned}
L_z L_y L_x &= \left[ 1 - \Delta t \left\{ U \frac{\partial}{\partial x} \right\} + \frac{1}{2} \Delta t^2 \left\{ U^2 \frac{\partial^2}{\partial x^2} \right\} \right] \\
&\cdot \left[ 1 - \Delta t \left\{ V \frac{\partial}{\partial x} \right\} + \frac{1}{2} \Delta t^2 \left\{ V^2 \frac{\partial^2}{\partial y^2} \right\} \right] \\
&\cdot \left[ 1 - \Delta t \left\{ W \frac{\partial}{\partial x} \right\} + \frac{1}{2} \Delta t^2 \left\{ W^2 \frac{\partial^2}{\partial z^2} \right\} \right] \\
&= 1 - \Delta t \left[ U \frac{\partial}{\partial x} + V \frac{\partial}{\partial y} + W \frac{\partial}{\partial z} \right] \\
&\quad - \frac{1}{2} \Delta t^2 \left[ U^2 \frac{\partial^2}{\partial x^2} + V^2 \frac{\partial^2}{\partial y^2} + W^2 \frac{\partial^2}{\partial z^2} + 2UV \frac{\partial^2}{\partial x \partial y} + 2UW \frac{\partial^2}{\partial x \partial z} + 2VW \frac{\partial^2}{\partial y \partial z} \right] \\
&\quad + \mathcal{O}(\Delta t^3)
\end{aligned} \tag{O.9}$$

which shows that

$$L_z L_y L_x = L + \mathcal{O}(\Delta t^3) \tag{O.10}$$

Thus, the sequence of one-dimensional operator,  $L_z L_y L_x$  is “the same” as the three dimensional operator up to  $\mathcal{O}(\Delta t^3)$ .





## Appendix P

# Direction cosines (Normal vectors)

The direction vector (interface normal) for a material is computed from the distribution of volume fractions surrounding the mixed cell. The mixed cell and the twenty-six cells surrounding the mixed cell are used to compute the gradients.

The first step in the process is to construct nodal averages of the volume fractions. Every node is surrounded by eight cells. The nodal volume fraction, for the material of interest, is computed as a simple average of these eight cell volume fractions. Let the nodal volume fractions, for material ( $m$ ), be designated by  $\hat{\phi}^m$ .

Once the volume fractions are averaged to the nodes, the derivatives of the volume fractions can be computed for each direction.

$$\vec{\mu} = \frac{\nabla \hat{\phi}_m}{|\nabla \hat{\phi}_m|} \quad (\text{P.1})$$

The partial derivatives are computed the same way the strain rates are computed in [Chapter 4 \[Equation 4.6\]](#). For example, the first component of the direction vector

$$\mu_1 = \frac{\partial \hat{\phi}}{\partial x} \rightarrow \frac{\bar{\phi}_i - \bar{\phi}_{i-1}}{\Delta x} \quad (\text{P.2})$$

where  $\bar{\phi}$  are the face centered volume fractions. Notice that this process has incorporated two averaging processes in the gradient computation. The other components of the direction vector are computed in the same way. The computed gradient contains information from 27 cells ( $3 \times 3 \times 3$ ) and is thought to be a good approximation to the normal of the material surface.

Graphic examples of the direction vectors (normals) can be seen in [Figure 5.2](#), [Figure C.1](#), [Figure G.1](#), [Figure G.2](#), and [Figure G.3](#).

The initial direction vectors  $\vec{\mu}$  are strongly related to the initial volume fraction computation ([Appendix B](#)). A poor choice of sample density (particle throw) will inevitably lead to a poor interface normal (direction vector) and the resulting interface. The material interfaces can be viewed with Enight<sup>®</sup>. Experience is the best guide to understanding the relationship between the particle throw and interfaces.

There is an interesting and rich literature associated with this subject. The interested reader can start with various references. [\[110, 21, 111, 112\]](#)



# References

- [1] J. Zukas. *Introduction to Hydrocodes*, volume 49. Elsevier, 2004.
- [2] L. Landau, E. Lifshitz. *Fluid Mechanics*. Pergamon Press, Addison-Wesley Publishing Company, Inc., 1959.
- [3] G. Batchelor. *An Introduction to Fluid Dynamics*. Cambridge University Press, New York, New York, 2000.
- [4] I. Sokolnikoff. *Mathematical Theory of Elasticity*. McGraw-Hill, New York, 1956.
- [5] D. Drew, S. Passman. *Theory of Multicomponent Fluids (Applied Mathematical Sciences 135)*.
- [6] S. E. Whittaker. *A History of the Theories of Aether and Electricity*. Dover Publications Inc., Mineola, New York, 1989.
- [7] W. H. Press, B. P. Flannery, S. A. Teukolsky, W. T. Vetterling. *Numerical Recipes in Fortran: The Art of Scientific Computing*. Cambridge University Press, New York, New York, 1992.
- [8] M. Shashkov. *Conservative Finite-Difference Methods on General Grids*. p. 6. CRC Press, Boca Raton, Florida, 1996.
- [9] F. Harlow, J. Welch. *Numerical Calculation of Time-Dependent Viscous Incompressible Flow of Fluid with Free Surface*. The Physics of Fluids, **8**, 2182 , 1965.
- [10] W. Johnson. *OIL, A Continuous Two Dimensional Eulerian Hydrodynamic Code*. Technical Report GAMD-5580, General Atomic, 1965.
- [11] C. Hirt, B. Nichols. *Volume of Fluid (VOF) Method for the Dynamics of Free Boundaries*. Journal of Computational Physics, **39**, 201 , 1981.
- [12] R. Richtmyer, K. Morton. *Difference Methods for Initial-Value Problems*. Krieger Publishing Company, Malabar Florida, 2 edition, 1994.
- [13] P. Morse, H. Feshbach. *Methods of Theoretical Physics, Part I*. McGraw Hill, New York, 1953.
- [14] G. Strang. *On the Construction and Comparison of Difference Schemes*. SIAM Journal of Numerical Analysis, **5**, 506 .
- [15] G. Marchuk. *Methods of Numerical Mathematics*. Springer-Verlag, New York, 2 edition, 1982.
- [16] D. Gottlieb. *Strang-Type Difference Schemes for Multi-Dimensional Problems*. SIAM Journal of Numerical Analysis, **9**, 650 , 1972.

- [17] C. Zemach. *Notes on Calculation of the Volume of a Stretched Cube behind a Truncating Volume*. Technical Report LA-UR-07-2274, Los Alamos National Laboratory, 2007.
- [18] D. L. Youngs. *Time-Dependent Multi-Material Flow with Large Fluid Distortion*. In K. Morton, M. Baines, editors, *Numerical Methods for Fluid Dynamics*, pp. 273 – 285. Academic Press, London England, 1982.
- [19] W. Weseloh. *PAGOSA Input Reference Manual Version 17.0*. Los Alamos National Laboratory, 2010.
- [20] A. Caboussat, M. Francois, R. Glowinski, D. Kothe, J. Sicilian. *A Numerical Method for Interface Reconstruction of Triple Points within a Volume Tracking Algorithm*. Mathematical and Computer Modelling, **48**, 1957 , 2008.
- [21] J. E. P. Jr., E. G. Puckett. *Second-Order Accurate Volume-of-Fluid Algorithms for Tracking Material Interfaces*. Journal of Computational Physics, **199**, 465 , 2004.
- [22] B. van Leer. *Towards the Ultimate Conservative Difference Scheme IV. A New Approach to Numerical Convection*. Journal of Computational Physics, **23**, 276 , 1977.
- [23] G. Forsythe, W. Wasow. *Finite Difference Methods for Partial Differential Equations*. Wiley, Hoboken, New Jersey, 1960.
- [24] A. Iserles, G. Strang. *The Optimal Accuracy of Difference Schemes*. Transactions of the American Mathematical Society, **277**, 779 , 1983.
- [25] D. J. Benson. *Momentum Advection on a Staggered Mesh*. Journal of Computational Physics, **100**, 143 , 1992.
- [26] R. Douglass, A. Stagg. *A Vertex-Staggered Hydrodynamics Model for Compressible Flows*. Technical Report LA-UR-07-6986, Los Alamos National Laboratory, 2007.
- [27] R. Feynman, N. Metropolis, E. Teller. *Equations of State of Elements Based on the Generalized Fermi-Thomas Theory*. Physical Review, **75**, 1561, 1949.
- [28] F. Harlow, W. Pracht. *Formation and Penetration of High-Speed Collapse Jets*. The Physics of Fluids, **9**, 1951 , 1966.
- [29] T. Riney. *Numerical Evaluation of Hypervelocity Impact Phenomena*. In R. Kinslow, editor, *High Velocity Impact Phenomena*, pp. 157 – 212. Academic Press, New York/London, 1970.
- [30] B. Lambourn. *Density Scaling for the Osborne Equation of State*. Technical Report HWH Note No. 3/80, Atomic Weapons Research Establishment (AWRE), Aldermaston, Berkshire, UK, 1980.
- [31] E. Lee, H. Hornig, J. Kury. *Adiabatic Expansion of High Explosive Detonation Products*. Technical Report UCRL-50422, Lawrence Radiation Laboratory, University of California, 1968.
- [32] H. Jones, A. Miller. *The Detonation of Solid Explosives: The Equilibrium Conditions in the Detonation Wave-Front and the Adiabatic Expansion of the Products of Detonation*. Proceedings of the Royal Society of London. Series A, Mathematical and Physical Sciences, **194**, 480 , 1948.
- [33] M. Wilkins. *The Equation of State of PBX 9404 and LX04-01*. Technical Report UCRL-7797, Lawrence Radiation Laboratory, University of California, 1964.

- [34] B. M. Dobratz. *Properties of Chemical Explosives and Explosive Simulants*. Technical Report UCRL-14592, Lawrence Livermore Laboratory, University of California, 1974.
- [35] M. van Thiel, A. Kusubov, A. Mitchell. *Compendium of Shock Wave Data*. Technical Report UCRL-50108, Volume 1, Supplement 1, Lawrence Radiation Laboratory, University of California, 1967.
- [36] S. P. Marsh. *LASL Shock Hugoniot Data*, 1980.
- [37] Y. Zel'dovich, Y. Raizer. *Physics of Shock Waves and High Temperature Hydrodynamic Phenomena*. Dover Publications, Mineola, New York, 2002.
- [38] S. Lyon, J. Johnson. *SESAME: the Los Alamos National Laboratory equation of state database*. Technical Report LA-UR-92-3407, Los Alamos National Laboratory, 1992.
- [39] K. Holian. *T-4 Handbook of Material Properties Data Bases, Volume Ic: Equations of State*. Technical Report LA-10160-MS, Los Alamos National Laboratory, 1984.
- [40] D. A. Pimentel. *EOSPAC 5 User Manual*. Technical Report LA-UR-03-4510, Version 5.35, Revision 0, Los Alamos National Laboratory, 2003.
- [41] W. Weseloh. *The Response of a Spherical Shell to an Impulsive Pressure*. Technical Report LA-UR-04-1683, Los Alamos National Laboratory, 2004.
- [42] B. Wescott, D. Stewart, W. Davis. *Equation of state and reaction rate for condensed-phase explosives*. Journal of Applied Physics, **98**, 2005.
- [43] T. Aslam. *Shock temperature dependent rate law for plastic bonded explosives*. Journal of Applied Physics, **123**, 2018.
- [44] C. Mader. *Numerical Modeling of Explosives and Propellants*. CRC Press, Boca Raton, Florida, 2 edition, 1998.
- [45] J. Walsh, R. Christian. *Equation of State for Metals from Shock Wave Measurements*. Physical Review, **97**, 1544 , 1955.
- [46] J. von Neumann, R. D. Richtmyer. *A Method for the Numerical Calculation of Hydrodynamic Shocks*. Journal of Applied Physics, **21**, 232 , 1950.
- [47] R. Landshoff. *A Numerical Method for Treating Fluid Flow in the Presence of Shocks*. Technical Report LA-1930, Los Alamos Scientific Laboratory, 1955.
- [48] W. Noh. *Errors for Calculations of Strong Shocks Using an Artificial Viscosity and an Artificial Heat Flux*. Technical Report UCRL-53669, Lawrence Livermore National Laboratory, 1985.
- [49] W. Noh. *Errors for Calculations of Strong Shocks Using an Artificial Viscosity and an Artificial Heat Flux*. Journal of Computational Physics, **72**, 78 , 1987.
- [50] M. Wilkins. *Use of Artificial Viscosity in Multidimensional Fluid Dynamic Calculations*. Journal of Computational Physics, **36**, 281 , 1980.
- [51] R. Courant, K. Friedrichs, H. Lewy. *Über die Partiellen Differenzengleichungen der Mathematischen Physik*. Mathematische Annalen, **100**, 32 , 1928.
- [52] T. Bennion, S. Clancy, W. Weseloh. *The PAGOSA 3D Programmed Burn Algorithm*. Technical Report LA-UR-09-04016, Revision 1, Los Alamos National Laboratory, 2009.

- [53] J. Zukas, W. Walters. *Explosive Effects and Applications*. Springer-Verlag Inc., New York, New York, 1998.
- [54] P. Cooper. *Explosives Engineering*. Wiley-VCH, New York, New York, 1996.
- [55] B. Bdzil, D. Stewart, T. Jackson. *Program Burn Algorithms Based on Detonation Shock Dynamics: Discrete Approximations of Detonation Flows with Discontinuous Front Models*. Journal of Computational Physics, **174**, 870 , 2001.
- [56] D. Lambert, D. Scott, S. Yoo, B. Wescott. *Experimental Validation of Detonation Shock Dynamics in Condensed Explosives*. Journal of Fluid Mechanics, **546**, 227 , 2006.
- [57] W. Weseloh. *PAGOSA sample problems*. Los Alamos National Laboratory, 2005.
- [58] V. Ransom, D. Hicks. *Hyperbolic Two-Pressure Models for Two-Phase Flow*. Journal of Computational Physics, **53**, 124 , 1984.
- [59] R. Feynman, R. Leighton, M. Sands. *The Feynman Lectures on Physics: Commemorative Issue, Three Volume Set*. Addison Wesley, Reading, Massachusetts, 1989.
- [60] P. Maudlin. *Constitutive Behavior of Model FCC, BCC, and HCP Metals: Experiments, Modeling and Validation*. Technical Report LA-UR-98-4891, Los Alamos National Laboratory, 1999.
- [61] J. J. Gilman. *Micromechanics of Flow in Solids*. McGraw-Hill, New York, New York, 1969.
- [62] A. Freudenthal, M. W. Geiringer. *The Mathematical Theories of the Inelastic Continuum*. In *Handbuch der Physik*, volume VI. Springer-Verlag, New York, New York, 1958.
- [63] R. von Mises. *Mechanik der Festen Korper im Plastisch Deformablen Zustand*. Göttingen Nachrichten Mathematische Physik, **1**, 582 , 1913.
- [64] D. Steinberg, S. Cochran, M. Guinan. *A Constitutive Model for Metals Applicable at High-Strain Rate*. Journal of Applied Physics, **51**, 1498 , 1980.
- [65] G. Johnson, W. Cook. *A Constitutive Model and Data for Metals Subjected to Large Strains, High Strain Rates, and High Temperatures*. In *Proceedings of Seventh International Symposium on Ballistics*, pp. 541 – 548. The Hague, The Netherlands, 1983.
- [66] D. Preston, D. Tonks, D. Wallace. *Model of Plastic Deformation for Extreme Loading Conditions*. Journal of Applied Physics, **93**, 211 , 1999.
- [67] P. Maudlin, R. Davidson, R. Henninger. *Implementation and Assessment of the Mechanical-Threshold-Stress Model Using EPIC2 and PINON Computer Codes*. Technical Report LA-11895-MS, Los Alamos National Laboratory, 1990.
- [68] D. Steinberg, M. Guinan. *Constitutive Relations for the KOSPALL code*. Technical Report UCID-16326, Lawrence Livermore National Laboratory, 1973.
- [69] J. Holloman, J. Lubahn. *Plastic Flow of Metals*. Physical Review, **70**, 775, 1946.
- [70] A. Bowen, P. Partridge. *Limitations of the Hollomon Strain-Hardening Equation*. Journal of Physics D, Applied Physics, **7**, 969 , 1974.
- [71] P. Ludwik. *Elemente der Technologischen Mechanik*. Springer, Berlin, Germany, 1909.

- [72] B. Clements, X. Ma. *Mechanically Activated Thermal CHEmistry (MATCH) model for PAGOSA users*. Technical Report LA-CP-18-20483, Los Alamos National Laboratory, 2018.
- [73] R. Menikoff, M. Shaw. *Reactive burn models and ignition and growth concept*. EPJ Web of Conferences, **10**, 2010.
- [74] J. S. Rinehart, J. Pearson. *Behavior of Metals under Impulsive Load*. Dover Publications Inc., New York, New York, 1954.
- [75] J. Johnson. *Dynamic Fracture and Spallation in Ductile Solids*. Journal of Applied Physics, **52**, 2812 , 1981.
- [76] J. Mackenzie. *The Elastic Constants of a Solid Containing Spherical Holes*. In *Proceeding of the Physical Society, Section B*, volume 63, pp. 2 – 11, 1950.
- [77] G. Johnson, W. Cook. *Fracture Characteristics of Three Metals Subjected to Various Strain Rates, Temperatures, and Pressures*. Engineering Fracture Mechanics, **21**, 31 , 1985.
- [78] G. Kerley. *CTH Equation of State Package: Porosity and Reactive Burn Models*. Technical Report SAND92-0553, Sandia National Laboratories, 1992.
- [79] W. Hermann. *Constitutive Equation for the Dynamic Compaction of Ductile Porous Materials*. Journal of Applied Physics, **40**, 2490 , 1969.
- [80] M. Carroll, A. Holt. *Static and Dynamic Pore-Collapse Relations for Ductile Porous Materials*. Journal of Applied Physics, **43**, 1626 , 1972.
- [81] B. Kashiwa, R. Ramuenzahn. *FLIP recipes: an evolving notebook*. Technical Report LA-UR-11-01860 ; LA-UR-11-1860, Los Alamos National Laboratory, 2011. Sponsor: DOE.
- [82] J. Brackbill, H. Ruppel. *FLIP: A method for adaptively zoned, particle-in-cell calculations of fluid flows in two dimensions*. Journal of Computational Physics, **65**, 314, 1986.
- [83] D. Sulsky, Z. Chen, H. Schreyer. *A particle method for history-dependent materials*. Computer Methods in Applied Mechanics and Engineering, **118**, 179 , 1994.
- [84] B. Kashiwa, R. Rauenzahn. *FLIP recipes: an evolving notebook*. Technical Report LA-UR-11-01860, Los Alamos National Laboratory, 2011. LA-UR-11-01860.
- [85] J. Dukowicz, J. Ramshaw. *Tensor viscosity method for convection in numerical fluid dynamics*. Journal of Computational Physics, **32**, 71 , 1979.
- [86] B. Kashiwa. *The MGGB equation-of-state for multifield applications : a numerical recipe for analytic expression of sesame EOS data*. Technical Report LA-14421, Los Alamos National Laboratory, 2010. Sponsor: DOE.
- [87] B. de Saint-Venant. *Note à Joindre au Mémoire sur la Dynamique des Fluids*. Comptes Rendus, **17**, 1240 , 1843. Originally presented on April 14, 1834.
- [88] G. Stokes. In *Transactions of the Cambridge Philosophical Society*, volume 8, p. 287, 1845. Also appears in the collected works G.G. Stokes, Mathematical and Physical Papers, Volume I, p. 75.
- [89] G. Arfken. *Mathematical Methods for Physicists*. Academic Press Inc., Harcourt Brace Jovanovich Publishers, Orlando Florida, 1970. It is sometimes called the permutation symbol.
- [90] H. Jeffreys. *Cartesian Tensors*. Cambridge University Press, New York, New York, 1979.

- [91] J. Painter. *An Overview of Particle Mapping for Generation of Material Volume Fractions in PAGOSA*. Technical Report LA-UR-11-00898, Los Alamos National Laboratory, 2011.
- [92] L. Dickson. *Note on the Volume of a Tetrahedron in Terms of the Coordinates of the Vertices*. The American Mathematical Monthly, **14**, 117 , 1907.
- [93] R. L. Bowers, J. R. Wilson. *Numerical Modeling in Applied Physics and Astrophysics*. Jones and Bartlett Publishers, Boston, Massachusetts, 1991.
- [94] B. van Leer. *Upwind and High-Resolution Methods for Compressible Flow: From Donor Cell to Residual-Distribution Schemes*. Communications in Computational Physics, **1**, 192 , 2006.
- [95] W. Weseloh. *An Advection Algorithm of Arbitrary Order using Polynomials*. Technical Report LA-UR-09-01193, Los Alamos National Laboratory, 2009.
- [96] W. Weseloh. *Finite Difference Solutions of the Advection Equation on a Non-Uniform Mesh*. Technical Report LA-UR-09-02187, Los Alamos National Laboratory, 2009.
- [97] B. van Leer. *Towards the Ultimate Conservative Difference Scheme V. A Second-Order Sequel to Godunov's Method*. Journal of Computational Physics, **32**, 101 , 1979.
- [98] R. J. LeVeque. *Numerical Methods for Conservation Laws*. Birkhäuser Verlag, New York, New York, 2 edition, 1992.
- [99] R. B. DeBar. *Fundamentals of the KRAKEN Code*. Technical Report UCIR760, Lawrence Livermore Laboratory, University of California, 1974.
- [100] D. R. Durran. *Numerical Methods for Wave Equations in Geophysical Fluid Dynamics*. Springer Verlag, New York, New York, 1999.
- [101] L. L. Tackas. *A Two-Step Scheme for the Advection Equation with Minimized Dissipation and Dispersion Errors*. Monthly Weather Review, **113**, 1050 , 1985.
- [102] W. Crowley. *Numerical Advection Experiments*. Monthly Weather Review, **96**, 1 , 1968.
- [103] D. Cauchy. *Mémoire sur les Dilatations, les Condensations et les Rotations Produites par un Changement de Forme dans un Système de Points Matériels*. In *Oeuvres Complètes D'Augustin Cauchy (Series 2)*, volume 12, pp. 343 – 367. Gauthier-Villars et Fils, Imprimeurs-Libraires du Bureau des Longitudes, de Lécole Polytechnique, Paris, 1841.
- [104] J. Dienes. *Analysis of Rotation and Stress Rate in Deforming Bodies*. Acta Mechanica, **32**, 217 , 1979.
- [105] G. Holzapfel. *Nonlinear Solid Mechanics*. John Wiley and Sons, Weinheim, Germany, 2001.
- [106] J. Synge, A. Schild. *Tensor Calculus*. Dover Publications Inc., Mineola, New York, 1978.
- [107] Jaumann. *Geschlossenes System Physikalischer und Chemischer Differentialgesetze*. Sitzungsberichte Akademie Wissenschaften Wien, **IIa**, 120, 1911.
- [108] S. Zaremba. *Sur une Forme Perfectionnée de la théorie de la Relaxation*. Bulletin International de l'Academie des Sciences de Cracovie, pp. 592 – 614, 1903.
- [109] *Mathematical Foundations of Elasticity*. (Prentice-Hall, Inc., Englewood Cliffs, New Jersey, 1983.



- [110] B. Parker, D. Youngs. *Two and Three Dimensional Eulerian Simulation of Fluid Flow with Material Interfaces*. Technical Report AWE 01/92, Atomic Weapons Establishment, 1992.
- [111] D. Kothe, W. Rider, S. Mosso, J. Brock, J. Hochstein. *Volume Tracking of Interfaces having Surface Tension in Two and Three Dimensions*. Technical Report LA-UR-96-0088, Los Alamos National Laboratory, 1996. Submitted to the AIAA 34th Science Meeting, Reno, Nevada (January 15- 18, 1996).
- [112] D. Benson. *Volume of Fluid Interface Reconstruction Methods for Multi- Material Problems*. Applied Mechanics Review, **55**, 151 , 2002.

# Index

- P*- $\alpha$  crush model, 132
- acceleration, 45
- adiabatic, 51
- advection, 2, 3, 30, 35
  - 1D, 36
  - derivation, 34
  - donor cell, 38
  - energy, 40
  - equation, 35
  - equation integration, 38
  - Lagrange plus advection steps, 34
  - limiters, 39
  - material priority, 35
  - orthogonal directions, 32
  - permutation order, 32
  - phase equations, 30
  - remap, 3
  - third order, 37
  - typical sequence, 31
  - volume fraction computation, 34
- advection volume, 171
- angular momentum, 10
- antisymmetrical, 11
- Arrhenius, 61
- arrival times, 191
- artificial viscosity, 2, 3, 33
  - entropy, 77
  - expansion vs. compression, 76
  - introduction, 76
  - linear form, 76
  - Q notation, 33, 76
  - spreading the shock, 78
- atomic mass, 55
- AWSD, 96
- AWSD Reactive Burn Model, 60
- axial vector associated with the vorticity tensor, 177
- bisection method, 58
- Bodner-Partom, 124
- boundary conditions, 3, 7, 10, 16, 86
  - other, 89
  - reflective, 21, 86
  - transmissive, 21, 87
- brittle, 107
- bulk modulus, 51, 55
- burn, 11
- burn time, 52
- burn times, 92
- Cartesian, xviii, 2
- Cauchy stress tensor, 108
- CD-ROM, 63
- cell
  - average pressure, 18
  - boundary density gradient, 38
  - cell-centered, 2
  - characteristic speed, 35
  - coordinates, 16
  - definition, 16
  - density, 33
  - density at boundary, 37
  - Eulerian, 33, 34
  - face, 18
  - gradients in, 24
  - information flow, 38
  - initial conditions for, 84
  - interface reconstruction, 51
  - interfaces, 35
  - mass flow across, 37
  - mixed, 18
  - mixed, divergence, 98
  - particle-in-cell, 2
  - pressure, 33
  - pure, 18
  - sampling for initial volume, 18
  - staggered, 17
  - surface area, 24

- transport through face, 3
- traversal time, 101
- upstream side, 37
- vertices, 17
- volume, 16
- cell centers, 17
- Chapman-Jouget, 92
- Chapman-Jouget adiabat, 53
- CJ Volume, 96
- coarse particle sampling, 147
- cold curve, 55
- compression, 2, 32
- conservation law
  - advection phase, 29
  - energy, 10
  - lagrangian phase, 29
  - mass, 10
  - momentum, 10
  - predictor-corrector, 46
- conservation laws, 3
- constitutive relation, 10, 46
- controlling timestep, 80
- corrector, 3, 7, 33, 45
- Courant number, 37
- Courant-Friedrichs-Lewy (CFL), 80
- crush, 11, 43, 56
- crush curve, 56
- CTH, 132
- cube
  - slicing with a plane, 153
- damage, 11
- decomposition theorem, 177
- DEFLAGRATE, 124
- Deflagration Model, 125
- density, 2, 50
- detonation, 92
  - limits of detonators, 94
  - simple cylinder, 93
  - simple line, 93
  - simple plane, 93
  - simple point, 92
  - simple ring, 94
  - simple sphere, 94
- detonation products, 52
- detonation velocity, 71
- deviatoric stress tensor, 10
- diagnostics, 185
- elastic distortional energy, 186
- internal energy, 185
- kinetic energy, 186
- mass, 185
- mass burned, 187
- mass melted, 186
- minimum and maximum statistics, 187
- mixed-cell statistics, 187
- plastic work, 186
- volume, 185
- dilatation, 11, 108
- direction cosines, 151
- direction vector, 34, 172
- discretized, 17
- distention ratio, 128, 132
- divergence, 26, 46, 108
  - pressure relaxation, 100
  - uniform, 98
  - void closure, 98
- divergence theorem, 24
- donor, 37, 39
- donor cell, 2
- downwind, 37, 39
- dual mesh, 19
- ductile, 107
- DynaBurn, 96
- dynamic tensile strength, 66
- elastic, 106
  - distortional energy, 46
  - versus plastic, 3
- elastic distortional energy, 12, 46
- elastic limit, 106
- elastic modulus, 106
- elastic predictor, 113
- elastic wave, 73
- Elastic-Perfectly-Plastic, 11
- elastic-plastic algorithm, 109
- elastic-plastic distortions, 111
- elastic-plastic transitions, 113
- energy, 3
  - conservation, 10, 29
  - elastic distortional, 46
- energy shift, 55
- entropy, 33
- EOS, 3, 10
- EOSPAC, 55, 72
- equation of state

- $U_S - U_P$ , 53
- Becker-Kistiakowsky-Wilson Explosive (BKW-HE), 62
- Davis, 58
- exponential, 58
- Grüneisen, 53
- ideal gas, 50
- Jones-Wilkins-Lee, 52
- JWL, 52
- modified Osborne, 51
- polynomial, 51
- quadratic, 51
- SESAME, 54
- void, 50
- Euler equations, 28
- Eulerian
  - cell area, 24
  - cell vertices, 17
  - cell volume, 16
  - cell widths, 16
  - face areas, 16
- Eulerian cell, 16
- Eulerian mesh, 3
- Eulerian tracer, 195
- evolution equation
  - density, 10
  - velocity, 10
- expansion, 32, 50
- fine-particle sampling, 147
- finite difference approximation, 19
- finite difference equations, 2
  - arbitrary, 19
  - divergence, 26
  - gradient, 25
  - mass, 157
  - strain rates, 26
- first law of thermodynamics, 69
- flow stress model, 114
  - elastic-perfectly plastic, 114
  - Johnson-Cook, 116
  - Kospall, 120
  - Mechanical threshold stress, 118
  - modified Steinberg-Cochran-Guinan, 114
  - Preston-Tonks-Wallace, 117
  - Steinberg-Cochran-Guinan, 115
  - thermal softening, 120
- flux
  - computation, 39
  - foams, 55
  - Forest Fire, 96
  - fracture, 11, 43
    - Johnson Spall model, 128
    - Johnson-Cook damage model, 129
  - frame indifference, 181
  - Frank-Kamenetskii, 124
  - ghost cells, 21
  - governing equations, 3, 16, 18
  - Grüneisen relationship, 53
  - gradient limiters, 39
  - grid spacing, 18
  - Heaviside, 62
  - Henson-Smilowitz, 124
  - high explosive, 58
  - high-explosive, 52
  - homologous temperature, 129
  - Hooke's Law, 106
  - Hooke's law, 10
  - Hotspot, 124
  - Hugoniot, 51, 53
  - hydrocodes, 18, 29
  - hydrostatic pressure, 108
  - hydrostatic state of stress, 108
  - ideal gas, 69
  - ideal gas law, 50
  - incompressible, 12
  - inite difference equations, 18
  - initial conditions, 3, 7, 84
  - initial timestep, 169
  - integration, 42
  - interface
    - mixed cells, 18
    - multiple in a cell, 35
    - reconstruction, 34, 35
  - internal energy, 2, 12, 40
  - invariants, 11
  - irrotational, 12
  - isentropic sound speed, 68
  - isotropic, 10
  - Jaumann derivative, 182
  - Jaumann-Zaremba rate, 182
  - Johnson-Cook, 11

- Kospall, 11
- Lagrange interpolation, 193
- Lagrangian momentum equations, 33
- Lagrangian phase, 3, 29, 30, 39, 45, 80
- Lagrangian surface, 157
- Lagrangian tracer, 195
- Levi-Civita pseudotensor, 145, 177
- Lie derivative, 182
- linear momentum, 10
- mass, 3, 33
- mass flux, 39
- MATCH, 96
- material rotation, 11
- Maxwell Model, 124
- mechanical spalling, 128
- mesh
  - Eulerian, 3, 19, 30
- Mie-Grüneisen, 58
- momentum, 3
  - advection, 38
  - conservation, 10
  - conservation in advection, 39
  - equations, 10, 28, 29
- momentum control volume, 19
- momentum flux, 39
- Monte Carlo, 149
- Monte-Carlo, 18
- multi-material, 2, 35
- Multi-Shock Forest Fire, 96
- Navier-Stokes, 7, 10
- Newton-Raphson method, 57
- Noh problem, 77
- numerical approximation, 24
- operator splitting, 28
  - stability, 37
- orthogonal tensor, 181
- PAGOSA, 2
- particle speed  $U_P$ , 54
- PBX, 124
- PBX 9502, 61
- permanent deformation, 107
- permutation, 32
- phase transitions, 12, 55
- pin diagnostic, 191
- plane
  - behind, 152
  - in front of, 152
- plastic
  - strain, 46
- plastic behavior, 108
- plastic deformation, 107
- plastic work, 12, 43
- plasticity, 11
- porosity, 128
- Prandtl-Reuss treatment, 108
- predictor, 3, 7, 33
- predictor stage, 43
- predictor-corrector, 42
- pressure, 10, 12, 50
- priority, 35
  - advection, 35
- program burn, 52
- programmed burn, 80, 92
- proportional limit, 106
- pure cell, 147
- ramp treatment, 56
- Rankine-Hugoniot, 76
- rarefaction, 2
- reactive burn, 96
- Richtmyer, 76
- Rosenbluth, 76
- rotation terms, 183
- safec, 80, 169
- safed, 80
- safety factors, 80
- safeu, 80
- sampling
  - pathological cases, 148
- sampling density, 147
- scaling ratio, 55
- secant method, 58
- second invariant, 109
- second invariant  $J_2$ , 11
- section
  - hexagonal, 154
  - pentagonal, 153
  - quadrilateral A, 153
  - quadrilateral B, 154
  - triangular, 153
- SESAME body internal energy iteration, 57

- shear modulus, 11
- shock speed  $U_S$ , 54
- shock waves, 76
- shock-less heating, 77
- shock-to-detonation, 61
- skew-symmetric, 11
- sound speed, 55
  - derived, 68
  - detonation products, 71
  - exponential EOS, 73
  - Grüneisen, 71
  - ideal gas, 69
  - isentropic, defined, 68
  - JWL, 71
  - modified Osborne EOS, 70
  - PAGOSA internal, 73
  - polynomial EOS, 69
  - quadratic EOS, 70
  - SESAME, 72
  - void, 69
- sound speeds, 3
- spall, 11
- spall stress, 129
- spatial centering
  - mass, 17
  - pressure, 17
  - specific internal energy, 17
  - velocity, 17
- specific internal energy, 50
- staggered grid, 17
- Steinberg-Cochran-Guinan, 11
- strain, 46
- strain hardening, 121
- strain rate, 24
- strain rate splitting, 108
- strain rate tensor, 11, 177
- strain rates, 3, 26
- strength, 43
- stress deviator, 108
- stress deviators, 43
- stress-vs-strain, 106
  - idealized, 107
- SURF, 96
- tabular, 12
- TATB, 62
- Taylor expansion, 54
- tensor
  - deviatoric stress, 145
- tetrahedron, 152
- thermodynamic closure, 60
- Thomas-Fermi-Dirac, 51
- time centering, 32
- timestep, 2, 3, 7, 17–19, 80
- timestep controls
  - CFL condition, 80
  - Courant condition, 3
  - Courant number, 37, 68, 80
  - detonation speed, 80
  - divergence, 80
- total stress tensor, 10
- tracer particle, 195
- transport, 3, 30
- trapezoidal, 42
- upwind, 35, 37
- van der Waals loop, 66
- vertex, 17, 25
- vertex-centered, 2
- Viscoelasticity, 124
- void closure, 51
- volume fraction
  - advection, 34
  - change in compression, 32
  - in equation of state, 50
  - in pressure relaxation, 101
  - in void closure, 98
  - initial, 147
  - initial conditions, 84
- volume fractions, 18
- von Mises, 3
- von Mises yield, 111
- von Neumann, 2, 76
- vorticity tensor, 12, 177
- VPS, 124
- wall heating, 77
- Walsh-Christian temperature, 63
- Work hardening, 121
- work hardening, 107
- yield criterion, 109
- yield limiting algorithm, 111
- yield point, 106
- yield surface, 109
- Youngs/van Leer gradient limiter, 38

zone, 16, 18